UNIVERSITÉ AIX-MARSEILLE
École Doctorale Sciences de l'Ingénieur : Mécanique, Physique, Micro et Nanoélectronique

THÈSE DE DOCTORAT
SPÉCIALITÉ : Mécanique et Physique des Fluides

Sébastien LE MARTELOT

CONTRIBUTION À LA SIMULATION NUMÉRIQUE DIRECTE DE L'ÉBULLITION

Soutenue publiquement le 15 Novembre 2013

Composition du Jury :

Dr. Pierre BOIVIN - SAFRAN Snecma, Space Engines Division	(Invité)
Pr. Roland BORGHI - Ecole Centrale de Marseille, laboratoire LMA	(Examinateur)
Pr. Sébastien CANDEL - Ecole Centrale de Paris, laboratoire EM2C	(Examinateur)
Pr. Paul CLAVIN - Aix Marseille Université, laboratoire IRPHE	(Examinateur)
Dr. Vincent GIOVANGIGLI - Dir. Rech. CNRS, laboratoire CMAP	(Rapporteur)
Pr. Marc MASSOT - Ecole Centrale de Paris, laboratoire EM2C	(Rapporteur)
Dr. Olivier MINSTER - Agence Spatiale Européenne (ESA)	(Invité)
Pr. Boniface NKONGA - Université de Nice, laboratoire JAD	(Directeur de thèse)
Dr. Stéphane PETITOT - Centre National d'Etudes Spatiales (CNES)	(Invité)
Pr. Richard SAUREL - Aix Marseille Université, laboratoire IUSTI	(Directeur de thèse)

Table des matières

Nomenclature

Grandeurs associées aux phases

γ_k : Rapport entre la capacité calorifique à pression constante et la capacité calorifique à volume constant, de la phase k pour l'équation d'état des gaz parfaits. Coefficient sans dimension pour l'équation d'état "stiffened-gas".
$P_{\infty,k}$ (Pa) : Paramètre de l'équation d'état "stiffened-gas" traduisant les effets intermoléculaires attractifs, pour la phase k.
$C_{v,k}$ $(J.kg^{-1}.K^{-1})$: Capacité calorifique massique à volume constant de la phase k.
$C_{p,k}$ $(J.kg^{-1}.K^{-1})$: Capacité calorifique massique à pression constante de la phase k.
ρ_k $(kg.m^{-3})$: Densité de la phase k.
v_k $(m^3.kg^{-1})$: Volume spécifique de la phase k.
p_k (Pa) : Pression de la phase k.
e_k $(J.kg^{-1})$: Energie interne de la phase k.
q_k $(J.kg^{-1})$: Energie interne de référence de la phase k.
T_k (K) : Température de la phase k.
h_k $(J.kg^{-1})$: Enthalpie de la phase k.
s_k $(J.K^{-1}.kg^{-1})$: Entropie de la phase k.
g_k $(J.kg^{-1})$: Energie libre de Gibbs de la phase k.
c_k $(m.s^{-1})$: Vitesse du son de la phase k.
Y_k : Fraction massique de la phase k.
α_k : Fraction volumique de la phase k.
λ_k $(W.m^{-1}.K^{-1})$: Conductivité thermique de la phase k.
$Z_k(kg.m^{-2}.s)$: Impédance acousique de la phase k.

Grandeurs associées au mélange

ρ $(kg.m^{-3})$: Densité de mélange.
v $(m^3.kg^{-1})$: Volume spécifique de mélange.
$\mathbf{u}$ $(m.s^{-1})$: Vecteur vitesse de mélanges $\mathbf{u} = (u, v, w)^T$.
E $(J.kg^{-1})$: Energie totale de mélange.
λ_c $(W.m^{-1}.K^{-1})$: Conductivité thermique de mélange.
T (K) : Température de mélange.
P (Pa) : Pression de mélange.
q $(J.kg^{-1})$: Energie interne de référence de mélange.
$\mathbf{q}$ $(W.m^{-2})$: Vecteur représentant le flux de chaleur associé au mélange.

Autres

μ $(Pa^{-1}.s^{-1})$: Coefficient de relaxation des pressions.
λ $(kg.m^{-3}.s^{-1})$: Coefficient de relaxation des vitesses.
ν $(kg.J^{-1}.s^{-1})$: Coefficient de relaxation des potentiels chimiques.
H $(W.k^{-1}.m^{-3})$: Coefficient de relaxation des températures.
σ $(N.m^{-1})$: Coefficient de tension de surface.
κ (m^{-1}) : Courbure locale.
$\mathbf{g}$ (N) : Vecteur représentant la force de gravité.

Introduction générale

Cette thèse à pour objectif la simulation numérique directe (DNS) de la croissance de bulles de vapeur en paroi. La figure (1) montre un exemple du niveau de simulation à atteindre pour la prédiction de l'évolution d'une bulle de gaz dans un liquide.

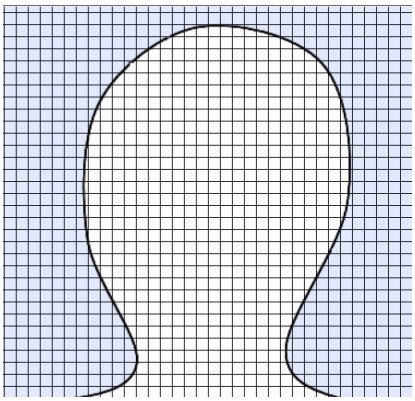

FIGURE 1 – Représentation schématique d'un domaine de calcul pour la simulation numérique directe de la croissance d'une bulle de vapeur dans un liquide.

La réalisation de ce type de simulation nécessite que les effets physiques internes aux phases et les interactions entre phases soient correctement modélisés et résolus. De ce fait, des maillages suffisamment fins sont requis pour pouvoir résoudre la structure de l'écoulement et les zones de forts gradients, en particulier à l'interface. Apparue il y a quelques décennies en turbulence, ce type d'approche s'est étendu à la mécanique des milieux hétérogènes ainsi qu'à la combustion. Une distinction doit néanmoins être précisée à ce niveau. En turbulence, la "simulation numérique directe" signifie que l'on s'intéresse à des structures très fines, qui ne sont pas considérées ici. En effet, par "simulation numérique directe" on entend résoudre les caractéristiques principales de l'écoulement intervenant lors de la croissance d'une bulle de vapeur (comme représenté sur la Figure 1).
L'approche développée dans ce manuscrit est relativement proche de la simulation numérique directe de flammes, à quelques nuances près. Par exemple, l'équation d'état subit de forts changements lors de la transition liquide-vapeur. De plus, les effets capillaires sont essentiels ici, alors qu'ils sont absents dans les flammes. Cependant, la réaction chimique (ou thermo-chimique) est ici très simple par rapport aux flammes, où une description cinétique détaillée est souvent nécessaire.

Les principales difficultés et différences vis-à-vis de la simulation numérique de flammes peuvent se résumer au travers des deux points suivants :
-Les équations fondamentales de l'écoulement ne sont pas bien connues, en particulier à cause des transferts de masse et de chaleur et du changement de comportement thermodynamique ayant lieu au travers des interfaces liquide-vapeur.
-Le comportement du liquide est celui d'un fluide incompressible tandis qu'il est primordial de considérer la compressibilité du gaz lors de la croissance "mécanique" de la bulle. Cette notion sera de nouveau abordée un peu loin dans cette introduction.

Contexte industriel

Au niveau des applications, cette thèse fait partie des recherches menées dans le cadre du développement du moteur cryotechnique Vinci, prévu pour propulser le dernier étage d'Ariane 6, la prochaine génération de lanceur d'Ariane Espace. La particularité principale de ce dernier étage réside dans sa capacité à être rallumé plusieurs fois lors d'une mission. Pour que les allumages successifs se déroulent correctement, l'hydrogène et l'oxygène doivent s'écouler à l'état liquide au travers des injecteurs, jusqu'à la chambre de combustion. Si ces conditions ne sont pas remplies, des instabilités d'allumage sont à attendre. Or, après chaque phase de fonctionnement, ou simplement sous l'effet du rayonnement solaire, les conduites et éléments solides sont à "haute température", c'est à dire environ 300K. Cette température est à comparer à la température maximale d'existence de l'hydrogène liquide (20K) et à celle de l'oxygène liquide (60K). Il est donc nécessaire de refroidir les conduites et éléments solides, ce qui est une opération non triviale. Le processus de refroidissement est complexe, à la fois de par l'utilisation de fluides à très basse température mais aussi à cause de la géométrie des divers canaux de refroidissement. Ces canaux sont représentés sur la Figure (2) qui montre la façon dont les fluides, oxygène et hydrogène, circulent au sein du moteur. Une des premières étapes de l'allumage du moteur est la mise en froid. Durant cette étape, de l'oxygène liquide est injecté dans les différentes zones du moteur de façon à refroidir les parois et organes solides, qui sont maintenus en présence d'oxygène liquide jusqu'à ce que le refroidissement soit complet. Seulement, la géométrie du moteur est telle que certaines zones ne peuvent pas être mises en froid de cette façon et se retrouvent ainsi très peu ou pas refroidies. C'est le cas, par exemple, des zones proches de la cavité d'injection. De ce fait, lors de la phase d'allumage, les liquides cryogéniques circulent dans ces zones non-refroidies provoquant l'apparition de vapeur, de bulles et d'hétérogénéités de toutes sortes. Ceci crée des problèmes durant le fonctionnement du moteur pouvant se traduire en instabilités de combustion.

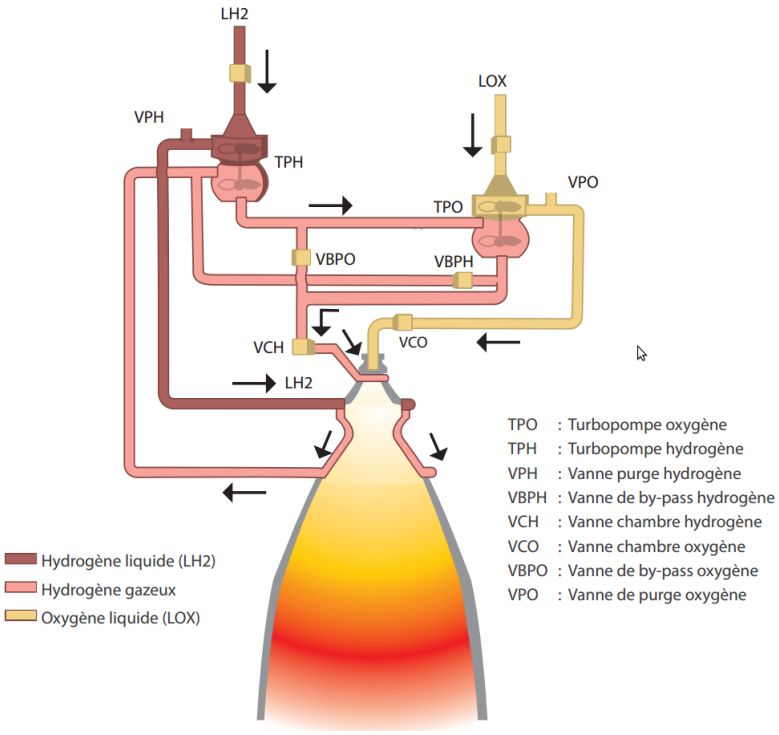

FIGURE 2 – Schéma du moteur Vinci représentant la circulation des fluides durant son fonctionnement (Source : Fiche produit du moteur Vinci).

De plus l'écoulement étant maintenant composé d'un liquide contenant des bulles de gaz, son comportement est totalement différent et devient complexe à prédire. Ce sont ces difficultés qui sont à l'origine des travaux présentés dans cette thèse au travers des problématiques suivantes :
-Quelles sont les conditions d'écoulement dans les zones qui ne peuvent pas être mises en froid ?
-Quels sont les transferts de chaleur aux parois à l'intérieur de ces zones durant l'allumage puis le fonctionnement du moteur ?
Il est très difficile de répondre à ces questions car il n'existe pas de corrélations d'échange de chaleur en régime instationnaire ainsi que pour des géométries aussi complexes. Ce manque est encore plus flagrant lorsque l'écoulement est diphasique. De ce fait, une solution est de réaliser la "simulation numérique directe" de l' écoulement diphasique (liquide-vapeur) à l'intérieur de ces zones dans le but d'en déduire des coefficients d'échange permettant de quantifier les transferts de chaleur et de masse au niveau des parois. Cependant, pour arriver à ces résultats, il faut s'assurer de la compréhension des phénomènes physiques mis en jeu ainsi que de leur résolution. On peut ainsi résumer les étapes nécessaires de la façon suivante :

1] Compréhension des phénomènes mis en jeu lors de l'ébullition.
2] Mise au point de modèles mathématiques et de schémas numériques adaptés.

3] Validation de l'approche choisie à travers la réalisation de simulations numériques dans des conditions simplifiées en présence de quelques sites de nucléations.
Pour ensuite apporter des réponses dans le domaine de l'ingénierie des systèmes spatiaux, il faut de plus :
4] Étendre la méthode pour la réalisation de simulations 3D d'ébullition avec de nombreux sites de nucléation.
5] Travailler sur l'efficacité des méthodes numériques car il s'agit de simulations très coûteuses en temps de calcul.
6] Prendre en compte les géométries complexes représentatives des géométries réelles.
7] S'assurer de la validation des simulations sur des solutions analytiques et sur des test en condition réelles.
8] Utiliser des fluides cryogéniques dans les simulations.
9] Déterminer les coefficients d'échanges.

Cette thèse a pour but d'apporter des éléments de réponse aux trois premières étapes de cette liste. De ce fait, on va tout d'abord s'intéresser à la modélisation des phénomènes physiques présents durant l'ébullition (présence d'une interface liquide-gaz, prise en compte de la compressibilité, capillarité, gravité, conduction de la chaleur, changement de phase...) pour ensuite construire un schéma numérique adapté au modèle et réaliser la simulation numérique d'écoulements bouillants.

État de l'art

La simulation numérique d'écoulements bouillants est un domaine difficile car il faut prendre en compte de nombreuses interfaces liquide-vapeur en présence d'effets physiques complexes. Il n'existe que peu de méthodes capables de traiter ce type d'écoulement. La plus naturelle est décrite dans les travaux de Tryggvason [81] et de Juric et Tryggvason [46] où les interfaces sont considérées comme des discontinuités dont la position est calculée par un algorithme de Front Tracking. La difficulté majeure de cette méthode concerne la détermination de la forme de l'interface et le déplacement associé. De façon schématique, ceci revient aux trois étapes suivantes :
-Détermination d'une fonction représentative de l'interface (polynômes, fonctions simples, etc.)
-Interpolation de cette fonction sur le maillage utilisé.
-Calcul de la nouvelle position de l'interface en utilisant une équation de transport.
-Correction de la position de l'interface suite à l'augmentation de pression et de volume dûe au transfert de masse.
Bien qu'efficace, cette méthode pose des problèmes pour des cas multi-dimensionnels lorsque la topologie de l'interface est complexe : il y a 800 cas particuliers de configuration d'interface à gérer en 3D [35]. De plus, il est assez difficile de déterminer l'état thermodynamique d'une maille contenant plusieurs fluides lorsqu'au moins l'un des deux est compressible.

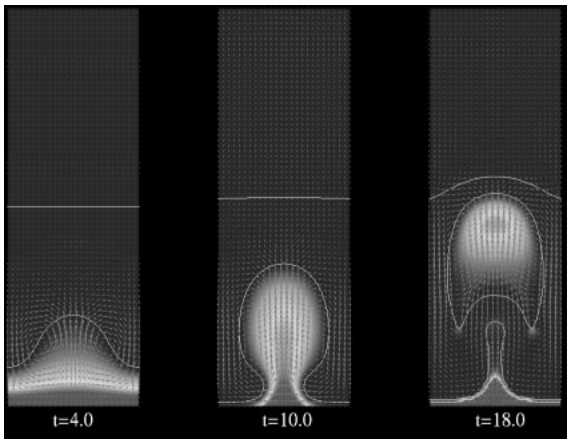

FIGURE 3 – Image extraite de la thèse de D. Juric (1996) représentant une simulation numérique d'ébullition en paroi à trois instants différents. Les lignes blanches représentent les interfaces liquide-vapeur tandis que les flèches représentent les vecteurs vitesse. Les températures sont représentées en niveau de gris. Les régions les plus chaudes sont proches du mur tandis que les régions les plus froides sont situées au sein du liquide. Ces résultats ont été obtenus par une méthode de suivi de front ("Front Tracking").

Les autres approches existantes considèrent les interfaces liquides/vapeur comme des zones diffuses. On peut ici distinguer deux classes de méthodes. La première classe est issue des travaux de Cahn et Hilliard [18] où toute la dynamique est pilotée par les gradients de densité et dans laquelle il est nécessaire de résoudre très finement l'interface pour prendre en compte les effets capillaires, comme montré dans le Système (1). Dans ce modèle de type Cahn-Hilliard-Korteweg (voir, par exemple, [34]), les effets capillaires sont pris en compte à travers le terme $\nu\rho grad\,(div\,(grad\,(\rho)))$, dont le caractère dispersif pose des difficultés numériques (épaisseur d'interface et approximation de l'opérateur). Ce modèle s'écrit :

$$\begin{aligned} &\frac{\partial \rho}{\partial t} + div\,(\rho \mathbf{u}) = 0 \\ &\frac{\partial \rho \mathbf{u}}{\partial t} + div\,(\rho \mathbf{u} \otimes u) + grad\,(P) = \nu\rho grad\,(div\,(grad\,(\rho))) \end{aligned} \tag{1}$$

ρ représente la densité, $\mathbf{u}$ le vecteur vitesse, P la pression et ν est lié à la tension de surface. Ceci pose des problèmes numériques (nécessité de résoudre une interface très mince ainsi qu'une équation contenant un terme de dispersion) et est limité au cas des fluides miscibles. En effet, la loi d'état $P = P(\rho)$ est de type cubique, ce qui pose la question de l'existence de la vitesse du son dans le mélange, en particulier dans la zone spinodale.
La seconde classe prends ses origines dans les méthodes de capture de choc ou de discontinuités avec l'utilisation de systèmes d'équations hyperboliques. Ces méthodes ne nécessitent pas une résolution fine des discontinuités, car les relations de saut sont directement issues de la formulation conservative des équations. De plus, contrairement au modèle de type Cahn-Hilliard, il n'est pas nécessaire de résoudre la structure interne des interfaces pour prendre en compte les effets capillaires [64]. Les méthodes de capture de discontinuités [36]

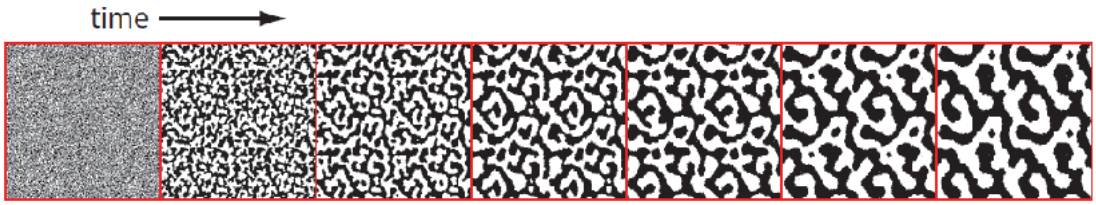

FIGURE 4 – Simulation numérique de la séparation de deux phases dans la zone spinodale réalisée avec une méthode de type Cahn-Hilliard[18]

sont maintenant très largement répandues en dynamique des gaz vis-à-vis des méthodes de suivi de front ([43],[61]). De nos jours, quasiment tous les outils de simulation résolvant des systèmes hyperboliques traitent les discontinuités (chocs et discontinuités de contact) comme des zones diffuses. En effet, il est plus simple et plus robuste de résoudre en tout point les même équations avec le même schéma numérique. Cependant, lorsqu'une interface entre deux fluides est présente, une discontinuité de loi d'état apparaît. De nombreuses méthodes, telles que les méthodes de suivi de front ([35], [81]) ou des méthodes de type Level Set ([30]), dont la méthode Ghost Fluid, ont été développées spécifiquement à cet usage.

Approche "interface diffuse"

La "philosophie" adoptée dans cette thèse consiste en la recherche d'équations et d'un schéma numérique pouvant être employés en tout point du domaine du calcul. Aussi bien dans le liquide pur que dans le gaz pur ainsi qu'à l'interface, qui sera capturée comme une zone diffuse.
La première méthode permettant de calculer correctement l'état thermodynamique (pression et température) au sein d'une maille mixte (contenant plusieurs fluides) est dûe à Saurel et Abgrall [70]. Les auteurs ont ainsi fait le choix de modéliser l'écoulement dans une maille mixte au moyen d'un modèle d'écoulement diphasique, sur la base du modèle de Baer et Nunziato [5], proposé initialement pour les milieux granulaires :

$$
\begin{aligned}
&\frac{\partial \alpha_1}{\partial t} + \mathbf{u}_I \cdot \mathbf{grad}\,(\alpha_1) = \mu(p_1 - p_2) \\
&\frac{\partial \alpha_1 \rho_1}{\partial t} + div\,(\alpha_1 \rho_1 \mathbf{u}_1) = 0 \\
&\frac{\partial (\alpha \rho \mathbf{u})_1}{\partial t} + div\,(\alpha \rho \mathbf{u} \otimes \mathbf{u} + \alpha P)_1 = p_I \nabla \alpha_1 + \lambda(u_2 - u_1) \\
&\frac{\partial (\alpha \rho E)_1}{\partial t} + div\,(\alpha(\rho E + P)\mathbf{u})_1 = (p_I \mathbf{u}_I)\nabla \alpha_1 + \lambda u_I'(u_2 - u_1) - \mu p_I'(p_1 - p_2) \\
&\frac{\partial \alpha_2 \rho_2}{\partial t} + div\,(\alpha_2 \rho_2 \mathbf{u}_2) = 0 \\
&\frac{\partial (\alpha \rho \mathbf{u})_2}{\partial t} + div\,(\alpha \rho \mathbf{u} \otimes \mathbf{u} + \alpha P)_2 = p_I \nabla \alpha_2 - \lambda(u_2 - u_1) \\
&\frac{\partial (\alpha \rho E)_2}{\partial t} + div\,(\alpha(\rho E + P)\mathbf{u}+)_2 = (p_I \mathbf{u}_I)\nabla \alpha_2 - \lambda u_I'(u_2 - u_1) + \mu p_I'(p_1 - p_2)
\end{aligned}
\tag{2}
$$

Ce modèle décrit le comportement de deux fluides en déséquilibre total. Chaque phase est décrite par un système d'équations de bilan (masse ($\alpha_k \rho_k$), mouvement ($\alpha_k \rho_k \mathbf{u}_k$) et énergie ($\alpha_k \rho_k E_k$)) contenant des termes non-conservatif ($p_I \nabla \alpha_1$,$\mathbf{u}_I \nabla \alpha_1$) traduisant les interactions entre les deux phases. De plus, ce système est complété par une équation de transport sur la fraction volumique de la phase 1 (α_1), permettant la localisation de l'interface et la détermination des deux pressions p_1 et p_2.

Pour ce modèle, mais aussi pour tous les autres modèles présentés dans ce manuscrit, une équation d'état par phase est nécessaire. Cette équation d'état doit garantir certaines propriétés, notamment la convexité de l'énergie par rapport à la densité et l'entropie [37]. Certaines équations d'états, telles que l'équation d'état des gaz parfaits, l'équation d'état "stiffened-gas" ou encore l'équation d'état de Mie-Gruneïsen, satisfont ces critères. Cependant, les équations d'état "cubiques", comme l'équation d'état de Van der Waals et ses extensions (Peng-Robinson, Redlich-Kwong, Benedict,...) ne les respectent pas dans tout le domaine des paramètres. En effet, dans le cadre d'un mélange diphasique, une zone dite "spinodale" apparaît. Dans cette zone, le carré de la vitesse du son est négatif. Les formulations de type Van der Waals sont donc à proscrire pour l'étude des milieux diphasiques. Dans ces travaux de thèse, l'équation d'état "stiffened-gas" ([40], [59]) est utilisée pour chacune des phases :

$$
p_k = (\gamma_k - 1)\rho_k(e_k - q_k) - \gamma_k P_{\infty,k} \tag{3}
$$

En effet, cette formulation, permet de décrire à la fois les gaz parfaits lorsque $P_{\infty,k} = 0$ et les milieux condensés lorsque $P_{\infty,k} > 0$. Le premier groupement de termes, $(\gamma_k - 1)\rho_k(e_k - q_k)$ traduit les effets d'agitation moléculaire d'origine thermique, q_k représentant l'énergie de formation du fluide. La deuxième partie de l'équation d'état, $-\gamma_k P_{\infty,k}$, représente les effets attractifs d'origine éléctromagnétique, responsables de la cohésion du milieu condensé.
Bien évidemment, le modèle qui précède (2) et ceux qui vont suivre peuvent être complétés par des lois d'états très diverses (voir [19] pour une application à la détonique). Cependant,

dans le cadre de ces travaux, l'équation d'état "stiffened-gas" contient les principaux effets nécessaires à la description d'un liquide et de sa vapeur, au moyen de deux lois d'état, une par phase. A partir de cette formulation (3), on peut déterminer les fonctions thermodynamiques associées :

$$\begin{aligned} h_k(T_k) &= \gamma_k C_{v,k} T_k + q_k \\ s_k(p_k, T_k) &= C_{v,k} ln\left(\frac{T_k^{\gamma_k}}{(p_k + P_{\infty,k})^{\gamma_k - 1}}\right) + s_{0,k} \\ g_k(p_k, T_k) &= (\gamma_k C_{v,k} - s_{0,k})\, T_k - C_{v,k} T_k ln\left(\frac{T_k^{\gamma_k}}{(p_k + P_{\infty,k})^{\gamma_k - 1}}\right) + q_k \end{aligned} \tag{4}$$

Où h_k, s_k et g_k représentent respectivement l'enthalpie, l'entropie et le potentiel chimique de la phase k. De ce fait, pour caractériser totalement l'état thermodynamique d'une phase, il est nécessaire déterminer les cinq paramètres γ_k, $P_{\infty,k}$, $C_{v,k}$, q_k, $s_{0,k}$ où $s_{0,k}$ représente l'entropie de réfèrence.
La détermination de ces paramètres s'effectue à partir des courbes thermodynamiques de référence, qui dépendent du matériaux et de la transformation étudiée (d'après la méthode présentée par Le Metayer et al [52]). En effet, les paramètres sont ajustés à partir de courbes de référence caractéristiques de la transformation étudiée. Par exemple, on utilisera la courbe d'Hugoniot si on s'intéresse à des applications faisant intervenir des chocs et on utilisera les courbes de saturation si on s'intéresse à des problèmes de transition de phase. Ainsi, si l'on prend par exemple le cas de l'eau liquide et de sa vapeur, on obtient les courbes suivantes (Fig. 5).

De ce fait, les paramètres (γ_k, $P_{\infty,k}$, $C_{v,k}$, q_k, $s_{0,k}$) ne sont valides que dans une gamme de température bien définie, qui est en général de quelques centaines de degrés. Il est ainsi important de vérifier que les températures présentes au sein de l'écoulement resteront dans la gamme de température choisie. De plus, une seconde limitation est à mentionner. En effet, si l'on étudie la dynamique d'ondes de choc en même temps que la transition de phase, ce ne sera possible que pour des chocs faibles.

Revenons maintenant au modèle diphasique hors d'équilibre représenté par le Système (2). L'idée principale des travaux de Saurel et Abgrall [70] consiste en l'utilisation d'un modèle où les phases évoluent en déséquilibre mais en présence de coefficients de relaxation mécanique (λ et μ) "raides". En d'autres termes, à chaque pas de temps, une force de traînée très intense et une relaxation de pression très rapide sont employées afin de forcer la condition d'équilibre mécanique $p_1 = p_2$, $u_1 = u_2$. En faisant en sorte d'obtenir la vitesse d'équilibre et la pression d'équilibre dans chaque maille de mélange à travers un processus de relaxation, les pressions et les vitesses normales des fluides de part et d'autre des interfaces deviennent égales. Les conditions d'interface entre fluides parfaits sont alors satisfaites. Le Système (2) est résolu en tout point par un unique schéma numérique complété par une étape de relaxation des pressions et des vitesses. La Figure 6 montre une interface liquide-gaz étalée sur plusieurs mailles, constituant la zone de mélange.

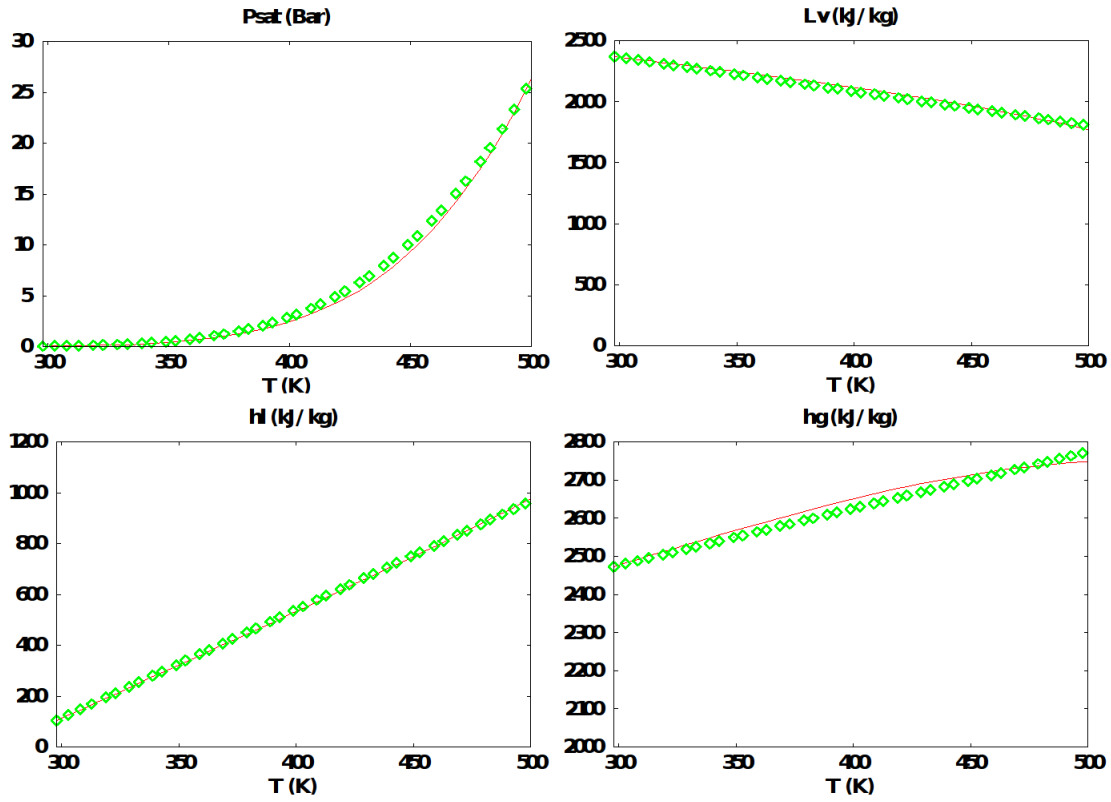

FIGURE 5 – Courbes de saturation expérimentales (en rouge) de l'eau liquide et sa vapeur et grandeurs obtenues avec l'équation d'état Stiffened-Gas (en symboles verts). Ces courbes représentent la pression de saturation (Psat), la chaleur latente de vaporisation (Lv), l'enthalpie du liquide (hl) et l'enthalpie du gas (hg). L'ajustement des paramètres a ici été réalisé pour une température comprise entre 300 et 500K.

Dans cette approche, l'interface est donc capturée au moyen d'un système hyperbolique relativement complexe et d'effets de relaxation raides. Cette approche a montré sa capacité à traiter des écoulements complexes, avec des rapports de pression et de densité très élevés, allant des détonations [66] des ondes de choc dans des milieux hétérogènes, en passant par les écoulements cavitants [66] ou encore les milieux élasto-plastiques-fluides [29]. De ce fait, cette approche peut être considérée comme robuste, précise et "multiphysique".

Cependant, il n'est pas toujours nécessaire de résoudre un modèle en déséquilibre complet (2) lorsque l'on s'intéresse à la simulation numérique d'écoulements diphasiques à interfaces. Pour certains types d'écoulements, comme les écoulements bouillants, il est possible d'utiliser des modèles réduits où les phases ont déjà atteint un certain niveau d'équilibre, ceci permettant une résolution numérique plus simple. On peut ainsi supposer que les deux phases sont, dans la zone interfaciale, toujours en équilibre mécanique [47], en équilibre mécanique et thermique ([25], [11]) ou encore en équilibre thermodynamique [22]. Ces différentes hypothèses

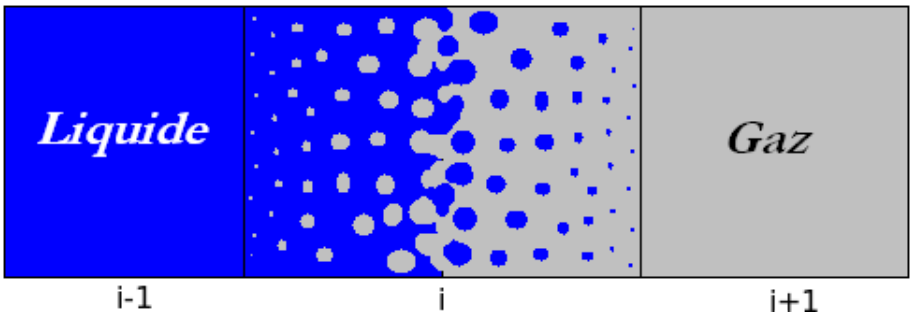

FIGURE 6 – Représentation de trois cellules de calcul successives entourant une interface liquide-gaz représentée par une zone de diffusion numérique considérée comme une zone de mélange. La fraction volumique de liquide évolue (de gauche à droite) de $1-\epsilon$ à ϵ. A l'intérieur de la zone de mélange, l'expansion/contraction des 'inclusions' va forcer l'équilibre des pressions. Un mécanisme similaire est utilisé pour forcer l'équilibre des vitesses. Cette méthode de relaxation "raide" des pressions et vitesses est employée pour satisfaire les conditions d'interface.

pourraient sembler trop restrictives car elles interdisent la prise en compte des nombreux phénomènes issus des déséquilibres mais il existe cependant des applications où certaines de ces hypothèses d'équilibre peuvent être considérées comme valides. A titre d'exemple, dans ce manuscrit sont à la fois présentés des résultats d'écoulement cavitant (Chapitre 1) et d'ébullition (Chapitre 3). Dans le cadre des écoulements cavitants, on a fait l'hypothèse d'équilibre mécanique pour les deux phases car les phénomènes dûs aux déséquilibres de vitesse et de pression sont du second ordre vis-à-vis de la simulation précise de la croissance des poches de cavitation où il est primordial de respecter les conditions d'interface. Pour cela, le modèle de Kapila et al [47], présenté ci-après (5) est utilisé :

$$
\begin{aligned}
&\frac{\partial \alpha_1}{\partial t} + \mathbf{u}\cdot\mathbf{grad}\left(\alpha_1\right) = K div\left(\mathbf{u}\right)\\
&\frac{\partial \alpha_1\rho_1}{\partial t} + div\left(\alpha_1\rho_1\mathbf{u}\right) = 0\\
&\frac{\partial \alpha_2\rho_2}{\partial t} + div\left(\alpha_2\rho_2\mathbf{u}\right) = 0 \qquad \text{où} \quad K = \frac{\rho_2 c_2^2 - \rho_1 c_1^2}{\frac{\rho_1 c_1^2}{\alpha_1} + \frac{\rho_2 c_2^2}{\alpha_2}}\\
&\frac{\partial \rho\mathbf{u}}{\partial t} + div\left(\rho\mathbf{u}\otimes\mathbf{u} + P\right) = 0\\
&\frac{\partial \rho E}{\partial t} + div\left((\rho E + P)\mathbf{u}\right) = 0
\end{aligned}
\tag{5}
$$

Où c_k représente la vitesse du son définie par $c_k^2 = \frac{\partial p_k}{\partial \rho_k}\Big)_{s_k}, k = 1, 2$, P la pression de mélange, E l'énergie totale de mélange, α_k la fraction volumique de la phase k et ρ_k représente la densité de la phase k. En utilisant une loi d'état de type Stiffened-Gas (3) par fluide, ce

système est fermé par la loi d'état de mélange suivante :

$$P = \frac{\rho e - (\frac{\alpha_1 \gamma_1 P_{\infty,1}}{\gamma_1 - 1} + \frac{\alpha_2 \gamma_2 P_{\infty,2}}{\gamma_2 - 1})}{\frac{\alpha_1}{\gamma_1 - 1} + \frac{\alpha_2}{\gamma_2 - 1}} \tag{6}$$

La vitesse du son de mélange est celle de Wood [87] :

$$\frac{1}{\rho c^2} = \frac{\alpha_1}{\rho_1 c_1^2} + \frac{\alpha_2}{\rho_2 c_2^2} \tag{7}$$

De plus, en l'absence de chocs, le Système (5) peut être complété par les équations d'entropies suivantes :

$$\frac{\partial \alpha_1 \rho_1 s_1}{\partial t} + div\left(\alpha_1 \rho_1 s_1 u\right) = 0, \qquad \frac{\partial \alpha_2 \rho_2 s_2}{\partial t} + div\left(\alpha_2 \rho_2 s_2 u\right) = 0. \tag{8}$$

En suivant un raisonnement analogue pour les écoulements bouillants, on a formulé l'hypothèse d'équilibre mécanique et thermique pour les deux phases. En effet, la présence de conduction thermique force la continuité de la température aux interfaces. En dehors des interfaces, utiliser l'hypothèse d'une température unique en tout point est conforme à la limite monophasique attendue. Dans le cadre de ce manuscrit, on a fait le choix d'utiliser le modèle suivant où les deux phases sont directement en équilibre mécanique et thermique :

$$\begin{aligned}
&\frac{\partial \rho}{\partial t} + div\left(\rho \mathbf{u}\right) = 0 \\
&\frac{\partial \rho \mathbf{u}}{\partial t} + div\left(\rho \mathbf{u} \otimes \mathbf{u} + P\underline{\underline{I}}\right) = 0 \\
&\frac{\partial \rho E}{\partial t} + div\left((\rho E + P)\mathbf{u}\right) = 0 \\
&\frac{\partial \rho Y_1}{\partial t} + div\left(\rho Y_1 \mathbf{u}\right) = 0
\end{aligned} \tag{9}$$

La diffusion thermique a été supprimée de façon à monter uniquement le modèle d'écoulement de base. La fermeture thermodynamique provient des relations $p_1 = p_2$, $T_1 = T_2$ et de la définition de l'énergie de mélange $\rho e = \alpha_1 \rho_1 e_1 + \alpha_2 \rho_2 e_2$. Elles conduisent à l'équation d'état de mélange :

$$P = \frac{1}{2}\left(A_1 + A_2 - (P_{\infty,1} + P_{\infty,2})\right) + \sqrt{\frac{1}{4}\left(A_2 - A_1 - (P_{\infty,2} - P_{\infty,1})\right)^2 + A_1 A_2} \tag{10}$$

Où $A_k = \dfrac{Y_k\left(\gamma_k - 1\right) C_{v,k}}{Y_1 C_{v,1} + Y_2 C_{v,2}}\left(\rho(e - q) - P_{\infty,k}\right)$ et $q = Y_1 q_1 + Y_2 q_2$.

La vitesse du son de mélange est définie par :

$$c^2 = \frac{1}{2}\left((e-q)(a_1+a_2) + \frac{\frac{1}{2}\left.\frac{\partial R_1}{\partial \rho}\right)_e R_1 + \left.\frac{\partial R_2}{\partial \rho}\right)_e}{\sqrt{\frac{1}{4}R_1R_1 + R_2}} + \frac{P}{\rho^2}\left(\rho(a1+a2) + \frac{\frac{1}{2}\left.\frac{\partial R_1}{\partial e}\right)_\rho R_1 + \left.\frac{\partial R_2}{\partial e}\right)_\rho}{\sqrt{\frac{1}{4}R_1R_1 + R_2}} \right)\right) \tag{11}$$

Où,

$a_1 = \frac{Y_1(\gamma_1-1)C_{v,1}}{Y_1C_{v,1}+Y_2C_{v,2}}$, $a_2 = \frac{Y_2(\gamma_2-1)C_{v,2}}{Y_1C_{v,1}+Y_2C_{v,2}}$,

$R_1 = a_2\rho(e-q) - a_2P_{\infty,2} - a_1\rho(e-q) + a_1P_{\infty,1} - P_{\infty,2} + P_{\infty,1}$,

$R_2 = a_1a_2(\rho(e-q) - P_{\infty,1})(\rho(e-q) - P_{\infty,2})$.

Des détails théoriques sur la propagation du son au sein de matériaux avec relaxation peuvent être trouvés, par exemple, dans [86].

De plus, en l'absence de chocs, le Système (9) peut être complété par l'équation d'entropie suivante :

$$\frac{\partial \rho S}{\partial t} + div\,(\rho S\mathbf{u}) = 0 \tag{12}$$

Où $S = Y_1s_1 + Y_2s_2$.

En utilisant l'équation d'état Stiffened-Gaz (3), les entropies des phases peuvent s'exprimer en utilisant les relations données dans [52] :

$$s_k = C_{v,k} ln\left(\frac{T^{\gamma_k}}{(P+P_{\infty,k})^{\gamma_k-1}}\right) \tag{13}$$

Ce modèle n'est pas sans rappeler les modèles type Euler multi-constituant utilisés pour décrire les mélange de gaz réactifs. La différence majeure avec ce type de modèle est qu'on utilise ici une loi d'état de mélange diphasique en lieu et place de la loi de Dalton, utilisée pour les mélanges de gaz parfaits. En effet, dans cette loi chaque phase occupe tout le volume disponible, ce qui n'a que de peu de sens lorsque l'on traite des mélanges liquide/gaz où chaque phase n'occupe qu'une partie du volume total. Le Système (9) sera ainsi le modèle de base pour le traitement des interfaces évaporantes. Bien évidemment, il sera nécessaire de le compléter par d'autres effets physiques tels que les effets capillaires, la diffusion de la chaleur ou encore la relaxation thermodynamique. Au préalable, sans insérer de physique supplémentaire, une difficulté principale apparaît pour la résolution numérique.

Difficultés liées aux faibles nombres de Mach

Dans le contexte des écoulements bouillants, où l'importance du changement de phase requiert la prise en compte de la compressibilité d'au moins une phase, une nouvelle contrainte est à prendre en compte. Dans notre approche, la compressibilité des deux phases, y compris celle du liquide, est considérée. Ceci est essentiel, par exemple pour la modélisation des

écoulements cavitants, comme on le verra plus loin. Ainsi, dans l'approche préconisée dans ce mémoire, le mouvement des bulles de vapeur au sein de la phase liquide met en jeu des nombres de Mach très faibles, ce qui rend difficile l'obtention de solutions numériques fiables dans le cadre d'une modélisation compressible résolue avec des schémas numériques de type Godunov. En effet, si l'on s'intéresse à la limite asymptotique des équations de la mécanique des fluides lorsque le nombre de Mach tends vers zéro on peut remarquer qu'il existe deux types de solutions :
-Les solutions où l'écoulement est considéré comme incompressible.
-Les solutions correspondant à la limite acoustique.
De ce fait, si l'on prend l'exemple d'un écoulement de liquide, il est naturellement compréhensible que la limite physique attendue soit la limite incompressible. Cependant, lorsque le schéma de Godunov est utilisé (ou n'importe quel schéma numérique utilisé pour résoudre des systèmes hyperboliques), les solutions obtenues tendent vers les solutions acoustiques, ce qui entraîne de nombreuses erreurs. Afin de remédier à ces défauts, une méthode de pré-conditionnement pour les équations d'Euler fut proposée par Turkel [82]. Il s'agit de modifier l'équation sur la pression comme suit :

$$\frac{1}{M_{ref}^2}\frac{\partial P}{\partial t} + u\frac{\partial P}{\partial x} + \rho c^2 \frac{\partial u}{\partial x} = 0 \tag{14}$$

Où M_{ref} est un nombre de Mach de référence compris entre 0 et 1 pouvant être arbitraire ou égal au nombre de Mach local en chaque point de l'écoulement.
Cette modification permet d'obtenir des solutions numériques qui convergent vers les solutions incompressibles d'écoulements à faible nombres de Mach, comme par exemple les écoulements d'air autour de profils d'ailes d'avions.
Cependant, il est important de noter que dans l'article de Turkel, le but est uniquement de converger vers des solutions stationnaires d'écoulements monophasiques. Ainsi les équations sont résolus en variables physiques (ρ, u, p), ce qui signifie que la présence de discontinuités est exclue. De ce fait, cette méthode, telle qu'elle est présentée dans les travaux de Turkel [82], ne peut pas être utilisée pour des simulations d'écoulements instationnaires en présence d'interfaces (cavitation, ébullition,...) mais aussi d'écoulements monophasiques à nombres de Mach quelconques (régime subsonique, sonique ou supersonique). Il est donc nécessaire de mettre au point des variantes de cette méthode pour des écoulements multiphasiques instationnaires.
L'extension de cette méthode aux écoulements monophasiques à tout nombre de Mach fut réalisée par Guillard et Viozat [38] tandis que la première extension multiphasique, pour le modèle de Kapila [47] où les phases sont en équilibre mécanique, fut développée par Murronne et Guillard [62]. Une autre méthode, mais appliquée à la résolution du modèle de Kapila [47] par la méthode de Saurel et al [74] est présentée dans le Chapitre 1 de ce manuscrit. Cette formulation est nécessaire car :
-La positivité des fractions volumiques n'est assurée que par la méthode de Saurel et al [74], ce qui assure la robustesse des simulations.
-La convergence vers les solutions exactes diphasiques présentées plus loin dans ce manuscrit nécessite cette formulation.

Cependant, il faut noter que l'utilisation de ce type de pré-conditionnement doit être restreint aux zones où le nombre de Mach est faible. En effet, là où le nombre de Mach n'est plus considéré comme faible, les effets de compressibilité sont importants et il ne faut plus forcer la convergence vers une écoulement "incompressible". Ce type de réflexion est important lorsque que l'on traite, par exemple, des écoulements cavitants car le nombre de Mach va être très faible dans le liquide mais sera supérieur à un dans le ou les poche(s) de cavitation, la vitesse du son ayant un comportement complexe (non-monotone par rapport à la fraction volumique). Aussi, il faut mettre en place une gestion du pré-conditionnement. Pour les travaux présentés dans ce manuscrit, on a choisi d'utiliser les règles suivantes pour le calcul du nombre de Mach de référence dans chaque maille de calcul i :

$$M_{ref}^{i} = \begin{cases} 1, \text{ si } M_i \geq 0.3 \\ M_i, \text{ si } 0.3 > M_i > M_{ref,min} \\ M_{ref,min}, \text{ si } M_i \leq M_{ref,min} \end{cases} \tag{15}$$

On considère ainsi que l'on ne doit plus utiliser de pré-conditionnement aux endroits où le nombre de Mach dépasse 0.3. De plus, une limite inférieure pour le nombre de Mach de référence local, $M_{ref,min}$, est mise en place car la vitesse du son obtenue à partir de l'équation de pression modifiée (14) peut être singulière lorsque le nombre de Mach de référence est très faible.
Bien que performante, cette méthode présente une forte contrainte de stabilité. Remarquée par Turkel et explicitée par Birken et Meister [15], cette contrainte modifie le pas de temps de la façon suivante :

$$\Delta t \leq M_{ref} \frac{\Delta x}{C_{max}} \tag{16}$$

Où Δx représente le pas d'espace, M_{ref} le nombre de Mach de référence et C_{max} la vitesse de l'onde la plus rapide à l'intérieur du domaine de calcul.
Ainsi, plus les nombres de Mach sont faibles au sein de l'écoulement plus le pas de temps numérique est réduit, augmentant fortement le temps de calcul nécessaire. A titre d'exemple, si l'on considère une bulle de vapeur se déplaçant à une vitesse d'un mètre par seconde dans un liquide, les nombre de Mach dans ce fluide sont alors de l'ordre de 10^{-3}, ce qui amène à diviser le pas de temps numérique par 1000. Les temps de calculs deviennent alors déraisonnables et il est nécessaire d'outrepasser cette contrainte si l'on souhaite être capable de réaliser des simulations numériques 2D ou 3D.
Dans le cadre des travaux présentés dans ce manuscrit, la solution retenue pour passer outre cette contrainte temporelle est la construction d'un schéma numérique implicite de type Godunov. Ceci revient à mettre à point un schéma implicite dans lequel seront prises en compte les contributions des termes conservatifs et non-conservatifs, ce qui implique l'utilisation de méthodes spécifiques pour chaque équation.
Une fois la solution numérique obtenue, il faut s'assurer de sa validité. En effet, bien qu'il existe des solutions exactes de problèmes de Riemann (monophasique ou diphasique) ou encore d'écoulements 1D de gaz parfait en tuyère, il est difficile de valider les techniques de préconditionnement faible Mach présentées précédemment pour des écoulements diphasiques.

Solutions de référence

En effet, la notion de validation devient très vite problématique lorsque l'on traite des écoulements multiphasiques. Pour reprendre l'exemple des profils d'ailes d'avions, il n'existe pas de solution analytique ou de référence lorsque l'on s'intéresse à des écoulements diphasiques, tel un écoulement d'eau contenant des bulles de gaz, autour de ces profils. Il devient ainsi très difficile de s'assurer de la fiabilité des résultats numériques.
Pour palier à ce manque de solutions permettant de valider les approches numériques, on s'est intéressé aux écoulements diphasiques à l'intérieur de tuyères ou de canaux de type Venturi [54]. En effet, de par leur grande flexibilité (le type d'écoulement obtenu ne dépendant que des variations de section droite et des conditions d'entrée/sortie), il est possible d'obtenir une grande variété d'écoulements. Il a été ainsi possible de déterminer des géométries et des conditions aux limites telles que les écoulements de liquide ou les écoulements diphasiques considérés aient des nombres de Mach très faibles. Cette flexibilité permet d'obtenir des cas tests représentatifs pour les méthodes de pré-conditionnement présentées précédemment. Une fois ces cas disponibles, des solutions analytiques de références ont été développées pour toutes les conditions d'écoulement en tuyère 1D. Pour cela, en s'inspirant des solutions analytiques bien connues d'écoulements unidimensionnels de gaz parfaits en tuyère, des solutions similaires ont été mises au point pour plusieurs cas limites d'écoulements diphasiques :
-Les deux phases sont en équilibre mécanique (équilibre des pressions et des vitesses).
-Les deux phases sont en équilibre mécanique et thermique (équilibre des pressions, des vitesses et des températures).
-Les deux phases sont en équilibre thermodynamique (équilibre des pressions, des vitesses, des températures et potentiels chimiques).
Ces cas représentent des cas limites où certains processus de relaxation (mécanique, thermique ou thermodynamique) sont considérés comme achevés. Bien entendu, ces solutions restant purement uni-dimensionnelles elles n'ont pas vocation à représenter la véritable physique des écoulements diphasiques en tuyères où de multiples phénomènes multi-dimensionnels tels que la cavitation par poches, jouent un rôle très important (Figure 7).

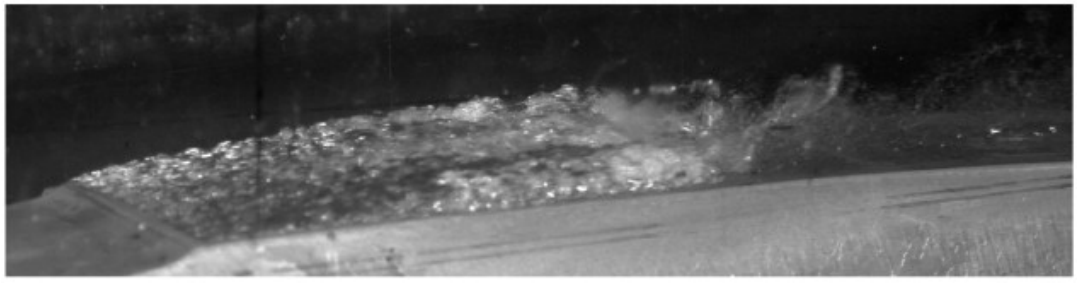

FIGURE 7 – Poche de cavitation stationnaire au col d'un canal hydraulique de type Venturi. Expériences conduites par Stéphane Barre au LEGI [10].

Néanmoins, l'existence de telles solutions de référence permet de valider précisément les schémas numériques utilisés à travers de simples écoulements 1D. De plus, il est aussi im-

portant de remarquer, que, bien que limitées au niveau de leur validité physique, ces solutions permettent de mettre en avant les comportements complexes et non-intuitifs des mélanges diphasiques.
Ainsi, ces solutions ont permis de vérifier la validité de l'ensemble (schéma numérique implicite et pré-conditionnement faible Mach) sur des cas d'écoulements diphasiques 1D en tuyères, et ce aussi bien pour le modèle en équilibre mécanique (5) que pour le modèle en équilibre méanique et thermique (9). Un exemple de ce type de solution est donné dans l'annexe B du Chapitre 1 tandis que la construction de ces solutions de référence dans le cas général fait l'objet du Chapitre 2 de ce manuscrit.
Les Figures 8 et 9 montrent des exemples d'écoulements diphasique eau liquide/air obtenus dans le cadre du modèle d'écoulement en équilibre mécanique (5). Sur ces courbes, sont représentés les profils de pression adimensionnés, de nombre de Mach et de fraction volumique d'eau liquide en fonction de plusieurs rapports de pression, $PR = \frac{P_{out}}{P_0}$, P_{out} représentant la pression imposée en sortie et P_0 la pression réservoir . Les rapport de pression critiques correspondants sont : cpr1= 0.80974, cpr2= 0.40989 et cpr3= $6.98159.10^{-8}$.
Il est important de remarquer que toutes les solutions présentées mettent en jeu des nombres de Mach très faibles (10^{-2}), que ce soit uniquement dans le convergent ou dans toute la tuyère. De ce fait, au vu des erreurs de convergence numérique obtenues en présence de faibles nombres de Mach, il est primordial d'utiliser une méthode de pré-conditionnement adaptée aux écoulements diphasiques pour obtenir des solutions numériques précises.

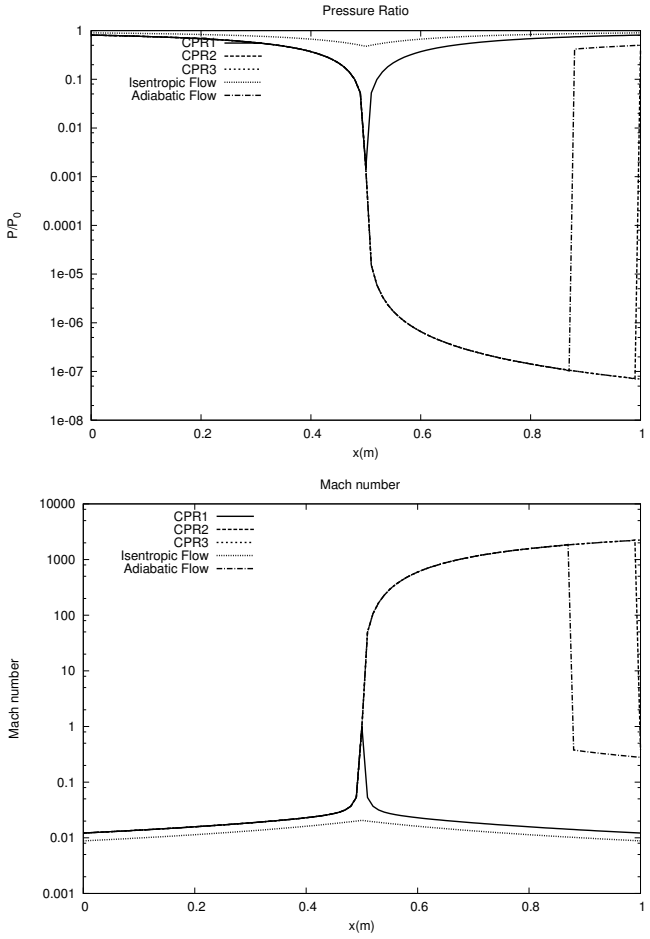

FIGURE 8 – Profils de pression adimensionnés et de nombre de Mach à l'intérieur de la tuyère pour différentes pressions de sortie correspondants à un col sonique (cpr1), à un écoulement isentropique supersonique (cpr3), à un écoulement avec un choc stationnaire en sortie (cpr2), à un écoulement subsonique isentropique (PR = 0.9) et à un choc stationnaire dans le divergent (PR = 0.5).

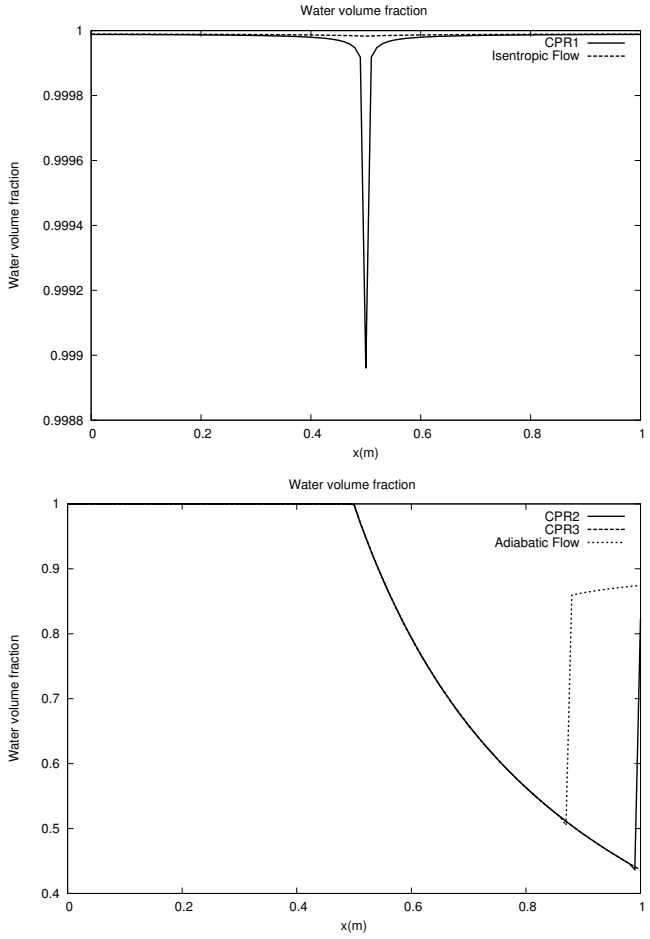

FIGURE 9 – Profil de fraction volumique d'eau liquide à l'intérieur de la tuyère pour différentes pressions de sortie correspondants à un col sonique (cpr1), à un écoulement isentropique supersonique (cpr3), à un écoulement avec un choc stationnaire en sortie (cpr2), à un écoulement subsonique isentropique (PR = 0.9) et à un choc stationnaire dans le divergent (PR = 0.5).

Cavitation

Une fois validé par rapport à ces solutions exactes, mais idéales, (car unidimensionnelles) l'outil de simulation multi-dimensionnel a été utilisé pour simuler en deux dimensions d'espace des écoulements cavitants tels que ceux présentés dans la Figure 7. Le modèle et les méthodes numériques utilisés, couplés à un processus de relaxation thermodynamique (abordé plus loin dans ce manuscrit), ont permis la reproduction des résultats expérimentaux en termes de longueur de poche et de fréquence de détachement sans utiliser un quelconque paramètre ajustable, ni modèle de turbulence (Figure 10) [53]. Un tel accord, sans ajustement, n'avait jamais été obtenu précédemment. Ces résultats permettent de valider l'approche détaillée jusqu'à présent sur un cas simplifié par rapport à l'ébullition, mais néanmoins complexe. Ce cas est simplifié par rapport à l'ébullition car la conduction et la

capillarité n'ont à priori pas d'effet dans le domaine de la supercavitation par poches.

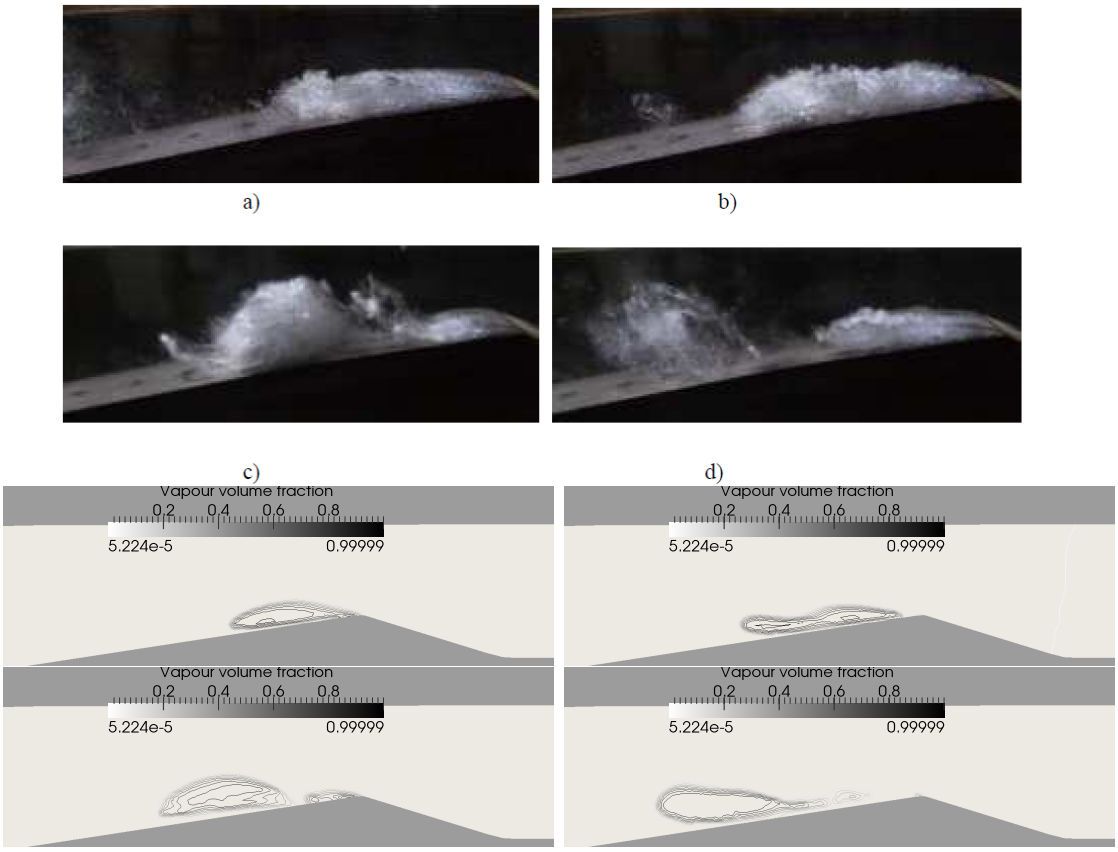

FIGURE 10 – Photos d'un cycle d'apparition et séparation de poches de vapeur dans le Venturi 8° du LEGI et contours de fraction volumique de vapeur d'eau obtenus numériquement (apparition de poche, étirement, striction, contraction). Cet exemple de cycle montre que les même quatre étapes sont observées numériquement et expérimentalement. La longueur de longueur de poche (45mm) et la fréquence du cycle expérimentales (45 Hz) sont parfaitement obtenues avec l'outil de simulation.

Ce cas particulier, où sont pris en compte un liquide et sa vapeur, montre ainsi, que l'approche "interfaces diffuses" permet aussi de traiter la séparation entre un milieu pur et un mélange, en satisfaisant les conditions d'interface.

Extension du modèle pour l'ébullition

Le but principal de ces travaux étant la simulation numérique de l'ébullition, l'étape suivante est la prise en compte des phénomènes physiques présents lors de l'ébullition.
Des tentatives dans cette direction, sur la base d'une approche "interfaces diffuses" ont été entreprises auparavant [27] [28]. Ici, on revient sur le modèle d'écoulement (9) et on va maintenant s'intéresser à la prise en compte des différents phénomènes physiques tels que la capillarité, la gravité, la conduction de la chaleur ou encore le changement de phase [55] (Figure 11).

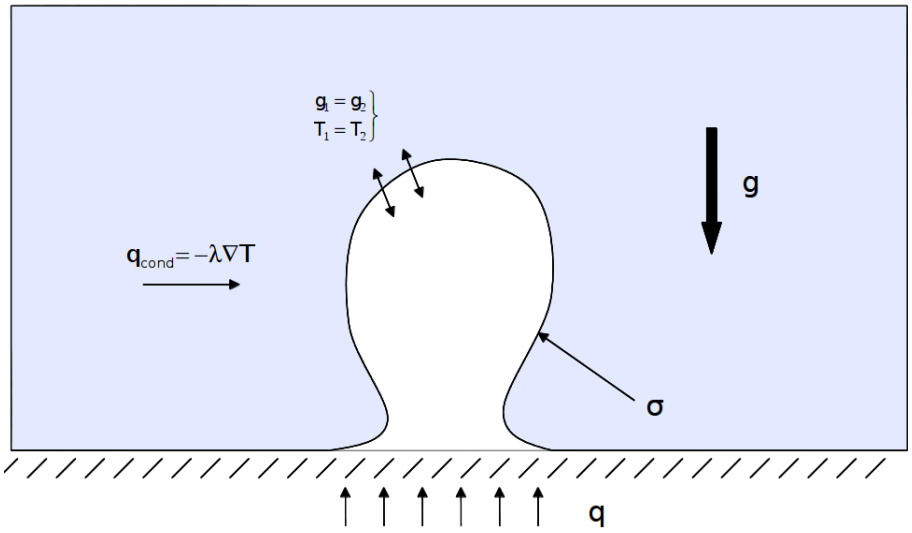

FIGURE 11 – Schématisation de la croissance d'une bulle à partir d'un site de nucléation isolé. Les différentes forces mises en jeu (capillarité et gravité) ainsi que les flux thermiques sont représentés.

Au niveau de la modélisation, les forces de gravité sont prises en compte de façon conventionnelle, $F_g = \rho \mathbf{g}$, tandis que la prise en compte de la capillarité au sein du modèle d'écoulement diphasique s'effectue en utilisant la méthode CSF (Continuum Surface Force) proposée par Brackbill [16]. Cette méthode fournit une écriture sous forme de force volumique de la tension de surface, permettant ainsi une prise en compte simplifiée des forces capillaires :

$$\mathbf{F}_\sigma = \sigma \kappa \overrightarrow{\nabla C} \tag{17}$$

Dans cette formule κ représente la courbure locale, σ la tension superficielle et C est une fonction de présence dont le but est de localiser l'interface entre les deux phases.
Bien que cette méthode ait montré son efficacité [64] [17], elle nécessite un calcul précis de la courbure locale et des gradients de la fonction de présence. De plus, elle est très dépendante de la façon dont est capturée l'interface. En effet, le but étant de réaliser une simulation numérique directe utilisant une approche d'interfaces diffuses, chaque interface est étalée sur plusieurs mailles de calcul. De ce fait, il est nécessaire de tenir compte des effets de diffusion

numérique de l'interface si l'on souhaite calculer correctement les effets capillaires tout au long de la simulation. C'est un des rôles de la fonction de présence.

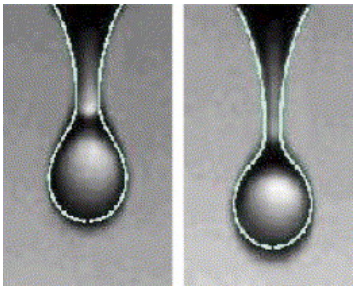

FIGURE 12 – Simulation numérique de la chute d'une goutte d'eau en utilisant la méthode CSF [16]. La solution numérique (en blanc) est superposée aux résultats expérimentaux. Ces résultats issus des travaux de Perigaud et Saurel [64] montrent un très bon accord entre les résultats numériques et expérimentaux.

La troisième partie du Chapitre 3 de ce manuscrit détaille la technique utilisée pour construire une fonction de présence telle que la tension de surface soit toujours correctement prise en compte.
Un autre point crucial de la simulation d'écoulement bouillant est la prise en compte de la conduction de la chaleur. Celle-ci est modélisée en par la loi de Fourier par fluide, appliquée à chaque fluide :

$$\mathbf{q}_k = -\lambda_k \overrightarrow{\bigtriangledown T_k}. \tag{18}$$

λ_k représente la conductivité thermique du fluide k et T_k sa température.
En utilisant cette approche dans le cadre du modèle hors équilibre (2) et en effectuant les développements asymptotiques nécessaires à l'obtention du modèle (9), on obtient uniquement une modification sur l'équation de conservation de l'énergie totale,

$$\frac{\partial \rho E}{\partial t} + div\left((\rho E + P)\mathbf{u}\right) + div\left(\mathbf{q}\right) = 0, \tag{19}$$

avec $\mathbf{q} = -\lambda_c \overrightarrow{\bigtriangledown T}$ et $\lambda_c = \alpha_1\lambda_1 + \alpha_2\lambda_2$. λ_c représente la conductivité thermique du mélange, λ_k la conductivité thermique de la phase k et T la température.

En ce qui concerne les transferts de masse, on va considérer une relaxation "instantanée" des deux phases vers l'équilibre thermodynamique. De même que pour les relaxations de pressions et de vitesse à taux infini évoquées précédemment (commentaires relatifs au Système 2 et Figure 6), cette méthode est utilisée au sein des zones de mélange (Figure 13).

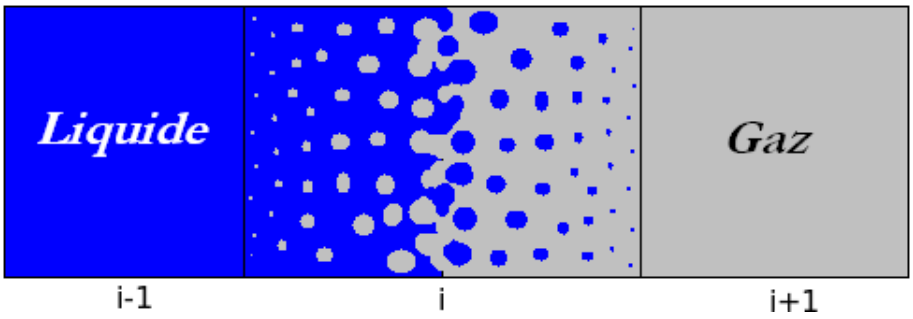

FIGURE 13 – Interface liquide-gaz représentée par une zone de diffusion numérique considérée comme une zone de mélange. La fraction volumique de liquide évolue (de gauche à droite) de $1 - \epsilon$ à ϵ. A l'intérieur de la zone de mélange, une méthode de relaxation "raide" des potentiels chimiques est utilisée pour atteindre l'équilibre thermodynamique dans la zone de mélange.

Il est important de remarquer que, dans le cadre cette méthode, le changement de phase est réalisé de façon cinétique et non pas de façon thermodynamique. En effet, comparée aux équations d'état cubiques, de type van der Walls, cette méthode permet de s'assurer de la positivité du carré de la vitesse du son dans la zone spinodale. La Figure 14 explique les principales différences entre ces deux approches.

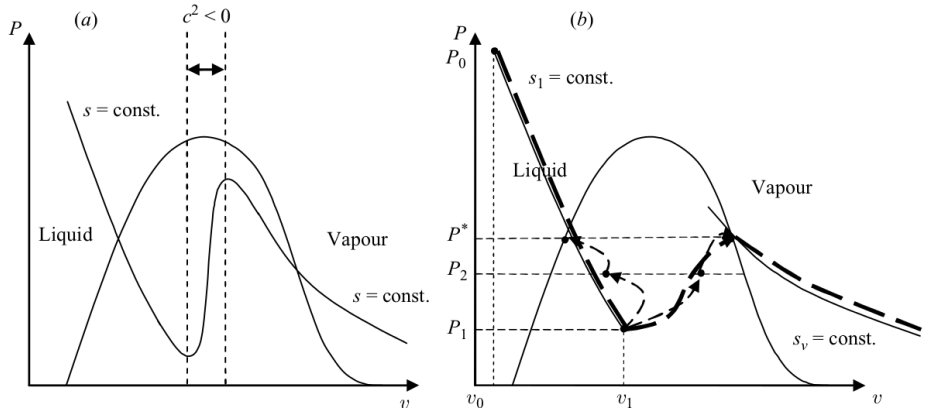

FIGURE 14 – Représentation schématique du chemin thermodynamique obtenu en utilisant une équation d'état cubique comparé à celui obtenu en utilisant un processus cinétique. (a) Avec une équation d'état cubique, l'hyperbolicité est perdue dans la zone spinodale. (b) Le modèle actuel consiste en la connexion de l'isentrope du liquide avec l'isentrope de la vapeur. Comme aucun chemin thermodynamique n'est défini, la vitesse du son de mélange reste toujours définie. Son expression est donnée plus loin.

Dans l'approche cinétique (interfaces diffuses), en considérant un liquide métastable (fin de l'isentrope de liquide), on obtient, à volume constant, un mélange de vapeur et de liquide en déséquilibre. La production de vapeur fait alors augmenter la pression. Durant l'évolution

cinétique, les points hors équilibre de vapeur et de liquide se déplacent vers les courbes de saturation. Les phases sont supposées en équilibre mécanique et thermique à chaque étape. Lorsque l'équilibre thermodynamique est atteint, le liquide et la vapeur ont atteint des états situés sur leurs courbes de saturation respectives. Puis, si le volume spécifique augmente, la concentration à l'équilibre évolue et, dans un cas limite, la vapeur évolue le long d'une isentrope issue de la courbe de saturation. Il est intéressant de noter que, lorsque les différents états hors équilibre sont omis, la transformation globale (pointillés en gras sur la Figure 14), composée de deux chemins thermodynamiques et d'un chemin cinétique, se rapproche de celle obtenue avec une loi de type van der Waals. Cette méthode a déjà été utilisée de façon intensive sur des problèmes variés, tels que la cavitation, l'évaporation flash et maintenant l'ébullition. On peut ainsi citer des validations [73] réalisées à partir des expériences menées en tube à choc par Simoes-Moreira et Shepherd [78]. La Figure 15 représente la configuration de ces expériences tandis que la Figure 16 montre une partie des résultats expérimentaux obtenus. Le front d'évaporation se propageant vers le bas.

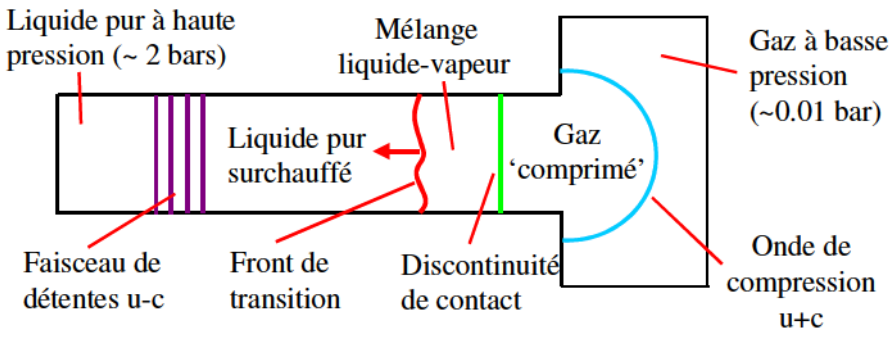

FIGURE 15 – Schéma du type d'expérience réalisé par Simoes-Moreira et Shepherd.

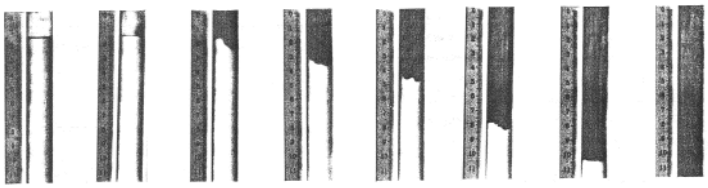

FIGURE 16 – Propagation d'un front de changement de phase tel qu'observé expérimentalement.

Dans ces expériences, du dodécane liquide est gardé stable à une température donnée et est violemment détendu par la mise en contact avec une chambre basse pression. Un front d'évaporation se propage alors dans le dodécane liquide métastable en éjectant un mélange liquide-vapeur à haute vitesse. La vitesse de ce front a été mesurée pour différentes

températures initiales du dodécane liquide. La figure (17) montre les différentes vitesses de front obtenues expérimentalement et numériquement.

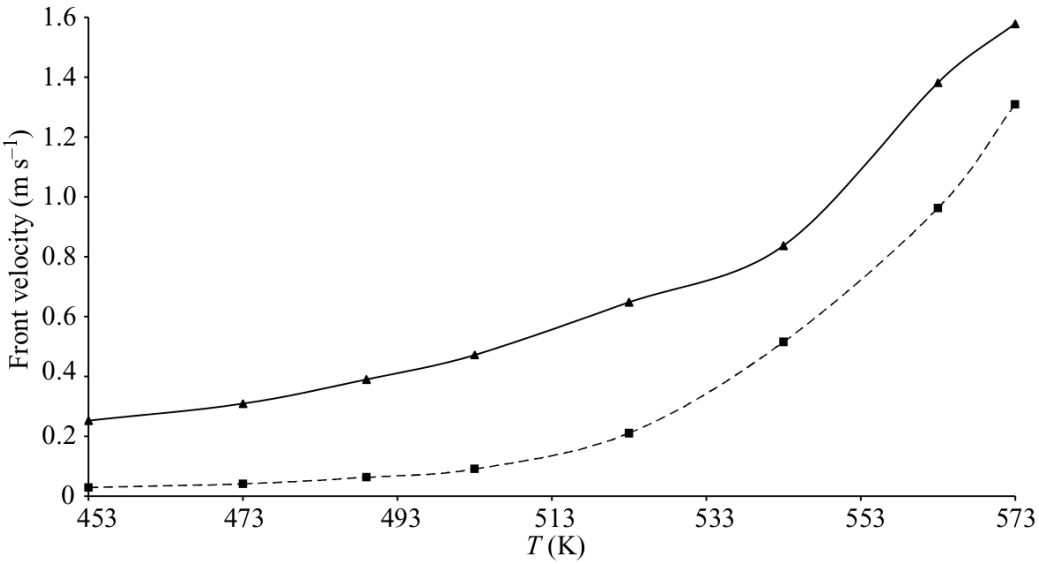

FIGURE 17 – Vitesse du front d'évaporation à l'intérieur du dodécane surchauffé en fonction de la température initiale du dodécane liquide. Les résultats expérimentaux de Simoes-Moreira et Spheperd (trait plein) sont comparés aux vitesses de front d'évaporation obtenues numériquement (pointillés). Les ordres de grandeur et les tendances des vitesses de front sont préservés.

Les résultats obtenus ne montrent pas un accord parfait mais les vitesses sont du même ordre de grandeur et les résultats numériques présentent la même tendance d'augmentation de la vitesse du front d'évaporation en fonction de la température. De plus, les différences entre les résultats expérimentaux et numériques peuvent être attribuées à la simplicité peut être excessive de l'équation d'état Stiffened-Gas. Utiliser une équation d'état plus complexe, telle que les équations d'état du type Mie-Grüneisen, serait une voie possible d'amélioration.

Un autre exemple de simulations est montré dans la Figure 18. Il s'agit d'une simulation de torpille sous-marine équipée d'un cavitateur. La présence de cet équipement provoque la détende du liquide, qui devient métastable, provoquant ainsi l'apparition d'une poche de vapeur dans laquelle se déplace la torpille. Les vitesses mises en jeu étant très importante ($\simeq$ 400 km/h), on parlera ici de super cavitation. Les transferts de chaleur et de masse aux interfaces sont résolus en choisissant des coefficients infiniment grands sur les interfaces évaporantes ce qui "force" localement la condition d'équilibre thermodynamique. Sur les interfaces de simple contact, ces coefficients sont nuls.

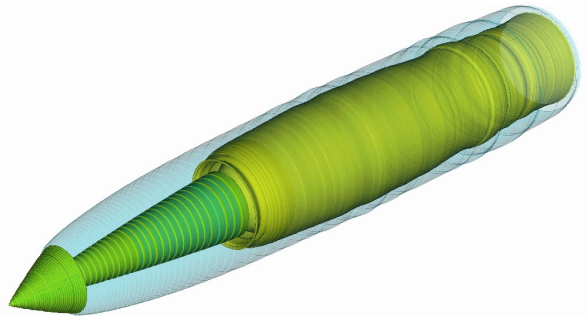

FIGURE 18 – Ecoulement cavitant autour d'une torpille sous-marine. Les gaz de combustion issus du moteur de la torpille sont représentés par des contours jaunes et sont en contact avec de la vapeur, en bleu. La vapeur est séparée du liquide (non représenté) par une interface évaporante. Ces résultats sont extraits de Petitpas et al [66].

L'intégration des différents phénomènes physiques détaillés jusqu'à présent au sein du modèle d'écoulement en équilibre mécanique et thermique (9) permet d'obtenir le modèle suivant, qui correspond au modèle mathématique permettant la simulation numérique directe de l'évaporation :

$$\begin{aligned}
&\frac{\partial \rho Y_1}{\partial t} + div\left(\rho Y_1 \mathbf{u}\right) = \rho\nu(g_2 - g_1) \\
&\frac{\partial \rho}{\partial t} + div\left(\rho \mathbf{u}\right) = 0 \\
&\frac{\partial \rho \mathbf{u}}{\partial t} + div\left(\rho \mathbf{u} \otimes \mathbf{u} + P\underline{\underline{I}}\right) = \sigma\kappa\overrightarrow{\bigtriangledown Y_1} + \rho\mathbf{g} \\
&\frac{\partial \rho E}{\partial t} + div\left((\rho E + P)\mathbf{u}\right) = div\left(\lambda_c \overrightarrow{\bigtriangledown T}\right) + \sigma\kappa\overrightarrow{\bigtriangledown Y_1} \cdot \mathbf{u} + \rho\mathbf{g} \cdot \mathbf{u}
\end{aligned} \tag{20}$$

Où $\lambda_c = \alpha_1\lambda_1 + \alpha_2\lambda_2$. λ_c représente la conductivité thermique du mélange, λ_k la conductivité thermique de la phase k et T la température.
Le coefficient ν représente la vitesse à laquelle la relaxation des potentiels chimiques g_k se produit, ce qui contrôle les transferts de chaleur et de masse. Comme annoncé précédemment, il sera considéré comme infini dans les zones de mélange :

$$\begin{aligned}
&\nu = +\infty \ si \quad \begin{array}{l} \epsilon \leq \alpha_{gaz} \leq 1 - \epsilon \\ \epsilon \leq Y_{gaz} \leq 1 - \epsilon \end{array} \\
&\nu = 0, \ sinon
\end{aligned} \tag{21}$$

Ce modèle est complété par l'équation d'état mentionnée précédemment (Equation 10) :

$$P = \frac{1}{2}\left(A_1 + A_2 - (P_{\infty,1} + P_{\infty,2})\right) + \sqrt{\frac{1}{4}\left(A_2 - A_1 - (P_{\infty,2} - P_{\infty,1})\right)^2 + A_1 A_2} \tag{22}$$

Où $A_k = \dfrac{Y_k\left(\gamma_k - 1\right)C_{v,k}}{Y_1 C_{v,1} + Y_2 C_{v,2}}\left(\rho(e - q) - P_{\infty,k}\right)$ et $q = Y_1 q_1 + Y_2 q_2$.

La vitesse du son de mélange est définie par :

$$c^2 = \frac{1}{2}\left((e-q)(a_1+a_2) + \frac{\frac{1}{2}\left.\frac{\partial R_1}{\partial \rho}\right)_e R_1 + \left.\frac{\partial R_2}{\partial \rho}\right)_e}{\sqrt{\frac{1}{4}R_1 R_1 + R_2}} + \frac{P}{\rho^2}\left(\rho(a1+a2) + \frac{\frac{1}{2}\left.\frac{\partial R_1}{\partial e}\right)_\rho R_1 + \left.\frac{\partial R_2}{\partial e}\right)_\rho}{\sqrt{\frac{1}{4}R_1 R_1 + R_2}} \right) \right) \tag{23}$$

Où,

$$a_1 = \frac{Y_1(\gamma_1 - 1)C_{v,1}}{Y_1 C_{v,1} + Y_2 C_{v,2}},\ a_2 = \frac{Y_2(\gamma_2 - 1)C_{v,2}}{Y_1 C_{v,1} + Y_2 C_{v,2}},$$

$$R_1 = a_2\rho(e-q) - a_2 P_{\infty,2} - a_1\rho(e-q) + a_1 P_{\infty,1} - P_{\infty,2} + P_{\infty,1},$$

$R_2 = a_1 a_2(\rho(e-q) - P_{\infty,1})(\rho(e-q) - P_{\infty,2})$.
De plus, en l'absence de chocs, le Système (20) peut être complété par l'équation d'entropie suivante :

$$\frac{\partial \rho S}{\partial t} + div\left(\rho S\mathbf{u} - \frac{\lambda_c \overrightarrow{\bigtriangledown T}}{T}\right) = \rho\nu\frac{(g_2 - g_1)^2}{T} + \lambda_c\frac{(\bigtriangledown T)^2}{T^2} \tag{24}$$

Où $S = Y_1 s_1 + Y_2 s_2$.
Ce système peut aussi s'écrire sous la forme conservative suivante :

$$\begin{aligned}
&\frac{\partial \rho Y_1}{\partial t} + div\left(\rho Y_1 \mathbf{u}\right) = \rho\nu(g_2 - g_1)\\
&\frac{\partial \rho}{\partial t} + div\left(\rho\mathbf{u}\right) = 0\\
&\frac{\partial \rho\mathbf{u}}{\partial t} + div\left(\rho\mathbf{u}\otimes\mathbf{u} + P\underline{\underline{I}} - \sigma\left(|\mathbf{m}|\underline{\underline{I}} - \frac{\mathbf{m}\otimes\mathbf{m}}{|\mathbf{m}|}\right)\right) = \rho\mathbf{g}\\
&\frac{\partial \rho E + \sigma|\mathbf{m}|}{\partial t} + div\left(\left(\rho E + P + \sigma|\mathbf{m}|\right)\mathbf{u} - \sigma\left(|\mathbf{m}|\underline{\underline{I}} - \frac{\mathbf{m}\otimes\mathbf{m}}{|\mathbf{m}|}\right)\cdot\mathbf{u} + \lambda_c\overrightarrow{\bigtriangledown T}\right) = \rho\mathbf{g}\cdot\mathbf{u}
\end{aligned} \tag{25}$$

La Figure 19 montre quelques résultats d'une simulation numérique 2D d'ébullition en paroi à différents instants. Un domaine fermé de 12cm x 7cm est divisé en deux parties. La moitié supérieure est remplie de vapeur d'eau tandis que l'autre moitié est remplie d'eau liquide. Trois germes de vapeur sont initialement présents sur le bas du domaine. Une température T=388 K est imposée progressivement (de T=373 K pour t=0 s à T=388 K pour t=0.1ms) sur le bas du domaine.
Les trois germes s'élèvent en raison de la force d'Archimède en direction de la surface libre tandis que l'eau autour d'eux s'échauffe et devient vapeur, formant un film. Puis, grâce aux rouleaux de convection créés par les trois premières bulles et à la tension de surface, de nouvelles bulles se créent. Une fois créées, ces nouvelles bulles s'élèvent à leur tour puis, à nouveau de l'eau liquide entre en contact avec la paroi et de nouvelles bulles apparaîssent et commencent à grossir.

Il est important de mentionner que les parois sont supposées parfaites, aucune cavité n'est présente et aucun traitement particulier n'est appliqué sur la paroi du bas en dehors d'une température imposée et de l'angle de contact constant pour les effets capillaires. Ceci signifie que les nouvelles bulles sont créées à ces positions spécifiques grâce aux rouleaux de convection, à la tension de surface et à la conduction thermique.

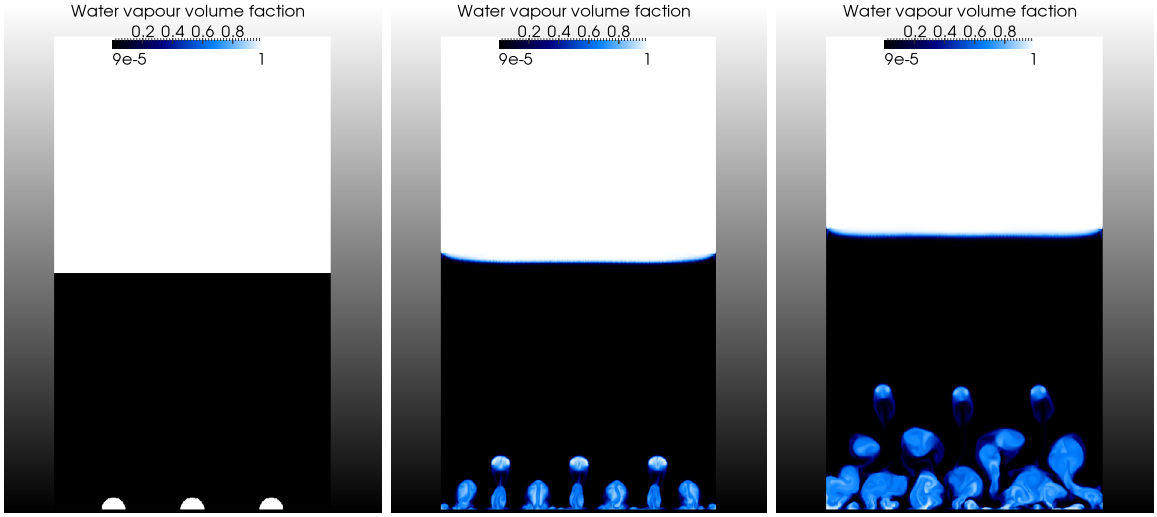

FIGURE 19 – Fraction volumique de vapeur d'eau aux temps $t = 0\,s$, $t = 80\,ms$ et $t = 160\,ms$. Les trois premières bulles s'élèvent vers la surface en raison de la force d'Archimède tandis que l'eau autour de ces bulles commence à bouillir et un film de vapeur se crée. Ces nouvelles bulles s'élèvent à leur tour tandis que de nouvelles bulles apparaissent en retrait. Il est important de remarquer que le bords du domaine sont des parois parfaites. Les bulles de vapeur se créent donc à ces positions grâce à l'échauffement local dû au flux parietal, aux rouleaux de convection et à la tension de surface. En dehors des perturbations initiales (les trois bulles), le système s'auto-entretient et sélectionne le nombre de bulles.

Les explications détaillées concernant la prise en compte des différents phénomènes physiques et leur intégration au schéma numérique implicite sont données dans le Chapitre 3 de ce manuscrit.

Structure du mémoire :

Dans le **Chapitre 1** seront abordés les problèmes numériques apparaissant lors de la simulation d'écoulements diphasiques à faibles nombres de Mach dans le cadre de deux phases considérées comme compressibles. Ces problèmes viennent du fait que, si l'on s'intéresse à la limite asymptotique des équations de la mécanique des fluides lorsque le nombre de Mach tends vers zéro on peut remarquer qu'il existe deux types de solutions limites :
-Les solutions où l'écoulement est considéré incompressible.
-Les solutions correspondant à la limite acoustique.
Ainsi, si l'on prend l'exemple d'un écoulement de liquide à vitesse modérée, il est naturellement compréhensible que la limite physique attendue soit la limite incompressible. Cependant, lorsque le schéma de Godunov est utilisé (ou n'importe quel schéma numérique utilisé pour résoudre des modèles compressibles), les solutions obtenues tendent vers les solutions acoustiques, ce qui entraîne de nombreuses erreurs.
Afin de pallier à ces erreurs, une méthode de pré-conditionnement est mise en place. Cette méthode est inspirée des travaux de Turkel [82] et utilise la modification proposée par Guillard et Viozat [38] afin d'obtenir des solutions précises dans le cas instationnaires. De ce fait, l'objectif principal de ce premier chapitre est de développer une extension multiphasique de cette méthode dans le cadre des modèles et méthodes numériques utilisées puis de valider cet ensemble à la fois dans des situations académiques (solutions de références 1D d'écoulements diphasiques en tuyère) et complexes (la cavitation). Cette dernière situation pouvant être qualifiée de complexe en tant qu'écoulement, mais cependant simplifié par rapport aux écoulements bouillants.

Dans le **second Chapitre**, on va s'intéresser à la détermination des solutions de référence monodimensionelles d'écoulements diphasiques dont une partie (subsonique) a été utilisée dans le premier chapitre. Il y a, en effet, un réel besoin pour ce type de solution de référence car les solutions exactes d'écoulements diphasiques sont rares. Habituellement, les méthodes de résolution d'écoulement à faible nombre de Mach sont comparées à des solutions incompressibles d'écoulement autour de profils d'ailes. Ces solutions ne sont en aucun cas des solutions exactes et leur extension au cas diphasique est problématique. De ce fait, le but de ce deuxième chapitre est la détermination de solutions d'écoulements diphasiques en tuyères pour différents modèles limites (Equilibre mécanique, équilibre mécanique et thermique, équilibre thermodynamique). Bien entendu, ces solutions restant purement unidimensionnelles elles n'ont pas vocation à représenter la véritable physique des écoulements diphasiques en tuyères où de multiples phénomènes multi-dimensionnels, tels que la cavitation par poches, jouent un rôle très important. Néanmoins, l'existence de telles solutions de référence permet de valider précisément les schémas numériques utilisés à travers de simples écoulements 1D.

A travers les deux chapitres précédents, un modèle de base d'écoulement capable de traiter des écoulements diphasiques avec et sans transfert de masse ainsi qu'une méthode permettant de résoudre ce modèle et ce, indépendamment des nombres de Mach mis en jeu, ont été développés et validés.

Le **Chapitre 3** traite de la prise en compte des phénomènes physiques supplémentaires présents lors de l'ébullition. Ainsi, ce chapitre est consacré à la prise en compte de ces différents phénomènes physiques tels que la capillarité, la gravité, la conduction de la chaleur ou encore le changement de phase.
En plus de cela, d'un point de vue numérique, il est nécessaire d'étudier l'extension du schéma numérique implicite présentée dans le Chapitre 1 aux écoulements bouillants ainsi que de la méthode de préconditionnement diphasique pour les écoulements à faibles nombres de Mach. De même que précédemment, la validation de cette approche est un point essentiel de ce chapitre. Les aspects thermiques et changement de phase seront validés au travers d'une comparaison avec une solution exacte 1D de front d'évaporation, inspirée des solutions exactes de fronts de flamme quasi-isobares. La prise en compte de la tension de surface, quant à elle, sera validée à l'aide d'un test statique permettant de vérifier la loi de Laplace sur une bulle de vapeur. Enfin, des exemples multi-dimensionnels d'écoulements à bulles, où tous les effets physiques sont activés, sont présentés.

Chapitre 1

Écoulements à faible nombre de Mach

Avant-propos

Simuler correctement un écoulement bouillant requiert une modélisation correcte de l'écoulement diphasique mais aussi une prise en compte précise des nombreux phénomènes physiques mis en jeu, tels que la tension de surface ou la conduction de la chaleur. De plus l'importance du changement de phase requiert la prise en compte complète de la compressibilité d'au moins une phase et une contrainte particulière apparaît. En effet, le mouvement de la vapeur au sein de la phase liquide met en jeu des nombres de Mach très faibles, ce qui rend difficile l'obtention de solutions numériques fiables dans le cadre de modèles compressibles. Ainsi , si l'on s'intéresse à la limite asymptotique des équations de la mécanique des fluides lorsque le nombre de Mach tends vers zéro on peut remarquer qu'il existe deux types de solutions :
-Les solutions où la densité est constante, correspondant à la limite incompressible.
-Les solutions où les variations de pression sont très faibles, correspondant à la limite acoustique.
De ce fait, si l'on prend l'exemple d'un écoulement de liquide à vitesse modérée, il est naturellement compréhensible que la limite physique attendue soit la limite incompressible. Cependant, lorsque le schéma de Godunov est utilisé (ou n'importe quel schéma numérique utilisé pour résoudre des modèles compressibles), les solutions obtenues tendent vers les solutions acoustiques, ce qui entraîne de nombreuses erreurs.
Afin de pallier à ces erreurs, une méthode de pré-conditionnement pour les équations d'Euler fut proposée par Turkel en 1987 [82]. Cette modification permet d'obtenir des solutions numériques qui convergent vers les solutions incompressibles d'écoulement à faible nombres de Mach, comme par exemple les écoulements d'air autour de profils d'ailes d'avions.
Cependant, il est important de noter que dans l'article de Turkel, le but est uniquement de converger vers des solutions stationnaires d'écoulements monophasiques. L'obtention de solutions instationnaires en présence de discontinuités a été traitée par Guillard et Viozat [38], toujours dans le contexte des équations d'Euler.

De ce fait, l'objectif principal de ce premier chapitre est de développer une extension multi-

phasique de cette méthode dans le cadre des modèles et méthodes numériques utilisées puis de valider cet ensemble dans un contexte complexe (la cavitation) mais simplifié par rapport aux écoulements bouillants.

1.1 Introduction

Liquid-gas mixtures and interfacial flows arise in many natural and industrial situations occurring in fluid mechanics, nuclear, environmental and chemical engineering. Many computational approaches consider the two fluids as incompressible (Hirt and Nichols [44], Lafaurie et al. [51], Menard et al. [58]) to cite a few. High Mach number flows with material interfaces have also been the subject of important efforts, with various approaches : Front Tracking [35], Level Set and Ghost Fluid [30], diffuse interfaces [1], [70], [74] and others. Between incompressible and highly compressible fluids, flows with phase change involve both compressible and incompressible effects. An example of boiling liquid-gas flow modelling is given in [46]. In cavitation zones, the liquid gas mixture is highly compressible as well as the pure gas zones while the pure liquid zones are weakly compressible. In phase change applications gas compressibility is of importance. In cavitating flows, compressibility of all phases is important as the liquid phase change occurs under liquid expansion effects. Moreover, when liquid-gas mixtures appear, the sound propagates with the mixture sound speed [87], which has a non monotonic behaviour with respect to the volume fraction, resulting in very low sound speed, of the order of a few meters per second. There is thus no difficulty to reach hypersonic flow conditions with liquid gas mixtures. Consequently, it is important to build numerical methods able to deal with incompressible flows, transonic flows and even hypersonic flows. This issue has been addressed intensively in the context of single phase flows since Harlow and Amsden [41] extending incompressible flow solvers to compressible one and Turkel [82] extending compressible flow solvers to the incompressible limit. Multiphase flows in the low Mach regime has been more addressed by methods issued from incompressible flows [68], [9]. However, this poses difficulties when wave dynamics is present, as incompressible flow solvers are not conservative in the compressible flow sense. Also, these methods have difficulties when large density ratios are present. At liquid gas interfaces, the density ratio may exceed several thousands. Turkel [82] approach, dealing with incompressible flow limit with compressible flow solvers, seems more appropriate. Two-phase cavitating flow models have been addressed in this direction [50], [85]. The same kind of approach is considered in the present work. More precisely, we address both liquid-gas interface and cavitating flows with the same theoretical flow model (Kapila et al [47]) and consider a flow solver close to the preconditioning method of Guillard and Viozat [38]. This approach has some advantages :

- The interfaces are handled routinely, like any point of the flow.
- The dynamic appearance of interfaces (not present initially) is possible thanks to the volume fraction equation structure that allows volume fraction to increase in zones where the velocity divergence is non zero. This occurs typically in expansion and compression waves and is of major importance in cavitating flows.

- Phase transition can be considered in a thermodynamically consistant way [73].
- The phases mass, mixture momentum and mixture energy are expressed under conservative form, insuring correct wave dynamics in pure fluid zones.
- The addition of surface tension [64] can be done quite easily. In other words, capillary effects are modelled with the help of a capillary tensor and there is no need to resolve the interface structure.

This approach has obviously some drawbacks :

- The interfaces can be excessively diffused, especially when dealing with long time evolutions. But this is exactly the same drawback as contact discontinuity smearing in gas dynamics computations. Efforts to reduce numerical diffusion have been done recently by Kokh and Lagoutière [49], Shuckla et al. [77] and So et al [79].
- Non-conservative equations are present and the numerical approximation of non-conservative terms poses difficulties in the presence of shocks [71], [65], [74], [67], [75].
- The building of all Mach number method for this kind of hyperbolic flow model is not an easy task, as it will be shown later.

As the flow model is conservative regarding the phases mass equations, mixture momentum and mixture energy and since the system is hyperbolic we will adopt a method issued from compressible flow dynamics [82], [20],[38]. This choice is motivated by the importance of the pressure waves present in many applications, by the presence of huge density ratios at interfaces, that are easier to handle with discontinuity capturing schemes and by the presence of huge Mach number variations. This is mandatory for specific applications, such as :

- liquid-gas flows in nozzles and Venturi tunnels,
- high performance turbo-pumps where cavitation appears,
- propellers,
- water waves breaking,
- flash vaporization.

The key issue when these applications are addressed with the Kapila et al.[47] model is related to the numerical approximation of the flow model in all speed conditions. This issue is addressed in the frame of Turkel-Guillard-Viozat [82],[38] formulation.

From a theoretical standpoint, mathematical analysis of the low Mach number limit for classical solutions of the compressible Navier-Stokes has been investigated by many authors (for example, Ebin [26] , Klainerman and Majda [48], Schochet [76], Metivier and Schochet [60]). Alazard [2] proved, in a rigorous analysis and general context, the existence of uniformly bounded incompressible limit of the full Navier-Stokes equations. The existence time is there independent of the Mach, the Reynolds and the Peclet numbers and thereby includes the limit for the Euler equation as well. On this theoretical basis, we first consider the single phase Euler equations and derive an approximate preconditioned Riemann solver. When the Godunov scheme is used with this Riemann solver, convergence to the exact nozzle flow solution is obtained. However, the method requires small time steps (much smaller that the conventional CFL restriction) to be stable. We thus consider implicit formulation to overcome this restriction. The HLLC solver of Toro et al. [80] is considered and a Taylor expansion is done to express its time variation. The method is first presented in the context of the one-dimensional Euler equations and then extended to the one-dimensional Kapila

et al. [47] model. After validation against the exact one-dimensional two-phase nozzle flow solution, 2D extension of the algorithm for unstructured meshes is presented. Computational examples are shown in 2D. In particular, a real cavitating flow in 2D Venturi channel is examined. With the help of the new method, very good agreement with the measured cavitation pocket size and detachment frequency is obtained without having recourse to any model or method parameter.
The paper is organized as follows. In Section 2 the Kapila et al. [47] flow model under interest is presented. Its pressure non-equilibrium analogue [74] is presented in the same section as this formulation is more suited to numerical resolution with the approach given in the same reference. In Section 3, the low Mach behaviour of a conventional Godunov type scheme is shown using a single phase nozzle flow solution. In Section 4 the low Mach single phase Riemann solver is presented. It uses the preconditioned Euler equations in the Riemann problem resolution only, while the conventional conservative formulation is used for the solution update. Its extension to the two-phase flow model is then examined. Section 5 deals with time implicit formulation of the preconditioned Godunov method in order to overcome severe stability restrictions. Computational example and validations against experiments are given in Section 6. Conclusions are given in Section 7.

1.2 Flow Model

We consider the two-phase flow model of Kapila et al [47]. It describes multiphase mixtures evolving in mechanical equilibrium (equal pressures and equal velocities). It is particularly suited to material interfaces computations, considered as numerical diffusion zones (see for example Saurel et al [74]). The Kapila et al [47] model reads :

$$
\begin{aligned}
&\frac{\partial \alpha_1}{\partial t} + \mathbf{u}\cdot\mathbf{grad}\left(\alpha_1\right) = K div\left(\mathbf{u}\right) \quad \text{where} \quad K = \frac{\rho_2 c_2^2 - \rho_1 c_1^2}{\frac{\rho_1 c_1^2}{\alpha_1} + \frac{\rho_2 c_2^2}{\alpha_2}},\\
&\frac{\partial \alpha_1\rho_1}{\partial t} + div\left(\alpha_1\rho_1\mathbf{u}\right) = 0,\\
&\frac{\partial \alpha_2\rho_2}{\partial t} + div\left(\alpha_2\rho_2\mathbf{u}\right) = 0,\\
&\frac{\partial \rho\mathbf{u}}{\partial t} + div\left(\rho\mathbf{u}\otimes\mathbf{u} + P\right) = 0,\\
&\frac{\partial \rho E}{\partial t} + div\left((\rho E + P)\mathbf{u}\right) = 0,
\end{aligned}
\tag{1.1}
$$

c_k represents the sound speed defined by $c_k^2 = \frac{\partial p_k}{\partial \rho_k}\Big)_{s_k}, k = 1, 2,$
P represents the mixture pressure,
E represents the mixture total energy,
α_k represent the phases volume fraction,
ρ_k represent the phases density.

The mixture sound speed is given by the Wood [87] formula and is a consequence of System

(1.1) :

$$\frac{1}{\rho c^2} = \frac{\alpha_1}{\rho_1 c_1^2} + \frac{\alpha_2}{\rho_2 c_2^2} \tag{1.2}$$

In the absence of shocks, System (1.1) can be complemented by the following entropy equations :

$$\frac{\partial \alpha_1 \rho_1 s_1}{\partial t} + div\,(\alpha_1 \rho_1 s_1 u) = 0, \qquad \frac{\partial \alpha_2 \rho_2 s_2}{\partial t} + div\,(\alpha_2 \rho_2 s_2 u) = 0. \tag{1.3}$$

The thermodynamic closure is achieved with the help of the mixture energy definition,

$$\rho e = \alpha_1 \rho_1 e_1 + \alpha_2 \rho_2 e_2$$

and the pressure equilibrium condition : $p_1 = p_2$.
In the present work, the Stiffened-Gas (SG) EOS is considered for each phase :

$$p_k = (\gamma_k - 1)\rho_k e_k - \gamma_k P_{\infty,k}. \tag{1.4}$$

γ_k and $P_{\infty,k}$ are parameters of the EOS, obtained from reference thermodynamic curves, characteristic of the material and transformation under study. See Le Metayer et al [52] for details.
In the context of fluids governed by SG EOS (1.4), the mixture EOS reads :

$$P = \frac{\rho e - (\frac{\alpha_1 \gamma_1 P_{\infty,1}}{\gamma_1 - 1} + \frac{\alpha_2 \gamma_2 P_{\infty,2}}{\gamma_2 - 1})}{\frac{\alpha_1}{\gamma_1 - 1} + \frac{\alpha_2}{\gamma_2 - 1}} \tag{1.5}$$

Obviously, other convex EOS can be considered instead of (1.4) for the building of (1.5). The numerical approximation of the Kapila et al. [47] model is addressed in the frame of Godunov type finite volume schemes. To overcome the difficulties related to the approximation of the non conservative term $Kdiv(u)$ in the volume fraction equation of System (1.1), a pressure non equilibrium System (1.6) is considered during the transport step and a proper projection is achieved to recover the target model (1.1). The pressure non equilibrium system reads :

$$\begin{aligned}
&\frac{\partial \alpha_1}{\partial t} + \mathbf{u} \cdot \mathbf{grad}\,(\alpha_1) = \mu(p_1 - p_2) \\
&\frac{\partial \alpha_1 \rho_1}{\partial t} + div\,(\alpha_1 \rho_1 \mathbf{u}) = 0 \\
&\frac{\partial \alpha_2 \rho_2}{\partial t} + div\,(\alpha_2 \rho_2 \mathbf{u}) = 0 \\
&\frac{\partial \alpha_1 \rho_1 e_1}{\partial t} + div\,(\alpha_1 \rho_1 e_1 \mathbf{u}) + \alpha_1 p_1 div\,(\mathbf{u}) = -p_I \mu(p_1 - p_2) \\
&\frac{\partial \alpha_2 \rho_2 e_2}{\partial t} + div\,(\alpha_2 \rho_2 e_2 \mathbf{u}) + \alpha_2 p_2 div\,(\mathbf{u}) = p_I \mu(p_1 - p_2) \\
&\frac{\partial \rho \mathbf{u}}{\partial t} + div\,(\rho \mathbf{u} \otimes \mathbf{u} + P) = 0 \\
&\frac{\partial \rho E}{\partial t} + div\,((\rho E + P)\mathbf{u}) = 0
\end{aligned} \tag{1.6}$$

Where,
μ represents the pressure relaxation coefficient,
p_I represents the interfacial pressure defined by $p_I = \dfrac{Z_1 p_2 + Z_2 p_1}{Z_1 + Z_2}$,
with $Z_k = \rho_k c_k$, the phase k acoustic impedance.
e_k and p_k represent the phase k internal energy and pressure respectively.

It is important to note that in this system the internal energies of each phase are independent variables and their evolution is described by two additional equations. The mixture pressure is now related to the phases' internal energies :

$$P = \alpha_1 p_1 + \alpha_2 p_2 \tag{1.7}$$

where $p_1 = p_1(\rho_1, e_1)$ and $p_2 = p_2(\rho_2, e_2)$.

The non-equilibrium system (1.6) is hyperbolic and appropriate to overcome the difficulties related to the discretization of the volume fraction equation, in particular regarding positivity issues. System (1.6) is used to reach solutions of System (1.1) in the limit of infinite pressure relaxation, i.e. when μ tends to infinity.
It is worth to mention that System (1.6) is overdetermined. Indeed, the total energy equation is a consequence of the phases energy equations and the mixture momentum one. This over determination will be used to correct the inaccuracies appearing during the numerical integration of $\alpha_k p_k div(\mathbf{u})$, the non conservative terms of the internal energy equations [74]. Overdetermined systems have already been considered for numerical approximation issues in different contexts by Babii et al. [4] for example.
Let us mention that this formulation is needed not only when two-phase shock waves are present but also when cavitation is considered, as in the present paper. Indeed, when cavitation comes from geometrical effects, closed to walls, a normal velocity discontinuity appears. Indeed, wall boundary conditions are solved with the help of a mirror state, resulting in unbounded velocity divergence and undefined non-conservative product in the volume fraction equation of System (1). It means that the building of a positive scheme based on System (1.1) in realistic cavitating flow conditions is an issue. Formulation (1.6) overcomes this difficulty. Also, many practical situations of cavitating flow involve huge Mach number variations, and robustness of the algorithm is mandatory. Formulation (1.6) is particularly robust. The algorithm based on the overdetermined formulation (1.6) can be summarized as follows. System (1.6) is rearranged as :

$$\frac{\partial \boldsymbol{U}}{\partial t} + div\left(\boldsymbol{F}(\boldsymbol{U})\right) + \boldsymbol{H}(\boldsymbol{U}) div\left(\mathbf{u}\right) = \mu\left(p_1 - p_2\right)\boldsymbol{S}(\boldsymbol{U}) \tag{1.8}$$

Where,

$$\boldsymbol{U} = \begin{pmatrix} \alpha_1 \\ \alpha_1\rho_1 \\ \alpha_1\rho_2 \\ \rho\mathbf{u} \\ \rho E \\ \alpha_1\rho_1 e_1 \\ \alpha_2\rho_2 e_2 \end{pmatrix}, \quad \boldsymbol{F}(\boldsymbol{U}) = \begin{pmatrix} \alpha_1\mathbf{u} \\ \alpha_1\rho_1\mathbf{u} \\ \alpha_1\rho_2\mathbf{u} \\ \rho\mathbf{u}\otimes\mathbf{u} + P \\ (\rho E + P)\mathbf{u} \\ \alpha_1\rho_1 e_1\mathbf{u} \\ \alpha_2\rho_2 e_2\mathbf{u} \end{pmatrix}, \quad \boldsymbol{H}(\boldsymbol{U}) = \begin{pmatrix} -\alpha_1 \\ 0 \\ 0 \\ 0 \\ 0 \\ \alpha_1 p_1 \\ \alpha_2 p_2 \end{pmatrix} \quad \text{and} \quad \boldsymbol{S}(\boldsymbol{U}) = \begin{pmatrix} 1 \\ 0 \\ 0 \\ 0 \\ 0 \\ -p_I \\ p_I \end{pmatrix} \tag{1.9}$$

Each integration time step is structured as follows [74] :

- **Initialization** : At a given time step, the flow is in mechanical equilibrium, in particular in pressure equilibrium. The set of variables is given by :

$$\boldsymbol{U}^n \equiv \boldsymbol{U}\left(\boldsymbol{V}^n\right) \quad \text{with} \quad \boldsymbol{V}^n = \left(\alpha_1^n,\ \rho_1^n,\ \rho_2^n, u^n,\ e_1^n(\rho_1^n, P^n),\ e_2^n(\rho_2^n, P^n),\ E^n\right)^T$$

- **Non equilibrium evolution** : The pressure relaxation terms are removed ($\mu = 0$) and the hyperbolic pressure non-equilibrium system is solved. At the end of this evolution step a temporary flow state is determined :

$$\frac{\partial \boldsymbol{U}}{\partial t} + div\left(\boldsymbol{F}(\boldsymbol{U})\right) + \boldsymbol{H}(\boldsymbol{U}) div\left(\mathbf{u}\right) = 0 \tag{1.10}$$

$$\mapsto \widetilde{\boldsymbol{U}}^{n+1} \equiv \boldsymbol{U}\left(\widetilde{\boldsymbol{V}}^{n+1}\right) \quad \text{with} \quad \widetilde{\boldsymbol{V}}^{n+1} = \left(\tilde{\alpha}_1^{n+1},\ \tilde{\rho}_1^{n+1},\ \tilde{\rho}_2^{n+1},\ u^{n+1},\ \tilde{e}_1^{n+1},\ \tilde{e}_2^{n+1}, E^{n+1}\right)$$

- **Projection to pressure equilibrium** : This step deals with the projection of the previous pressure non equilibrium state onto a pressure equilibrium one :

$$\frac{\partial \boldsymbol{U}}{\partial t} = \mu\left(p_1 - p_2\right)\boldsymbol{S}(\boldsymbol{U}) \qquad \mapsto \qquad \boldsymbol{U}^{n+1} \equiv \boldsymbol{U}\left(\boldsymbol{V}^{n+1}\right)$$

$$\text{with} \quad \boldsymbol{V}^{n+1} = \left(\alpha_1^{n+1},\ \rho_1^{n+1},\ \rho_2^{n+1}, u^{n+1},\ e_1^{n+1}(\rho_1^{n+1}, P^{n+1}),\ e_2^{n+1}(\rho_2^{n+1}, P^{n+1}),\ E^{n+1}\right)$$

This is done by determining the asymptotic solution of the remaining relaxation ODE system in the limit $\mu \to +\infty$.The asymptotic state is determined by the resolution of a non-linear algebraic equation. Details may be found, for example, in [74]. In particular, it is shown in the Appendix B of this reference, that this strategy results in approximating solutions of (1.1).

It is worth to mention that :

- The equilibrium pressure P^{n+1} is determined from the mixture EOS (1.5), based on the mixture total energy E^{n+1}, for which there is no conservation issue.
- Both steps in this strategy preserve volume fraction positivity.
- Both steps preserve phases' mass conservation, mixture momentum and energy conservation.

- The entropy inequality is also preserved during each step.

This algorithm has shown robustness, accuracy and versatility for various flow models ranging from interfaces, supercavitating flows [73], detonation waves [66], powder compaction [72], solid-fluid coupling [29] in severe high speed conditions. We address here arbitrary velocity flow conditions and particularly low Mach number conditions.

1.3 Low Mach behaviour of conventional Godunov type schemes

To illustrate the fundamental difficulties of low Mach number computations, we consider a basic situation of 1D nozzle flow. We first examine the behaviour of the Godunov method in this limit for single phase liquid flows. We consider the nozzle geometry given in Figure 1.1 connected to an inlet imposed mass flow rate m_0 and imposed stagnation enthalpy H_0 and to a prescribed outlet pressure, p_{out}. The first order Godunov method with HLLC approximate Riemann solver is used to compute the smooth varying nozzle flow. Details are given in the Appendix A. Computations to steady state are achieved with uniform meshes of different sizes. The exact quasi-1D solution is computed using the method described in [13].

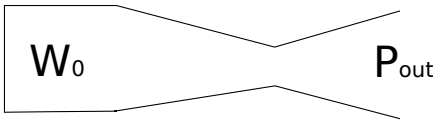

FIGURE 1.1 – Nozzle connected to a tank at the inlet and to a prescribed pressure at the outlet

All computations are achieved with a time step satisfying CFL=0.5. The outlet pressure boundary condition and the inlet stagnation enthalpy and mass flow rate are solved by the method of Osher and Chakravarthy [63]. The geometrical data and boundary conditions for the liquid flow are :
- Inlet cross section : 0.14657 m^2.
- Throat cross section : 0.06406 m^2.
- Outlet cross section : 0.14657 m^2.

The nozzle profile is piecewise linear with respect to the surface area. The nozzle length is 1 m while the throat is located 0.5 m from the inlet. The boundary conditions are given by :

$$\left\{ \begin{array}{l} m_0 = 7000\, kg.m^{-2}.s^{-1}, \quad H_0 = \frac{p_0+\gamma P_\infty}{(\gamma-1)\rho_0} + \frac{p_0}{\rho_0} + \frac{m_0^2}{2\rho_0} \\ \quad \text{with} \quad p_0 = 0.1\, MPa, \quad \rho_0 = 1000\, kg.m^{-3}, \quad \gamma = 4.4, \quad P_\infty = 600\, MPa \end{array} \right.$$

The exact and computed velocity and pressure profiles are shown in the Figure 3 for various mesh sizes : 100, 1000 and 10,000 cells.

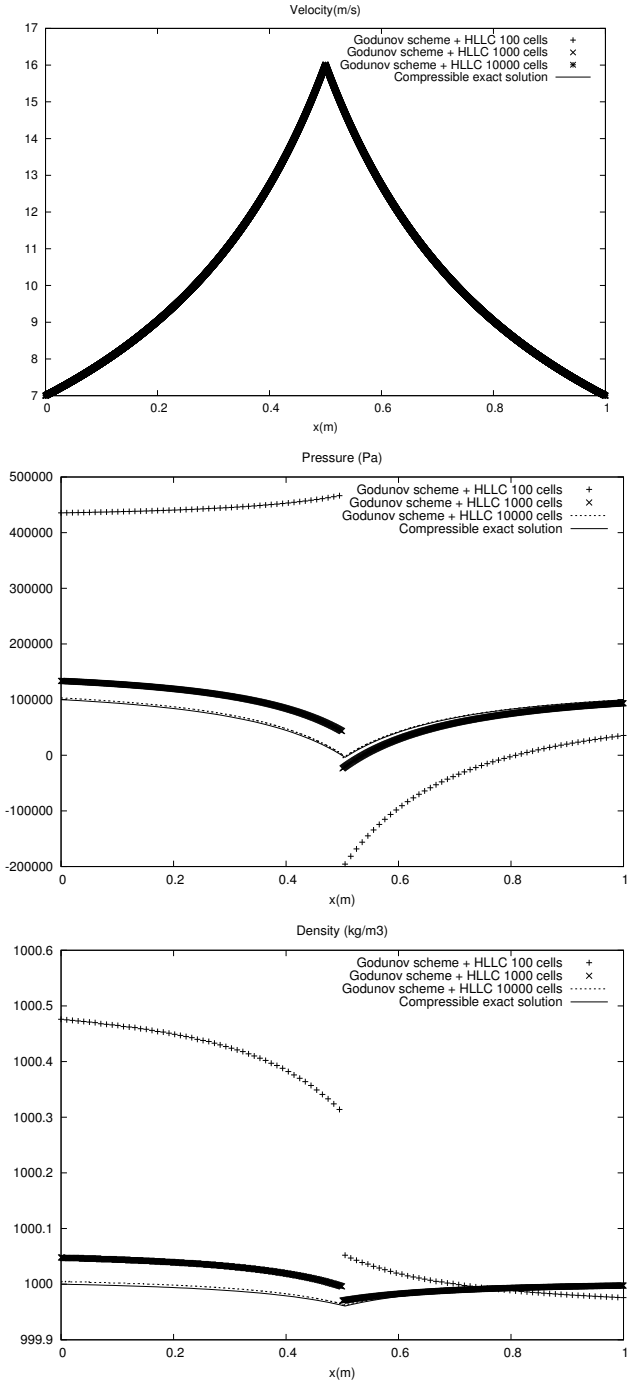

FIGURE 1.2 – Computed velocity, pressure and density profiles in the Laval liquid nozzle flow with 100, 1000 and 10,000 cells against the compressible exact solution. The Godunov scheme solutions present severe fluctuations. The error decreases under mesh refinement.

The computed and exact velocity profiles are in excellent agreement but the pressure and density fields present large errors. Regarding the pressure field, the jump at throat is

not a computational artefact due to a lack of "well balance" effect in the Riemann solver, boundary conditions or slope singularity at throat. The 500% error is strictly due to density fluctuations combined with the SG EOS (1.4) stiffness. Mesh refinement analysis illustrates the convergence issue, that is clearly not a consistence one. Quasi convergent results are obtained with 10,000 cells (Figures 1.2). Table 1.1 shows computational times to reach steady state inside the piecewise linear nozzle versus mesh size. It is clear that the method is extremely expensive, even for 1D computations.

Mesh size	Calculation time
100 cells	20 s
1000 cells	33 min 56 s
10000 cells	59 h 16 min 48 s

TABLE 1.1 – Computational time versus mesh size for the 1D liquid nozzle flow test.

1.4 Improving numerical convergence at low Mach number limit

As single phase computations have shown serious issues under low Mach number conditions (Figure 1.2), it is clear that efforts have to be done to improve the asymptotic behaviour of Godunov type schemes at low Mach. This has to be done prior to consider numerical approximation of the two-phase flow model (1.1). We thus address the numerical approximation of the Euler equation first. The two-phase flow model (1.1) will be addressed in a second part. For the sake of simplicity, the analysis is carried out in 1D, multi-D extension being addressed later.

1.4.1 Low Mach number preconditioning

As shown previously, the conventional Godunov method converges to the exact solution under low Mach conditions if very fine resolution is used. Such meshes being impracticable for multi-dimensional applications, modifications have to be done. We are seeking a numerical method valid for all speeds flows, from transonic to low Mach number. In this area, Turkel [82] established a preconditioning method to guarantee convergence of the results at steady state. Unsteady extensions have been done with several approaches. Choi and Merkle [20] introduced an approach with two time steps, an artificial one and an physical one. An analysis of various compressible flow approaches for unsteady flows is given in [83]. Recent extension to discontinuous Galerkin methods is given in [14]. Moreover, extension of dual time stepping methods to cavitating two-phase flows has been addressed by several authors [50], [85], [32]. Another approach was derived by Guillard and Viozat [38] where only the flux numerical dissipation was modified to reach convergence in both low and high

Mach number conditions. This approach is considered in the present work as it guarantees conservation and convergence even when discontinuities such as shock waves are present. Indeed, the conservative formulation of the equations as well as the equation of state are unmodified. This results in unchanged jump conditions across the various waves and correct wave speeds computation.
This strategy is presented hereafter in the context of the Euler equations. The HLLC Riemann solver of Toro et al. [80] is considered and wave speeds for all Mach number flow situations are estimated following Muronne and Guillard [62] and Braconnier and Nkonga [17] with the help of the following analysis. For the approximate Riemann problem resolution only (not for the solution update), the Euler equations are considered under primitive variables formulation :

$$\begin{aligned}
&\frac{\partial \rho}{\partial t} + \rho \frac{\partial u}{\partial x} + u \frac{\partial \rho}{\partial x} = 0 \\
&\frac{\partial u}{\partial t} + u \frac{\partial u}{\partial x} + \frac{1}{\rho} \frac{\partial p}{\partial x} = 0 \\
&\frac{\partial p}{\partial t} + u \frac{\partial p}{\partial x} + \rho c^2 \frac{\partial u}{\partial x} = 0
\end{aligned} \tag{1.11}$$

Dimensionless variables

These equations are expressed in dimensionless variables with the help of the following definitions : $\rho = [\rho]\tilde{\rho}$, $u = [u]\tilde{u}$, $p = [p]\tilde{p}$, $x = [x]\tilde{x}$ and $t = [t]\tilde{t}$, where $[f]$ represents a characteristic scale of the corresponding variable and $\tilde{f}$ the dimensionless one. System (1.11) becomes :

$$\begin{aligned}
&\frac{\partial \tilde{\rho}}{\partial \tilde{t}} + \tilde{\rho} \frac{\partial \tilde{u}}{\partial \tilde{x}} + \tilde{u} \frac{\partial \tilde{\rho}}{\partial \tilde{x}} = 0 \\
&\frac{\partial \tilde{u}}{\partial \tilde{t}} + \tilde{u} \frac{\partial \tilde{u}}{\partial \tilde{x}} + \frac{[p]}{[\rho][u]^2 \tilde{\rho}} \frac{\partial \tilde{p}}{\partial \tilde{x}} = 0 \\
&\frac{\partial \tilde{p}}{\partial \tilde{t}} + \tilde{u} \frac{\partial \tilde{p}}{\partial \tilde{x}} + \frac{[\rho][c]^2}{[p]} \tilde{\rho} \tilde{c}^2 \frac{\partial \tilde{u}}{\partial \tilde{x}} = 0
\end{aligned} \tag{1.12}$$

A pressure scaling has to defined. At least, three options are possible :
- An 'acoustic' scaling, corresponding to,

$$[p] = [\rho][c][u] \tag{1.13}$$

- A 'dynamic pressure' scaling, corresponding to,

$$[p] = [\rho][u]^2 \tag{1.14}$$

-A 'bulk modulus' scaling, corresponding to,

$$[p] = [\rho][c]^2 \tag{1.15}$$

The two first scaling lead to wrong wave speed propagation. Indeed, combining the pressure and the mass equations to eliminate the velocity divergence, the following result is obtained :

$$\left(\frac{\partial \tilde{p}}{\partial \tilde{t}} + \tilde{u} \frac{\partial \tilde{p}}{\partial \tilde{x}} \right) - \frac{[\rho][c]^2}{[p]} \tilde{c}^2 \left(\frac{\partial \tilde{\rho}}{\partial \tilde{t}} + \tilde{u} \frac{\partial \tilde{\rho}}{\partial \tilde{x}} \right) = 0 \tag{1.16}$$

Therefore $\dfrac{\partial \tilde{p}}{\partial \tilde{t}} = \dfrac{[\rho][c]^2}{[p]}\tilde{c}^2$. Thus, the only admissible scaling for the pressure is the bulk modulus, otherwise, the sound speed definition, or the isentropic condition, is violated. With the "bulk modulus" scaling, the System becomes :

$$\begin{aligned}
&\frac{\partial \tilde{\rho}}{\partial \tilde{t}} + \tilde{\rho}\frac{\partial \tilde{u}}{\partial \tilde{x}} + \tilde{u}\frac{\partial \tilde{\rho}}{\partial \tilde{x}} = 0 \\
&\frac{\partial \tilde{u}}{\partial \tilde{t}} + \tilde{u}\frac{\partial \tilde{u}}{\partial \tilde{x}} + \frac{1}{M^2\tilde{\rho}}\frac{\partial \tilde{p}}{\partial \tilde{x}} = 0 \\
&\frac{\partial \tilde{p}}{\partial \tilde{t}} + \tilde{u}\frac{\partial \tilde{p}}{\partial \tilde{x}} + \tilde{\rho}\tilde{c}^2\frac{\partial \tilde{u}}{\partial \tilde{x}} = 0,
\end{aligned} \tag{1.17}$$

As shown in the next subsection, the 'bulk modulus' scaling formally admits the incompressible Euler equations as asymptotic limit when the Mach number tends to zero. We thus consider System (1.17) in the following where the symbol $\sim$ is dropped for the sake of simplicity.

Asymptotic analysis

We now examine the limit system associated to System (1.17) when the Mach number tends to zero. To do so, an asymptotic analysis is done. The various flow variables 'f' are expanded as :

$$f = f_0 + \epsilon f_1 + \epsilon^2 f_2, \qquad \text{where } \epsilon \to 0^+.$$

The mass equation becomes :

$$\frac{\partial\left(\rho_0 + \epsilon\rho_1 + \epsilon^2\rho_2\right)}{\partial t} + \left(\rho_0 + \epsilon\rho_1 + \epsilon^2\rho_2\right)\frac{\partial\left(u_0 + \epsilon u_1 + \epsilon^2 u_2\right)}{\partial x} + \left(u_0 + \epsilon u_1 + \epsilon^2 u_2\right)\frac{\left(\rho_0 + \epsilon\rho_1 + \epsilon^2\rho_2\right)}{\partial x} = 0 \tag{1.18}$$

I.e,

$$\begin{aligned}
&\frac{\partial \rho_0}{\partial t} + \epsilon\frac{\partial \rho_1}{\partial t} + \epsilon^2\frac{\partial \rho_2}{\partial t} \\
&+ \rho_0\frac{\partial u_0}{\partial x} + \epsilon\rho_0\frac{\partial u_1}{\partial x} + \epsilon^2\rho_0\frac{\partial u_2}{\partial x} + \epsilon\rho_1\frac{\partial u_0}{\partial x} + \epsilon^2\rho_1\frac{\partial u_1}{\partial x} + \epsilon^2\rho_2\frac{\partial u_0}{\partial x} \\
&+ u_0\frac{\partial \rho_0}{\partial x} + \epsilon u_0\frac{\partial \rho_1}{\partial x} + \epsilon^2 u_0\frac{\partial \rho_2}{\partial x} + \epsilon u_1\frac{\partial \rho_0}{\partial x} + \epsilon^2 u_1\frac{\partial \rho_1}{\partial x} + \epsilon^2 u_2\frac{\partial \rho_0}{\partial x} = 0
\end{aligned} \tag{1.19}$$

Grouping terms, we have :

$$\begin{aligned}
&\frac{\partial \rho_0}{\partial t} + \rho_0\frac{\partial u_0}{\partial x} + u_0\frac{\partial \rho_0}{\partial x} \\
&+ \epsilon\left(\frac{\partial \rho_1}{\partial t} + \rho_0\frac{\partial u_1}{\partial x} + \rho_1\frac{\partial u_0}{\partial x} + u_0\frac{\partial \rho_1}{\partial x} + u_1\frac{\partial \rho_0}{\partial x}\right) \\
&+ \epsilon^2\left(\frac{\partial \rho_2}{\partial t} + \rho_0\frac{\partial u_2}{\partial x} + \rho_1\frac{\partial u_1}{\partial x} + \rho_2\frac{\partial u_0}{\partial x} + u_0\frac{\partial \rho_2}{\partial x} + u_1\frac{\partial \rho_1}{\partial x} + u_2\frac{\partial \rho_0}{\partial x}\right) = 0
\end{aligned} \tag{1.20}$$

Or,

$$\begin{aligned}&\frac{\partial \rho_0}{\partial t}+\frac{\partial \rho_0 u_0}{\partial x}\\&+\epsilon\left(\frac{\partial \rho_1}{\partial t}+\frac{\partial \rho_0 u_1}{\partial x}+\frac{\partial \rho_1 u_0}{\partial x}\right)\\&+\epsilon^2\left(\frac{\partial \rho_2}{\partial t}+\frac{\partial \rho_0 u_2}{\partial x}+\frac{\partial \rho_1 u_1}{\partial x}+\frac{\partial \rho_2 u_0}{\partial x}\right)=0\end{aligned} \tag{1.21}$$

This polynomial function of ϵ implies three equations :
- At zero order :$\frac{\partial \rho_0}{\partial t}+\frac{\partial \rho_0 u_0}{\partial x}=0.$
- At ϵ order : $\frac{\partial \rho_1}{\partial t}+\frac{\partial\left(\rho_0 u_1+\rho_1 u_0\right)}{\partial x}=0.$
- At ϵ^2 order : $\frac{\partial \rho_2}{\partial t}+\frac{\partial \rho_0 u_2}{\partial x}+\frac{\partial \rho_1 u_1}{\partial x}+\frac{\partial \rho_2 u_0}{\partial x}=0$

A $\epsilon \rightarrow 0^+$, the mass equation at leading order reduces to :

$$\frac{\partial \rho_0}{\partial t}+\frac{\partial \rho_0 u_0}{\partial x}=0 \tag{1.22}$$

We now examine the momentum equation :

$$\frac{\partial u}{\partial t}+u\frac{\partial u}{\partial x}+\frac{1}{\rho M^2}\frac{\partial p}{\partial x}=0 \tag{1.23}$$

It becomes,

$$\frac{\partial\left(u_0+\epsilon u_1+\epsilon^2 u_2\right)}{\partial t}+\left(u_0+\epsilon u_1+\epsilon^2 u_2\right)\frac{\partial\left(u_0+\epsilon u_1+\epsilon^2 u_2\right)}{\partial x}+\frac{1}{M^2}\left(\tau_0+\epsilon\tau_1+\epsilon^2\tau_2\right)\frac{\partial\left(p_0+\epsilon p_1+\epsilon^2 p_2\right)}{\partial x}=0, \tag{1.24}$$

with $\tau=\frac{1}{\rho}$.
Expanding the momentum equation we have :

$$\begin{aligned}&\frac{\partial u_0}{\partial t}+u_0\frac{\partial u_0}{\partial x}+\frac{1}{M^2}\tau_0\frac{\partial p_0}{\partial x}\\&+\epsilon\left(\frac{\partial u_1}{\partial t}+\frac{\partial u_0 u_1}{\partial x}+\frac{1}{M^2}\tau_0\frac{\partial p_1}{\partial x}+\frac{1}{M^2}\tau_1\frac{\partial p_0}{\partial x}\right)\\&+\epsilon^2\left(\frac{\partial u_2}{\partial t}+\frac{\partial u_0 u_2}{\partial x}+\frac{\partial\left(\frac{u_1^2}{2}\right)}{\partial x}+\frac{1}{M^2}\tau_2\frac{\partial p_0}{\partial x}+\frac{1}{M^2}\tau_0\frac{\partial p_2}{\partial x}+\frac{1}{M^2}\tau_1\frac{\partial p_1}{\partial x}\right)=0\end{aligned} \tag{1.25}$$

In the low Mach number limit, $M \simeq \epsilon$. It implies :
- At the order $\frac{1}{\epsilon^2}$: $\frac{\partial p_0}{\partial x}=0.$

- At the order $\frac{1}{\epsilon}$: $\frac{\partial p_1}{\partial x} = 0.$

- At zero order : $\frac{\partial u_0}{\partial t} + u_0 \frac{\partial u_0}{\partial x} + \tau_0 \frac{\partial p_2}{\partial x} = 0.$

- At the order ϵ : $\frac{\partial u_1}{\partial t} + \frac{\partial u_0 u_1}{\partial x} = 0.$

- At the order ϵ^2 : $\frac{\partial u_2}{\partial t} + \frac{\partial u_0 u_2}{\partial x} + \frac{\partial \left(\frac{u_1^2}{2} \right)}{\partial x} = 0.$

It means that, at leading order, the momentum equation reads :

$$\frac{\partial u_0}{\partial t} + u_0 \frac{\partial u_0}{\partial x} + \tau_0 \frac{\partial p_2}{\partial x} = 0. \tag{1.26}$$

This equation involves the second order pressure fluctuation gradient, as both zero and first order pressure gradients are zero in this limit.
Making the same calculations with the pressure evolution equation, the following result is obtained at leading order :

$$\frac{\partial p_0}{\partial t} + \rho c_0^2 \frac{\partial u_0}{\partial x} = 0 \tag{1.27}$$

The limit leading order system thus reads :

$$\begin{aligned} &\frac{\partial \rho_0}{\partial t} + u_0 \frac{\partial \rho_0}{\partial x} + \rho_0 \frac{\partial u_0}{\partial x} = 0, \\ &\frac{\partial u_0}{\partial t} + u_0 \frac{\partial u_0}{\partial x} + \frac{1}{\rho_0} \frac{\partial p_2}{\partial x} = 0, \\ &\frac{\partial p_0}{\partial t} + \rho_0 c_0^2 \frac{\partial u_0}{\partial x} = 0. \end{aligned} \tag{1.28}$$

Under the condition,

$$\frac{\partial p_0}{\partial t} = 0, \tag{1.29}$$

System (1.28) tends formally to the incompressible Euler equations,

$$\begin{aligned} &\rho_0 = const, \\ &\frac{\partial u_0}{\partial x} = 0, \\ &\frac{\partial u_0}{\partial t} + u_0 \frac{\partial u_0}{\partial x} + \frac{1}{\rho_0} \frac{\partial p_2}{\partial x} = 0. \end{aligned} \tag{1.30}$$

To enforce condition (1.29), an extra coefficient is added to the pressure equation of System (1.28) :

$$\frac{1}{M^2} \frac{\partial p_0}{\partial t} + \rho_0 c_0^2 \frac{\partial u_0}{\partial x} = 0 \tag{1.31}$$

This penalization strategy, due to Turkel [82], forces solutions of System (1.28) to converge to incompressible solutions of System (1.30).

System considered for the Riemann problem solution

Inserting (1.31) in (1.28) and using $\frac{\partial p_0}{\partial x} = 0$ and $\frac{\partial p_1}{\partial x} = 0$, the fluctuation pressure gradient $\frac{\partial p_2}{\partial x}$ can be expressed as :

$$\frac{\partial p_2}{\partial x} = \frac{\partial (p_0 + p_1 + p_2)}{\partial x} = \frac{\partial p}{\partial x} \tag{1.32}$$

Therefore, the following leading order system is obtained :

$$\begin{aligned} &\frac{\partial \rho}{\partial t} + u\frac{\partial \rho}{\partial x} + \rho\frac{\partial u}{\partial x} = 0 \\ &\frac{\partial u}{\partial t} + u\frac{\partial u}{\partial x} + \frac{1}{\rho}\frac{\partial p}{\partial x} = 0. \\ &\frac{\partial p}{\partial t} + M^2 u\frac{\partial p}{\partial x} + M^2\rho c^2\frac{\partial u}{\partial x} = 0 \end{aligned} \tag{1.33}$$

This system is hyperbolic and has the following wave speeds : $u, u + \tilde{c}_+, u - \tilde{c}_-$, with,

$$\tilde{c}_- = \frac{(1-M^2)u + \sqrt{(M^2-1)^2u^2 + 4M^2c^2}}{2}, \quad \tilde{c}_+ = \frac{(M^2-1)u + \sqrt{(M^2-1)^2u^2 + 4M^2c^2}}{2}. \tag{1.34}$$

These wave speeds are directly used in the HLLC solver (1.74). It is worth to mention that the Euler system is modified in the Riemann problem resolution only, where formulation (1.33) is used. With the fluxes computed with the HLLC solver, the Godunov method (1.73) is used with the conventional conservative formulation of the Euler equations and unmodified equation of state. Thus, the solved flow model corresponds exactly to the Euler equations with the EOS (1.4). In this variant of the Turkel [82] method, due to Guillard and Viozat [38], the preconditioning only appears in the flux computation. The formulation remains conservative and guarantees correct jumps across waves, as will be illustrated later. It only acts on the numerical dissipation. As the conservative formulation is used, even strong discontinuities can be handled by the method. Also, as the Mach number can be varied in (1.33), the method is able to compute fast flows. This remarkable feature is due to Guillard and Viozat [38]. The validity and efficiency of this method is illustrated later. We now address an extension to the two-phase flow model (1.1) and its pressure non equilibrium variant (1.6).

Two-phase low Mach preconditioning

The pressure non-equilibrium model (1.6) in primitive variables formulation, reads :

$$\begin{aligned}
&\frac{\partial \alpha_1}{\partial t} + u\frac{\partial \alpha_1}{\partial x} = 0 \\
&\frac{\partial \alpha_1\rho_1}{\partial t} + \alpha_1\rho_1\frac{\partial u}{\partial x} + u\frac{\partial \alpha_1\rho_1}{\partial x} = 0 \\
&\frac{\partial \alpha_2\rho_2}{\partial t} + \alpha_2\rho_2\frac{\partial u}{\partial x} + u\frac{\partial \alpha_2\rho_2}{\partial x} = 0 \\
&\frac{\partial u}{\partial t} + u\frac{\partial u}{\partial x} + \frac{1}{\rho}\frac{\partial P}{\partial x} = 0 \\
&\frac{\partial e_1}{\partial t} + u\frac{\partial e_1}{\partial x} + \frac{p_1}{\rho_1}\frac{\partial u}{\partial x} = 0 \\
&\frac{\partial e_2}{\partial t} + u\frac{\partial e_2}{\partial x} + \frac{p_2}{\rho_2}\frac{\partial u}{\partial x} = 0 \\
&\frac{\partial P}{\partial t} + u\frac{\partial P}{\partial x} + \rho c^2\frac{\partial u}{\partial x} = 0
\end{aligned} \tag{1.35}$$

Where $P = \alpha_1 p_1 + \alpha_2 p_2$.
The pressure relaxation terms have been omitted as they are solved separately. This system admits the following frozen sound speed defined by :

$$c_f = \sqrt{Y_1 c_1^2 + Y_2 c_2^2} \tag{1.36}$$

This sound speed is very different from the mechanical equilibrium one given by (1.2). However, the equilibrium sound speed is recovered after the projection to pressure equilibrium, as summarized in Section 2. Theoretical details on sound propagation in media with relaxation may be found, for example, in [86]. In the present two-phase flow context, the sound speed has dramatic variations, from formula (1.36) to (1.2). Theoretical proof is given in [47] or [74].
As System (1.6) is overdetermined (see again Section 2 for details), its primitive formulation is also overdetermined. In particular, the mixture pressure equation and the two internal energy equations form an overdetermined subsystem.
During low Mach preconditioning, in order to force the incompressibility condition,

$$\frac{\partial u}{\partial x} = 0, \tag{1.37}$$

when the Mach number tends to zero, the pressure equation has been modified with a penalization coefficient (Equation 1.31), resulting in System (1.33) in the single phase flows context. Here, the same preconditioned pressure formulation is adopted :

$$\frac{1}{M^2}\frac{\partial P}{\partial t} + u\frac{\partial P}{\partial x} + \rho c^2\frac{\partial u}{\partial x} = 0 \tag{1.38}$$

Modifying the mixture pressure equation immediately modifies the wave speeds, as previously in the single phase flow case :

$$\tilde{c}_- = \frac{(1-M^2)u + \sqrt{(M^2-1)^2u^2 + 4M^2c_f^2}}{2} \quad \tilde{c}_+ = \frac{(M^2-1)u + \sqrt{(M^2-1)^2u^2 + 4M^2c_f^2}}{2} \tag{1.39}$$

These two last formulas are identical to those given by Murrone and Guillard [62] and Braconnier and Nkonga [17]. However, the Mach number is calculated with the sound speed (1.36). With the help of (1.37), the incompressible limit of System (1.35) becomes :

$$\begin{aligned}
&\frac{\partial \alpha_1}{\partial t} + u\frac{\partial \alpha_1}{\partial x} = 0,\\
&\frac{\partial \rho_1}{\partial t} + u\frac{\partial \rho_1}{\partial x} = 0,\\
&\frac{\partial \rho_2}{\partial t} + u\frac{\partial \rho_2}{\partial x} = 0,\\
&\frac{\partial u}{\partial t} + u\frac{\partial u}{\partial x} + \frac{1}{\rho}\frac{\partial P}{\partial x} = 0,\\
&\frac{\partial p_1}{\partial t} + u\frac{\partial p_1}{\partial x} = 0 \text{ or alternatively } \frac{\partial e_1}{\partial t} + u\frac{\partial e_1}{\partial x} = 0,\\
&\frac{\partial p_2}{\partial t} + u\frac{\partial p_2}{\partial x} = 0 \text{ or alternatively } \frac{\partial e_2}{\partial t} + u\frac{\partial e_2}{\partial x} = 0,\\
&\frac{\partial u}{\partial x} = 0
\end{aligned} \tag{1.40}$$

The limit internal energy equations will be of particular help to determine appropriate jump relations for the low Mach Riemann solver presented hereafter.

Solving the Riemann problem Using the notations given in Figure (1.3), the various wave speeds are given by :

$$Sl = u_l - \tilde{c}_l, \quad Sr = u_r + \tilde{c}_r, \text{ with definition (1.39)} \tag{1.41}$$

and

$$S_M = \frac{S_R(\rho u)_R - S_L(\rho u)_L - ((\rho u^2 + p)_R - (\rho u^2 + p)_L)}{S_R\rho_R - S_L\rho_L - ((\rho u)_R - (\rho u)_L)}. \tag{1.42}$$

The two-phase Riemann problem is solved as detailed in [74], except for the internal energy equations.
The U_L^* and U_R^* states are determined with the following relations :

$$(\alpha_k\rho_k)_R^* = (\alpha_k\rho_k)_R\frac{S_R - u_R}{S_R - S_M} \tag{1.43}$$

$$(\alpha_k\rho_k)_L^* = (\alpha_k\rho_k)_L\frac{S_L - u_L}{S_L - S_M} \tag{1.44}$$

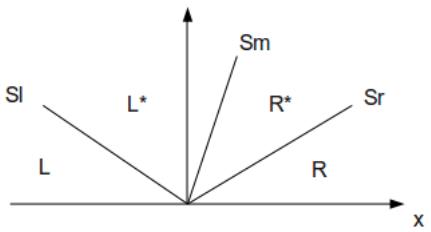

FIGURE 1.3 – Schematics representation of the Riemann problem and associated wave speeds.

$$p^* = p_R + \rho_R u_R(u_R - S_R) - \rho_R^* S_M(S_M - S_R), \text{ where } \rho_R^* = \sum_k (\alpha_k \rho_k)_R^* \tag{1.45}$$

$$E_R^* = \frac{\rho_R E_R(u_R - S_R) + p_R u_R - p^* S_M}{\rho_R^*(S_M - S_R)} \tag{1.46}$$

$$E_L^* = \frac{\rho_L E_L(u_L - S_L) + p_L u_L - p^* S_M}{\rho_L^*(S_M - S_L)} \tag{1.47}$$

In the absence of relaxation effects, the volume fraction is constant along fluid trajectories :

$$\alpha_{k,R}^* = \alpha_{k,R},\ \alpha_{k,L}^* = \alpha_{k,L} \tag{1.48}$$

Once U_L^* and U_R^* are determined, the solution flux vector, F^*, is computed using Relation (1.74) and the following definitions :

$$U = \begin{pmatrix} \alpha_1 \\ \alpha_1\rho_1 \\ \alpha_2\rho_2 \\ \alpha_1\rho_1 e_1 \\ \alpha_2\rho_2 e_2 \\ \rho u \\ \rho E \end{pmatrix} \quad F = \begin{pmatrix} \alpha_1 u \\ \alpha_1\rho_1 u \\ \alpha_2\rho_2 u \\ \alpha_1\rho_1 e_1 u \\ \alpha_2\rho_2 e_2 u \\ \rho u^2 + P \\ (\rho E + P)u \end{pmatrix} \tag{1.49}$$

In the low Mach number limit, the internal energy equations reduce to :

$$\begin{aligned} \frac{\partial e_1}{\partial t} + u\frac{\partial e_1}{\partial x} &= 0 \\ \frac{\partial e_2}{\partial t} + u\frac{\partial e_2}{\partial x} &= 0 \end{aligned} \tag{1.50}$$

Therefore, there is no internal energy jump through the Sl and Sr waves. Thus, the internal energies in the L^* and R^* states are computed as follows :

$$\begin{aligned} e_{k,L}^* &= e_{k,L} \\ e_{k,R}^* &= e_{k,R} \end{aligned} \tag{1.51}$$

These two last relations are very different from the isentropes used in Murrone and Guillard [62]. Let us also mention that equations (1.50) correspond to the asymptotic limit of the entropy equations of System (1.35) and that they also correspond to the same limit of the entropy equations (1.3) corresponding to the mechanical equilibrium System. The influence of the jump relations (1.51) will be examined later with computational experiments.

1.4.2 Preconditioned Riemann solvers illustrations

Single phase nozzle flow

The explicit Godunov scheme of Appendix A with HLLC Riemann solver is used, with the preconditioned wave speed (1.34) derived previously.
In the formulation (1.33), and consequently in the associated Riemann solver given in Appendix A, the Mach number M is set to a reference value M_{ref} which is either used as a constant in the entire flow field or considered variable at each cell boundary. To illustrate the method efficiency, the same nozzle flow problem as studied previously in Figure (1.2) is considered.
A coarse mesh with 100 grid points is considered and the M_{ref} influence is studied. Corresponding results are shown in the Figures (1.4) at steady state.

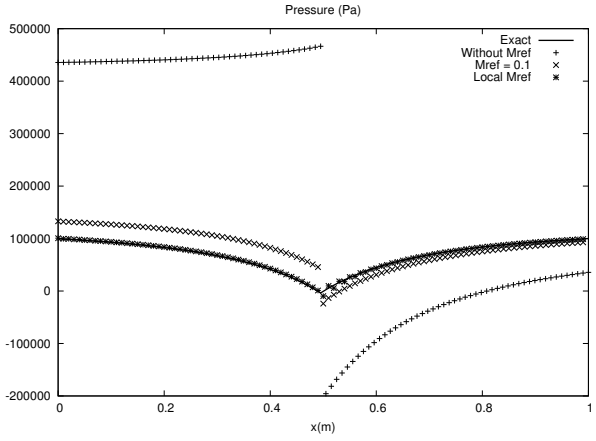

FIGURE 1.4 – Computed pressure profiles in the Laval liquid nozzle flow test with M_{ref}=0.1, M_{ref}=local Mach number and without M_{ref} are compared against the compressible exact solution. The error decreases dramatically as soon as M_{ref} is used and tends to the local Mach number.

On this test case, the unpreconditioned Godunov method predicts negative pressure inside the nozzle divergent, which is possible in the frame of SG EOS. Preconditioning the method corrects this defect. These results clearly show the benefit of the Riemann solver preconditioning as close agreement with the exact solution is reached. However, the explicit scheme is not efficient enough for practical applications because of the stability restriction (1.54), due to [15]. An implicit formulation will be addressed later to overcome this restriction. Be-

fore addressing this extension, the explicit formulation is examined (for obvious simplicity reasons) in the two-phase flow context.

Two-phase nozzle flow

To illustrate the two-phase low Mach number preconditioning, the same nozzle flow problem as studied previously is considered. However, the liquid water at the inflow now contains a small fraction of air.
Mass flow rate and total enthalpy are imposed at left while the right outlet is opened to the atmosphere. The fluids used in the calculations correspond to liquid water and air, with the following SG EOS (1.4) parameters $\gamma_{water} = 4.4$, $P_{\infty,water} = 600MPa$, $\gamma_{air} = 1.4$, $P_{\infty,air} = 0Pa$. The imposed conditions at left inflow are the following :

$$m = 6500\, kg.m^{-2}.s^{-1} \quad \rho_{water} = 1000\, kg.m^{-3} \quad \rho_{air} = 1\, kg.m^{-3} \quad \alpha_{water} = 0.9999 \quad P = 0.1\, MPa$$

The imposed total enthalpy is computed with $\rho_{water}, \rho_{air}, \alpha_{water}$ and P. With these boundary conditions, the numerical solution has been computed using different values of $M_{ref,min}$: 0.1, 0.05, 0.01 and two meshes containing 100 cells and 200 cells, respectively. $M_{ref,min}$ will be defined in the next subsection. The quasi-1D two-phase reference solution is computed using the method described in Appendix B. Figure (1.5) shows clearly that the waves' speeds choice and modification of the solver have dramatic consequences on method convergence in the low Mach number limit. These results are compared to the ones obtained with Murrone and Guillard [62] low Mach preconditioning technique on Figure (1.6). These results show that, even though the Murrone and Guillard [62] low Mach preconditioning technique improve solution accuracy, convergence to the exact solution is not reached at all. This is mainly a consequence of inappropriate energy jump conditions used in the Riemann solver by these authors in the low Mach limit. Murrone and Guillard method uses isentropic evolutions across the left and right facing waves whereas Relations (1.51) are used herein.

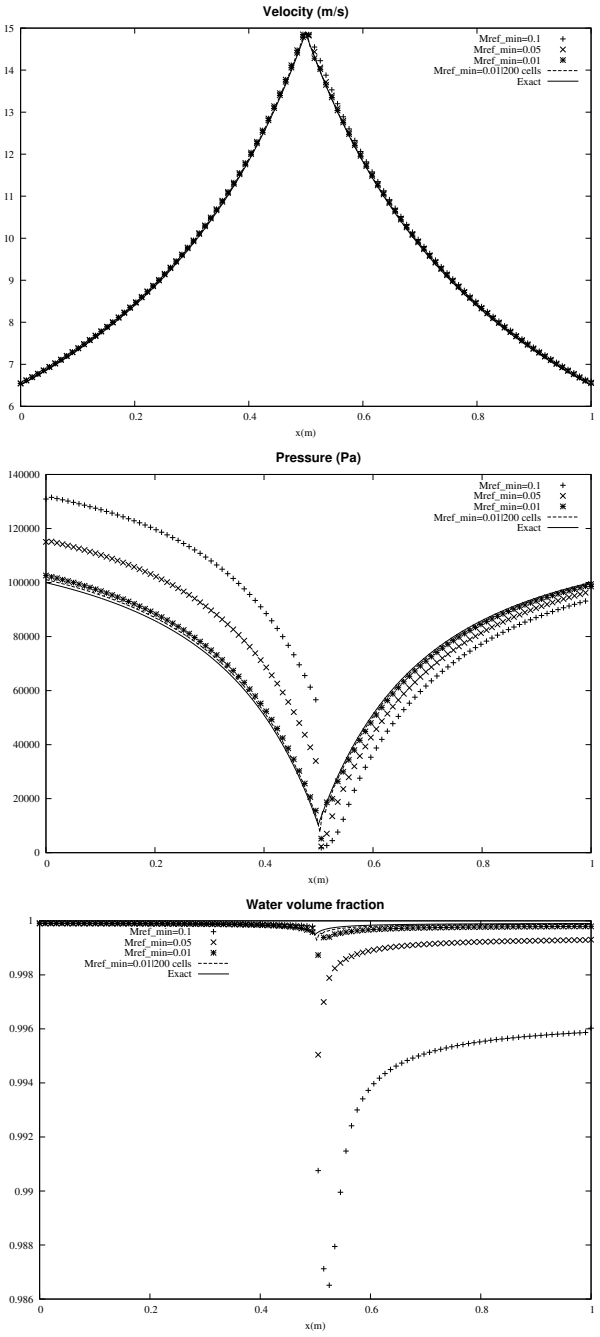

FIGURE 1.5 – Computed mixture velocity, mixture pressure, and water volume fraction profiles in the two-phase nozzle using different values of M_{ref} against the compressible exact solution. The error decreases dramatically as soon as M_{ref} is used and tends to the local Mach number.

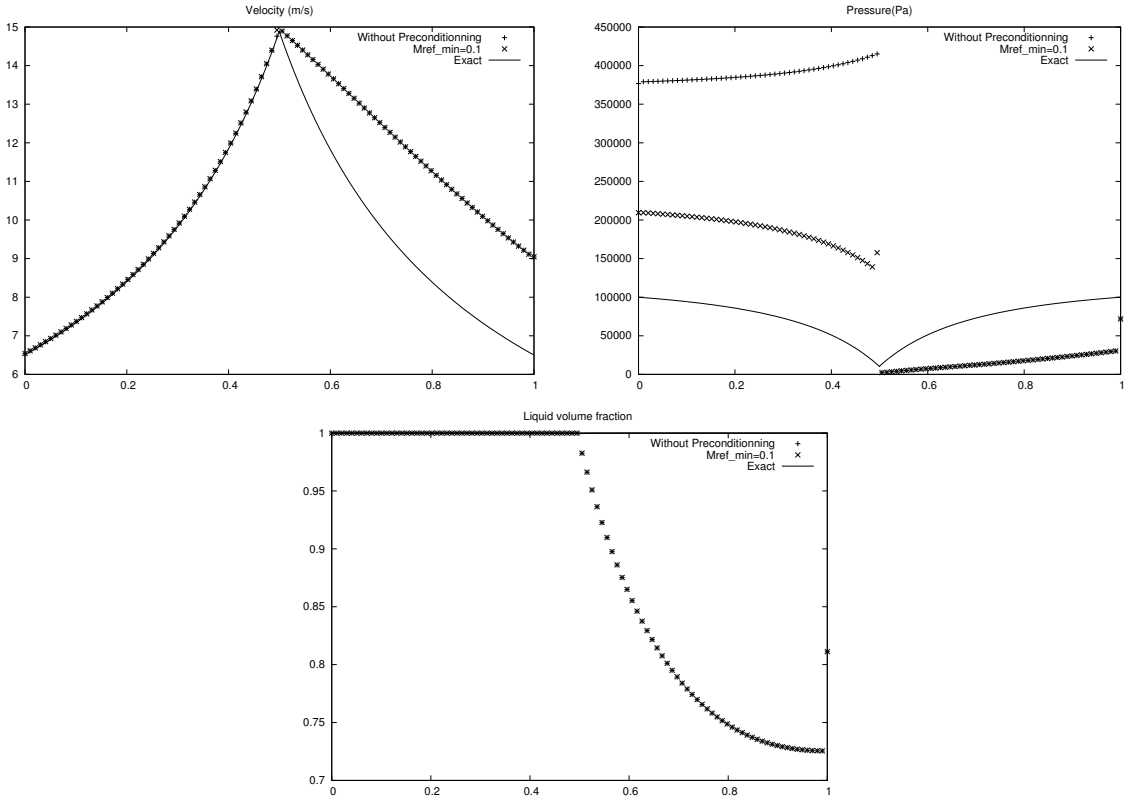

FIGURE 1.6 – Computed mixture pressure, velocity and water volume fraction profiles in the two-phase nozzle using Murrone and Guillard [62] low Mach preconditioning technique compared to the exact compressible solution. This technique clearly has convergence issues for two-phase solutions.

Preconditioning method precautions

It appears clearly that the waves' speed choice in the HLLC solver has dramatic consequences on method convergence in the low Mach number limit. It is also clear that the more M_{ref} tends to the local Mach number, in the low Mach limit, the better the accuracy is. Therefore, the best solution consists in setting the reference Mach number, M_{ref}, to the local one, M_i. But, as the artificial "sound speeds" (1.34) tend to wrong values when M tends to 0, the following function is used :

$$M_{ref}^i = \begin{cases} 1, \text{ if } M_i \geq 0.3 \\ M_i, \text{ if } 0.3 > M_i > M_{ref,min} \\ M_{ref,min}, \text{ if } M_i \leq M_{ref,min} \end{cases} \tag{1.52}$$

The upper limit, 0.3 has been chosen in reference to the "common" arbitrary barrier between a compressible and an incompressible flow. Nevertheless, depending on the applications, changing this limit might have some impacts on the solution. In the test cases considered in this paper, using 0.3 was appropriate.

The minimum Mach number, $M_{ref,min}$ is typically 10^{-2} or 10^{-3}. The preconditioned sound speeds must be computed with a unique M^*_{ref} at a given cell boundary for the Riemann problem resolution :

$$M^*_{ref} = Max(M^L_{ref}, M^R_{ref}) \tag{1.53}$$

Where the superscripts "L" and "R" denote the left and right states of a cell boundary.
It is also important to report the computational cost to reach steady state on the previous computational example with this method . The stability restriction for such scheme is more restrictive than conventional CFL criterion for compressible flows. Indeed, the time step has to fulfil [15] :

$$\Delta t \leq CFL\, M_{ref,min} \frac{\Delta x}{Max(|u| + c)} \tag{1.54}$$

This modified CFL restriction is due to the added dissipation by the modified wave speeds (1.39). It explains the computational costs reported in the Tables (1.2 - 1.3) :

$M_{ref,min}$	CPU
0.1	3min 17s
Minimum local Mach	1h 23min 12s

TABLE 1.2 – Computational time versus $M_{ref,min}$ for the Laval **single phase** nozzle test problem with 100 cells.

$M_{ref,min}$	CPU
0.1	4min 06s
0.01	44min
0.01	2h 36min (200 cells)

TABLE 1.3 – Computational time versus $M_{ref,min}$ for the Laval **two-phase** nozzle test problem with 100 and 200 cells.

The corresponding Godunov scheme with low Mach preconditioning is thus accurate but still expensive due to the time step restriction (1.54). Is is thus mandatory to derive an implicit scheme.

1.5 Implicit scheme

1.5.1 Implicit scheme for the Euler equations

In order to overcome aforementioned stability restrictions, an implicit scheme has to be used. For the sake of simplicity, the implicit scheme is first presented for the Euler equations in 1D. Multi-D and multiphase extensions is addressed later.

Implicit Godunov scheme

The implicit version of the Godunov scheme reads :

$$U_i^{n+1} - U_i^n = -\frac{\Delta t}{\Delta x}(F_{i+\frac{1}{2}}^{n+1} - F_{i-\frac{1}{2}}^{n+1}) \tag{1.55}$$

Where the flux vectors $F_{i+\frac{1}{2}}^{n+1}$ and $F_{i-\frac{1}{2}}^{n+1}$ are computed according to variables at time t^{n+1}. Under Taylor expansion, the flux vectors become :

$$F_{i+\frac{1}{2}}^{n+1} = F_{i+\frac{1}{2}}^n + \left(\frac{\partial F_{i+\frac{1}{2}}}{\partial U_i}\right)^n (U_i^{n+1} - U_i^n) + \left(\frac{\partial F_{i+\frac{1}{2}}}{\partial U_{i+1}}\right)^n (U_{i+1}^{n+1} - U_{i+1}^n) \tag{1.56}$$

$$F_{i-\frac{1}{2}}^{n+1} = F_{i-\frac{1}{2}}^n + \left(\frac{\partial F_{i-\frac{1}{2}}}{\partial U_i}\right)^n (U_i^{n+1} - U_i^n) + \left(\frac{\partial F_{i-\frac{1}{2}}}{\partial U_{i-1}}\right)^n (U_{i-1}^{n+1} - U_{i-1}^n) \tag{1.57}$$

Let's take the example of the right cell boundary. The corresponding flux, $F_{i+\frac{1}{2}}^n$, is solution of the Riemann problem and is consequently function of the left and right states : $F_{i+\frac{1}{2}}^n = F^*\left(U_i^n, U_{i+1}^n\right)$. The Riemann solver used here is the HLLC solver, already presented (1.74). Let's denote the variation :

$$\delta U_i = U_i^{n+1} - U_i^n \tag{1.58}$$

Rewriting Relations (1.55), (1.56) and (1.57) using (1.58), the following scheme is obtained :

$$\begin{aligned} &-\frac{\Delta t}{\Delta x}\left(\frac{\partial F_{i-\frac{1}{2}}}{\partial U_{i-1}}\right)^n \delta U_{i-1} + \delta U_i \left[I + \frac{\Delta t}{\Delta x}\left(\frac{\partial F_{i+\frac{1}{2}}}{\partial U_i}\right)^n - \frac{\Delta t}{\Delta x}\left(\frac{\partial F_{i-\frac{1}{2}}}{\partial U_i}\right)^n\right] + \frac{\Delta t}{\Delta x}\left(\frac{\partial F_{i+\frac{1}{2}}}{\partial U_{i+1}}\right)^n \delta U_{i+1} \\ &= -\frac{\Delta t}{\Delta x}(F_{i+\frac{1}{2}}^n - F_{i-\frac{1}{2}}^n) \end{aligned} \tag{1.59}$$

It forms a block tridiagonal linear system composed of full matrices. This tridiagonal system can be solved either by direct or by iterative methods. We have implemented the Gauss-Siedel iterative method as well as a connexion with the PETSC libraries [7] [6] [8], which use the Krylov subspace method.

It is worth to mention that this Taylor expansion method is a particular case of the Newton-Raphson method which can be presented as follows. Let's consider the function $G(\delta U)$ whose components are $G_i(\delta U) = \delta U + \frac{\Delta t}{\Delta x}(F_{i+\frac{1}{2}}^{n+1} - F_{i-\frac{1}{2}}^{n+1})$. The goal is to solve,

$$G(\delta U) = 0. \tag{1.60}$$

As $F_{i+\frac{1}{2}}^{n+1}$ and $F_{i-\frac{1}{2}}^{n+1}$ are non-linear functions of δU_i, one way to solve this equation is to use the Newton-Raphson method, which, in this case, reads :

$$G(\delta U^{k+1}) = G(\delta U^k) + \left(\frac{\partial G(\delta U^k)}{\partial \delta U^k}\right)\left(\delta U^{k+1} - \delta U^k\right) \tag{1.61}$$

As the $G(\delta U^{k+1}) = 0$ condition has to be reached, the following formula is obtained :

$$\delta U^{k+1} = \delta U^k - \left[\left(\frac{\partial G(\delta U^k)}{\partial \delta U^k}\right)\right]^{-1} G(\delta U^k) \tag{1.62}$$

where δU^k represents δU at the k step of the iterative method. For practical applications, one or two iterations only are used.
The implicit Godunov type scheme needs an approximate Riemann solver to compute the numerical fluxes $F^n_{i\pm\frac{1}{2}}$ as well as the various flux derivatives. The HLLC flux (1.74) is used and the flux derivatives appearing in (1.59) are given by :

$$\frac{\partial F_{LR}}{\partial U_L} = \frac{1}{2}\frac{\partial F_L}{\partial U_L} - \frac{1}{2}\sum_j^{n_w} sign(\lambda_j)\frac{\partial \delta W_j}{\partial U_L}, \quad \frac{\partial F_{LR}}{\partial U_R} = \frac{1}{2}\frac{\partial F_R}{\partial U_R} - \frac{1}{2}\sum_j^{n_w} sign(\lambda_j)\frac{\partial \delta W_j}{\partial U_R} \tag{1.63}$$

The calculation details for the HLLC Riemann solver are given in the Appendix C.

For the considered test cases shown in this paper, solving the linear system takes about 70% of the computation time.

Illustrations

To illustrate the implicit scheme efficiency, we consider the same test problem as before (Section 1.4.2). A coarse mesh with 100 grid points is considered. Corresponding results are shown in the Figures (1.7) at steady state.

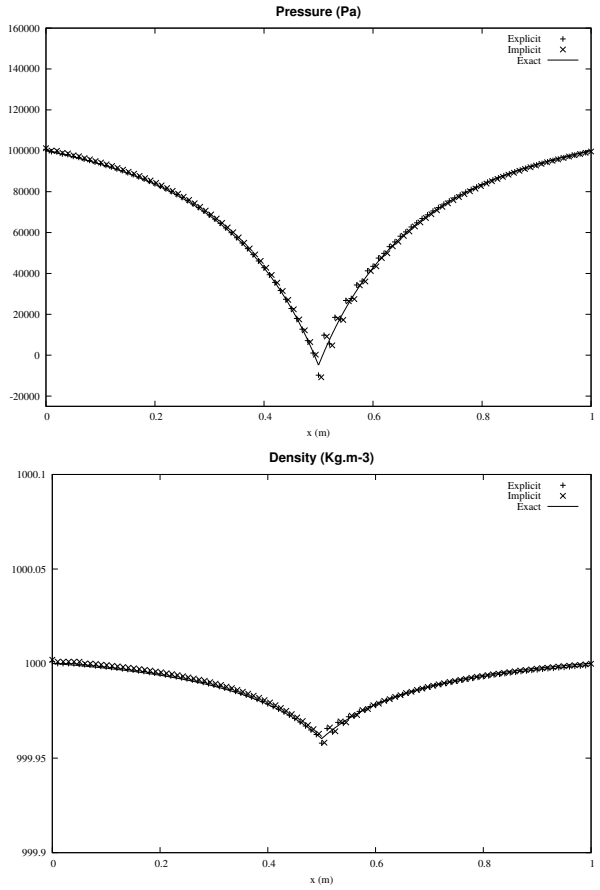

FIGURE 1.7 – Computed pressure and density profiles in the Laval liquid nozzle flow with $M_{ref} = M_i$ compared against the compressible exact solution. Implicit, explicit and exact solutions show excellent agreement.

As expected, the implicit scheme is numerically stable for larger time steps. It is worth to mention that the computational time is now 4 min, with a CFL coefficient equal to 15, to be compared to the computational time of 43 min needed by the explicit scheme, with stability condition (1.54) .

Time accuracy

The previous sections have illustrated the implicit scheme ability to converge to exact steady solutions using low Mach number preconditioning . In order to check its time accuracy capabilities, a liquid-liquid shock tube test-case is considered. The domain is a 1m long shock tube containing two chambers separated by an interface at the location x=0.5m. In this tube, each chamber contains pure liquid water ($\gamma_{water} = 4.4$, $P_{\infty,water} = 600MPa$) at an initial density of 1000 $kg.m^{-3}$. The initial pressure in the left chamber is set equal to 1 MPa while the initial pressure in the right chamber is set equal to 0.1 MPa.

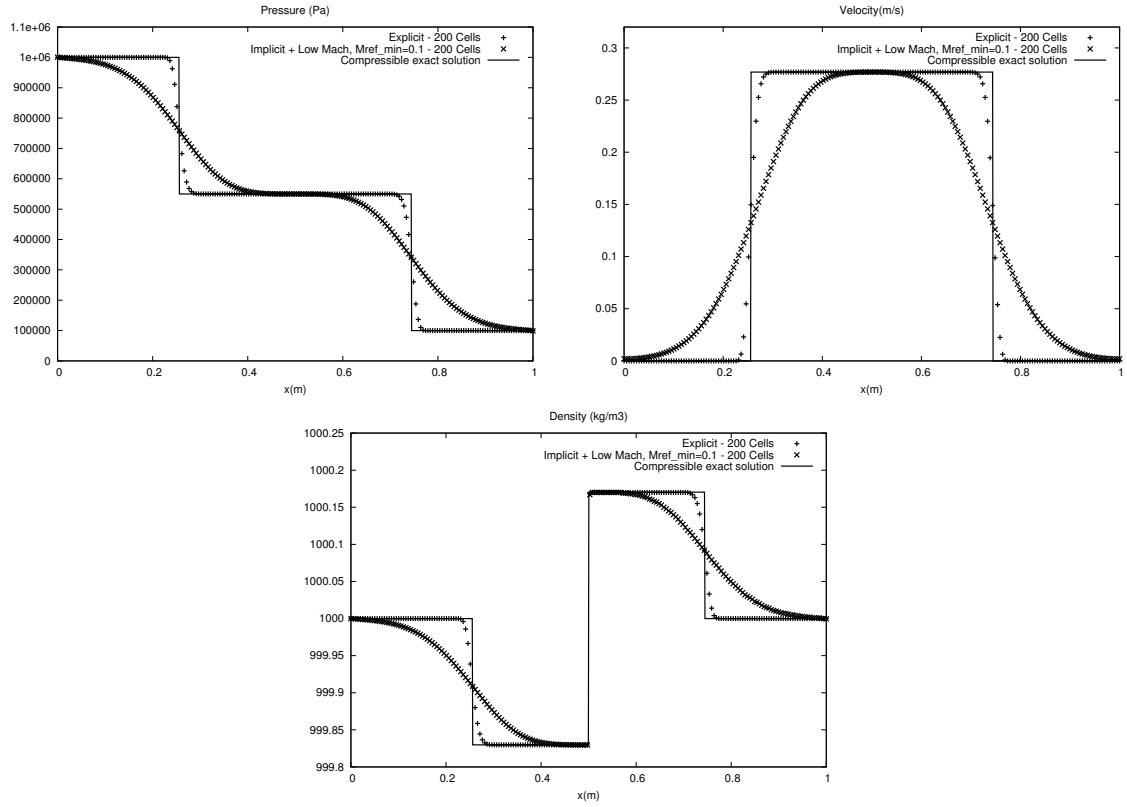

FIGURE 1.8 – Computed pressure, velocity and density profiles in the liquid-liquid shock tube with the conventional explicit Godunov scheme and the implicit scheme with low Mach preconditioning ($M_{ref,min} = 0.1$) compared against the compressible exact solution. The implicit scheme using low Mach preconditioning is clearly diffused but predicts the correct jumps through the shock and expansion wave.

The explicit scheme and the implicit scheme with low Mach preconditioning numerical solutions are compared to the exact solution of the Euler equations at a physical time equals to $t = 0.15ms$ (Figure 1.8). These computations are made on a mesh composed of 200 uniform cells with a CFL coefficient equal to 0.8 for the explicit low Mach computations and 8.0 for the implicit ones. These results show that the low Mach preconditioning preserves waves propagation. Indeed, although the results calculated with the implicit scheme and low Mach number preconditioning are clearly diffused, they predict the correct jumps through the shock and expansion wave as well as the correct mean waves positions. This time accuracy capability is of fundamental importance to predict cavitation instabilities in industrial systems as those illustrated in Figures 1.12 and 1.15. These instabilities are closely linked to pressure wave propagation. The present method is clearly time accurate.

1.5.2 Multi-D extension

Multi-D extension of the method requires Riemann solver preconditioning as developed previously. Indeed, even if it has been argued that low Mach convergence difficulties were vanishing when using triangular cells [39], [24] with conventional Godunov methods, this "miracle" strictly due to triangles was only possible for open domains, i.e in the absence of boundary conditions. This is not at all the case for practical applications. Therefore we address in the following a multi-D extension of the implicit method presented previously. Let's consider a cell, i, and denote by $V(i)$ its volume and by $Vo(i)$ the set of neighbouring and cells, as shown in the Figure 1.9. Therefore, the implicit Godunov finite volumes scheme

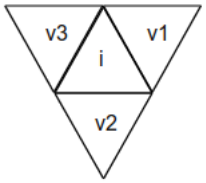

FIGURE 1.9 – Schematic representation of a triangular cell with its set of neighbours, $Vo(i) = \{V_1, V_2, V_3\}$

reads :

$$(U_i^{n+1} - U_i^n) = -\frac{\Delta t}{V(i)} \sum_{j \in Vo(i)} F_{i,j}^{n+1} \tag{1.64}$$

Under similar notations as in 1D, the fluxes are expanded as follows :

$$F_{i,j}^{n+1} = F_{i,j}^n + \frac{\partial F_{i,j}}{\partial U_i}\Big)^n \left(U_i^{n+1} - U_i^n\right) + \frac{\partial F_{i,j}}{\partial U_j}\Big)^n \left(U_j^{n+1} - U_j^n\right) \tag{1.65}$$

Denoting the variation by $\delta U_i = U_i^{n+1} - U_i^n$ and using (1.65) in (1.64) the following scheme is obtained,

$$\left(I + \frac{\Delta t}{V(i)} \sum_{j \in Vo(i)} A_{ii}^j\right) \delta U_i + \frac{\Delta t}{V(i)} \sum_{j \in Vo(i)} \left(A_{ij}^j \delta U_j\right) = -\frac{\Delta t}{V(i)} \sum_{j \in Vo(i)} F_{i,j}^{n+1} \tag{1.66}$$

with,

$$A_{ii}^j = \frac{\partial F_{i,j}}{\partial U_i}\Big)^n, \quad A_{ij}^j = \frac{\partial F_{i,j}}{\partial U_j}\Big)^n.$$

Under compact form it reads,

$$M \delta U = D,$$

where,

$$\delta U = \begin{bmatrix} \delta U_1 \\ . \\ . \\ . \\ \delta U_N \end{bmatrix}, \quad D = \begin{bmatrix} . \\ . \\ -\dfrac{\Delta t}{V(i)} \sum_{j \in Vo(i)} F_{i,j}^{n+1} S(ij) \\ . \\ . \end{bmatrix}.$$

The M matrix shape depends on the number of faces per cell. In order to save computational time, the sparse character of the M matrix has to be exploited. In this work, the CSC (Compressed Sparse Column) method is used, which is detailed in [69].
Higher order extension of the method is detailed in Appendix D.

1.5.3 Implicit scheme for the two-phase flow model

In this section, the implicit scheme for the hyperbolic two-phase flow model is addressed. The model under consideration corresponds to System (1.6) without relaxation terms. It is considered hereafter in 1D for the sake of simplicity. These equations can be arranged in two sets : Conservative equations on one hand and non-conservatives equations on the other hand. The conservative set of equations reads :

$$\frac{\partial \Omega}{\partial t} + \frac{\partial F(U)}{\partial x} = 0 \tag{1.67}$$

The non-conservative set of equations reads :

$$\frac{\partial V}{\partial t} + \frac{\partial G(U)}{\partial x} + H(U)\frac{\partial u}{\partial x} = 0 \tag{1.68}$$

Where,

$$U = \begin{pmatrix} \Omega \\ V \end{pmatrix}, \Omega = \begin{pmatrix} \alpha_1\rho_1 \\ \alpha_1\rho_2 \\ \rho\mathbf{u} \\ \rho E \end{pmatrix}, V = \begin{pmatrix} \alpha_1 \\ \alpha_1\rho_1 e_1 \\ \alpha_2\rho_2 e_2 \end{pmatrix} \tag{1.69}$$

and,

$$F(U) = \begin{pmatrix} \alpha_1\rho_1\mathbf{u} \\ \alpha_1\rho_2\mathbf{u} \\ \rho\mathbf{u}^2 + P \\ (\rho E + P)\mathbf{u} \end{pmatrix}, G(U) = \begin{pmatrix} \alpha_1\mathbf{u} \\ \alpha_1\rho_1 e_1\mathbf{u} \\ \alpha_2\rho_2 e_2\mathbf{u} \end{pmatrix}, H(U) = \begin{pmatrix} -\alpha_1 \\ \alpha_1 p_1 \\ \alpha_2 p_2 \end{pmatrix} \tag{1.70}$$

The implicit scheme derived previously for the Euler equations is used for the conservative system with some modifications. Indeed, the pressure, P, and the mixture total energy, E, are now functions of $\rho, e, \alpha_1, \alpha_2$ (1.7). Therefore, the derivatives involved in the implicit flux computation are more complex. Their expressions are given in Appendix E. Most of the

efforts are focused on the implicit scheme for the non-conservative system. Approximating (1.8) implicitly reads :

$$V_i^{n+1} = V_i^n - \frac{\Delta t}{\Delta x}\left(G^{*,n+1}_{i+\frac{1}{2}} - G^{*,n+1}_{i-\frac{1}{2}} + H(U)_i^{n+1}\left(u^{*,n+1}_{i+\frac{1}{2}} - u^{*,n+1}_{i-\frac{1}{2}}\right)\right). \tag{1.71}$$

Using the same development as previously (1.56 - 1.57), the following scheme is obtained :

$$\begin{aligned}
&-\frac{\Delta t}{\Delta x}\left[\frac{\partial G_{i-\frac{1}{2}}}{\partial U_{i-1}} + H_i^n \frac{\partial u^*_{i-\frac{1}{2}}}{\partial U_{i-1}}\right]\delta V_{i-1} \\
&+\left[I + \frac{\Delta t}{\Delta x}\left(\frac{\partial G^n_{i+\frac{1}{2}}}{\partial U_i} - \frac{\partial G^n_{i-\frac{1}{2}}}{\partial U_i} + H_i^n\left[\frac{\partial u^*_{i+\frac{1}{2}}}{\partial U_i} - \frac{\partial u^*_{i-\frac{1}{2}}}{\partial U_i}\right] + (u^*_{i+\frac{1}{2}} - u^*_{i-\frac{1}{2}})\frac{\partial H_i^n}{\partial U_i}\right)\right]\delta V_i \\
&+\frac{\Delta t}{\Delta x}\left[\frac{\partial G_{i+\frac{1}{2}}}{\partial U_{i+1}} + H_i^n \frac{\partial u^*_{i+\frac{1}{2}}}{\partial U_{i+1}}\right]\delta V_{i+1} \\
&= -\frac{\Delta t}{\Delta x}\left(G^{*,n}_{i+\frac{1}{2}} - G^{*,n}_{i-\frac{1}{2}} + H_i^n\left(u^{*,n}_{i+\frac{1}{2}} - u^{*,n}_{i-\frac{1}{2}}\right)\right)
\end{aligned} \tag{1.72}$$

The various expressions for the derivatives are detailed in Appendix F.

1.6 Illustrations and validations

1.6.1 One dimensional two-phase nozzle flow

To illustrate the behaviour of the two phase implicit scheme, we consider the same two-phase nozzle flow test as before (Section 1.4.2).The numerical solution has been computed using different values of $M_{ref,min}$(0.1 and 0.01) as well as two different meshes (100 and 200 cells). Corresponding results are shown in the Figure (1.10) at steady state.

The implicit scheme has the same behaviour and accuracy as the explicit version. The corresponding computational cost is reported in the Table 1.4, with stability condition (1.54).

$M_{ref,min}$	CPU (Implicit scheme)	Implicit CFL	Explicit CFL
0.1	46s	30.0	0.9
0.01	8min 45s (200 cells)	150.0	0.9

TABLE 1.4 – Computational time versus $M_{ref,min}$ for the Laval **two-phase** nozzle test problem with the implicit scheme.

Compared to explicit calculation times (Table 1.3), considerable saving appear as the implicit scheme reduces the computation times cost by a factor 18. To conclude, the implicit scheme presented in the previous section is efficient and accurate for two-phase flow calculations. Multi-D two-phase examples are addressed in the next paragraph.

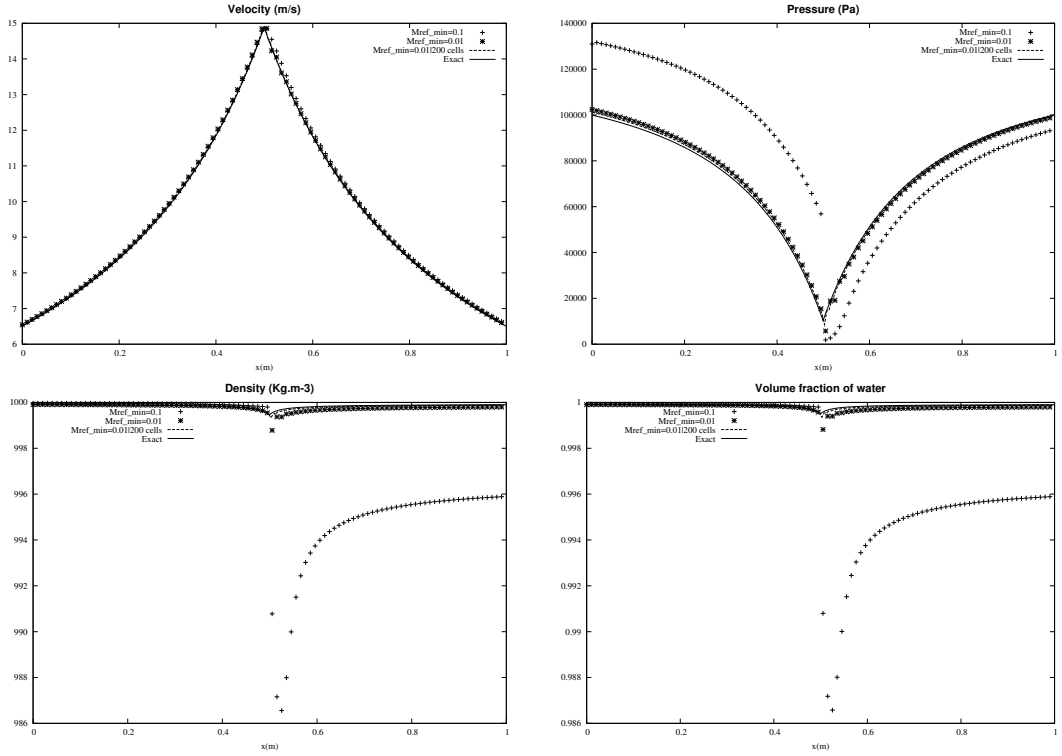

FIGURE 1.10 – Computed mixture pressure, velocity, density and water volume fraction profiles in the two-phase nozzle using different values of $M_{ref,min}$ against the compressible exact solution. The exact solution is reached when $M_{ref,min}$ is equal to 0.01.

1.6.2 2D computations of cavitating flows in Venturi channels

In this paragraph, 2D two phase nozzle flow computation is addressed. We first present the geometry and the various flow parameters. Then, numerical results are compared against experimental records.

Test problem

The experimental facility has been built at LEGI Laboratory, Grenoble, France by the group led by S. Barre. The test section corresponds to a Venturi channel with a nozzle divergent inclined at an angle of 8°. The geometry is shown in the Figure 1.11.

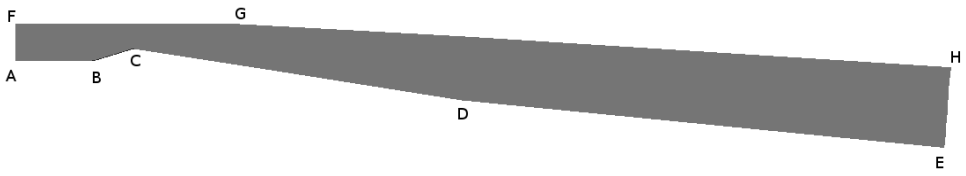

FIGURE 1.11 – LEGI 8° Venturi geometry

The corresponding point coordinates are given in the Table 1.5.

	X (abscissa) (m)	Y (m)		X(abscissa) (m)	Y (m)
A	0	0	E	1.225	-0.114
B	0.1	0	F	0	0.0488
C	0.153	0.0157	G	0.271	0.0488
D	0.588	-0.0517	H	1.233	-0.00845

TABLE 1.5 – Venturi 8° points coordinates.

As phase transition occurs at the throat, heat and mass transfer have to be considered. These effects are accounted for by considering extra relaxation effects in addition to pressure relaxation. Indeed, as detailed in Saurel et al. [73], temperature and Gibbs free energy relaxation have to be considered. Appropriate relaxation solver is summarized in the Appendix G. Simulating phase transition requires appropriate EOS parameters. The fluids considered correspond to liquid water and water vapour, with the following SG EOS (1.4) parameters : $\gamma_{liq} = 1.234$, $P_{\infty,liq} = 2532.302\,atm$, $\gamma_{vap} = 1.316$ and $P_{\infty,vap} = 0\,Pa$. These parameters have been computed following the method detailed in [52].
Mass inflow rate and stagnation enthalpy are imposed and a prescribed pressure is imposed at the outlet. The imposed conditions at the left inlet are the following,

$$m = 7514.917\,kg.m^{-2}.s^{-1} \quad \rho_{liq} = 1067.566\,kg.m^{-3} \quad \rho_{vap} = 0.387\,kg.m^{-3} \quad \alpha_{liq} = 0.999 \quad P = 51825\,Pa$$

while, at the right outlet, the prescribed pressure is $P = 72025Pa$.

Experimental results

The 8° Venturi channel of Figure 1.11 has been used at LEGI (Grenoble, France) to study cavitating flows. With the boundary conditions reported in the previous paragraph, a periodic flow is observed, as shown in the Figure 1.12. In the first stage of the cycle (a), a cavitation sheet is attached to the throat and grows. In a second stage, the sheet reaches its maximum length (b) and breaks in two parts (c). At the end, the downstream part is swept along within the stream and starts to collapse while the attached part starts another cycle (d). The mean attached cavity length value is 45 ± 5 mm while the quasi-periodic vapour clouds shedding frequency is about 45 Hz. The cloud shedding frequency is calculated using spectral analysis of pressure measurement in the Venturi divergent.

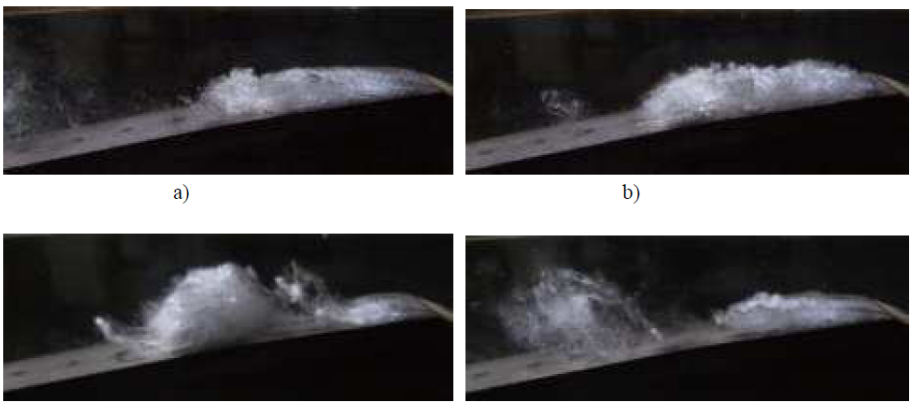

FIGURE 1.12 – Instantaneous pictures of a break off cycle in the 8° Venturi channel of LEGI. Courtesy of S.Barre, LEGI, Grenoble, France.

Numerical results

A 2D unstructured mesh containing 52450 cells is used, as shown in the Figure 1.13. The grid is refined at the throat in order to capture the cavitation pocket. The average cell size is 0.013 mm at the throat and 0.08 mm elsewhere.

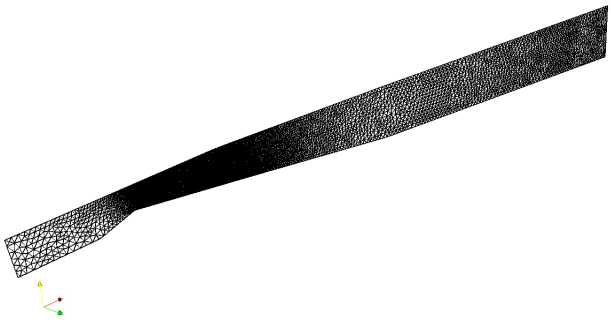

FIGURE 1.13 – Venturi 8° 2D unstructured mesh.

We first address again the remark mentioned at the beginning of Section 5.2, related to the "triangle miracle" [39], [24]. With the mesh shown in Figure (1.13), made of triangles, the two-phase 2D explicit scheme is used without low-Mach preconditioning to reach 1.8s of physical time. As shown in the volume fraction contours of Figure 1.14, the obtained pockets does not present any cloud shedding and they only contain around 27% of vapour. The vapour pocket size as well as the observed behaviour are in total disagreement with the experimental results. Indeed, the mean vapour pocket length is about 18mm and no oscillatory behaviour is observed.

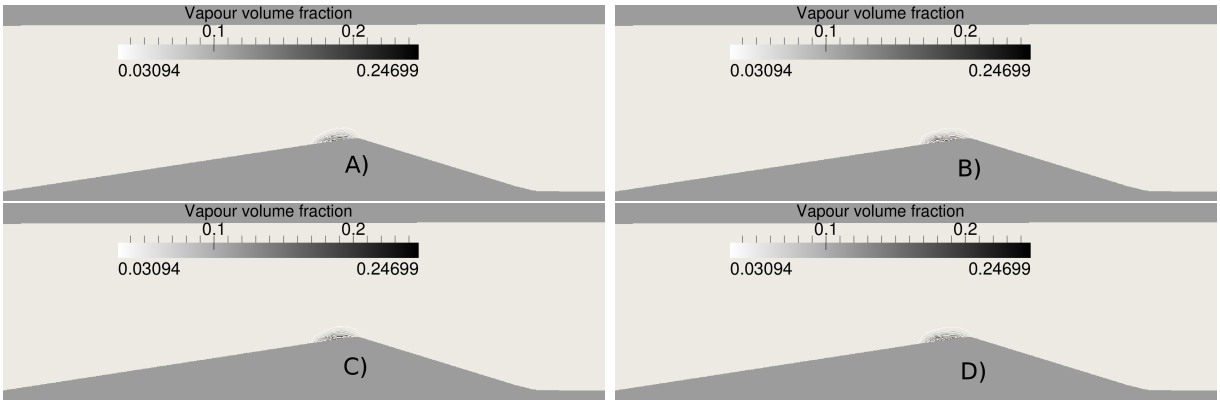

FIGURE 1.14 – Computed contours of volume fraction of water vapor without low Mach preconditioning. The computed results do not present any shedding and the vapour pocket size as well as the computed flow are in complete disagreement with the experiments. The flow is coming from right to left.

We now consider the same mesh with the two-phase 2D implicit scheme along with the two phase low Mach preconditioning ($M_{ref,min}$ is set to 0.04). Using a cluster with 24 CPU, 1.8s of physical time is reached in about 97h with an average CFL coefficient equal to 28. It's worth to mention that the projected calculation time (obtained after running the simulation for two days) using an explicit scheme with the same low Mach preconditioning is about 5107h ($\simeq$ 7 months). Therefore, using the implicit scheme allows for a projected acceleration factor of about 53.
This physical time was long enough to obtain a quasi-stationary flow with quasi-periodic vapour cloud shedding. An example of the obtained cloud shedding is shown in the volume fraction contours of Figure 1.15. Moreover, the velocity magnitude and Mach number countours at the end of the cycle are shown in Figure 1.16. The Mach number is built using the equilibrium sound speed. From the Figures 1.14 and 1.15, it appears that the quasi-incompressible behaviour of the liquid must be considered, otherwise cavitation pockets present huge discrepancies. But, its is also clear that compressible effects are also important, as shown in Figure 1.16. This illustrates the difficulty of cavitating flows computations. A pressure signal is also recorded using a numerical gauge located in the middle of the $\overline{EH}$ segment, at the end of the Venturi divergent (Fig. 1.11). Examining the water vapor volume fraction contours oscillations, a vapour pocket shedding frequency of about 43Hz is determined. In order to check this observed frequency, a spectral analysis of the recorded pressure signal was performed. The obtained spectrum is shown in Figure 1.17. The analysis has been made using the automatic routines of Octave, which uses FFTW librairies [33] in order to compute every needed parameters. Nevertheless, we first subtracted the mean value of the signal, in order to have a zero-centered signal. The maximum intensity is reached for frequencies between 40 and 50Hz, which is in very good agreement with the observed clouds shedding frequency based on the vapour pocket oscillations. By performing measurements during every cycle, an average attached cavity length of about 45 mm has been measured

from the computations. These results show again very good agreement with the experiments. Indeed, experimental measurements gave a mean attached cavity length equals to 45 $\pm$ 5 mm.
An important remark regarding the modelling of such flows appears. It is possible to reproduce the large structures of such cavitating flows without having recourse to adjustable parameter nor turbulence modelling. The present results show that,

- a model in agreement with the fundamental principles of total energy conservation and entropy inequality, and,
- an algorithm suited for two-phase all Mach number conditions,

reproduce with high fidelity the experiments, at least in the present conditions.

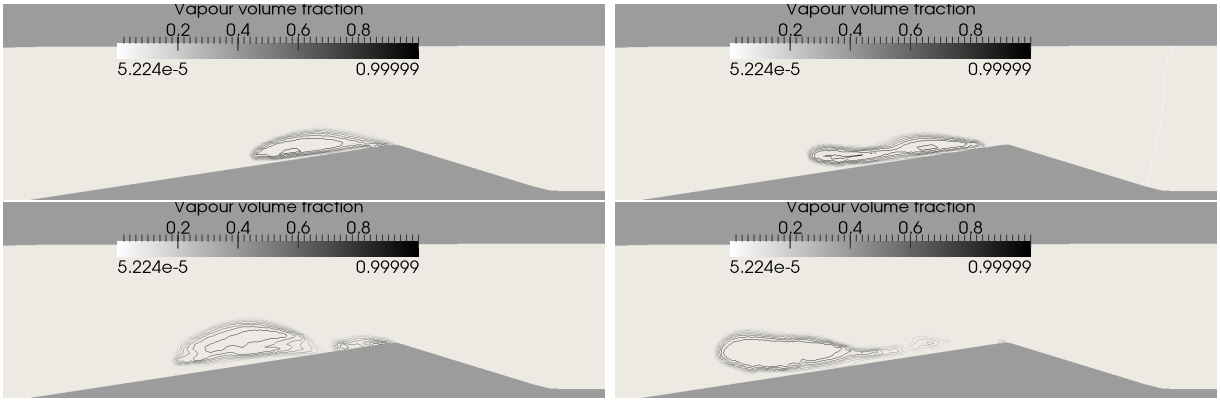

FIGURE 1.15 – Computed contours of volume fraction of water vapour. This example of the computed break off cycles shows the same four different parts as those observed during the experimental studies and shown in the Figure 1.12. The mean attached cavity length is about 45mm, in perfect agreement with the experiments.

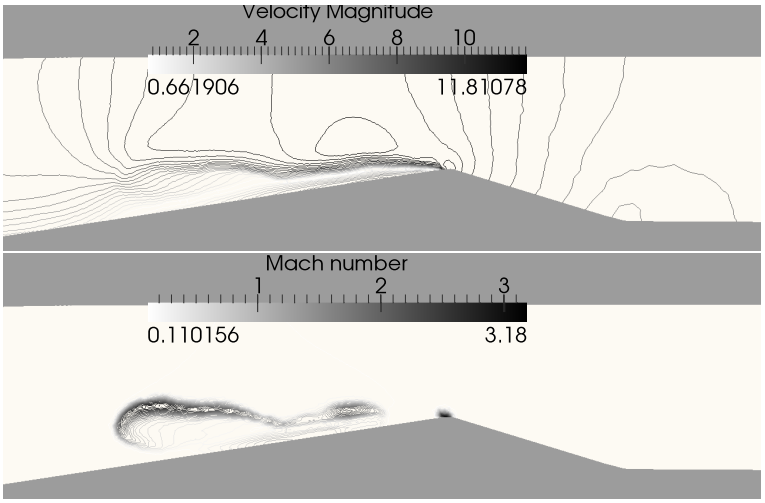

FIGURE 1.16 – Velocity magnitude and Mach number contours at the end of the cycle (D). Throat close-up. The Mach number is built with the equilibrium sound speed.

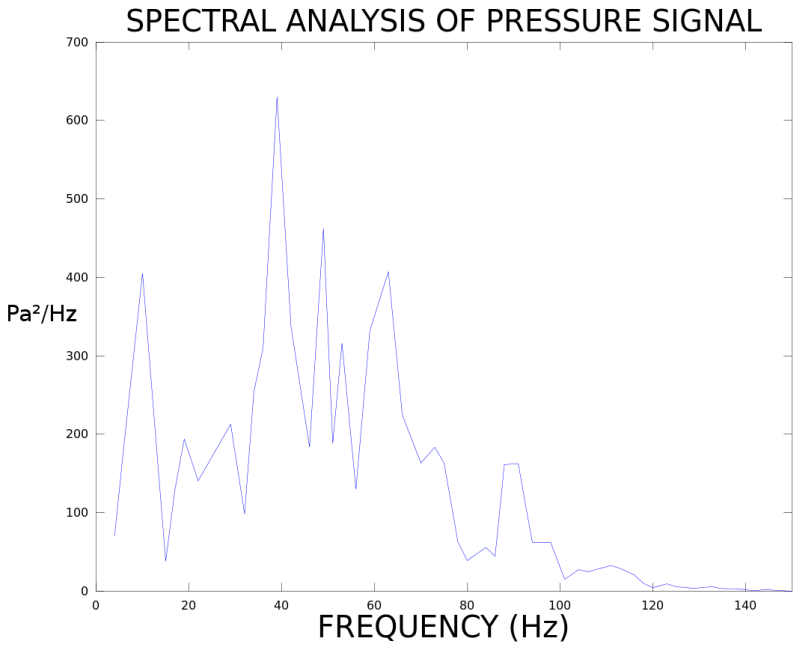

FIGURE 1.17 – Spectral analysis of the recorded pressure signal using a pressure gauge located at the end of the Venturi divergent. The obtained spectrum shows maximum intensity for frequencies between 40 and 50 Hz. This is in excellent agreement with the computed cloud shedding frequency of 43Hz and in excellent agreement with the experimental frequency of 45 ± 5 Hz.

1.7 Conclusion

The Turkel preconditioned formulation has been used in the Riemann problem solution determination and embedded in the Godunov method with HLLC scheme, in both explicit and implicit versions. This variant of the Turkel method, due to Guillard and Viozat [38], has shown particular efficiency for all Mach number single phase flow conditions. It has been extended to the two-phase flow model of Kapila et al [47], particularly suited for interfacial flows [74] as well as cavitating flows [73]. Compared to conventional cavitating flow models widely used in industry, this model conserves energy. Also, phase transition is modelled in a thermodynamically consistent way. The preconditioning method requires mild modifications on the internal energy jumps conditions in the Riemann solver that have important consequences on method convergence. The method has been validated against exact 1D solutions and experimental 2D cavitating Venturi flows. Without using any adjustable parameter, the method has shown its ability to reproduce many challenging features of cavitating flows.

Acknowledgments The first author has been partly supported by CNES and SAFRAN Snecma, space Engines Division. Drs. S. Petitot and P. Boivin are gratefully acknowledged. The authors would like to acknowledge fruitful discussions and works with Dr. F. Petitpas.

Appendix A - Godunov-HLLC scheme for the Euler equations in ducts of smooth varying cross sections

Let's consider a computational cell corresponding to an arbitrary control volume inside a nozzle, as shown in the Figure 1.18. The conventional 1D Godunov scheme for ducts of smooth varying cross sections reads :

$$U_i^{n+1} = U_i^n - \frac{\Delta t}{V_i}\left(F^*_{i+\frac{1}{2}} S_{i+\frac{1}{2}} - F^*_{i-\frac{1}{2}} S_{i-\frac{1}{2}}\right) + \frac{\Delta t}{V_i} G_i \left(S_{i+\frac{1}{2}} - S_{i-\frac{1}{2}}\right) \tag{1.73}$$

with

$$U = \begin{pmatrix} \rho \\ \rho u \\ \rho E \end{pmatrix} \quad F = \begin{pmatrix} \rho u \\ \rho u^2 + p \\ (\rho E + p)u \end{pmatrix} \quad G_i = \begin{pmatrix} 0 \\ p_i^n \\ 0 \end{pmatrix}$$

Where :
- U represents the conservative variables vector,
- F represents the flux vector,
- S represents the cell boundary surface,
- V_i represents the cell volume .

This basic first-order version is used to avoid artefacts in the various computational test. The HLLC Riemann solver (Toro et al.) [80] is used to compute the inter-cell flux F^*. At

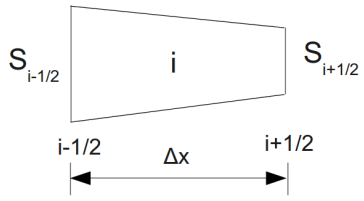

FIGURE 1.18 – Nozzle computational cell i with its two cell boundaries, i+1/2 and i-1/2.

cell boundary $i + \frac{1}{2}$, it reads :

$$F_{L,R} = \frac{1}{2}(F_L + F_R) - sign(S_L)\frac{S_L}{2}(U_L^* - U_L) - sign(S_M)\frac{S_M}{2}(U_R^* - U_L^*) - sign(S_R)\frac{S_R}{2}(U_R - U_R^*) \tag{1.74}$$

The subscripts L and R denote the left and right state of the Riemann problem, respectively.

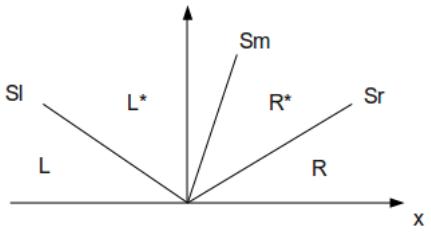

FIGURE 1.19 – Schematization of the Euler equations Riemann problem under HLLC approximation and associated wave speeds.

The wave speeds S_R and S_L are estimated with Davis approximation [23],

$$S_R = Max(u_R + c_R, u_L + c_L), \qquad S_L = Max(u_R - c_R, u_L - c_L), \tag{1.75}$$

while S_M is estimated under HLL [42] approximation,

$$S_M = \frac{S_R U_R(2) - S_L U_L(2) - (F_R(2) - F_L(2))}{S_R U_R(1) - S_L U_L(1) - (F_R(1) - F_L(1))}. \tag{1.76}$$

The states U_L^* and U_R^* are determined with the help of Rankine-Hugoniot jump relations across the S_R and S_L waves,

$$F_L^* - S_L U_L^* = F_L - S_L U_L, \qquad F_R^* - S_R U_R^* = F_R - S_R U_R, \tag{1.77}$$

and interface relations, $u_L^* = u_R^* = S_M$ and $p_L^* = p_R^* = p^*$ across the contact wave. It results in :

$$U_L^* = \frac{1}{S_M - S_L}[F_L - S_L U_L - (0, p^*, S_M.p^*)^T], \qquad U_R^* = \frac{1}{S_M - S_R}[F_R - S_R U_R - (0, p^*, S_M.p^*)^T] \tag{1.78}$$

Appendix B - Exact steady two-phase nozzle solution with imposed mass flow rate and stagnation enthalpy

In many practical situations, the mass flux m_0 is imposed as well as the stagnation enthalpy H_0. For two-phase flows, the mixture enthalpy reads :

$$H_0 = Y_{0,1}h_{0,1} + Y_{0,2}h_{0,2} + \frac{1}{2}u_0^2 \tag{1.79}$$

It means that the mass fractions have to be imposed, as well as the volume fraction of one of the phases, $\alpha_{0,1}$, for example. It is thus necessary to impose m_0, $h_{k,0}$, $Y_{k,0}$ and $\alpha_{1,0}$. Another option being to impose m_0, P_0, $\rho_{k,0}$ and $\alpha_{1,0}$. The exact solution determination with such boundary conditions follows the same methodology as the one detailed previously in [13] for single phase flows.

Outlet state determination for subsonic isentropic flows. The outlet pressure is prescribed and denoted by P_{out}. Using the SG EOS (1.4) the phase total enthalpy is expressed at the outlet as :

$$h_{k,0} = \frac{\gamma_k(P_{out} + P_{\infty,k})v_{k,out}}{(\gamma_k - 1)} + \frac{1}{2}u_{out}^2 \tag{1.80}$$

With the help of the mass flow rate conservation ($m_0 = \rho_{out}A_{out}u_{out}$) and the mixture density definition ($\frac{1}{\rho_{out}} = Y_{1,0}v_{1,out} + Y_{2,0}v_{2,out}$), the two following equations are obtained :

$$h_{1,0} = \frac{\gamma_1(P_{out} + P_{\infty,1})v_{1,out}}{(\gamma_1 - 1)} + \frac{1}{2}\left(\frac{m_0}{A_{out}}\right)^2 (Y_{1,0}v_{1,out} + Y_{2,0}v_{2,out})^2 \tag{1.81}$$

$$h_{2,0} = \frac{\gamma_2(P_{out} + P_{\infty,2})v_{2,out}}{(\gamma_2 - 1)} + \frac{1}{2}\left(\frac{m_0}{A_{out}}\right)^2 (Y_{1,0}v_{1,out} + Y_{2,0}v_{2,out})^2 \tag{1.82}$$

Combining these two relations, an expression linking $v_{1,out}$ and $v_{2,out}$ is obtained :

$$v_{1,out} = \frac{(\gamma_1 - 1)}{\gamma_1(P_{out} + P_{\infty,1})}\left[h_{1,0} - h_{2,0} + \frac{\gamma_2(P_{out} + P_{\infty,2})v_{2,out}}{(\gamma_2 - 1)}\right] \tag{1.83}$$

Using this expression in Relation (1.82), a second order polynomial in $v_{2,out}$ is obtained. The positive solution, $v_{1,out}$ is retained. Once $v_{1,out}$ and $v_{2,out}$ are known, the mixture density at the outlet section is obtained by,

$$\frac{1}{\rho_{out}} = Y_{1,0}v_{1,out} + Y_{2,0}v_{2,out} \tag{1.84}$$

and the outlet velocity is deduced by,

$$u_{out} = \frac{m_0}{\rho_{out}A_o}. \tag{1.85}$$

Last, the volume fractions are determined with the help of mass fractions conservation,

$$\alpha_{k,0} = Y_{k,0}\rho_{out}v_{k,out}. \tag{1.86}$$

Variables state determination in an arbitrary cross section The flow is isentropic between a section of arbitrary area (A) and the outlet section. Thus, writing the phase total enthalpy conservation between a section of arbitrary area and the outlet gives the following relation :

$$h_{k,out} = \frac{\gamma_k(P + P_{\infty,k})v_k(P)}{(\gamma_k - 1)} + \frac{1}{2}\left(\frac{m_0}{A}\right)^2 \left(Y_{1,0}v_{1,out}(P) + Y_{2,0}v_{2,out}(P)\right)^2 \tag{1.87}$$

The mixture pressure, P, is therefore determined by solving one of these relations using the Newton-Raphson method. Once P is known, the phase densities are determined using phases isentropes while the other variables are computed as previously.

Appendix C - HLLC Riemann solver derivatives

The HLLC approximate Riemann solver is recalled hereafter in the context of the Euler equations, where U_L^* and U_R^* are defined by Relation (1.78) :

$$F_{L,R} = \frac{1}{2}(F_L + F_R) - sign(S_L)\frac{S_L}{2}(U_L^* - U_L) - sign(S_M)\frac{S_M}{2}(U_R^* - U_L^*) - sign(S_R)\frac{S_R}{2}(U_R - U_R^*),$$

The flux vector derivatives are given by :

$$\frac{\partial F_{LR}}{\partial U_L} = \frac{1}{2}\frac{\partial F_L}{\partial U_L} - sign(S_L)\frac{S_L}{2}(\frac{\partial U_L^*}{\partial U_L} - 1) - sign(S_M)\frac{S_M}{2}(\frac{\partial (U_R^* - U_L^*)}{\partial U_L}) + sign(S_R)\frac{S_R}{2}(\frac{\partial U_R^*}{\partial U_L}) \tag{1.88}$$

$$\frac{\partial F_{LR}}{\partial U_R} = \frac{1}{2}\frac{\partial F_R}{\partial U_R} - sign(S_L)\frac{S_L}{2}\frac{\partial U_L^*}{\partial U_R} - sign(S_M)\frac{S_M}{2}(\frac{\partial (U_R^* - U_L^*)}{\partial U_R}) - sign(S_R)\frac{S_R}{2}(1 - \frac{\partial U_R^*}{\partial U_R}) \tag{1.89}$$

Where :

$$\frac{\partial U_L^*}{\partial U_L} = \frac{(\frac{\partial F_L}{\partial U_L} - S_L - \frac{\partial}{\partial U_L}(0, p^*, S_M.p^*)^T)(S_M - S_L) - (F_L - S_L U_L - (0, p^*, S_M.P^*)^T)\frac{\partial S_M}{\partial U_L}}{(S_M - S_L)^2} \tag{1.90}$$

$$\frac{\partial U_L^*}{\partial U_R} = \frac{-\frac{\partial}{\partial U_L}((0, p^*, S_M.p^*)^T)(S_M - S_L) - (F_L - S_R U_L - (0, p^*, S_M.p^*)^T)\frac{\partial S_M}{\partial U_R}}{(S_M - S_L)^2} \tag{1.91}$$

$$\frac{\partial U_R^*}{\partial U_L} = \frac{-\frac{\partial}{\partial U_L}((0, p^*, S_M.p^*)^T)(S_M - S_R) - (F_R - S_R U_R - (0, p^*, S_M.p^*)^T)\frac{\partial S_M}{\partial U_L}}{(S_M - S_R)^2} \tag{1.92}$$

$$\frac{\partial U_R^*}{\partial U_R} = \frac{(\frac{\partial F_R}{\partial U_R} - S_R - \frac{\partial}{\partial U_R}(0, p^*, S_M.p^*)^T)(S_M - S_R) - (F_R - S_R U_R - (0, p^*, S_M.p^*)^T)\frac{\partial S_M}{\partial U_R}}{(S_M - S_R)^2} \tag{1.93}$$

Using Relations (1.77), and $p_L^* = p_R^* = p^*$, two expressions for p^* are obtained :

$$p^* = F_L(2) - S_L U_L(2) - S_M(F_L(1) - S_L U_L(1)), \quad p^* = F_R(2) - S_R U_R(2) - S_M(F_R(1) - S_R U_R(1)) \tag{1.94}$$

Nevertheless, in order to compute a more precise pressure derivative, the following average expression is used for p^* :

$$p^* = \frac{F_R(2) - S_R U_R(2) - S_M(F_R(1) - S_R U_R(1)) + F_L(2) - S_L U_L(2) - S_M(F_L(1) - S_L U_L(1))}{2} \tag{1.95}$$

It results in the following pressure derivatives :

$$\frac{\partial p^*}{\partial U_L} = \frac{1}{2}\left[\frac{\partial F_L(2)}{\partial U_L} - S_L(0,1,0)^T - S_M\left(\frac{\partial F_L(1)}{\partial U_L} - S_L(1,0,0)^T\right) - (F_L(1) - S_L U_L(1))\frac{\partial S_M}{\partial U_L}\right], \tag{1.96}$$

$$\frac{\partial p^*}{\partial U_R} = \frac{1}{2}\left[\frac{\partial F_R(2)}{\partial U_R} - S_R(0,1,0)^T - S_M\left(\frac{\partial F_R(1)}{\partial U_R} - S_R(1,0,0)^T\right) - (F_R - S_R U_R)\frac{\partial S_M}{\partial U_R}\right], \tag{1.97}$$

$$S_M = \frac{S_R U_R(2) - S_L U_L(2) - (F_R(2) - F_L(2))}{S_R U_R(1) - S_L U_L(1) - (F_R(1) - F_L(1))}, \tag{1.98}$$

$$\begin{aligned}\frac{\partial S_M}{\partial U_L} =& \frac{(\frac{\partial F_L(2)}{\partial U_L} - S_L\frac{\partial U_L(2)}{\partial U_L})(S_R U_R(1) - S_L U_L(1) - (F_R(1) - F_L(1)))}{(S_R U_R(1) - S_L U_L(1) - (F_R(1) - F_L(1)))^2} \\ & - \frac{(S_R U_R(2) - S_L U_L(2) - (F_R(2) - F_L(2)))(\frac{\partial F_L(1)}{\partial U_L} - S_L\frac{\partial U_L(1)}{\partial U_L})}{(S_R U_R(1) - S_L U_L(1) - (F_R(1) - F_L(1)))^2},\end{aligned} \tag{1.99}$$

$$\begin{aligned}\frac{\partial S_M}{\partial U_R} =& \frac{(S_R\frac{\partial U_R(2)}{\partial U_R} - \frac{\partial F_R(2)}{\partial U_R})(S_R U_R(1) - S_L U_L(1) - (F_R(1) - F_L(1)))}{(S_R U_R(1) - S_L U_L(1) - (F_R(1) - F_L(1)))^2} \\ & - \frac{(S_R U_R(2) - S_L U_L(2) - (F_R(2) - F_L(2)))(S_R\frac{\partial U_R(1)}{\partial U_R} - \frac{\partial F_R(1)}{\partial U_R})}{(S_R U_R(1) - S_L U_L(1) - (F_R(1) - F_L(1)))^2}.\end{aligned} \tag{1.100}$$

These various derivatives require the knowledge of $\frac{\partial F_L}{\partial U_L}$ and $\frac{\partial F_R}{\partial U_R}$. They correspond to the Jacobian matrix of the Euler equations. Slight changes have to be done with the two-phase flow model. They are detailed in Appendix E and F.

Appendix D - High order extension

MUSCL type reconstruction [84] is considered. Variables extrapolation from the cell center i and the cell boundary (ij) is achieved by the following relation :

$$f_{ij} = f_i + \Phi_i \overrightarrow{\nabla f}_i \cdot \overrightarrow{r_{ij}} \tag{1.101}$$

where $\overrightarrow{r_{ij}}$ is the vector connecting the cell center and the inter-cell face, $\overrightarrow{\nabla f}_i$ is the approximate gradient of variable f in cell i and Φ_i the limiter ($\Phi_i \leq 1$).

The gradient is approximated by weighted least squares. From the gradient $\overrightarrow{\nabla f}$ definition,

$$df = \overrightarrow{\nabla f} \cdot \overrightarrow{dM}, \tag{1.102}$$

with the following notations,

$$\overrightarrow{\nabla f} = \begin{pmatrix} a \\ b \\ c \end{pmatrix},$$

the various gradient components a, b and c, are determined as follows. Relation (1.102) expressed between the various cell faces and the cell center provides N relations ($N = 3$ for triangles) :

$$f_j - f_i = a(x_j - x_i) + b(y_j - y_i) + c(z_j - z_i), j = 1, N \tag{1.103}$$

where f_j represents the value of the f function at the center of the j cell while x_j, y_j and z_j represent the coordinates of the j cell center.

Thus, the following overdetermined system is obtained :

$$M\Delta f = D \tag{1.104}$$

where M is a (Nx3) matrix whereas Δf and D are size 3 vectors. To make benefit of this over-determination, System (1.104) is multiplied by the M transpose.

$$M^T M\Delta f = M^T D \tag{1.105}$$

A new system is thus obtained,

$$M^*\Delta f = D^*, \tag{1.106}$$

However, the matrix M^* determinant can become very small if some cells are very deformed. To overcome this situation, one way to proceed is to use weights. A very simple weighting procedure has been proposed in [57]. It consists in using the weight $w_{i,j} = \frac{1}{\sqrt{\Delta x_{i,j}^2 + \Delta y_{i,j}^2 + \Delta z_{i,j}^2}}$.
This correction guarantees that the determinant of M^* is $O(1)$.

The last step in the higher order extension method deals with gradients limitation. The Barth and Jespersen [12] method is adopted.

Appendix E - Mixture pressure derivatives

The mixture pressure for the two-phase non-equilibrium model reads :

$$P = \sum_{k=1}^{N} \alpha_k p_k$$

where N is the number of fluids.
With the help of the EOS (1.4) it becomes :

$$P = \sum_{k=1}^{N} \left[(\gamma_k - 1)\alpha_k \rho_k e_k - \alpha_k \gamma_k P_{\infty,k} \right] \tag{1.107}$$

The volume fraction of fluid N is determined from the saturation constraint :

$$\alpha_N = 1 - \sum_{k=1}^{N-1} \alpha_k$$

Thus, equation (1.107) becomes :

$$P = \sum_{k=1}^{N} (\gamma_k - 1)\alpha_k \rho_k e_k + \sum_{k=1}^{N-1} \alpha_k (\gamma_N P_{\infty,N} - \gamma_k P_{\infty,k}) - \gamma_N P_{\infty,N} \tag{1.108}$$

With the following derivatives :

$$\frac{\partial P}{\partial \alpha_k \rho_k e_k} = \gamma_k - 1. \quad \frac{\partial P}{\partial \alpha_k} = (\gamma_N P_{\infty,N} - \gamma_k P_{\infty,k})$$

Appendix F - Implicit schemes for non-conservative equations of the two-phase flow model

Volume fraction implicit scheme

In one-dimension, the volume fraction equation of System (1.6) reads :

$$\frac{\partial \alpha_1}{\partial t} + u \frac{\partial \alpha_1}{\partial x} = 0$$

The Godunov method for advection equations reads :

$$\alpha_{1,i}^{n+1} = \alpha_{1,i}^{n} + \frac{\Delta t}{\Delta x} \left[\left(\alpha_{1,i-1}^{n} - \alpha_i^n \right) S_{M,i-\frac{1}{2}}^{+} - \left(\alpha_{1,i+1}^{n} - \alpha_i^n \right) S_{M,i+\frac{1}{2}}^{-} \right]$$

Where :
S_M represents the contact wave speed and

$$S^+_{M,i-\frac{1}{2}} = \frac{1}{2}\left(1 + sign(S_{M,i-\frac{1}{2}})\right) S_{M,i-\frac{1}{2}}, \quad S^-_{M,i+\frac{1}{2}} = \frac{1}{2}\left(1 - sign(S_{M,i+\frac{1}{2}})\right) S_{M,i+\frac{1}{2}}.$$

Let's denote by,

$$\begin{cases} f^n_{Li} = \left(\alpha^n_{1,i-1} - \alpha^n_i\right) S^+_{M,i-\frac{1}{2}} = \left(1 + sign(S_{M,i-\frac{1}{2}})\right)\left(\alpha^n_{1,i-1} - \alpha^n_i\right)\dfrac{S_{M,i-\frac{1}{2}}}{2} \\ f^n_{Ri} = \left(\alpha^n_{1,i+1} - \alpha^n_i\right) S^-_{M,i+\frac{1}{2}} = \left(1 - sign(S_{M,i+\frac{1}{2}})\right)\left(\alpha^n_{1,i+1} - \alpha^n_i\right)\dfrac{S_{M,i+\frac{1}{2}}}{2} \end{cases}$$

Thus, the implicit scheme for the volume fraction equation reads :

$$\alpha^{n+1}_{1,i} = \alpha^n_{1,i} - \frac{\Delta t}{\Delta x}\left[f^{n+1}_{Ri} - f^{n+1}_{Li}\right] \tag{1.109}$$

It is worth to mention that $f_{Ri} \neq f_{Li+1}$ as the equation is non-conservative.

Using the same development as previously (1.56 - 1.57), with $\delta\alpha_i = \alpha^{n+1}_{1,i} - \alpha^n_{1,i}$, the following scheme is obtained,

$$-\frac{\Delta t}{\Delta x}\frac{\partial f_{Ri}}{\partial U_{i-1}}\delta\alpha_{i-1} + \left[I + \frac{\Delta t}{\Delta x}\left(\frac{\partial f_{Ri}}{\partial U_i} - \frac{\partial f_{Li}}{\partial U_i}\right)\right]\delta\alpha_i + \frac{\Delta t}{\Delta x}\frac{\partial f_{Ri}}{\partial U_{i+1}}\delta\alpha_{i+1} = -\frac{\Delta t}{\Delta x}\left(f^n_{Ri} - f^n_{Li}\right), \tag{1.110}$$

where U represents the whole conservative variables vector.

Internal energies implicit scheme

In one-dimension, the internal energy equations read ($k = 1, 2$) :

$$\frac{\partial \alpha_k \rho_k e_k}{\partial t} + \frac{\partial \alpha_k \rho_k e_k u}{\partial x} + \alpha_k p_k \frac{\partial u}{\partial x} = 0 \tag{1.111}$$

The explicit scheme used for this equation reads :

$$(\alpha\rho e)^{n+1}_k = (\alpha\rho e)^n_k - \frac{\Delta t}{\Delta x}\left((\alpha\rho eu)^{*,n}_{k,i+\frac{1}{2}} - (\alpha\rho eu)^{*,n}_{k,i-\frac{1}{2}} + (\alpha p)^n_{k,i}\left(u^{*,n}_{i+\frac{1}{2}} - u^{*,n}_{i-\frac{1}{2}}\right)\right) \tag{1.112}$$

where the product $(\alpha_k p_k)^n_i$ is assumed constant during the time step and the superscript "*" denotes the Riemann problem solution state .

Thus, the implicit scheme for the internal energy equations read :

$$(\alpha\rho e)^{n+1}_k = (\alpha\rho e)^n_k - \frac{\Delta t}{\Delta x}\left((\alpha\rho eu)^{*,n+1}_{k,i+\frac{1}{2}} - (\alpha\rho eu)^{*,n+1}_{k,i-\frac{1}{2}} + (\alpha p)^{n+1}_{k,i}\left(u^{*,n+1}_{i+\frac{1}{2}} - u^{*,n+1}_{i-\frac{1}{2}}\right)\right) \tag{1.113}$$

Using the same development as previously (1.56 - 1.57) with $F_{ek} = (\alpha\rho eu)_k$ and $\delta(\alpha\rho e)_{k,o} = (\alpha\rho e)^{n+1}_{k,i} - (\alpha\rho e)^n_{k,i}$, the following scheme is obtained :

$$
\begin{aligned}
&- \frac{\Delta t}{\Delta x}\left[\frac{\partial F_{ek,i-\frac{1}{2}}}{\partial U_{i-1}} + (\alpha p)^n_{k,i}\frac{\partial u^*_{i-\frac{1}{2}}}{\partial U_{i-1}}\right]\delta(\alpha\rho e)_{k,i-1} \\
&+ \left[I + \frac{\Delta t}{\Delta x}\left(\frac{\partial F^n_{ek,i+\frac{1}{2}}}{\partial U_i} - \frac{\partial F^n_{ek,i-\frac{1}{2}}}{\partial U_i} + (\alpha p)^n_{k,i}\left[\frac{\partial u^*_{i+\frac{1}{2}}}{\partial U_i} - \frac{\partial u^*_{i-\frac{1}{2}}}{\partial U_i}\right] + (u^*_{i+\frac{1}{2}} - u^*_{i-\frac{1}{2}})\frac{\partial(\alpha p)^n_{k,i}}{\partial U_i}\right)\right]\delta(\alpha\rho e)_{k,i} \\
&+ \frac{\Delta t}{\Delta x}\left[\frac{\partial F_{ek,i+\frac{1}{2}}}{\partial U_{i+1}} + (\alpha p)^n_{k,i}\frac{\partial u^*_{i+\frac{1}{2}}}{\partial U_{i+1}}\right]\delta(\alpha\rho e)_{k,i+1} \\
&= -\frac{\Delta t}{\Delta x}\left((\alpha\rho eu)^{*,n}_{k,i+\frac{1}{2}} - (\alpha\rho eu)^{*,n}_{k,i-\frac{1}{2}} + (\alpha p)^n_{k,i}\left(u^{*,n}_{i+\frac{1}{2}} - u^{*,n}_{i-\frac{1}{2}}\right)\right)
\end{aligned}
\tag{1.114}
$$

Where $\frac{\partial F_{ek,i+\frac{1}{2}}}{\partial U_i}$, $\frac{\partial F_{ek,i+\frac{1}{2}}}{\partial U_{i+1}}$, $\frac{\partial F_{ek,i-\frac{1}{2}}}{\partial U_i}$ and $\frac{\partial F_{ek,i-\frac{1}{2}}}{\partial U_{i-1}}$ are calculated using the HLLC flux derivatives (Appendix C).

Appendix G - Stiff thermodynamic relaxation

The following relaxation solver is used to compute the thermodynamic state and in particular the various mass fractions when stiff thermodynamic relaxation is assumed. A two-phase liquid-vapour mixture in thermodynamic equilibrium is considered. Both phases are thus in pressure, temperature and Gibbs free energy equilibrium.
The thermodynamic equilibrium state is determined by considering the following algebraic system :

$$
\begin{aligned}
&v = \frac{1}{\rho} = Y_1 v_1 + Y_2 v_2 = cte = v_0 \\
&e = Y_1 e_1 + Y_2 e_2 = cte = e_0 \\
&T_1 = T_2 = T \\
&p_1 = p_2 = P \\
&g_1 = g_2
\end{aligned}
\tag{1.115}
$$

Where $Y_1 = \frac{\alpha_1\rho_1}{\rho}$ and $Y_2 = \frac{\alpha_2\rho_2}{\rho} = 1 - Y_1$ denote the mass fractions of both phases, which are not constant during the relaxation process.
The first two equations of this system come from the mass conservation and mixture total energy conservation, respectively. The last equation represents the Gibbs free energies equality ($g = h - Ts$).
The liquid and its vapour are denoted by the subscripts "1" and "2", respectively.
The specific volumes and the internal energies of each phase are given by the following

expressions, based on the stiffened gas EOS (1.4) :

$$v_k = \frac{(\gamma_k - 1)C_{v,k}T_k}{P + p_{\infty,k}} \tag{1.116}$$

$$e_k = C_{v,k}T_k(1 + \frac{(\gamma_k - 1)p_{\infty,k}}{P + p_{\infty,k}}) + q_k \tag{1.117}$$

Each parameter involved in the previous expressions $(\gamma_k, C_{v,k}, p_{\infty,k}, q_k)$ is calculated in order to fit the liquid-vapour phase diagram, more precisely the corresponding saturation curves. Details regarding the EOS parameters determination are given in [52] and [73].
Denoting the final state by the superscript '*', the mass conservation constraint becomes :

$$v_0 = Y_1^* v_1^*(P^*) + Y_2^* v_2^*(P^*) = Y_1^* v_1^*(P^*) + (1 - Y_1^*)v_2^*(P^*), \tag{1.118}$$

with $v_1^*(P^*) = \dfrac{(\gamma_k - 1)C_{v,k}T^*(P^*)}{P^* + p_{\infty,k}}$.
Constraints of pressures, temperatures and Gibbs free energies equilibrium have been used in Relation (1.118). Indeed, the Gibbs free energies equality leads to a relationship between the pressure and the temperature :

$$T^*(P^*) = T_{sat}(P^*). \tag{1.119}$$

$v_1^*(P^*)$ and $v_2^*(P^*)$ represent the saturated specific volumes of both phases. A first relation linking the liquid mass fraction and the pressure is thus obtained,

$$Y_1^* = \frac{v_2^*(P^*) - v_0}{v_2^*(P^*) - v_1^*(P^*)}. \tag{1.120}$$

Consider now the mixture total energy conservation,

$$e_0 = Y_1^* e_1^*(P^*) + Y_2^* e_2^*(P^*) = Y_1^* e_1^*(P^*) + (1 - Y_1^*)e_2^*(P^*) \tag{1.121}$$

with $e_k(P^*) = C_{v,k}T_k^*(P^*)(1 + \dfrac{(\gamma_k - 1)p_{\infty,k}}{P^* + p_{\infty,k}}) + q_k$.
A second relation linking the liquid mass fraction and the pressure is thus obtained,

$$Y_1^* = \frac{e_0 - e_2^*(P^*)}{e_1^*(P^*) - e_2^*(P^*)}. \tag{1.122}$$

This relation can be also expressed as a function of the specific enthalpies of the phases,

$$Y_1^* = \frac{h_2^*(P^*) - (e_0 - P^* v_0)}{h_2^*(P^*) - h_1^*(P^*)}. \tag{1.123}$$

Where h_1 and h_2 are linked by $h_2^*(P^*) - h_1^*(P^*) = L_v(P^*)$, $L_v(P^*)$ representing the latent heat of vaporization, which is a function of the pressure.
From the previous mass fraction equations, a single function of the pressure is obtained,

$$\frac{h_2^*(P^*) - (e_0 - P^* v_0)}{h_2^*(P^*) - h_1^*(P^*)} - \frac{v_2^*(P^*) - v_0}{v_2^*(P^*) - v_1^*(P^*)} = 0. \tag{1.124}$$

Its solution is computed with the Newton method. Once the relaxed pressure is determined, the remaining variables are easily computed with the preceding thermodynamic relations.

Chapitre 2

Solutions de référence

Avant-propos

Bien qu'il existe plusieurs moyens de valider des résultats issus de simulations numériques, tels que des solutions exactes de problèmes de Riemann (monophasique ou diphasique) ou d'écoulements 1D de gaz parfaits en tuyère, il est difficile de valider les techniques de préconditionnement faible Mach présentées précédemment pour des écoulements diphasiques. En effet, la notion de validation devient très vite problématique lorsque l'on traite des écoulements multiphasiques. Comme montré dans le Chapitre 1, il est primordial d'être capable de valider les méthodes numériques utilisées sur des cas simples 1D avant de s'intéresser à des simulations multidimensionnelles. Habituellement, les validations ou comparaisons sont réalisées par rapport à des solutions incompressibles d'écoulement autour de profils d'ailes. Ces solutions ne sont en aucun cas des solutions exactes et leur extension au cas diphasique est problématique. De plus, l'étude d'écoulements 1D dans des configurations de conduites rectilignes n'apporte aucune solution non-triviale. Cependant, les écoulements 1D dans des conduites à sections variables offrent des possibilités que l'on va exploiter dans ce chapitre.

Le but de ce chapitre est la détermination d'écoulements diphasiques en tuyères pour différents modèles limites. Ainsi, trois cas d'écoulements diphasiques seront étudiés dans ce chapitre :
-Les deux phases évoluent en équilibre mécanique (équilibre des pressions et des vitesses).
-Les deux phases évoluent en équilibre mécanique et thermique (équilibre des pressions, des vitesses et des températures).
-Les deux phases évoluent en équilibre thermodynamique (équilibre des pressions, des vitesses, des températures et potentiels chimiques).
Bien entendu, ces solutions restant purement uni-dimensionnelles elles n'ont pas vocation à représenter la véritable physique des écoulements diphasiques en tuyères où de multiples phénomènes multi-dimensionnels tels que la cavitation par poches, jouent un rôle très important. Néanmoins, l'existence de telles solutions de référence permet de valider précisément les schémas numériques utilisés à travers de simples écoulements 1D. De plus, il est aussi important de remarquer, que, bien que limitées au niveau de leur validité physique, ces

solutions permettent de mettre en avant les comportements complexes et non-intuitifs des mélanges diphasiques en tuyère.

2.1 Introduction

Multiphase nozzle flows play are present in many fundamental and industrial areas such as cooling systems, propulsion, safety analysis in pressured reactors or oil engineering, to cite a few. The aim of the present paper is to derive exact nozzle flow solutions for various limit models of two-phase flows. These solutions extend the one-dimensional ideal gas nozzle steady flow solutions, detailed in any compressible fluid mechanics textbook, to various limit two-phase flow models. To be more precise, various reduced two-phase flow models are considered, each one of them corresponding to a limit situation where one or several relaxation effects are infinitely stiff. The first two-phase model considered in the present paper is a reduction of a well-known full non-equilibrium two-phase flow model (Baer and Nunziato) in the limit of stiff mechanical relaxation. The corresponding model was derived by [47] and describes multiphase mixtures out of thermal equilibrium but in velocity and pressure equilibrium. This model becomes popular in advanced multiphase flow codes dealing with applications that seem disjointed at a first glance but are in reality loosely linked at the modelling level. These applications range from cavitating flows ([73], [66], [53]), reactive multiphase flows ([67]) and interfacial flows ([47],[62], [64], [74]) to cite a few. The second reduction deals with a flow model in both mechanical and thermal equilibrium. It is very similar to the reactive Euler equations, except regarding the equation of state that is very different of the one resulting of the Dalton's law, widely used in combustion and gaseous reacting mixtures. The corresponding multiphase flow model is known as the Homogeneous Relaxation Model (HRM) (see for example [25]) and is widely used in cavitating and flashing flows ([11]). The third reduced model corresponds to the thermodynamic equilibrium limit of the HRM model (equal pressures, equal velocities, equal temperatures and equal Gibbs free energies) and is known as the Homogeneous Equilibrium Model (HEM) (see, for example [22]). This model corresponds to the mixture Euler equations with a specific mixture equation of state, and specific definitions for the mixture variables. All models considered in the present work involve a single velocity. This restriction can be understood in two ways :
-For liquid-gas mixtures evolving in smooth nozzles with highly viscous liquid and small bubbles such as the phase separation cannot occur.
-As reference solutions for computer codes when stiff relaxation effects are considered. As shown in [53], these nozzle flow solutions are very selective.
In the present work, all fluids are considered compressible. This is quite obvious for the gas phase, but not necessarily for the liquid. However, when dealing with cavitating and flashing flows, phase transition appears as a consequence of liquid expansion. Thus, liquid compressibility has to be considered. Liquid compressibility is considered through the simplest complete equation of state, i.e., the SG EOS , that reproduces the main thermodynamic behaviour of a liquid. Its parameters are determined through the phase diagram and are valid in a finite temperature range. Their determination is detailed in [52] (see

also [73] for a summary). This EOS in hand, the second section of the present paper deals with the determination of nozzle flow solutions for single phase liquids. It extends the well known nozzle flows ideal gas solutions to compressible liquids. This section also presents the methodology for the determination of the various solution branches, and provides the overall algorithm employed for the various two-phase flow solutions determination. The third section deals with the exact nozzle flow solutions for two-phase flows in mechanical equilibrium, described by the [47] model and shock relations of [71]. The fourth section deals with nozzle flow solutions for the HRM model in the absence of phase transition, corresponding to frozen two-phase mixtures with respect to mass transfer, but in velocity, pressure and temperature equilibrium. The fifth section provides the same type of solutions for two-phase mixtures in thermodynamic equilibrium. As the acoustic properties related to sound propagation have strong variations from the pure liquid situation to the thermodynamic equilibrium one, important changes are observed each time an equilibrium constraint is added. Last, conclusions are given in Section 6.

2.2 Single phase nozzle flow

In this section, the single phase nozzle flow exact solution determination is addressed. It corresponds to the extension of the ideal gas compressible nozzle flow solution given in all gas dynamics text books to compressible liquids governed by SG EOS. This section also provides the solution algorithms employed to determine the various two-phase nozzle flow solutions given in the subsequent sections.

2.2.1 Flow model

The single phase model corresponds to the Euler equations :

$$\begin{aligned} &\frac{\partial \rho}{\partial t} + div\left(\rho \mathbf{u}\right) = 0 \\ &\frac{\partial \rho \mathbf{u}}{\partial t} + div\left(\rho \mathbf{u} \otimes \mathbf{u} + p\right) = 0 \\ &\frac{\partial \rho E}{\partial t} + div\left((\rho E + p)\mathbf{u}\right) = 0 \end{aligned} \tag{2.1}$$

where ρ represents the density, $\mathbf{u}$ the velocity vector, p the pressure and E the total energy, with $E = e + \frac{1}{2}\mathbf{u}^2$, with e the internal energy. In the absence of shocks, System (2.1) is complemented by the following entropy equation :

$$\frac{\partial \rho s}{\partial t} + div\left(\rho s \mathbf{u}\right) = 0 \tag{2.2}$$

where s represents the entropy.
This equation will be helpful for the determination of reference nozzle flow solution. The

thermodynamic closure is achieved by a convex EOS : $p = p(\rho, e)$. In the present work the SG EOS ([40] and [59]) is used :

$$p = (\gamma - 1)\rho(e - q_0) - \gamma P_\infty \tag{2.3}$$

γ, P_∞ and q_0 are parameters of the EOS, obtained from reference thermodynamic curves, characteristic of the material and transformation under study. See [52] for details.
The SG EOS sound speed reads :

$$c = \sqrt{\gamma \frac{p + P_\infty}{\rho}} \tag{2.4}$$

For the sake of simplicity, the reference internal energy, q_0, will be omitted in the first three sections as it is only useful when heat and mass transfer are present.

2.2.2 Problem statement

A nozzle connected to a tank at left and opened to the atmosphere at the right outlet, as shown in the Figure 2.1, is considered. The tank state is denoted by subscript "0" while

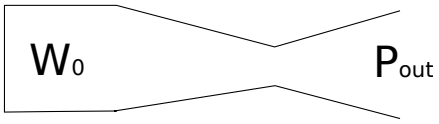

FIGURE 2.1 – Nozzle connected to a tank at the inlet and to a prescribed pressure at the outlet

the outlet state is denoted by subscript "out". The tank state is defined by the density ρ_0, the pressure p_0 and the velocity $u_0 = 0$.
The steady nozzle flow solution is determined on the basis of System (2.1) and Equation (2.2) integrated with respect to a control volume delimited by two cross-sections, denoted A^+ and A^-. As the momentum equation integration results in a non-conservative equation, the entropy equation (2.2) replaces the momentum one. It results in the following algebraic system :

$$\rho^+ u^+ A^+ = \rho^- u^- A^-, \qquad s^+ = s^- \quad \text{and} \quad H^+ = H^-. \tag{2.5}$$

Where H represents the stagnation enthalpy, defined by $H = e + \dfrac{p}{\rho} + \dfrac{1}{2}u^2$.
In order to determine the nozzle flow solution, it is first necessary to determine the flow configuration. It can be subsonic everywhere, supersonic in the divergent or supersonic with a shock in the divergent. All theses configurations have to be considered. To do so, various critical pressure ratios have to be determined.

2.2.3 Critical pressure ratios

The first critical pressure ratio corresponds to the appearance of a sonic state at throat. Obviously, for pure liquids, such sonic state requires very high pressure ratios. But, as it will be shown later, such state can be reached with moderate pressure ratios when dealing with two-phase mixtures.

Critical pressure ratio 1 (cpr1) The critical pressure ratio, cpr1, is defined as the outlet/tank pressure ratio corresponding to a subsonic flow everywhere except at the throat where chocking conditions ($u = c$) appear. As the flow is isentropic everywhere, the following relations are used :

$$H^* = H_0 \quad \text{and} \quad s^* = s_0 \tag{2.6}$$

Where the "*" superscript represents the nozzle throat state for which $u^* = c^*$.

Using the SG EOS, Relations (2.6) become :

$$\frac{\gamma\,(p^* + P_\infty)}{(\gamma - 1)\,\rho^*} + \frac{1}{2}u^{*2} = H_0 \quad \text{and} \quad \frac{p^* + P_\infty}{\rho^{*\gamma}} = \frac{p_0 + P_\infty}{\rho_0^\gamma} \tag{2.7}$$

The last unknown is the velocity at the nozzle throat, u^*.
As $u^* = c^*$, combining relations (2.7) and (2.4) yields the throat pressure, p^* :

$$p^* + P_\infty = (p_0 + P_\infty)(\frac{2}{\gamma + 1})^{\frac{\gamma}{\gamma - 1}} \tag{2.8}$$

As the critical pressure, p^*, is known, the complete critical state W^* is determined with the help of relations (2.7).
Now, it is necessary to determine the state in the outlet section. Relations (2.7) can be used again as :

$$\frac{\gamma\,(p_{out} + P_\infty)}{(\gamma - 1)\,\rho_{out}} + \frac{1}{2}u_{out}^2 = H_0 \quad \text{and} \quad \frac{p_{out} + P_\infty}{\rho_{out}^\gamma} = \frac{p_0 + P_\infty}{\rho_0^\gamma} \tag{2.9}$$

The closure relation now corresponds to the mass conservation between the throat and the outlet section :

$$m_{out} = \rho_{out} u_{out} A_{out} = \rho^* u^* A^* = m^* \tag{2.10}$$

where A_{out} represents the outlet cross section and A^* the nozzle throat cross section.
Using Equation (2.9), the density in the outlet section can be expressed as a function of p_{out} only. Thus, the following expression is obtained for the velocity in the outlet section u_{out} :

$$u_{out} = \frac{m^*}{\rho_{out}(p_{out}) A_{out}} \quad \text{with} \quad \rho_{out} = \rho_0 \left(\frac{p_{out} + P_\infty}{p_0 + P_\infty} \right)^{\frac{1}{\gamma}} \tag{2.11}$$

Combining relations (2.11) and (2.9), a non-linear function of p_{out} is obtained :

$$\frac{\gamma\left(p_{out}+P_{\infty}\right)}{(\gamma-1)\,\rho_{out}(p_{out})}+\frac{1}{2}\left(\frac{m^{*}}{\rho_{out}(p_{out})A_{out}}\right)^{2}-H_{0}=0 \tag{2.12}$$

This equation admits two roots : $p_{out}=p_{cpr1}$ and $p_{out}=p_{cpr3}$.
The subsonic branch corresponds to the pressure ratio cpr1. To determine it, the Newton method is used with initial guess for the outlet pressure $p_{out}=p^{*}$. Then, cpr1 is defined as $cpr1=\dfrac{p_{cpr1}+P_{\infty}}{p_{0}+P_{\infty}}$.

Critical pressure ratio 3 (cpr3) This solution corresponds to the supersonic branch of Equation (2.12). It is obtained again from (2.12) with the Newton method by taking the initial pressure guess $p_{out}=(1+10^{-6})P_{\infty}$. When convergence is reached, the outlet pressure is determined as $p_{out}=p_{cpr3}$. The critical pressure ratio cpr3 is obtained as $cpr3=\dfrac{p_{cpr3}+P_{\infty}}{p_{0}+P_{\infty}}$.

Critical pressure ratio 2 (cpr2) The critical pressure ratio, cpr2, corresponds to a supersonic flow in the nozzle divergent except at the outlet section where a steady shock is present.
The flow entering the shock has precisely the state corresponding to W_{cpr3}. The shocked state is obtained with the help of the Rankine-Hugoniot relations :

$$(\rho u)_{cpr3}=(\rho u)_{cpr2} \tag{2.13}$$

$$\left(\rho u^{2}+p\right)_{cpr3}=\left(\rho u^{2}+p\right)_{cpr2} \tag{2.14}$$

$$e_{cpr2}-e_{cpr3}+\frac{p_{cpr2}+p_{cpr3}}{2}\left(v_{cpr2}-v_{cpr3}\right)=0 \tag{2.15}$$

Combining Relations (2.13), (2.14) and (2.15), an expression of p_{cpr2} is obtained :

$$p_{cpr2}=(p_{cpr3}+p_{\infty})\left(\frac{2\gamma}{\gamma+1}\left(\frac{m^{*}}{\rho_{cpr3}c_{cpr3}A_{out}}\right)^{2}-\frac{\gamma-1}{\gamma+1}\right)-p_{\infty} \tag{2.16}$$

2.2.4 Derivation of the nozzle flow : isentropic solution

When the pressure ratio $PR=\dfrac{p_{out}+P_{\infty}}{p_{0}+P_{\infty}}$ is either greater than cpr1 or lower than cpr2, the flow is isentropic everywhere in the nozzle. As the outlet pressure is given, the remaining variables at this section are computed.

$$\rho_{out}=\rho_{0}\left(\frac{p_{out}+P_{\infty}}{p_{0}+P_{\infty}}\right)^{\frac{1}{\gamma}} \tag{2.17}$$

The outlet velocity is obtained from the first Relation of System (2.7) expressed in the the outlet section :

$$u_{out} = \sqrt{2\left[H_0 - \frac{\gamma(p_{out} + P_\infty)}{(\gamma - 1)\rho_{out}}\right]} \tag{2.18}$$

Then, from the variables computed at the outlet and Relations (2.7) expressed for any cross section A_i, the corresponding state is determined from :

$$\rho_i u_i A_i = m^* \tag{2.19}$$

$$\frac{\gamma(p_i + P_\infty)}{(\gamma - 1)\rho_i} + \frac{1}{2}u_i^2 = H_0, \tag{2.20}$$

$$\frac{p_i + P_\infty}{\rho_i^\gamma} = \frac{p_0 + P_\infty}{\rho_0^\gamma}. \tag{2.21}$$

Combining previous relations, a non-linear function giving the pressure p_i at a given section is obtained :

$$\frac{\gamma\,(p_i + P_\infty)}{(\gamma - 1)\,\rho_i(p_i)} + \frac{1}{2}\left(\frac{m^*}{\rho_i(p_i)A_i}\right)^2 - H_0 = 0 \tag{2.22}$$

It is solved again with the Newton method. Once the pressure p_i is determined, the density ρ_i and the velocity u_i are determined from (2.21) and (2.19) respectively.

2.2.5 Derivation of the nozzle flow : adiabatic solution.

For pressure ratio $PR = \dfrac{p_{out} + P_\infty}{p_0 + P_\infty}$ lower than crp1 and greater than crp2, a stationary shock wave appears in the divergent. The shock position is determined by a dichotomy method :

- As the shock is in the divergent, the initial guess for the shock cross section area is $A_C = \dfrac{A_* + A_{out}}{2}$. Where A_* is the throat area and A_{out} the outlet section area.
- Then the isentropic flow is solved from the inlet tank to the shock section.
- Rankine-Hugoniot relations are used across the shock to define the shocked state at the section immediately above the shock.
- The shocked state is connected to the outlet section with the help of isentropic solution.
- If the computed outlet pressure corresponds to the imposed one, the shock location is correct. Otherwise it has to be changed until the computed and imposed outlet pressure are the same.

2.2.6 Solution examples

The various 1D exact solution examples given in the present paper are computed with the following Laval nozzle data, piecewise linear with respect to the surface area :

	Inlet Section	Throat Section	Outlet Section
Position	$0.0m$	$0.5m$	$1.0m$
Surface area	$0.14657\ m^2$	$0.06406\ m^2$	$0.14657\ m^2$

The inlet is connected to a tank while the outlet is connected to a prescribed pressure. The fluid used in the computations corresponds to liquid water, with the following SG EOS (2.3) parameters $\gamma = 4.4$, $P_\infty = 600MPa$. The tank state is defined by :

$$\rho_0 = 1000\, kg.m^{-3}, \quad u_0 = 0\, m.s^{-1} \quad \text{and} \quad p_0 = 100MPa$$

Figure (2.2) shows typical solutions behavior for different pressure ratio PR $= \dfrac{p_{out} + P_\infty}{p_0 + P_\infty}$. Using the previous geometrical and thermodynamic data, the associated critical pressure ratios are :

cpr1	0.91039
cpr2	0.24526
cpr3	0.00267

Flows are always subsonic and isentropic in the convergent nozzle and different flow patterns occur in the nozzle divergent according to the pressure ration PR :

- When PR =cpr1, the flow is sonic at the throat and subsonic in the divergent.
- When PR =cpr2, the flow is supersonic in the divergent Xwith a steady shock at the exit section.
- When PR =cpr3, the flow is sonic at the throat and supersonic in the divergent.
- When PR = 0.93428, the flow is strictly subsonic at the throat and in the divergent,
- When PR = 0.42857, the flow is sonic at the throat, with a steady shock located in the divergent.

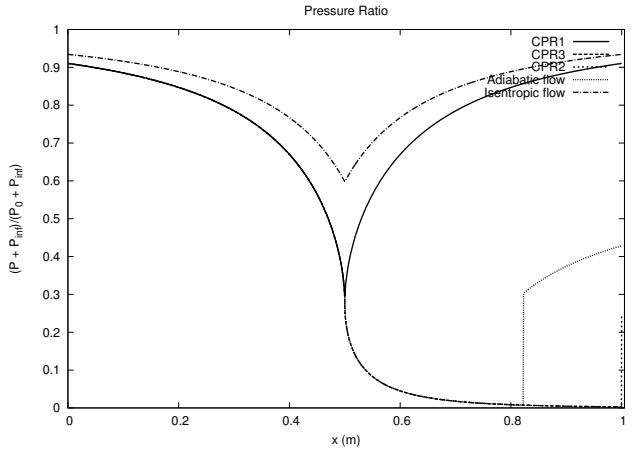

FIGURE 2.2 – Dimensionless pressure profiles in the Laval nozzle for different exit pressures corresponding to subsonic flow with sonic throat (cpr1), supersonic isentropic flow (cpr3), flow with a steady shock in the exit section (cpr2), subsonic isentropic solution (PR = 0.93428), adiabatic steady shock in the divergent (PR = 0.42857).

2.3 Two-phase flow in mechanical equilibrium

2.3.1 Flow model

This model has been derived by [47] to describe multiphase mixtures in mechanical equilibrium. This model is able to deal with cavitating and flashing flows [73], detonation waves and interface motion [66]. It has been the subject of special attention for non-barotropic modelling of cavitating flows ([53]). The [47] model reads :

$$\begin{aligned}
&\frac{\partial \alpha_1}{\partial t} + \mathbf{u}\cdot\mathbf{grad}\,(\alpha_1) = K div\,(\mathbf{u}) \\
&\frac{\partial \alpha_1\rho_1}{\partial t} + div\,(\alpha_1\rho_1\mathbf{u}) = 0 \\
&\frac{\partial \alpha_2\rho_2}{\partial t} + div\,(\alpha_2\rho_2\mathbf{u}) = 0 \qquad \text{where} \quad K = \frac{\rho_2 c_2^2 - \rho_1 c_1^2}{\frac{\rho_1 c_1^2}{\alpha_1} + \frac{\rho_2 c_2^2}{\alpha_2}} \\
&\frac{\partial \rho\mathbf{u}}{\partial t} + div\,(\rho\mathbf{u}\otimes\mathbf{u} + P) = 0 \\
&\frac{\partial \rho E}{\partial t} + div\,((\rho E + P)\mathbf{u}) = 0
\end{aligned} \tag{2.23}$$

c_k represents the sound speed defined by $c_k^2 = \frac{\partial p_k}{\partial \rho_k}\Big)_{s_k}, k = 1, 2,$
P represents the mixture pressure,
E represents the mixture total energy,
α_k represent the phases volume fraction,
and ρ_k represent the phase densities.

The resulting mixture sound speed corresponds to the [87] formula :

$$\frac{1}{\rho c^2} = \frac{\alpha_1}{\rho_1 c_1^2} + \frac{\alpha_2}{\rho_2 c_2^2} \tag{2.24}$$

In the absence of shocks, System (2.23) can be complemented by the following entropy equations :

$$\begin{aligned} &\frac{\partial \alpha_1 \rho_1 s_1}{\partial t} + div\left(\alpha_1 \rho_1 s_1 u\right) = 0, \\ &\frac{\partial \alpha_2 \rho_2 s_2}{\partial t} + div\left(\alpha_2 \rho_2 s_2 u\right) = 0. \end{aligned} \tag{2.25}$$

These equations will be helpful for the determination of two-phase nozzle flow solutions. Model's thermodynamic closure is achieved with the help of the mixture energy definition :

$$\rho e = \alpha_1 \rho_1 e_1 + \alpha_2 \rho_2 e_2 \tag{2.26}$$

and the pressure equilibrium condition : $p_1 = p_2$. In the context of fluids governed by the SG EOS (2.3), the mixture EOS reads :

$$P = \frac{\rho e - (\frac{\alpha_1 \gamma_1 P_{\infty,1}}{\gamma_1 - 1} + \frac{\alpha_2 \gamma_2 P_{\infty,2}}{\gamma_2 - 1})}{\frac{\alpha_1}{\gamma_1 - 1} + \frac{\alpha_2}{\gamma_2 - 1}} \tag{2.27}$$

2.3.2 Problem statement

We now consider the same nozzle flow problem as the one depicted in Figure 2.1 but in the context of the flow model ([47]). The steady nozzle flow solution is determined on the basis of System (2.23) and Equations (2.25). It results in the following algebraic system, valid in the absence of shocks :

$$\rho^+ u^+ A^+ = \rho^- u^- A^-, \quad s_1^+ = s_1^-, \quad s_2^+ = s_2^-, \quad Y_1^+ = Y_1^-, \quad Y_2^+ = Y_2^- \quad \text{and} \quad H^+ = H^- \tag{2.28}$$

The mass fractions are defined by $Y_k = \dfrac{\alpha_k \rho_k}{\rho}$ where ρ denotes the mixture density, $\rho = \alpha_1 \rho_1 + \alpha_2 \rho_2$, while the total enthalpy is defined by : $H = Y_1 h_1 + Y_2 h_2 + \dfrac{1}{2} u^2$.

As previously, two cross sections A^+ and A^- have been considered with smooth flow conditions. In addition to the single phase configuration, two entropies and two mass fractions are now invariant. Each fluid is assumed governed by the SG EOS (2.3) and the mixture evolves in pressure equilibrium : $p_1 = p_2$. The tank state is now defined by :

$$W_0 = (\rho_0,\ \alpha_{1,0},\ Y_{1,0},\ P_0)^T \text{, where } Y_k = \frac{\alpha_k \rho_k}{\rho}$$

or equivalently by $W_0 = (\rho_{1,0},\ \rho_{2,0},\ \alpha_{1,0},\ P_0)^T$.

When shocks are present, the following system has to be considered ([71]) to determine corresponding jumps :

$$(\rho u)_{cpr3} = (\rho u)_{cpr2} \tag{2.29}$$

$$\left(\rho u^2 + P\right)_{cpr3} = \left(\rho u^2 + P\right)_{cpr2} \tag{2.30}$$

$$e_{1,cpr2} - e_{1,cpr3} + \frac{P_{cpr2} + P_{cpr3}}{2}\left(v_{1,cpr2} - v_{1,cpr3}\right) = 0 \tag{2.31}$$

$$e_{2,cpr2} - e_{2,cpr3} + \frac{P_{cpr2} + P_{cpr3}}{2}\left(v_{2,cpr2} - v_{2,cpr3}\right) = 0 \tag{2.32}$$

$$Y_{k,cpr2} = Y_{k,cpr3} \tag{2.33}$$

2.3.3 Critical pressure ratios

The various flow regimes occurring in the Laval nozzle are related, as previously for single phase flows, to the outlet/inlet pressure ratio.

Critical pressure ratio 1 (cpr1) In this flow regime, the throat has a sonic state, while it is subsonic elsewhere. To determine the throat pressure associated to the sonic state, the following relations are used :

$$H_* = H_0, \quad s_{1,*} = s_{1,0}, \quad s_{2,*} = s_{2,0}, \quad Y_{1,*} = Y_{1,0}, \quad Y_{2,*} = Y_{2,0} \quad \text{and} \quad u_* = c_* \tag{2.34}$$

The total enthalpy is expressed as a function of the pressure :

$$Y_{1,0}h_{1,*}(P_*) + Y_{2,0}h_{2,*}(P_*) + \frac{1}{2}c_*^2(P_*) = H_0 \tag{2.35}$$

with $h_{k,*} = \dfrac{\gamma_k(P_* + P_{\infty,k})}{(\gamma_k - 1)\rho_{k,*}}$.
The isentropes are expressed as :

$$\rho_{k,*} = \rho_{k,*}(P_*) = \rho_{k,0}\left(\frac{P_* + P_{\infty,k}}{P_0 + P_{\infty,k}}\right)^{\frac{1}{\gamma_k}} \tag{2.36}$$

The mixture sound speed is given by Relation (2.24). The mixture density is given by :

$$\frac{1}{\rho_*} = \frac{Y_{1,0}}{\rho_{1,*}(P_*)} + \frac{Y_{2,0}}{\rho_{2,*}(P_*)} \tag{2.37}$$

The squared sound speeds are given by their definition :

$$c_{k,*}^2 = \gamma_k \frac{P_* + P_{\infty,k}}{\rho_{k,*}(P_*)} \tag{2.38}$$

The volume fractions $\alpha_{k,*}$ are determined from the mass fractions definition :

$$\alpha_{k,*} = \frac{Y_{k,0}\rho_*(P_*)}{\rho_{k,*}(P_*)} \tag{2.39}$$

All these relations are used in Relation (2.35) that forms a non-linear function of P_*. Is is solved by the Newton-Raphson method. Once the star pressure is determined, all subsequent variables at the sonic throat are determined.

There is thus no difficulty to determine the first critical pressure ratio (cpr1). To do so, the mass flow rate is expressed at throat,

$$m_* = \rho_* u_* A_*. \tag{2.40}$$

This mass flow rate is the same in the outlet section. Thus, the velocity in the outlet section reads,

$$u_{out}(P_{out}) = \frac{m_* v_{out}(P_{out})}{A_{out}}, \tag{2.41}$$

where the outlet pressure P_{out} has to be determined. The specific volumes at the outlet section are given by :

$$v_{k,out} = v_{k,0} \left(\frac{P_0 + P_{\infty,k}}{P_{out} + P_{\infty,k}} \right)^{\frac{1}{\gamma_k}} \tag{2.42}$$

and the mixture specific volume reads,

$$v_{out} = Y_{1,0} v_{1,out}(P_{out}) + Y_{2,0} v_{2,out}(P_{out}). \tag{2.43}$$

These relations are inserted in the total enthalpy conservation expressed between the tank and the outlet section :

$$Y_{1,0} h_{1,out}(P_{out}) + Y_{2,0} h_{2,out}(P_{out}) + \frac{1}{2} u^2_{out}(P_{out}) - H_0 = 0 \tag{2.44}$$

This equation admits two roots. To determine the critical pressure ratio cpr1, the Newton method is initialized with $P_{out} = P_*$. Once P_{out} is determined, the critical pressure ratio is deduced as :

$$cpr1 = \frac{P_{out}}{P_0} = \frac{P_{cpr1}}{P_0} \tag{2.45}$$

Critical pressure ratio 3 (cpr3) The same relation (2.44) is solved with the Newton method taking $P_{out} = (1 + 10^{-6}) Min(P_{\infty,1}, P_{\infty,2})$ as initial guess for the outlet pressure. Once P_{out} is determined, the critical pressure ratio is deduced as :

$$cpr3 = \frac{P_{out}}{P_0} = \frac{P_{cpr3}}{P_0} \tag{2.46}$$

Critical pressure ratio 2 (cpr2) This pressure ratio is associated to the presence of a steady shock wave in the outlet section. Thus, the flow enters the shock at a pressure equal to P_{cpr3}. The shock jump relations (2.29 - 2.33) are used. Inserting the SG EOS in the energy jump relations, the specific volumes are expressed as functions of the shock state pressure :

$$\frac{v_{1,cpr2}}{v_{1,cpr3}} = \frac{(\gamma_1 - 1)(P_{cpr2} + P_{\infty,1}) + (\gamma_1 + 1)(P_{cpr3} + P_{\infty,1})}{(\gamma_1 - 1)(P_{cpr3} + P_{\infty,1}) + (\gamma_1 + 1)(P_{cpr2} + P_{\infty,1})} \tag{2.47}$$

$$\frac{v_{2,cpr2}}{v_{2,cpr3}} = \frac{(\gamma_2 - 1)(P_{cpr2} + P_{\infty,2}) + (\gamma_2 + 1)(P_{cpr3} + P_{\infty,2})}{(\gamma_2 - 1)(P_{cpr3} + P_{\infty,2}) + (\gamma_2 + 1)(P_{cpr2} + P_{\infty,2})} \tag{2.48}$$

Combining Relations (2.29) and (2.30), the following relation is obtained,

$$P_{cpr2} = P_{cpr3} + \rho_{cpr3} u_{cpr3}^2 \left(1 - \frac{v_{cpr2}}{v_{cpr3}}\right). \tag{2.49}$$

The mixture specific volume v_{cpr2} is expressed as a function of the pressure P_{crp2} as :

$$v_{crp2} = Y_{1,0} v_{1,crp2}(P_{crp2}) + Y_{2,0} v_{2,crp2}(P_{crp2}) \tag{2.50}$$

Combining these two last relations, a non-linear function of P_{crp2} is obtained.
It is solved by the Newton-Raphson method by taking $P_{crp2} = P_{crp1}$ as initial guess. The critical pressure ratio $cpr2$ is then deduced as :

$$cpr2 = \frac{P_{out}}{P_0} = \frac{P_{cpr2}}{P_0} \tag{2.51}$$

2.3.4 Derivation of the nozzle flow : Two-phase isentropic

As for the single phase case, the flow is isentropic when the pressure ratio $PR = \dfrac{P_{out}}{P_0}$ is either greater than $cpr1$ or lower than $cpr2$. The outlet pressure P_{out} is imposed as boundary condition and the remaining state variables are determined from :

$$\rho_{1,out} = \rho_{1,0} \left(\frac{P_{out} + P_{\infty,1}}{P_0 + P_{\infty,1}}\right)^{\frac{1}{\gamma_1}} \tag{2.52}$$

$$\rho_{2,out} = \rho_{2,0} \left(\frac{P_{out} + P_{\infty,2}}{P_0 + P_{\infty,2}}\right)^{\frac{1}{\gamma_2}} \tag{2.53}$$

$$v_{out} = Y_{1,0} v_{1,out} + Y_{2,0} v_{2,out} \tag{2.54}$$

$$h_{1,out} = \frac{\gamma_1 \left(P_{out} + P_{\infty,1}\right)}{\left(\gamma_1 - 1\right) \rho_{1,out}} \tag{2.55}$$

$$h_{2,out} = \frac{\gamma_1 \left(P_{out} + P_{\infty,2}\right)}{\left(\gamma_2 - 1\right) \rho_{2,out}} \tag{2.56}$$

$$\alpha_{k,out} = \frac{Y_{k,0} \rho_{out}(P_{out})}{\rho_{k,out}(P_{out})} \tag{2.57}$$

The velocity at the outlet is determined from the total enthalpy definition :

$$u_{out} = \sqrt{2\left[h_0 - \left(Y_{1,0} h_{2,out}(P_{out}) + Y_{2,0} h_{2,out}(P_{out})\right)\right]} \tag{2.58}$$

From the outlet state knowledge, there is no difficulty to determine the mixture mass flow rate :

$$m = \rho_{out} u_{out} A_{out} \tag{2.59}$$

In a given area of cross section A_i, the velocity reads :

$$u_i = \frac{m v_i(P_i)}{A_i}, \tag{2.60}$$

where the pressure P_i has to be determined. The total enthalpy conservation expressed between the tank and the A_i section reads,

$$Y_{1,0} h_{1,i}(P_i) + Y_{2,0} h_{2,i}(P_i) + \frac{1}{2} u^2(P_i) - H_0 = 0 \tag{2.61}$$

where the enthalpies $h_{1,i}$ and $h_{2,i}$ are deduced from the same set of relations (2.52 - 2.56). Relation (2.61) is solved by the Newton-Raphson method with $P_i = P_0$ as the initial guess in the nozzle convergent and $P_i = P_{out}$ in the nozzle divergent. Once the pressure P_i is determined, the volume fractions are determined by the same relations (2.57).

2.3.5 Derivation of the nozzle flow profile : Two-phase adiabatic

When the pressure ratio, $PR = \frac{P_{out}}{P_0}$ is lower than crp1 and greater than crp2 a steady shock wave appears in the divergent. To determine the shock position we use the same method as previously, for single phase nozzle flows, except that the Rankine-Hugoniot jump relations correspond now to System (2.29-2.32).

2.3.6 Solution examples

The exact solutions calculation is addressed with the same geometry as previously (cf Section 2.2.6). The fluids used in the calculations correspond to liquid water and air, with the following SG EOS (2.3) parameters $\gamma_{water} = 4.4$, $P_{\infty,water} = 600 MPa$, $\gamma_{air} = 1.4$, $P_{\infty,air} = 0 Pa$. The tank state is defined by :

$$W_0 = \begin{pmatrix} \rho_{1,0} = 1000\, kg.m^{-3} \\ \rho_{2,0} = 1\, kg.m^{-3} \\ u_0 = 0\, m.s^{-1} \\ \alpha_{1,0} = 0.99999 \\ P_0 = 1\, MPa \end{pmatrix}.$$

Where subscripts "1" and "2" correspond to the water and the air, respectively. Figure (2.3) shows different typical solutions according to their respective pressure ratio $PR = \frac{P_{out}}{P_0}$. In this case, critical pressure ratios are respectively : cpr1= 0.80974, cpr2= 0.40989 and cpr3= $6.98159.10^{-8}$.

The pressure profiles corresponding to each pressure ratio are shown in the Figure 2.3. In addition, an isentropic pressure profile is shown in dashed lines for a subsonic flow in both convergent and divergent nozzle parts. It corresponds to the pressure ratio PR = 0.9. An extra solution example is shown with a steady shock in the nozzle divergent. It corresponds to the pressure ratio PR = 0.5. Furthermore, Mach number and water volume fraction profiles are shown in the Figures 2.3 and 2.4.

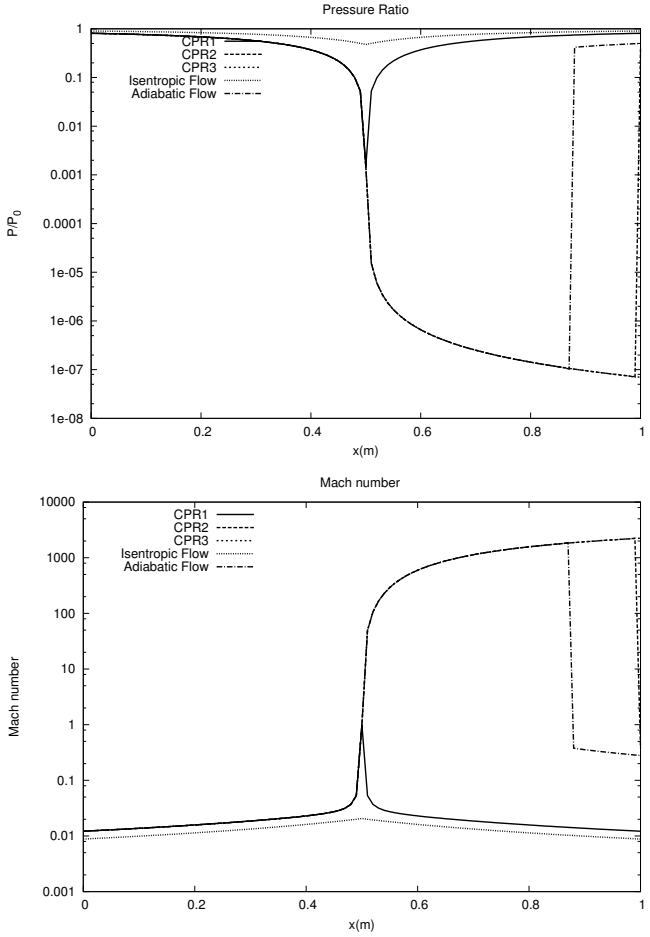

FIGURE 2.3 – Dimensionless pressure profiles in the Laval nozzle and Mach number profiles in the Laval nozzle for different outlet pressures corresponding to subsonic flow with sonic throat (cpr1), supersonic isentropic flow (cpr3), flow with a steady shock in the outlet section (cpr2), subsonic isentropic solution (PR = 0.9) and steady shock in the divergent (PR = 0.5).

The sonic state at throat appears for weak pressure ratios ($cpr \leq 0.8$) which are quite easy to reach in practical systems. From that pressure ratio, when the outlet pressure is lowered (or the tank pressure is increased) part of the divergent is supersonic. The Mach number increases dramatically, as the sound speed is non monotonic with respect to the volume fraction. Thus, the gas volume fraction increases as the pressure decreases and cavitation

zones appear. It is worth to mention that the obtained cavitating nozzle flow is "ideal", at least for two reasons :

- The cavitation zone that appears in the divergent is not due to liquid-gas phase change but only to bubbles growth, imposed by the pressure equilibrium condition.
- The reference solution derived previously is 1D whereas experimental ones always deal with multi-D effects. Indeed, cavitation zones correspond to multi-D pockets, separating gas and liquid in the nozzle. Experimental and numerical examples of such flows in Venturi channels may be found in [53] and [10].

These multi-D effects also imply velocity disequilibrium in a given 1D cross-section, which is not considered in this paper. The two-phase reference solution derived previously is however clearly helpful to examine the accuracy and convergence of numerical schemes for two-phase flows in all Mach number conditions.

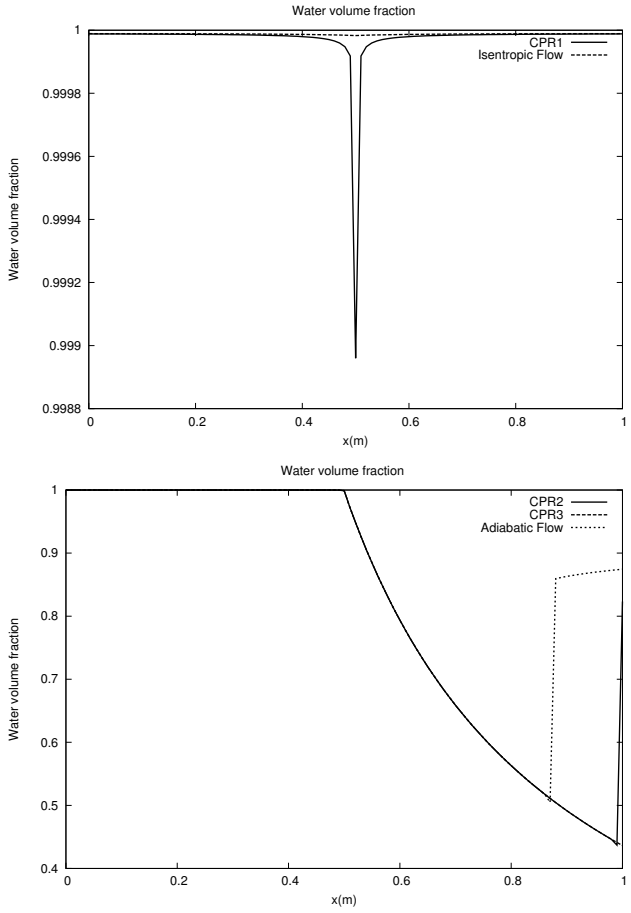

FIGURE 2.4 – Volume fraction of water profiles in the Laval nozzle for different outlet pressures corresponding to subsonic flow with sonic throat (cpr1), subsonic isentropic solution (PR = 0.9), supersonic isentropic flow (cpr3) and flow with a steady shock in the outlet section (cpr2) and steady shock in the divergent (PR = 0.5).

2.4 Two-phase flow in mechanical and thermal equilibrium

We now address a more constrained flow model where the phases evolve in both mechanical and thermal equilibrium. It means that heat exchanges among the phases are stiff.

2.4.1 Flow model

The model describing multiphase mixtures evolving in mechanical and thermal equilibrium can be derived from [73] :

$$
\begin{aligned}
&\frac{\partial \alpha_1}{\partial t} + \mathbf{u}\cdot\mathbf{grad}\,(\alpha_1) = \frac{\rho_2 c_2^2 - \rho_1 c_1^2}{\frac{\rho_1 c_1^2}{\alpha_1} + \frac{\rho_2 c_2^2}{\alpha_2}} div\,(\mathbf{u}) + \rho\nu(g_2 - g_1)\frac{\frac{c_1^2}{\alpha_1} + \frac{c_2^2}{\alpha_2}}{\frac{\rho_1 c_1^2}{\alpha_1} + \frac{\rho_2 c_2^2}{\alpha_2}} + \frac{(\frac{\Gamma_1}{\alpha_1} + \frac{\Gamma_2}{\alpha_2})}{\frac{\rho_1 c_1^2}{\alpha_1} + \frac{\rho_2 c_2^2}{\alpha_2}} H(T_2 - T_1)\\
&\frac{\partial \alpha_1\rho_1}{\partial t} + div\,(\alpha_1\rho_1\mathbf{u}) = \rho\nu(g_2 - g_1)\\
&\frac{\partial \alpha_2\rho_2}{\partial t} + div\,(\alpha_2\rho_2\mathbf{u}) = -\rho\nu(g_2 - g_1)\\
&\frac{\partial \rho\mathbf{u}}{\partial t} + div\left(\rho\mathbf{u}\otimes\mathbf{u} + P\underline{\underline{I}}\right) = 0\\
&\frac{\partial \rho E}{\partial t} + div\,((\rho E + P)\mathbf{u}) = 0
\end{aligned}
\tag{2.62}
$$

In the limit of stiff temperature relaxation (infinite H) and in the absence of mass transfer ($\nu = 0$), System (2.62) reduces to :

$$
\begin{aligned}
&\frac{\partial \rho}{\partial t} + div\,(\rho\mathbf{u}) = 0\\
&\frac{\partial \rho\mathbf{u}}{\partial t} + div\left(\rho\mathbf{u}\otimes\mathbf{u} + P\underline{\underline{I}}\right) = 0\\
&\frac{\partial \rho E}{\partial t} + div\,((\rho E + P)\mathbf{u}) = 0\\
&\frac{\partial \rho Y_1}{\partial t} + div\,(\rho Y_1\mathbf{u}) = 0
\end{aligned}
\tag{2.63}
$$

Where $Y_k = \dfrac{\alpha_k\rho_k}{\rho}$ represents the mass fraction of phase k. The mixture total energy is still defined by $E = Y_1 e_1 + Y_2 e_2 + \frac{1}{2}\mathbf{u}\cdot\mathbf{u}$. The thermodynamic closure is achieved by the following EOS,

$$
P = \frac{1}{2}\left(A_1 + A_2 - (P_{\infty,1} + P_{\infty,2})\right) + \sqrt{\frac{1}{4}\left(A_2 - A_1 - (P_{\infty,2} - P_{\infty,1})\right)^2 + A_1 A_2}, \tag{2.64}
$$

where $A_k = \dfrac{Y_k\left(\gamma_k - 1\right)Cv_k}{Y_1 Cv_1 + Y_2 Cv_2}\left(\rho(e - q) - P_{\infty,k}\right)$,

and the constraints of mechanical and thermal equilibrium, $p_1 = p_2$ and $T_1 = T_2$. These constraints lead to a relation linking the mixture temperature and pressure,

$$\frac{1}{\rho T} = \frac{Y_1(\gamma_1 - 1)C_{v,1}}{P + P_{\infty,1}} + \frac{Y_2(\gamma_2 - 1)C_{v,2}}{P + P_{\infty,2}}, \tag{2.65}$$

where $q = Y_1 q_1 + Y_2 q_2$ represents the mixture reference energy, e the mixture internal energy and ρ the mixture density.
System (2.63) is hyperbolic with three wave speeds, $\lambda_0 = u$ (two times fold), $\lambda_1 = u + c$ and $\lambda_2 = u - c$ with the following square sound speed :

$$c^2 = \frac{1}{2}\left((e-q)(a_1+a_2) + \frac{\frac{1}{2}\frac{\partial R_1}{\partial \rho}\Big)_e R_1 + \frac{\partial R_2}{\partial \rho}\Big)_e}{\sqrt{\frac{1}{4}R_1 R_1 + R_2}} + \frac{P}{\rho^2}\left(\rho(a1+a2) + \frac{\frac{1}{2}\frac{\partial R_1}{\partial e}\Big)_\rho R_1 + \frac{\partial R_2}{\partial e}\Big)_\rho}{\sqrt{\frac{1}{4}R_1 R_1 + R_2}} \right) \right) \tag{2.66}$$

Where,

$a_1 = \dfrac{Y_1(\gamma_1 - 1)Cv_1}{Y_1 Cv_1 + Y_2 Cv_2}$, $a_2 = \dfrac{Y_2(\gamma_2 - 1)Cv_2}{Y_1 Cv_1 + Y_2 Cv_2}$,

$R_1 = a_2\rho(e-q) - a_2 P_{\infty,2} - a_1\rho(e-q) + a_1 P_{\infty,1} - P_{\infty,2} + P_{\infty,1}$,

$R_2 = a_1 a_2(\rho(e-q) - P_{\infty,1})(\rho(e-q) - P_{\infty,2})$.
Theoretical details on sound propagations in media with relaxation may be found, for example, in [86].

In the absence of shocks, System (2.63) can be complemented by the following entropy equation :

$$\frac{\partial \rho S}{\partial t} + div\,(\rho S \mathbf{u}) = 0 \tag{2.67}$$

Where $S = Y_1 s_1 + Y_2 s_2$.
Using the SG EOS, the phases' entropies can be expressed using the relation given in [52] :

$$s_k = C_{v,k} ln\left(\frac{T^{\gamma_k}}{(P + P_{\infty,k})^{\gamma_k - 1}} \right) \tag{2.68}$$

2.4.2 Problem statement

We now consider the same nozzle flow problem as the one depicted in Figure 2.1 but in the context of the previous mechanical and thermal equilibrium model (2.63). The steady nozzle flow solution is determined on the basis of this model and relation (2.67). It results in the following algebraic system :

$$\rho^+ u^+ A^+ = \rho^- u^- A^-, \quad Y_1^+ = Y_1^-, \quad Y_2^+ = Y_2^-, \quad S_+ = S_- \quad \text{and} \quad H^+ = H^- \tag{2.69}$$

The tanks state is now defined by :

$$W_0 = (P_0,\ u_0,\ Y_{1,0},\ T_0)^T \text{ , where } Y_k = \frac{\alpha_k \rho_k}{\rho}$$

Or alternatively,

$$W_0 = (P_0,\ u_0,\ \alpha_{k,0},\ T_0)^T$$

In the presence of shocks, the following System has to be considered :

$$(\rho u)_{cpr3} = (\rho u)_{cpr2} \tag{2.70}$$

$$\left(\rho u^2 + P\right)_{cpr3} = \left(\rho u^2 + P\right)_{cpr2} \tag{2.71}$$

$$e_{cpr2} - e_{cpr3} + \frac{P_{cpr2} + P_{cpr3}}{2}\left(v_{cpr2} - v_{cpr3}\right) = 0 \tag{2.72}$$

$$Y_{k,cpr2} = Y_{k,cpr3} \tag{2.73}$$

2.4.3 Critical pressure ratios

Critical pressure ratio 1 (cpr1) In this flow regime, the throat has a sonic state, while it is subsonic elsewhere. To determine the throat pressure associated to the sonic state, the following relations are used :

$$u^* = c^*, \quad Y_1^* = Y_1^0, \quad Y_2^* = Y_2^0, \quad S^* = S_0 \quad \text{and} \quad H^* = H^0 \tag{2.74}$$

The total enthalpy is defined by $H = Y_1 h_1 + Y_2 h_2 + \frac{1}{2}u^2$. In the case of mechanical and thermal equilibrium and using SG EOS, this relation reduces to :

$$H = C_m T + \frac{1}{2}u^2 \tag{2.75}$$

Where $C_m = Y_1\gamma_1 C_{v,1} + Y_2\gamma_2 C_{v,2}$. These relations are expressed as functions of the pressure :

$$C_m T^*(P^*) + \frac{1}{2}u^2(P^*) = H_0 \tag{2.76}$$

Using the mixture isentrope (2.67) and definition (2.68), the mixture temperature is expressed as a function of the mixture pressure :

$$ln(T^*) = \frac{S_0 + Y_1^0 C_{v,1}(\gamma_1 - 1)ln(P^* + P_{\infty,1}) + Y_2^0 C_{v,2}(\gamma_2 - 1)ln(P^* + P_{\infty,2})}{C_m} \tag{2.77}$$

This relation may be rewritten in a more simple form :

$$\frac{T^*}{T_0} = \left(\frac{P^* + P_{\infty,1}}{P_0 + P_{\infty,1}}\right)^{\frac{Y_1^0 C_{v,1}(\gamma_1 - 1)}{C_m}} \times \left(\frac{P^* + P_{\infty,2}}{P_0 + P_{\infty,2}}\right)^{\frac{Y_2^0 C_{v,2}(\gamma_2 - 1)}{C_m}} \tag{2.78}$$

The sound speed of System (2.63) corresponds to Relation (2.66). In this relation, the mixture density is determined by Relation (2.65) :

$$\frac{1}{\rho^*} = T_* \left(\frac{Y_1^0(\gamma_1 - 1)C_{v,1}}{P^* + P_{\infty,1}} + \frac{Y_2^0(\gamma_2 - 1)C_{v,2}}{P^* + P_{\infty,2}} \right) \tag{2.79}$$

while the mixture total energy is defined by Relation (2.26).
All these relations are used in Relation (2.76) that forms a non-linear function of P^*. Is is solved by the Newton-Raphson method. Once the star pressure is determined, all subsequent variables at the sonic throat are determined.
There is thus no difficulty to determine the first critical pressure ratio (cpr1). To do this, the mass flow rate is expressed at throat,

$$m_* = \rho_* u_* A_* \tag{2.80}$$

This mass flow rate is the same in the outlet section. Thus, the velocity in the outlet section reads,

$$u_{out}(P_{out}) = \frac{m_* v_{out}(P_{out})}{A_{out}}, \tag{2.81}$$

where the outlet pressure P_{out} has to be determined. The mixture temperature at the outlet section is given by,

$$ln(T_{out}) = \frac{S_0 + Y_1^0 C_{v,1}(\gamma_1 - 1)ln(P_{out} + P_{\infty,1}) + Y_2^0 C_{v,2}(\gamma_2 - 1)ln(P_{out} + P_{\infty,2})}{C_m}, \tag{2.82}$$

while the mixture density is given by Relation (2.65) expressed at the outlet section,

$$\frac{1}{\rho_{out}} = T_{out} \left(\frac{Y_1^0(\gamma_1 - 1)C_{v,1}}{P_{out} + P_{\infty,1}} + \frac{Y_2^0(\gamma_2 - 1)C_{v,2}}{P_{out} + P_{\infty,2}} \right). \tag{2.83}$$

These relations are inserted in the total enthalpy conservation expressed between the tank and the outlet section :

$$C_m T_{out}(P_{out}) + \frac{1}{2} u_{out}^2(P_{out}) = H_0 \tag{2.84}$$

This equation admits two roots. To determine the critical pressure ratio cpr1, the Newton method is initialized with $P_{out} = P^*$. Once P_{out} is determined, the critical pressure ratio is deduced as :

$$cpr1 = \frac{P_{out}}{P_0} = \frac{P_{cpr1}}{P_0} \tag{2.85}$$

Critical pressure ratio 3 (cpr3) The same relation (2.84) is solved with the Newton method taking $P_{out} = (1 + 10^{-6})Min(P_{\infty,1}, P_{\infty,2})$ as initial guess for the outlet pressure. Once P_{out} is determined, the critical pressure ratio is deduced as :

$$cpr3 = \frac{P_{out}}{P_0} = \frac{P_{cpr3}}{P_0} \tag{2.86}$$

Critical pressure ratio 2 (cpr2) This pressure ratio is associated to the pressure corresponding to a steady shock wave in the outlet section. Thus, the flow enters the shock at a pressure equal to P_{cpr3}.
Using energy conservation (2.26) expressed with the help of SG EOS and constraints $p_1 = p_2$, $T_1 = T_2$, the following expression is obtained :

$$\frac{e-q}{T} = Y_1 C_{v,1} + Y_2 C_{v,2} + \frac{Y_1(\gamma_1 - 1)C_{v,1}P_{\infty,1}}{P + P_{\infty,1}} + \frac{Y_2(\gamma_2 - 1)C_{v,2}P_{\infty,2}}{P + P_{\infty,2}} \tag{2.87}$$

Expressing the mixture temperature, T, using relation (2.65), a relation linking e, P, ρ and Y_k is obtained :

$$e = v\frac{Y_1 C_{v,1} + Y_2 C_{v,2} + \frac{Y_1(\gamma_1 - 1)C_{v,1}P_{\infty,1}}{P + P_{\infty,1}} + \frac{Y_2(\gamma_2 - 1)C_{v,2}P_{\infty,2}}{P + P_{\infty,2}}}{\frac{Y_1(\gamma_1 - 1)C_{v,1}}{P + P_{\infty,1}} + \frac{Y_2(\gamma_2 - 1)C_{v,2}}{P + P_{\infty,2}}} \tag{2.88}$$

The shock jump relations are the ones given previously (2.70 - 2.73) where the mixture internal energy e is now expressed as (2.88). Therefore, a non-linear function of P_{crp2} is obtained.
It is solved by the Newton-Raphson method by taking $P_{crp2} = P_{crp1}$ as initial guess. The critical pressure ratio $cpr2$ is then deduced as :

$$cpr2 = \frac{P_{out}}{P_0} \tag{2.89}$$

2.4.4 Derivation of the nozzle flow profile : Two-phase isentropic

The flow is isentropic when the pressure ratio $PR = \frac{P_{out}}{P_0}$ is either greater than $cpr1$ or lower than $crp2$. The outlet pressure P_{out} is imposed as boundary condition and the remaining state variables are determined from,

$$ln(T_{out}) = \frac{S_0 + Y_1^0 C_{v,1}(\gamma_1 - 1)ln(P_{out} + P_{\infty,1}) + Y_2^0 C_{v,2}(\gamma_2 - 1)ln(P_{out} + P_{\infty,2})}{C_m} \tag{2.90}$$

$$\frac{1}{\rho_{out}} = T_{out}\left(\frac{Y_1^0(\gamma_1 - 1)C_{v,1}}{P_{out} + P_{\infty,1}} + \frac{Y_2^0(\gamma_2 - 1)C_{v,2}}{P_{out} + P_{\infty,2}}\right) \tag{2.91}$$

The velocity at the outlet is determined from the total enthalpy definition :

$$u_{out} = \sqrt{2\left[H_0 - C_m T_{out}\right]} \tag{2.92}$$

From the outlet state knowledge, there is no difficulty to determine the mixture mass flow rate :

$$m = \rho_{out} u_{out} A_{out} \tag{2.93}$$

In a given area of cross section A_i, the velocity reads :

$$u_i = \frac{mv_i(P_i)}{A_i}, \tag{2.94}$$

where the pressure P_i has to be determined. The total enthalpy conservation expressed between the tank and the A_i section reads,

$$C_m T_i(P_i) + \frac{1}{2} u_i^2(P_i) = H_0 \tag{2.95}$$

where T_i and u_i are deduced from relations (2.90 - 2.91) and (2.94). Relation (2.95) is solved by the Newton-Raphson method with $P_i = P_0$ as the initial guess in the nozzle convergent and $P_i = P_{out}$ in the nozzle divergent. Once the pressure P_i is determined, the mixture density and the mixture pressure are determined using Relations (2.90 - 2.91). The volume fractions are determined by the relations,

$$\alpha_{k,i} = \frac{Y_{k,0}\rho_i(P_i)}{\rho_{k,i}\left(P_i\right)}, \tag{2.96}$$

where $\rho_{k,i}$ is expressed using the caloric SG EOS for a given phase :

$$\rho_{i,k} = \frac{P_i + P_{\infty,k}}{(\gamma_k - 1)C_{v,k}T_i} \tag{2.97}$$

2.4.5 Derivation of the nozzle flow profile : Two-phase adiabatic

When the pressure ratio, $PR = \dfrac{P_{out}}{P_0}$ is lower than crp1 and greater than crp2 a steady shock wave appears in the divergent. To determine the shock position we use the same method as previously, for single phase nozzle flows, except that the mixture internal energy is expressed using Relation (2.88).

2.4.6 Solution examples

The exact solutions calculation is addressed with the same geometry as previously (cf Section 2.2.6). The fluids used in the calculations correspond to liquid water and air, with the following SG EOS (2.3) parameters $\gamma_{water} = 4.4$, $P_{\infty,water} = 600MPa$, $C_{v,water} = 588.33$, $\gamma_{air} = 1.4$, $P_{\infty,air} = 0Pa$, $C_{v,air} = 833.33$. The tank state is defined by :

$$W_0 = \begin{pmatrix} T_0 = 300K \\ u_0 = 0\, m.s^{-1} \\ \alpha_{1,0} = 0.99999 \\ P_0 = 1\, MPa \end{pmatrix}.$$

Where subscripts "1" and "2" correspond to the water and the air, respectively. Figure (2.5) shows different typical solutions according by their respective pressure ratio $PR = \dfrac{P_{out}}{P_0}$. In

this case, critical pressure ratios are respectively : cpr1= 0.81096527, cpr2= 0.49138809 and cpr3= $7.6818310.10^{-6}$.
The pressure profiles corresponding to each pressure ratio are shown in the Figure (2.5). In addition, an isentropic pressure profile is shown in dashed lines for a subsonic flow in both convergent and divergent nozzle parts. It corresponds to the pressure ratio PR = 0.9. An extra solution example is shown with a steady shock in the nozzle divergent. It corresponds to the pressure ratio PR = 0.6. Furthermore, Mach number and water volume fraction profiles are shown in the Figures (2.5) and (2.6). The sonic state at throat appears for weak pressure ratios ($cpr \leq 0.81$) which are quite easy to reach in practical systems. From that pressure ratio, when the outlet pressure is lowered (or the tank pressure is increased) part of the divergent is supersonic. The Mach number increases dramatically, as the sound speed is non monotonic versus volume fraction. Thus, the gas volume fraction increases as the pressure decreases and cavitation zones appear. This cavitation corresponds to gas pocket growth, in pressure and temperature equilibrium condition.

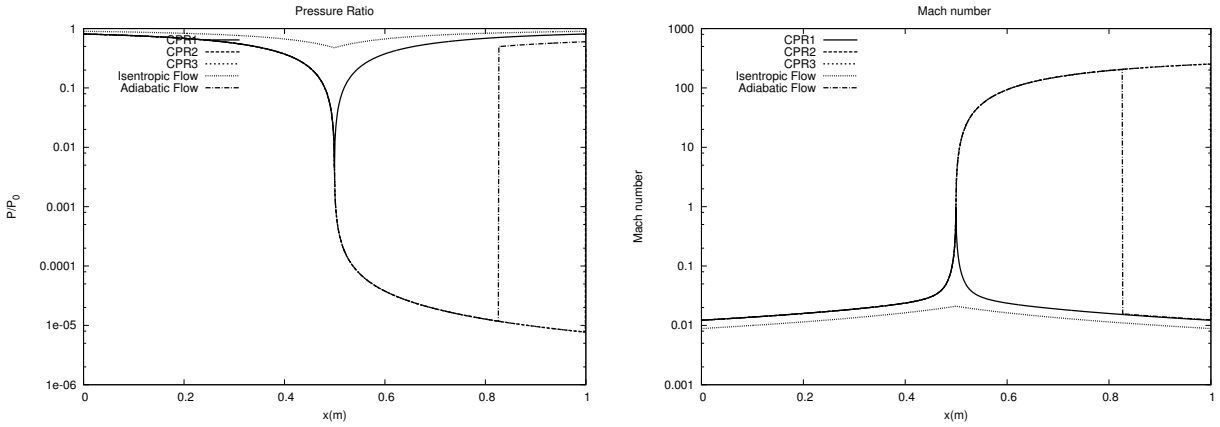

FIGURE 2.5 – Dimensionless pressure and Mach number profiles in the Laval nozzle for different outlet pressures corresponding to subsonic flow with sonic throat (cpr1), supersonic isentropic flow (cpr3), flow with a steady shock in the outlet section (cpr2), subsonic isentropic solution (PR = 0.9) and steady shock in the divergent (PR = 0.6).

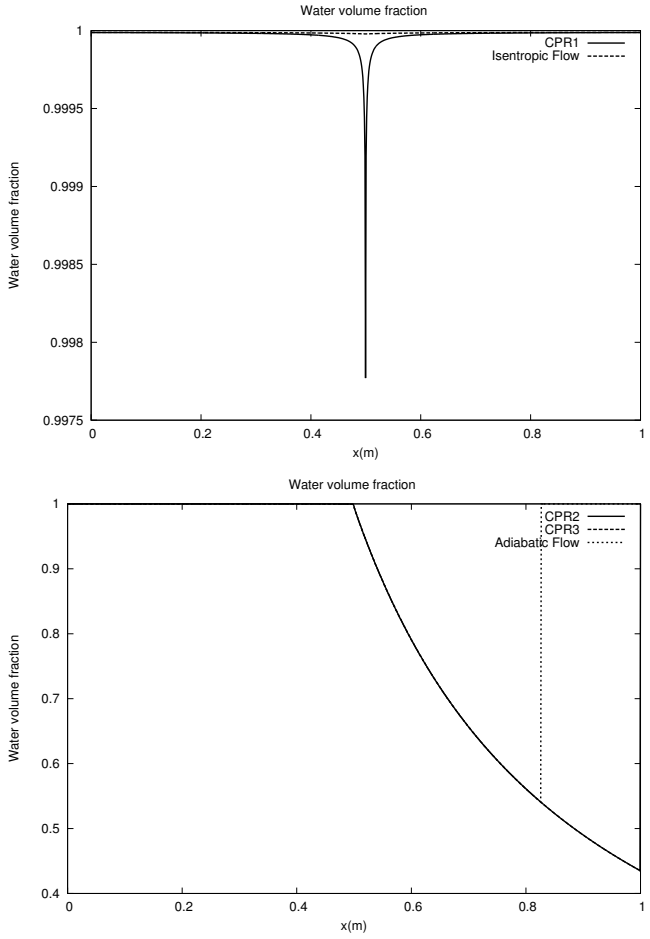

FIGURE 2.6 – Volume fraction of water profiles in the Laval nozzle for different outlet pressures corresponding to subsonic flow with sonic throat (cpr1), subsonic isentropic solution (PR = 0.9), supersonic isentropic flow (cpr3), flow with a steady shock in the outlet section (cpr2) and steady shock in the divergent (PR = 0.6).

2.5 Two-phase flow in thermodynamic equilibrium

2.5.1 Flow model

To derive the flow model for fluid mixtures in thermodynamic equilibrium we consider the asymptotic limit of System (2.62) with both stiff thermal and Gibbs free energy relaxation

(infinite H and infinite ν). Details may be found in [31] and [56]. The reduced model reads :

$$\begin{aligned} &\frac{\partial \rho}{\partial t} + div\,(\rho \mathbf{u}) = 0 \\ &\frac{\partial \rho \mathbf{u}}{\partial t} + div\,(\rho \mathbf{u} \otimes \mathbf{u} + P) = 0 \\ &\frac{\partial \rho E}{\partial t} + div\,((\rho E + P)\mathbf{u}) = 0 \end{aligned} \tag{2.98}$$

Where,
ρ represents the mixture density,
P represents the mixture pressure,
and E represents the mixture total energy.

In this model both phases are assumed to fulfil the thermodynamic equilibrium assumption (equality of pressure, temperature and Gibbs free energy). These equalities lead to a relation linking the pressure and the temperature (see [52] for details). This relation corresponds to the well-known saturated vapour pressure depending on the temperature or inversely : $T = T_{sat}(P)$.
In the following let us denote by subscripts L and V the liquid and vapour phases respectively that obey the Stiffened Gas EOS.
The mixture specific volume reads :

$$V = \frac{1}{\rho} = Y_L v_L + Y_V v_V = v_V - Y_L(v_V - v_L) \tag{2.99}$$

where the specific volume of each phase depends on the pressure only :

$$v_k = v_k(P) = \frac{(\gamma_k - 1) C_{v,k} T_{sat}(P)}{P + P_{\infty,k}}$$

In relation (2.99), Y_L and Y_V represent the mass fraction of the liquid and the vapour respectively.
The mixture internal energy reads :

$$e = Y_L e_L + Y_V e_V = e_V - Y_L(e_V - e_L) \tag{2.100}$$

where the internal energies of both phases are given by the following relation :

$$e_k = e_k(P) = \frac{P + \gamma_k P_{\infty,k}}{P + P_{\infty,k}} C_{v,k} T_{sat}(P) + q_k$$

In terms of specific enthalpies, the mixture internal energy (2.100) can be rewritten as :

$$e = h_V - Y_L(h_V - h_L) - PV \tag{2.101}$$

where $h_V - h_L = L_v$ corresponds to the latent heat of vaporization and h_k is the specific enthalpy of phase k :

$$h_k(P) = C_{p,k} T_{sat}(P) + q_k$$

Combining relations (2.99) and (2.101) leads to a relation where the liquid mass fraction has been eliminated :

$$e = e(P,V) = h_V - (v_V - V)\frac{(h_V - h_L)}{(v_V - v_L)} - PV \tag{2.102}$$

This last relation (2.102) corresponds to the thermodynamic closure law of system (2.98) where $h_k(P)$ and $v_k(P)$ are respectively saturated specific enthalpies and volumes of both phases.
According to the relation (2.102) the mixture sound speed writes :

$$\left(\frac{V}{c}\right)^2 = Y_V \left(\frac{v_V}{c_V}\right)^2 + Y_L \left(\frac{v_L}{c_L}\right)^2 + T_{sat}(P)\left(\frac{Y_V}{C_{p,V}}\left(\frac{ds_V}{dP}\right)^2 + \frac{Y_L}{C_{p,L}}\left(\frac{ds_L}{dP}\right)^2\right) \tag{2.103}$$

where c_k and s_k represent respectively the saturated sound speed and specific entropy of phase k given by the relations :

$$c_k = c_k(P) = \sqrt{\gamma_k (P + P_{\infty,k}) v_k} = \sqrt{(\gamma_k - 1) C_{p,k} T_{sat}(P)}$$

$$s_k = s_k(P) = C_{v,k} ln\left(\frac{(T_{sat}(P))^{\gamma_k}}{(P + P_{\infty,k})^{\gamma_k - 1}}\right) + s_{0,k}$$

In the absence of shocks system (2.98) may be complemented by the following equation :

$$\frac{\partial \rho S}{\partial t} + div(\rho S \mathbf{u}) = 0 \tag{2.104}$$

where $S = Y_V s_V + Y_L S_L = s_V - Y_L (s_V - s_L)$ is the mixture entropy.

2.5.2 Problem statement

The same geometrical configuration of the nozzle depicted in Figure 1 is considered. The steady nozzle flow solution is now determined on the basis of mechanical equilibrium between phases according to system (2.98) and equation (2.104). It results in the following algebraic system :

$$\rho^+ u^+ A^+ = \rho^- u^- A^-, \quad S^+ = S^- \quad and \quad H^+ = H^- \tag{2.105}$$

Contrary to the previous cases the mass fractions of each phase are now varying through the nozzle.
The tank state is now defined as :

$$W_0 = (P_0, Y_{0,L})^T \tag{2.106}$$

or alternatively,

$$W_0 = (P_0, \alpha_{0,L})^T \tag{2.107}$$

2.5.3 Critical pressure ratios

The various flow regimes occuring in the nozzle are related as previously to the outlet/inlet pressure ratio.

Critical pressure ratio 1 (cpr1) In this particular configuration the flow is subsonic everywhere except at the throat where a sonic state is reached. The relations aimed to determine the sonic state are the following :

$$u^* = c^*, \qquad S^* = S_0 \quad and \quad H^* = H_0 \tag{2.108}$$

The total enthalpy equality may be rewritten as :

$$H^* = h^* + \frac{1}{2}u^{*2} = h_V^* - Y_L^* \left(h_V^* - h_L^*\right) + \frac{1}{2}c^{*2} = H_0 \tag{2.109}$$

In this relation the variables h_k^*, Y_L^* and c^* are functions of the pressure P^* only. Indeed the liquid mass fraction may be expressed in function of the pressure by using the mixture entropy equality (2.108) :

$$Y_L^* = Y_L^*(P^*) = \frac{s_V^* - S_0}{s_V^* - s_L^*} \tag{2.110}$$

The mixture sound speed c^* obeys the relation (2.103) and is also a function of the pressure P^*.
Then the relation (2.109) forms a non-linear function of P^* that may be solved by an iterative method. Once the pressure is determined all associated throat variables are computed with the corresponding preceding relations. In particular the mass flow rate is determined by :

$$m^* = \frac{c^* A^*}{V^*} \tag{2.111}$$

where A^* corresponds to the throat area of the nozzle.
The mass flow rate being constant across the nozzle the two-phase mixture velocity may be expressed in function of the pressure at the outlet level :

$$u_{out}(P_{out}) = \frac{m^* v_{out}(P_{out})}{A_{out}} \tag{2.112}$$

where

$$v_{out}(P_{out}) = v_{V,out}(p_{out}) - Y_{L,out}(P_{out})(v_{V,out}(P_{out}) - v_{L,out}(P_{out})) \tag{2.113}$$

$$Y_{L,out}(P_{out}) = \frac{s_{V,out}(P_{out}) - S_0}{s_{V,out}(P_{out}) - s_{L,out}(P_{out})} \tag{2.114}$$

These last relations are inserted in the total enthalpy conservation equation (2.108) leading to a single function of the pressure p_{out} :

$$h_{V,out}(P_{out}) - Y_{L,out}(P_{out})(h_{V,out}(P_{out}) - h_{L,out}(P_{out})) + \frac{1}{2}\left(u_{out}(P_{out})\right)^2 = H_0 \tag{2.115}$$

The equation (2.115) admits two roots p_{cpr1} and p_{cpr3} corresponding to subsonic and supersonic regimes.
The subsonic critical pressure ratio is thus determined by :

$$cpr1 = \frac{P_{cpr1}}{P_0} \tag{2.116}$$

Critical pressure ratio 3 (cpr3) The supersonic critical pressure ratio is determined by :

$$cpr3 = \frac{P_{cpr3}}{P_0} \tag{2.117}$$

Critical pressure ratio 2 (cpr2) This particular critical pressure ratio corresponds to a flow regime where a steady shock wave is precisely located at the outlet of the nozzle. Then the two-phase flow enters the shock at the $cpr3$ state and the relations aimed to determine the pressure p_{cpr2} are the shock jump relations associated to the system (2.98) and the closure relation (2.102). These ones still correspond to relations (13-15) where the thermodynamic equilibrium assumption between phases is used.
This system leads to a single relation where P_{cpr2} is the only unknown :

$$P_{cpr2} - P_{cpr3} = \left(\frac{m^*}{A_{out}}\right)^2 (V_{cpr3} - V_{cpr2}(P_{cpr2})) \tag{2.118}$$

where $V_{cpr2}(P_{cpr2})$ is obtained by combining relations (15) and (2.102).
An iterative numerical method is still necessary to retrieve the pressure P_{cpr2} from the relation (2.118). Then the critical pressure ratio 2 is deduced by :

$$cpr2 = \frac{P_{cpr2}}{P_0} \tag{2.119}$$

2.5.4 Derivation of the nozzle flow profile : two-phase isentropic

The flow is isentropic inside the nozzle when the pressure ratio $PR = \frac{P_{out}}{P_0}$ between the tank and the external medium is either greater than $cpr1$ or lower than $cpr2$. In the first case the flow is subsonic at the nozzle outlet. In the second case the flow is supersonic at the outlet section and the associated pressure is given by $P_{out} = P_{cpr3}$.
The first step is to determine the mass flow rate through the nozzle. When the flow is subsonic it is determined from the knowledge of the outlet pressure P_{out}. Indeed the mass flow rate is expressed by $m = \frac{u_{out} A_{out}}{V_{out}}$ where u_{out} and V_{out} depend on the pressure P_{out}.
The specific volume of the mixture V_{out} is determined by relations (2.113) and (2.114).
The velocity u_{out} is determined by the following relation :

$$u_{out} = \sqrt{2\left(H_0 - h_{V,out} + Y_{L,out}(h_{V,out} - h_{L,out})\right)} \tag{2.120}$$

When the flow is supersonic the mass flow rate corresponds directly to the critical one $m = m^*$.
Once the mass flow rate is determined the second step consists in computing variables at each area of cross section A_i. The associated velocity may be obtained by the following relation :

$$u_i = \frac{mV_i(P_i)}{A_i} \tag{2.121}$$

where P_i has to be determined.
The total enthalpy conservation reads :

$$h_{V,i} - Y_{L,i}(h_{V,i} - h_{L,i}) + \frac{1}{2}u_i^2 = H_0 \tag{2.122}$$

where the liquid mass fraction $Y_{L,i}$ is given by :

$$Y_{L,i} = \frac{s_{V,i} - S_0}{s_{V,i} - s_{L,i}} \tag{2.123}$$

Then the only unknown in relation (2.122) is the pressure P_i. Again an iterative method is necessary to get the associated value. The other variables are computed with the help of the relations above.

2.5.5 Derivation of the nozzle flow profile : two-phase adiabatic

When the pressure ratio $PR = \frac{P_{out}}{P_0}$ is between $cpr1$ and $cpr2$ a steady shock wave is present in the divergent. The shock location is determined by the same method used in the single-phase section except that the mixture evolves under thermodynamic equilibrium assumption. Then the jump relations associated to the system (2.98) and the closure relation (2.102) are considered here.

2.5.6 Solution examples

Some exact solutions are now addressed with the same nozzle geometry used in the previous sections. The phases under consideration are liquid water and steam whose parameters are given by :

$$\gamma_L = 2.04 \quad P_{\infty,L} = 8.525 \times 10^8 Pa \quad C_{v,L} = 2069 J/(kg.K) \quad q_L = -1.151 \times 10^6 J/kg$$

$$\gamma_V = 1.34 \quad P_{\infty,V} = 0 Pa \quad C_{v,V} = 1265 J/(kg.K) \quad q_V = 1.968 \times 10^6 J/kg$$

All the preceding Stiffened Gas parameters are computed according to the method explained in [52]. In particular they are determined by fitting theoretical and experimental saturation curves associated to the corresponding liquid/vapour couple.
The tank state is defined by :

$$W_0 = \begin{pmatrix} P_0 = 10^6 Pa \\ \alpha_{0,L} = 0.99999 \end{pmatrix}$$

As a consequence, the corresponding temperature and mixture specific volume are respectively $T_0 = T_{sat}(P_0) \simeq 452.8K$ and $v_0 \simeq 1.142 \times 10^{-3} m^3/kg$.
The following results compare the exact profiles of some characteristic variables inside the nozzle obtained according to the three flow configurations developed in this paper : two-phase flow at mechanical equilibrium ($p_L = p_V$ and $u_L = u_V$), at thermal equilibrium ($p_L = p_V$, $T_L = T_V$ and $u_L = u_V$) and at thermodynamic equilibrium ($p_L = p_V$, $T_L = T_V$, $g_L = g_V$ and $u_L = u_V$).
First a subsonic flow configuration is considered and obtained with the following external pressure $P_{out} = 9.95 \times 10^5 Pa$.
The associated results are represented in the Figure 2.7 and show the profiles of some characteristic variables : the velocity (m/s), the pressure ratio $\frac{P}{P_0}$, the liquid volume fraction, the liquid mass fraction and finally the temperature ratio $\frac{T}{T_0}$.
In this figure, one can first notice that the results related to the mechanical and thermal equilibrium assumptions are similar except for the temperature ratio graph. In this one the mixture temperature obtained when the two-phase flow is in thermal equilibrium is close to the liquid phase temperature obtained with a mechanical equilibrium assumption. Besides, in this last configuration the vapour temperature is obviously different from the liquid one. When mass transfer is enabled (two-phase flow at thermodynamic equilibrium) it can also be noticed that the corresponding profiles are far from the others. In particular the pressure and temperature drops are higher when mass exchanges are present.
A supersonic flow configuration is now addressed with the following external pressure $p_{out} = 10^2 Pa$.
The results showing the profiles of the same preceding flow variables are represented in the Figure 2.8. Again the results related to the mechanical and thermal equilibrium assumptions are very similar except for temperatures. When the two-phase flow is in thermodynamic equilibrium the resulting vapour appearance throughout the nozzle leads to a stronger acceleration in the divergent as well as a lesser pressure drop at the outlet.

2.6 Conclusion

References nozzle flow solution for various limit models of two-phase flows have been derived. Using the one-dimensional ideal gas nozzle steady flow solution as a base, these different solutions, ranging from mechanical equilibrium to thermodynamic equilibrium, have shown different complex and non-intuitive behaviours.
The resulting solutions can be used in several aims, from engineering systems to benchmark for computer code. The various solutions highlight the importance of relaxation effects between phases.

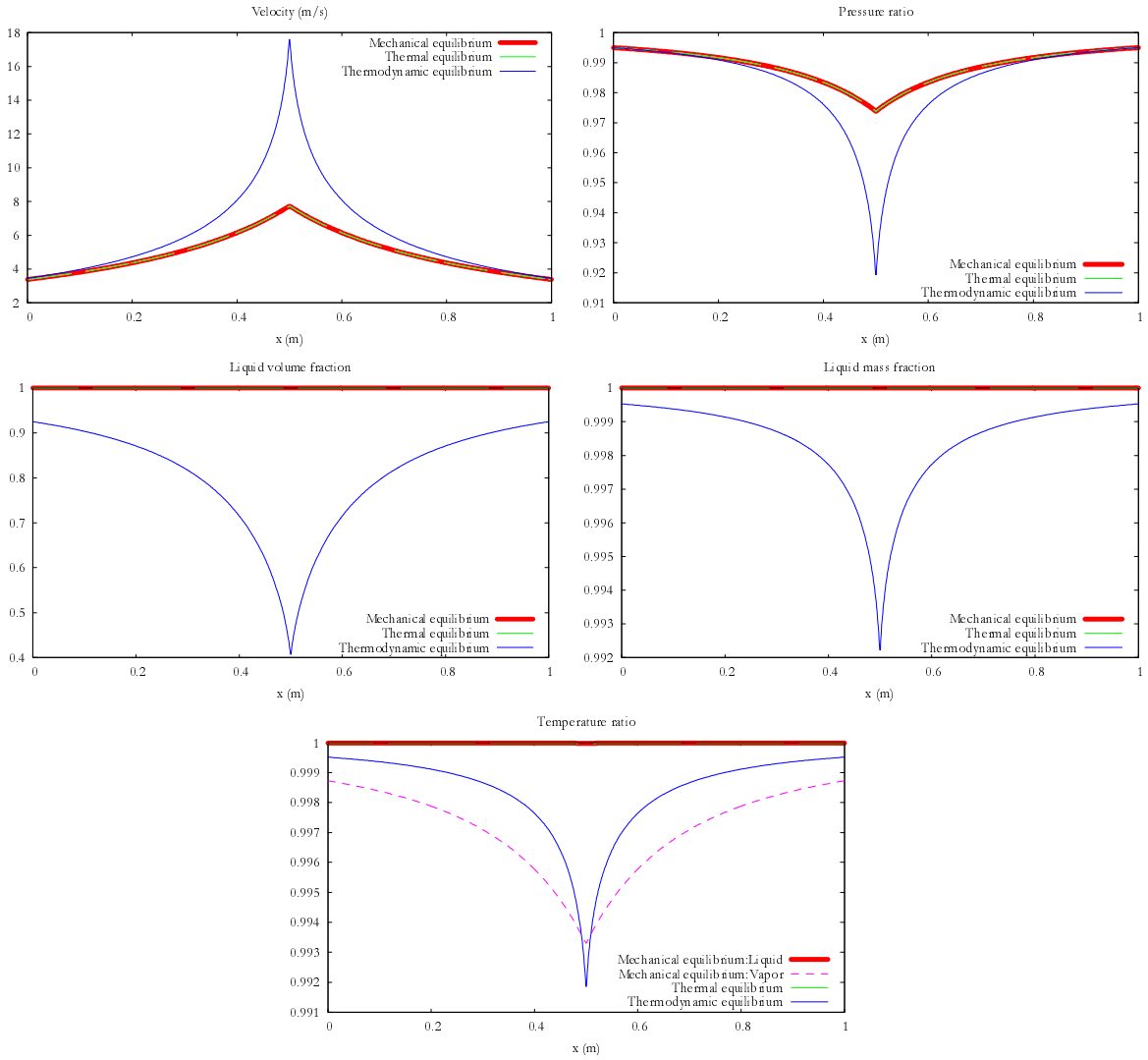

FIGURE 2.7 – Exact profiles of some characteristic flow variables inside the nozzle in function of x : subsonic configuration.

Acknowledgements The first author has been partly supported by CNES and and SAFRAN Snecma, space Engines Division. S. Petitot and P. Boivin are gratefully acknowledged. The authors would like to acknowledge fruitful discussion and works with Dr. F. Petitpas and Prof. B. Nkonga.

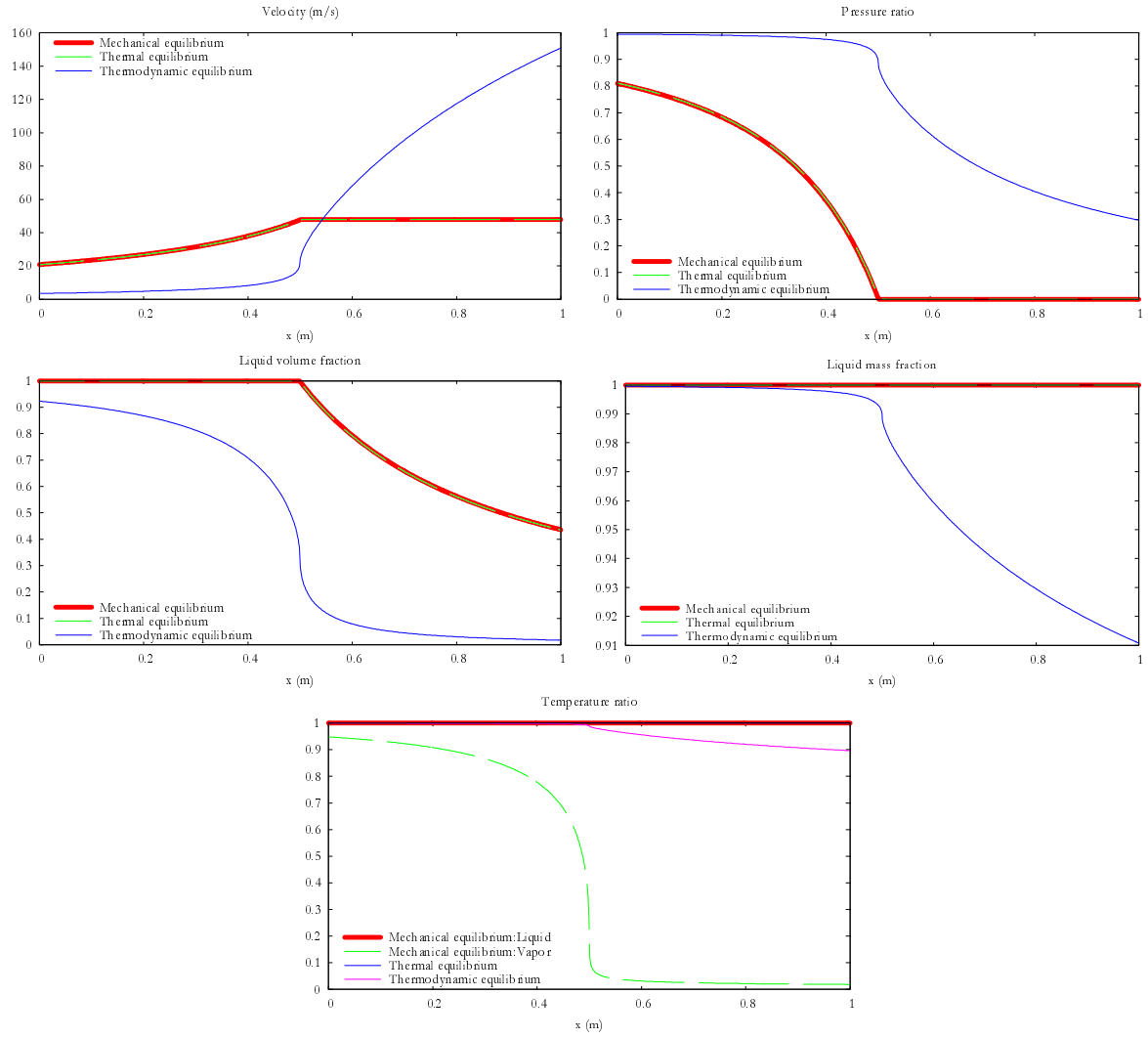

FIGURE 2.8 – Exact profiles of some characteristic flow variables inside the nozzle in function of x : supersonic configuration

Chapitre 3

Simulation numérique de l'ébullition

Avant-propos

Le modèle de base d'écoulement capable de traiter des écoulements diphasiques avec et sans transfert de masse ainsi qu'une méthode permettant de résoudre ce modèle et ce, indépendamment des nombres de Mach mis en jeu, ont été développés dans les chapitres précédents.
Ainsi, le but principal de ces travaux étant la simulation numérique de l'ébullition, l'étape suivante est l'intégration des phénomènes physiques présents lors de l'ébullition. Ainsi, ce chapitre est consacré à la prise en compte de ces différents phénomènes physiques tels que la capillarité, la gravité, la conduction de la chaleur ou encore le changement de phase. Il est important de comprendre chacun d'eux afin de rechercher et d'utiliser une formulation en adéquation avec le type de modèle préconisé jusqu'à présent.
De plus, d'un point de vue numérique, il est nécessaire d'étudier l'extension du schéma numérique implicite présentée dans le Chapitre 1 aux écoulements bouillants ainsi que de la méthode de préconditionnement diphasique pour les écoulements à faible nombres de Mach.

De même que précédemment, la validation de cette approche est un point essentiel de ce chapitre. Les aspects thermiques et changement de phase seront validés au travers d'une comparaison avec une solution exacte 1D de front d'évaporation, inspirée des solutions exactes de fronts de flamme quasi-isobares. La prise en compte de la tension de surface, quant à elle, sera validée à l'aide d'un test statique permettant de vérifier la loi de Laplace sur une bulle de vapeur. Enfin, des exemples multi-dimensionnels d'écoulements à bulles, où tous les effets physiques sont activés, sont présentés.

3.1 Introduction

This paper deals with the numerical simulation of boiling flows with a DNS-like approach (Direct Numerical Simulation). This research topic has important applications in nuclear and space engineering for example, as it is important to determine heat exchanges

in boiling flows. Existing heat and mass exchange correlations widely used in averaged multiphase flow models and codes have important limitations. The error bar covers several orders of magnitude. Flow topology changes, from bubbly flows to separated flows with vapor film at walls, have dramatic consequences on heat exchanges. The main issue relies on the fact that averaged two-phase flow models are unable to account for flow topology changes. Therefore, DNS-like of boiling flows may help for the derivation of subscale models. However, this research area is difficult as liquid-gas interfaces are present, in conjunction with heat conduction, phase transition and surface tension effects. Only a few numerical approaches deal with such flows, the most natural being due to Tryggvason and coworkers [81],[46] where the interface is considered as a sharp discontinuity, solved with a front tracking algorithm during time evolution. The other approaches consider the interface as a diffuse zone. With diffuse interface models, two different kinds of approaches have to be mentioned.
The first one takes essence in chemical-physics and in the pioneer work of Cahn and Hilliard [18], also called in the literature "second gradient theory" and "theory of Korteweg-type fluids". This theory works quite well in the vicinity of the thermodynamic critical point where liquid and vapor density become very close. The fluid density is considered as the order parameter and the fluid internal energy is considered as a function of the density and the density gradient. Considerable efforts have been done in this modeling direction (see [3] for example). Examples of computational works in this frame are reported in this last reference and in [45]. In addition to the very limited density ratio at interfaces, another limitation appears. The interface capillary structure has to be resolved, which results in very fine meshes and associated computational limitations.
The second diffuse interface approach takes essence in discontinuity capturing methods and particularly Godunov contributions. In this frame, discontinuities are captured as a consequence of conservative formulation of the equations. There is no need to resolve the internal structure of discontinuities as jump conditions are involved in the formulation. This approach has been competing with front tracking methods during the 70s, with artificial viscosity methods during the 80s, and is now used in nearly all computational codes dealing with gas dynamics equations and more generally with hyperbolic systems of conservation laws. The present work belongs to this class of approach.
The diffuse interface approach based on a multiphase description of mixture cells, with the help of hyperbolic systems with relaxation is due to [70]. This approach has shown its efficiency for the computation of flows in severe conditions, with arbitrarily high pressure and density ratios, with applications ranging from detonation physics [66], shock waves in heterogeneous materials, cavitating flows [66] to solid mechanics [29]. Therefore, this approach is very robust, accurate and versatile. The difficulties are related to the models and numerical schemes building, especially when non-conservative equations are present. Here, the model under consideration is conservative, but the building of an implicit preconditioned scheme is needed to guarantee solution accuracy in low Mach number regions. An adaptation of the LeMartelot et al. [53] method will be detailed.
The first issue addressed in the present paper deals with the diffuse interface model derivation. The derivation is made gradually. Surface tension, gravity, heat conduction and chemical relaxation are omitted and the basic flow model in temperature and pressure equilibrium

is derived. It corresponds to a reduction of the Saurel et al. [73] model, where heat exchange is considered as a stiff relaxation process. This last model is an extension of the mechanical equilibrium model of Kapila et al. [47] in the presence of heat and mass transfers. These models enter in the class of diffuse interface models in the sense that they are able to fulfill interface conditions of simple contact with the Kapila et al. [47] version, and evaporating interfaces with the Saurel et al. [73] version. With these approaches, the same equations are solved everywhere, with the same hyperbolic flow solver, and the interface is captured routinely, like the various discontinuities present in gas dynamics. Relaxation solvers like, for example, pressure, temperature and Gibbs free energy relaxation solvers are used to force appropriate interface conditions. Example of pressure relaxation solver is given in [74] while pressure-temperature-Gibbs free energy solver examples are given in [73] and [53].This last version corresponds to a thermodynamic equilibrium solver with a liquid-phase mixture.
The reduced model considered in the present paper is thus a temperature equilibrium version of the model derived in [73]. This reduction is justified as, to model phase change, conductive heat transfer is needed. As a consequence there is no temperature discontinuity (in the form of DNS like approach) at the interface and a single temperature model is appropriate. To be more precise, the Kapila et al. [47] model involves two temperatures and is well suited for interfaces computations as temperature and entropy discontinuities are present when the interface separates two non-miscible fluids, such as for example liquid water and air. When heat conduction is present, the temperature becomes continuous and a single temperature model is more appropriate. Indeed, the conduction layer has to be solved with the present approach, similarly as flame computations. The temperature equilibrium model involves four partial differential equations only, is hyperbolic and conservative. Gibbs free energy relaxation terms are considered, in agreement with the second law of thermodynamics.
The model is reminiscent of the reactive Euler equations, widely used in combustion modeling. The main difference appears in the fact that each phase occupies its own volume, contrarily to gas mixtures, where each gas component occupies the entire volume. This difference has serious consequences regarding the thermodynamic closure. For gas mixtures, the mixture equation of state derives of the Dalton law. Here, it is derived from the mixture energy definition, temperature and pressure equilibrium conditions. Another consequence is related to sound propagation that may be very slow in such equilibrium mixtures.
From the basic temperature equilibrium flow model with four equations, extra physics is added to deal with boiling flows. Surface tension effects are modeled with the Brackbill et al.[16] method, already considered in the context of compressible fluids by [64]. Heat conduction and gravity effects are also added. The second issue addressed in the paper is related to the numerical approximation of the flow model that contains difficulties related to the hyperbolic and elliptic parts as well as capillary terms and thermochemical relaxation.
The hyperbolic step is solved with a variant of the preconditioned implicit hyperbolic solver detailed in [53]. It is an extension of the Guillard and Viozat [38] method for low Mach number flows, this method being itself a conservative and time accurate extension of the Turkel [82] preconditioning algorithm. The relaxation solver used to fulfill interface conditions of evaporating interfaces is recalled. The hyperbolic and relaxation solvers are then combined to solve the flow model in 1D, obviously in absence of capillary effects, to check model

and method convergence against an exact solution of sharp evaporating interface. Convergence being reached in 1D, computational boiling flows examples are shown in 2D with the various needed physical effects. A 2D configuration with several bubbles is considered and computed. A new physical feature appears, never reported before in the authors knowledge. Starting from an initial situation where some nucleation sites are present, bubbles appear dynamically from the location where these sites were initially present, but also from other locations where perfect wall conditions are used. The appearance and size selections of the bubbles near the wall thus appear as a self sustained process that doesn't need nucleation sites, except at the very beginning.

3.2 Model building

The starting point of the analysis relies on the mechanical equilibrium, temperatures non-equilibrium flow model of Kapila et al. [47], where heat and mass exchanges have been inserted [73].

3.2.1 Out of equilibrium model

Saurel et al [73] model describes two-phase mixtures out of equilibrium regarding temperatures and Gibbs free energies in the presence of heat and mass exchanges. It reads :

$$
\begin{aligned}
&\frac{\partial \alpha_1}{\partial t} + \mathbf{u}\cdot\mathbf{grad}\,(\alpha_1) = \frac{\rho_2 c_2^2 - \rho_1 c_1^2}{\frac{\rho_1 c_1^2}{\alpha_1} + \frac{\rho_2 c_2^2}{\alpha_2}} div\,(\mathbf{u}) + \rho\nu(g_2 - g_1)\frac{\frac{c_1^2}{\alpha_1} + \frac{c_2^2}{\alpha_2}}{\frac{\rho_1 c_1^2}{\alpha_1} + \frac{\rho_2 c_2^2}{\alpha_2}} + \frac{(\frac{\Gamma_1}{\alpha_1} + \frac{\Gamma_2}{\alpha_2})}{\frac{\rho_1 c_1^2}{\alpha_1} + \frac{\rho_2 c_2^2}{\alpha_2}} H(T_2 - T_1)\\
&\frac{\partial \alpha_1\rho_1}{\partial t} + div\,(\alpha_1\rho_1\mathbf{u}) = \rho\nu(g_2 - g_1)\\
&\frac{\partial \alpha_2\rho_2}{\partial t} + div\,(\alpha_2\rho_2\mathbf{u}) = -\rho\nu(g_2 - g_1)\\
&\frac{\partial \rho\mathbf{u}}{\partial t} + div\left(\rho\mathbf{u}\otimes\mathbf{u} + P\underline{\underline{I}}\right) = 0\\
&\frac{\partial \rho E}{\partial t} + div\,((\rho E + P)\mathbf{u}) = 0
\end{aligned}
\tag{3.1}
$$

The total energy is defined as $E = Y_1 e_1 + Y_2 e_2 + \frac{1}{2}\mathbf{u}\cdot\mathbf{u}$ where $Y_k = \dfrac{\alpha_k\rho_k}{\rho}$ represent the mass fractions and $\rho = \sum_k (\alpha_k\rho_k)$ the mixture density. This model is hyperbolic with the same wave speeds as the gas dynamics equations but with the Wood [87] sound speed, which presents a non monotonic behaviour with respect to the volume fractions (α_k) :

$$
\frac{1}{\rho c_w^2} = \sum_k \frac{\alpha_k}{\rho_k c_k^2} \tag{3.2}
$$

It is worth to mention that the sound speed is defined in all space of variables, contrarily to models based on cubic equations of state, like the Van der Waals type. The equation of state providing the thermodynamic closure is obtained from the mixture energy definition and the pressure equilibrium condition. This equation of state involves at least three arguments : $p = p(\rho, e, \alpha_1)$. For example, when each phase obeys the stiffened gas equation of state (see [52] for parameters determination),

$$p_k = (\gamma_k - 1)\rho_k(e_k - q_k) - \gamma P_{\infty,k}, \tag{3.3}$$

the mixture equation of state then reads,

$$P(\rho, e, \alpha_1) = \frac{\rho e - (\dfrac{\alpha_1\gamma_1 P_{\infty,1}}{\gamma_1 - 1} + \dfrac{\alpha_2\gamma_2 P_{\infty,2}}{\gamma_2 - 1})}{\dfrac{\alpha_1}{\gamma_1 - 1} + \dfrac{\alpha_2}{\gamma_2 - 1}} \tag{3.4}$$

Parameters q_k, γ_k and $P_{\infty,k}$ are characteristic constants of material k. When dealing with phase transition applications, their determination is based on the saturation curves of the phase diagram. As this model involves a single pressure but two mass equations and a volume fraction equation, it is possible to determine two temperatures ($T_k = T_k(P, \rho_k)$) and two entropies. This last feature is useful for phase transition modelling. The mixture entropy equation reads,

$$\frac{\partial \rho S}{\partial t} + div\,(\rho S \mathbf{u}) = \frac{H(T_2 - T_1)^2}{\rho} + \nu\frac{\rho(g_2 - g_1)^2}{T_I} \tag{3.5}$$

where T_I represents the "interface temperature" defined as $T_I = \dfrac{\dfrac{\Gamma_1 T_1}{\alpha_1} + \dfrac{\Gamma_2 T_2}{\alpha_2}}{\dfrac{\Gamma_1}{\alpha_1} + \dfrac{\Gamma_2}{\alpha_2}}$, showing agreement with the second law of thermodynamics. Some comments are due regarding the volume fraction equation. The first term in the right hand side, present in the Kapila [47] model, represents mechanical relaxation effects, present in all zones where the velocity divergence is non zero (shocks, compressions, expansions). The second term represents volume variations due to mass transfer, in a context where both phases are compressible. The last group of terms represents dilatation effects due to heat transfer. Γ_k represents the Grüneisen coefficient of phase k.

System (3.1) being non conservative, non conventional shock relations have to be determined. Appropriate set of jump conditions is given in [71]. Heat and mass transfer in System (3.1) are considered as kinetic processes, controlled respectively by relaxation rates H and ν. The Gibbs free energies are denoted by $g_k = h_k - T_k s_k$.

The degrees of freedom with this modeling are related to the relaxation rates H and ν . When the fluids in contact at an interface are non miscible (liquid water and air for example), H and ν are set to zero, and the correct jump conditions of equal normal velocities and pressure are recovered. Computational examples and comparisons with exact solutions are given in [74]. When phase transition occurs at the interface between a liquid and its

vapour, provided that one of the phase is metastable (overheated), local thermodynamic equilibrium is assumed, meaning that phase transition occurs infinitely fast (infinite H and ν). As relaxation parameters are set infinite locally only, phase transition fronts propagating at global finite rate [73] are correctly reproduced, at least for flashing flow situations. To remove the difficulty related to the resolution of stiff differential systems, relaxation solvers have been built in the same reference and in [53].
This model is thus able to deal with interfaces of simple contact, when heat and mass transfers are removed and evaporating (or condensing) interfaces at local thermodynamic equilibrium when heat and mass relaxation coefficients are taken infinite. To illustrate model's capabilities, Figure 3.1 shows a computational example of cavitating underwater rocket involving these two kinds of interfaces.

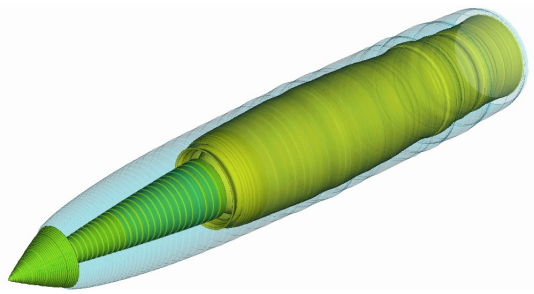

FIGURE 3.1 – Cavitating flow around a hypervelocity underwater rocket. Combustion gases issued from a rocket motor are shown in yellow contours and are in contact with vapour, in blue colour. The vapour is separated from the liquid (not shown) by an evaporating interface. Two different types of interfaces are thus present in this example. These results are issued of [66].

The present paper being focused on boiling flow modeling, immiscible fluids and interfaces of simple contact are out of interest. Moreover, as it is mandatory to consider heat diffusion when dealing with boiling flow, a unique temperature will be present at interfaces. Therefore, the flow model (3.1) can be reduced.

3.2.2 Temperature equilibrium model

In the limit of stiff temperature relaxation (infinite H), System (3.1) reduces to :

$$\begin{aligned}
&\frac{\partial \rho}{\partial t} + div\left(\rho \mathbf{u}\right) = 0 \\
&\frac{\partial \rho \mathbf{u}}{\partial t} + div\left(\rho \mathbf{u} \otimes \mathbf{u} + P\underline{\underline{I}}\right) = 0 \\
&\frac{\partial \rho E}{\partial t} + div\left((\rho E + P)\mathbf{u}\right) = 0 \\
&\frac{\partial \rho Y_1}{\partial t} + div\left(\rho Y_1 \mathbf{u}\right) = \rho\nu(g_2 - g_1)
\end{aligned} \tag{3.6}$$

The total energy is still defined by $E = Y_1 e_1 + Y_2 e_2 + \frac{1}{2}\mathbf{u}\cdot\mathbf{u}$. Formally, System (3.6) is reminiscent of the reactive Euler equations, widely used in combustion modeling. However a fundamental difference appears regarding the thermodynamic closure. In combustion modeling, mixtures of gases are considered and the Dalton law is used to compute the pressure. Dalton law states that each constituent occupies the entire volume. This is not the case with two-phase mixtures where the fluids are separated by an interface, each one of them occupying its own volume. To determine the thermodynamical closure of System (3.6), let's first consider the mixture specific volume definition,

$$v = Y_1 v_1 + Y_2 v_2, \tag{3.7}$$

With the help of the caloric equation of state for a given phase,

$$e_k = C_{v,k} T + \frac{P_{\infty,k}}{\rho_k} + q_k \tag{3.8}$$

the SG EOS (3.3) becomes,

$$p_k = (\gamma_k - 1)\rho_k C_{v,k} T - P_{\infty,k}, \tag{3.9}$$

and the specific volume for a given phase can be expressed as :

$$v_k = \frac{(\gamma_k - 1) C_{v,k} T}{P + P_{\infty,k}} \tag{3.10}$$

A first relation resulting of (3.7) and (3.10) is the obtained, linking the temperature, the pressure and the mixture specific volume :

$$\frac{1}{T} = \frac{Y_1(\gamma_1 - 1)C_{v,1}}{v(P + P_{\infty,1})} + \frac{Y_2(\gamma_2 - 1)C_{v,2}}{v(P + P_{\infty,2})} \tag{3.11}$$

We now consider the mixture energy definition,

$$e = Y_1 e_1 + Y_2 e_2, \tag{3.12}$$

Combining (3.8) and (3.10), the specific internal energy for a given phase reads :

$$e_k = C_{v,k} T \frac{P + \gamma_k P_{\infty,k}}{P + P_{\infty,k}} + q_k \tag{3.13}$$

The mixture energy definition (3.12) becomes :

$$\frac{1}{T} = \frac{Y_1 C_{v,1} + \dfrac{Y_1(\gamma_1 - 1)C_{v,1}P_{\infty,1}}{P + P_{\infty,1}} + Y_2 C_{v,2} + \dfrac{Y_2(\gamma_2 - 1)C_{v,2}P_{\infty,2}}{P + P_{\infty,2}}}{e - (Y_1 q_1 + Y_2 q_2)} \tag{3.14}$$

Combining relations (3.11) and (3.14), the following equation linking the pressure, the mixture specific volume and mixture energy and the mass fractions is obtained :

$$\rho\left[\frac{Y_1(\gamma_1-1)C_{v,1}}{P+P_{\infty,1}}+\frac{Y_2(\gamma_2-1)C_{v,2}}{P+P_{\infty,2}}\right]=\frac{Y_1C_{v,1}+\frac{Y_1(\gamma_1-1)C_{v,1}P_{\infty,1}}{P+P_{\infty,1}}+Y_2C_{v,2}+\frac{Y_2(\gamma_2-1)C_{v,2}P_{\infty,2}}{P+P_{\infty,2}}}{e-(Y_1q_1+Y_2q_2)} \tag{3.15}$$

It corresponds to a quadratic function of the pressure. The positive root is given by :

$$p=\frac{1}{2}\left(A_1+A_2-(P_{\infty,1}+P_{\infty,2})\right)+\sqrt{\frac{1}{4}\left(A_2-A_1-(P_{\infty,2}-P_{\infty,1})\right)^2+A_1A_2} \tag{3.16}$$

Where $A_k=\dfrac{Y_k\left(\gamma_k-1\right)C_{v,k}}{Y_1C_{v,1}+Y_2C_{v,2}}\left(\rho(e-q)-P_{\infty,k}\right)$. The mixture energy entropy equation associated with System (3.6) and present thermodynamic closure reads :

$$\frac{\partial\rho S}{\partial t}+div\left(\rho S\mathbf{u}\right)=\frac{\rho\nu(g_2-g_1)^2}{T} \tag{3.17}$$

3.2.3 Hyperbolicity and sound speed

System (3.6) is hyperbolic with three wave speeds, $\lambda_0=u$ (two times fold), $\lambda_1=u+c$ and $\lambda_2=u-c$ with the following square sound speed :

$$c^2=\frac{1}{2}\left(\begin{array}{l}(e-q)(a_1+a_2)+\dfrac{\frac{1}{2}\left(\frac{\partial R_1}{\partial\rho}\right)_e R_1+\left(\frac{\partial R_2}{\partial\rho}\right)_e}{\sqrt{\frac{1}{4}R_1R_1+R_2}}\\ \\ +\dfrac{P}{\rho^2}\left(\rho(a1+a2)+\dfrac{\frac{1}{2}\left(\frac{\partial R_1}{\partial e}\right)_\rho R_1+\left(\frac{\partial R_2}{\partial e}\right)_\rho}{\sqrt{\frac{1}{4}R_1R_1+R_2}}\right)\end{array}\right) \tag{3.18}$$

Where,

$a_1=\dfrac{Y_1(\gamma_1-1)C_{v,1}}{Y_1C_{v,1}+Y_2C_{v,2}}$, $a_2=\dfrac{Y_2(\gamma_2-1)C_{v,2}}{Y_1C_{v,1}+Y_2C_{v,2}}$,

$R_1=a_2\rho(e-q)-a_2P_{\infty,2}-a_1\rho(e-q)+a_1P_{\infty,1}-P_{\infty,2}+P_{\infty,1}$,

$R_2=a_1a_2(\rho(e-q)-P_{\infty,1})(\rho(e-q)-P_{\infty,2})$.

This sound speed can be compared to the Wood's sound speed (3.2). As Wood's sound speed deals with multiphase mixtures in mechanical equilibrium but out of thermal equilibrium, it should be always greater than the sound speed corresponding to multiphase mixtures in mechanical and thermal equilibrium. This behavior is illustrated in Figure (3.2).

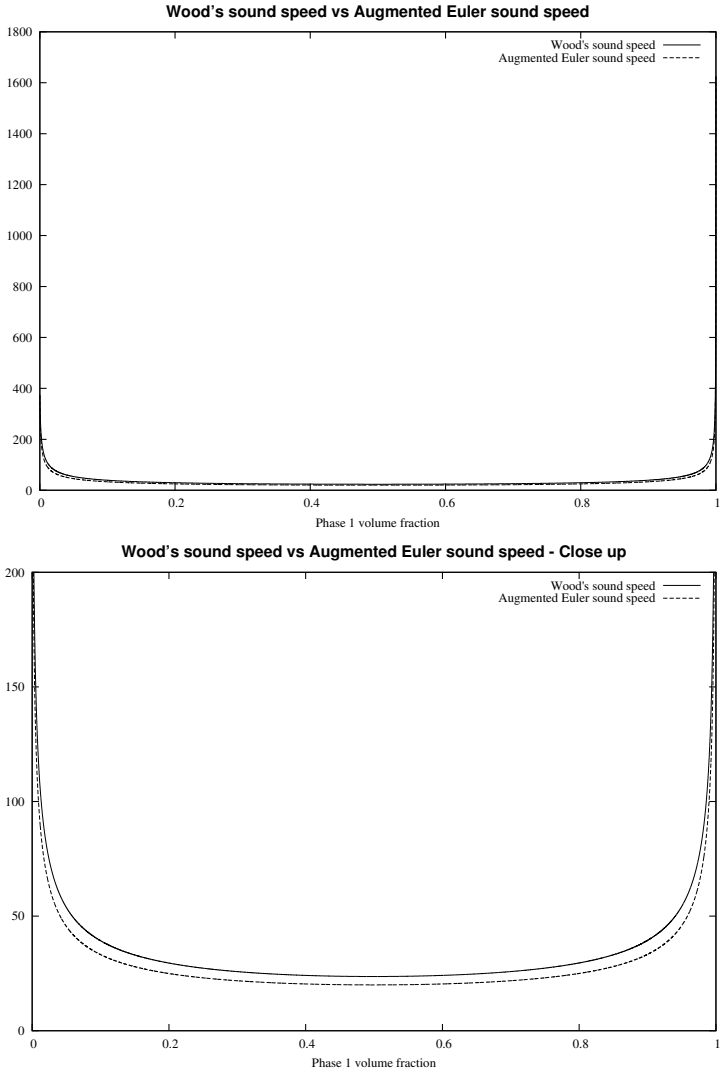

FIGURE 3.2 – The sound speed of System (3.6) given by (3.18) is compared to the Wood sound speed (3.2). Full view and close up.

3.3 Extra physics modeling

To deal with DNS of boiling flows, System (3.6) has to be complemented with extra physical effects, such as :
- buoyancy,
- surface tension,
- heat conduction,
- phase transition.

This list can be completed by extra effects, as for example, viscous ones, but we prefer to focus on those which are absolutely necessary. Modeling of the various effects is addressed

gradually hereafter.

3.3.1 Surface and body forces

Surface tension effects are considered through the Continuum Surface Force (CSF) method of Brackbill [16]. The capillary force is modeled as,

$$\mathbf{F}_\sigma = \sigma\kappa\overrightarrow{\bigtriangledown C} \tag{3.19}$$

where σ represents the surface tension coefficient ($N.m^{-1}$), κ represents the local curvature (m^{-1}) and C is a color function whose goal is to locate the interface between the two phases and to compute the local curvature,

$$\kappa = -div\left(\frac{\overrightarrow{\bigtriangledown C}}{|\overrightarrow{\bigtriangledown C}|}\right). \tag{3.20}$$

In this paper, the chosen color function is the mass fraction of phase 1, Y_1, as this variable is invariant across shock and expansion waves. It varies at interfaces only.
The gravity force is modeled as :

$$\mathbf{F}_g = \rho\mathbf{g}$$

Where $\mathbf{g}$ represents gravity field.
Therefore, the non-conservative formulation of System (3.6), without phase transition, including body and surface forces reads :

$$\begin{aligned}
&\frac{\partial \rho Y_1}{\partial t} + div\left(\rho Y_1 \mathbf{u}\right) = 0\\
&\frac{\partial \rho}{\partial t} + div\left(\rho \mathbf{u}\right) = 0\\
&\frac{\partial \rho \mathbf{u}}{\partial t} + div\left(\rho \mathbf{u}\otimes\mathbf{u} + P\underline{\underline{I}}\right) = \sigma\kappa\overrightarrow{\bigtriangledown Y_1} + \rho\mathbf{g}\\
&\frac{\partial \rho E}{\partial t} + div\left((\rho E + P)\mathbf{u}\right) = \sigma\kappa\overrightarrow{\bigtriangledown Y_1}\cdot\mathbf{u} + \rho\mathbf{g}\cdot\mathbf{u}
\end{aligned} \tag{3.21}$$

For the sake of simplicity, Gibbs energy relaxation effects have been removed.
A conservative formulation of System (3.21) can be derived [64] :

$$\begin{aligned}
&\frac{\partial \rho Y_1}{\partial t} + div\left(\rho Y_1 \mathbf{u}\right) = 0\\
&\frac{\partial \rho}{\partial t} + div\left(\rho \mathbf{u}\right) = 0\\
&\frac{\partial \rho \mathbf{u}}{\partial t} + div\left(\rho \mathbf{u}\otimes\mathbf{u} + P\underline{\underline{I}} - \sigma\left(|\mathbf{m}|\underline{\underline{I}} - \frac{\mathbf{m}\otimes\mathbf{m}}{|\mathbf{m}|}\right)\right) = \rho\mathbf{g}\\
&\frac{\partial \rho E + \sigma|\mathbf{m}|}{\partial t} + div\left(\left(\rho E + P + \sigma|\mathbf{m}|\right)\mathbf{u} - \sigma\left(|\mathbf{m}|\underline{\underline{I}} - \frac{\mathbf{m}\otimes\mathbf{m}}{|\mathbf{m}|}\right)\cdot\mathbf{u}\right) = \rho\mathbf{g}\cdot\mathbf{u}
\end{aligned} \tag{3.22}$$

Where $\mathbf{m} = \overrightarrow{\bigtriangledown Y_1}$

Combining the mixture energy, mixture momentum, mass equations and thanks to the Gibbs identity for each phase,

$$Tds_k = de_k + Pdv_k, \tag{3.23}$$

The mixture entropy equation is obtained :

$$\frac{\partial \rho S}{\partial t} + div(\rho S \mathbf{u}) = 0, \tag{3.24}$$

where $S = Y_1 s_1 + Y_2 s_2$.
Therefore, System (3.22) is thermodynamically consistent.

3.3.2 Heat conduction

To insert conductive effects in System (3.6) a two-phase flow model in total non-equilibrium is first considered :

$$\begin{aligned}
&\frac{\partial \alpha_1}{\partial t} + \mathbf{u}_1 \cdot \mathbf{grad}\,(\alpha_1) = \mu(p_1 - p_2)\\
&\frac{\partial \alpha_1\rho_1}{\partial t} + div\,(\alpha_1\rho_1\mathbf{u}_1) = 0\\
&\frac{\partial (\alpha\rho\mathbf{u})_1}{\partial t} + div\,(\alpha\rho\mathbf{u}\otimes\mathbf{u} + \alpha p)_1 = p_I\nabla\alpha_1 + \lambda(u_2 - u_1)\\
&\frac{\partial (\alpha\rho E)_1}{\partial t} + div\,(\alpha(\rho E + p)\mathbf{u} + \alpha\mathbf{q})_1 = (p_I u_I + \mathbf{q}_I)\nabla\alpha_1 + \lambda u_I'(u_2 - u_1) - \mu p_I'(p_1 - p_2) + H(T_2 - T_1)\\
&\frac{\partial \alpha_2\rho_2}{\partial t} + div\,(\alpha_2\rho_2\mathbf{u}_2) = 0\\
&\frac{\partial (\alpha\rho\mathbf{u})_2}{\partial t} + div\,(\alpha\rho\mathbf{u}\otimes\mathbf{u} + \alpha p)_2 = p_I\nabla\alpha_2 - \lambda(u_2 - u_1)\\
&\frac{\partial (\alpha\rho E)_2}{\partial t} + div\,(\alpha(\rho E + p)\mathbf{u} + \alpha\mathbf{q})_2 = (p_I u_I + \mathbf{q}_I)\nabla\alpha_2 - \lambda u_I'(u_2 - u_1) + \mu p_I'(p_1 - p_2) - H(T_2 - T_1)
\end{aligned} \tag{3.25}$$

The precise expressions for the interfacial variables p_I, u_I and heat flux $\mathbf{q}_I$ are useless as well as the precise expressions for the various relaxation parameters μ (pressure relaxation), λ (velocity relaxation) and H (temperature relaxation). Indeed, the limit model when these relaxation effects are stiff is under interest. In other words, an asymptotic analysis can be carried out in the limit of stiff mechanical and thermal relaxation :
For each flow variable f an asymptotic expansion, $f = f^0 + \epsilon f^1$ is considered. f^0 representing the equilibrium state and f^1 a small perturbation. Furthermore, each relaxation coefficient (μ,λ and H) is supposed stiff :

$$\mu = \frac{\mu_0}{\epsilon}, \lambda = \frac{\lambda_0}{\epsilon}, H = \frac{H_0}{\epsilon} \tag{3.26}$$

where $\epsilon \to 0$

In this limit, the leading order system corresponds to the extension of System (3.6) to heat conduction effects :

$$\begin{aligned}
&\frac{\partial \rho Y_1}{\partial t} + div\left(\rho Y_1 \mathbf{u}\right) = 0 \\
&\frac{\partial \rho}{\partial t} + div\left(\rho \mathbf{u}\right) = 0 \\
&\frac{\partial \rho \mathbf{u}}{\partial t} + div\left(\rho \mathbf{u} \otimes \mathbf{u} + P\right) = 0 \\
&\frac{\partial \rho E}{\partial t} + div\left((\rho E + P)\mathbf{u}\right) + div\left(\mathbf{q}\right) = 0
\end{aligned} \tag{3.27}$$

Where $\mathbf{q} = -\lambda_c \overrightarrow{\bigtriangledown T}$ and $\lambda_c = \alpha_1\lambda_1 + \alpha_2\lambda_2$. λ_c represents the mixture thermal conductivity determined from the asymptotic analysis. λ_k represents the thermal conductivity of phase k and T the temperature.

3.3.3 Phase transition

The present diffuse interface approach summarized by System (3.6) corresponds to a multiphase description of a flow mixture evolving in mechanical and thermal equilibrium but out of thermodynamical equilibrium. This model is developed to be used in mixture cells at evaporating interfaces, separating a liquid and its vapour. Therefore, the first point to precise is the interfacial zone detection criterion. An interface is supposed to be present if the mass fractions product is greater than a certain tolerance ($Y_1Y_2 > \epsilon$). Then, in this mixture zone, the goal is to mimic sharp interfaces jump conditions. As the local thermodynamic assumption is assumed valid for most situations of evaporating interfaces, locally the condition,

$$g_1)_I = g_2)_I \tag{3.28}$$

has to be fulfilled. In conjunction with the mechanical and thermal equilibrium conditions of flow model (3.6), local thermodynamical equilibrium is reached as soon as stiff Gibbs free energy relaxation is considered. It means that the Gibbs free energy relaxation coefficient ν is considered as tending to infinity in the interfacial mixture zone, and is considered zero outside, in pure fluid zone. As mentioned in [73], this approach means that in the interfacial zone, the mixture Euler equations are solved (mixture mass, mixture momentum and mixture energy equations), with the following definitions :

$$\begin{aligned}
&\rho = \alpha_1\rho_1 + \alpha_2\rho_2 \text{ or alternatively } v = \frac{1}{\rho} = Y_1v_1 + Y_2v_2, \\
&e = Y_1e_1 + Y_2e_2, \\
&T_1 = T_2 = T, \\
&p_1 = p_2 = P, \\
&g_1 = g_2.
\end{aligned} \tag{3.29}$$

In order to avoid numerical issues related to time integration of stiff differential equations, when ν (appearing in System 3.6) tends to infinity, the thermodynamical equilibrium state

of (3.29) is determined by the method that follows.

The specific volumes and the internal energies of each phase are expressed as functions of the pressure and temperature by (3.10) and (3.13). Each parameter involved in these expressions $(\gamma_k, C_{v,k}, P_{\infty,k}, q_k)$ is calculated in order to fit the liquid-vapor phase diagram, more precisely the corresponding saturation curves. Details regarding the EOS parameters determination are given in [52] and [73].
Denoting the relaxed state solution of System (3.29) by the superscript '*', the mass conservation constraint becomes,

$$v_0 = Y_1^* v_1^*(P^*) + Y_2^* v_2^*(P^*) = Y_1^* v_1^*(P^*) + (1 - Y_1^*) v_2^*(P^*), \tag{3.30}$$

where $v_k^*(P^*) = v_k(P^*, T^*)$.
Constraints of pressures, temperatures and Gibbs free energies result in,

$$T^*(P^*) = T_{sat}(P^*). \tag{3.31}$$

Therefore, $v_1^*(P^*)$ and $v_2^*(P^*)$, the specific volumes become function of the pressure only. A first relation linking the liquid mass fraction and the pressure is thus obtained,

$$Y_1^* = \frac{v_2^*(P^*) - v_0}{v_2^*(P^*) - v_1^*(P^*)}. \tag{3.32}$$

As the kinetic energy is constant, the mixture total energy definition reads :

$$e_0 = Y_1^* e_1^*(P^*) + Y_2^* e_2^*(P^*) = Y_1^* e_1^*(P^*) + (1 - Y_1^*) e_2^*(P^*) \tag{3.33}$$

A second relation linking the liquid mass fraction and the pressure is thus obtained,

$$Y_1^* = \frac{e_0 - e_2^*(P^*)}{e_1^*(p^*) - e_2^*(P^*)}. \tag{3.34}$$

This relation can be also expressed as a function of the specific enthalpies of the phases,

$$Y_1^* = \frac{h_2^*(P^*) - (e_0 - P^* v_0)}{h_2^*(P^*) - h_1^*(P^*)}. \tag{3.35}$$

Where h_1 and h_2 are linked by $h_2^*(P^*) - h_1^*(P^*) = L_v(P^*)$, $L_v(P^*)$ representing the latent heat of vaporization, which is a function of the pressure.
From the previous mass fraction equations, a single function of the pressure is obtained,

$$\frac{h_2^*(P^*) - (e_0 - P^* v_0)}{h_2^*(P^*) - h_1^*(P^*)} - \frac{v_2^*(P^*) - v_0}{v_2^*(P^*) - v_1^*(P^*)} = 0. \tag{3.36}$$

Its solution is computed with the Newton method. Once the relaxed pressure is determined, the remaining variables are easily computed with the preceding thermodynamic relations.

3.3.4 The general model

Adding the extra effects detailed in the previous sections, the following general model is obtained :

$$\begin{aligned}
&\frac{\partial \rho Y_1}{\partial t} + div\left(\rho Y_1 \mathbf{u}\right) = \rho\nu(g_2 - g_1) \\
&\frac{\partial \rho}{\partial t} + div\left(\rho \mathbf{u}\right) = 0 \\
&\frac{\partial \rho \mathbf{u}}{\partial t} + div\left(\rho \mathbf{u} \otimes \mathbf{u} + P\underline{\underline{I}}\right) = \sigma\kappa\overrightarrow{\bigtriangledown Y_1} + \rho\mathbf{g} \\
&\frac{\partial \rho E}{\partial t} + div\left((\rho E + P)\mathbf{u}\right) = div\left(\lambda_c \overrightarrow{\bigtriangledown T}\right) + \sigma\kappa\overrightarrow{\bigtriangledown Y_1} \cdot \mathbf{u} + \rho\mathbf{g} \cdot \mathbf{u}
\end{aligned} \tag{3.37}$$

A conservative form is available :

$$\begin{aligned}
&\frac{\partial \rho Y_1}{\partial t} + div\left(\rho Y_1 \mathbf{u}\right) = \rho\nu(g_2 - g_1) \\
&\frac{\partial \rho}{\partial t} + div\left(\rho \mathbf{u}\right) = 0 \\
&\frac{\partial \rho \mathbf{u}}{\partial t} + div\left(\rho \mathbf{u} \otimes \mathbf{u} + P\underline{\underline{I}} - \sigma\left(|\mathbf{m}|\underline{\underline{I}} - \frac{\mathbf{m} \otimes \mathbf{m}}{|\mathbf{m}|}\right)\right) = \rho\mathbf{g} \\
&\frac{\partial \rho E + \sigma|\mathbf{m}|}{\partial t} + div\left(\left(\rho E + P + \sigma|\mathbf{m}|\right)\mathbf{u} - \sigma\left(|\mathbf{m}|\underline{\underline{I}} - \frac{\mathbf{m} \otimes \mathbf{m}}{|\mathbf{m}|}\right) \cdot \mathbf{u} - \lambda_c \overrightarrow{\bigtriangledown T}\right) = \rho\mathbf{g} \cdot \mathbf{u}
\end{aligned} \tag{3.38}$$

The Gibbs energy relaxation effects are solved with the method given in Section 3.3.3 at interfaces only :

$$\begin{cases}
\nu = +\infty \; if & \epsilon \leq \alpha_{gaz} \leq 1 - \epsilon \\
& \epsilon \leq Y_{gaz} \leq 1 - \epsilon \\
\nu = 0, \text{ otherwise}
\end{cases} \tag{3.39}$$

This System is closed by the EOS (3.16). Hyperbolicity is preserved through the waves speeds given in Section (2.3). The entropy equation associated with System (3.37) reads,

$$\frac{\partial \rho S}{\partial t} + div\left(\rho S\mathbf{u} - \frac{\lambda_c \overrightarrow{\bigtriangledown T}}{T}\right) = \frac{\rho\nu(g_2 - g_1)^2}{T} + \lambda_c \frac{(\bigtriangledown T)^2}{T^2} \tag{3.40}$$

and shows agreement with the second law of thermodynamics.

3.4 Numerical method

3.4.1 Introduction

In this section we address the numerical methods used to approximate solutions of System (3.37). This formulation, where capillary and gravity terms are considered as "source terms", has been chosen because of its simplicity regarding both Riemann solver (only three

waves are present instead of four) and numerical schemes formulations.

In addition, numerical simulation of boiling flows leads to two main classes of numerical issues. The first one concerns the extra physics (surface tension, heat conduction and phase transition) and the corresponding numerical solvers. This issue will be addressed in Sections 3.4.2 and 3.4.3.
The second issue is related to the presence of compressible effects in conjunction with Low Mach number conditions. As the flow speed is low ($\simeq$1m/s) and a compressible flow formulation is used, very low Mach numbers, between 10^{-4} and 10^{-1} are expected. As shown in [38] and [53], using Godunov-type scheme for low Mach number flows leads to large computational errors. A way to overcome this issue is to use a preconditioning technique such as the one of [38] or [53] in the context of two-phase model of diffuse interface.
As shown in this last reference, it is mandatory to use an implicit scheme. The method developed in this reference is used with the present model, which presents several specific issues.
For the sake of simplicity, the analysis is carried out in 2D.

3.4.2 Implicit scheme

The system being hyperbolic, a Godunov type scheme is considered to solve System (3.37) in a Cartesian finite volume framework. A computational cell is schematized in Figure 3.3. The implicit 2D Godunov scheme reads :

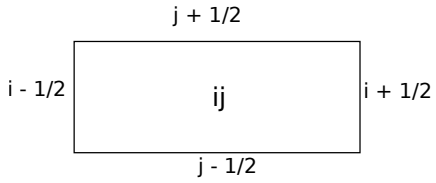

FIGURE 3.3 – Computational cell (i,j) bounded with its four cell boundaries, (i+1/2,j), (i-1/2,j), (i,j+1/2) and (i,j-1/2).

$$U_{i,j}^{n+1} - U_{i,j}^{n} = -\frac{\Delta t}{\Delta x}(F_{i+\frac{1}{2},j}^{n+1} - F_{i-\frac{1}{2},j}^{n+1}) - \frac{\Delta t}{\Delta y}(G_{i,j+\frac{1}{2}}^{n+1} - G_{i,j-\frac{1}{2}}^{n+1}) + \Delta t S_{i,j}^{n+1} \tag{3.41}$$

where

$$U = \begin{pmatrix} \rho Y_1 \\ \rho \\ \rho u \\ \rho v \\ \rho E \end{pmatrix} \quad F = \begin{pmatrix} \rho Y_1 u \\ \rho u \\ \rho u^2 + P \\ \rho v u \\ (\rho E + P)u \end{pmatrix} \quad G = \begin{pmatrix} \rho Y_1 v \\ \rho v \\ \rho u v \\ \rho v^2 + P \\ (\rho E + P)v \end{pmatrix}$$

$$S = \begin{pmatrix} 0 \\ 0 \\ \sigma\kappa\overrightarrow{\bigtriangledown Y_1}|_x + \rho\mathbf{g}|_x \\ \sigma\kappa\overrightarrow{\bigtriangledown Y_1}|_y + \rho\mathbf{g}|_y \\ div\left(\lambda_c\overrightarrow{\bigtriangledown T}\right) + \sigma\kappa\overrightarrow{\bigtriangledown Y_1}\cdot\mathbf{u} + \rho\mathbf{g}\cdot\mathbf{u} \end{pmatrix}$$

The flux $F^{n+1}_{i+\frac{1}{2}j}$, $F^{n+1}_{i-\frac{1}{2}j}$, $G^{n+1}_{ij-\frac{1}{2}}$, $G^{n+1}_{i-j\frac{1}{2}}$ and source $S^{n+1}_{i,j}$ vectors are computed according to variables at time t^{n+1}. Let us consider a generic form of these vectors :

$$\Phi^{n+1} = \Phi^{n+1}\left(U^{n+1}_{i,j}, U^{n+1}_{i-1,j}, U^{n+1}_{i+1,j}, U^{n+1}_{i,j-1}, U^{n+1}_{i,j+1}\right) \tag{3.42}$$

Under first order Taylor expansion it becomes

$$\begin{aligned}\Phi^{n+1} = \Phi^n + \frac{\partial\Phi}{\partial U_{i,j}}\Big)^n (U^{n+1}_{i,j} - U^n_{i,j}) + \frac{\partial\Phi}{\partial U_{i-1,j}}\Big)^n (U^{n+1}_{i-1,j} - U^n_{i-1,j}) + \frac{\partial\Phi}{\partial U_{i+1,j}}\Big)^n (U^{n+1}_{i+1,j} - U^n_{i+1,j}) \\ + \frac{\partial\Phi}{\partial U_{i,j-1}}\Big)^n (U^{n+1}_{i,j-1} - U^n_{i,j-1}) + \frac{\partial\Phi}{\partial U_{i,j+1}}\Big)^n (U^{n+1}_{i,j+1} - U^n_{i,j+1})\end{aligned} \tag{3.43}$$

Rewriting Relations (3.41) and (3.43), the following scheme is obtained :

$$\begin{aligned}&\left[I + \frac{\Delta t}{\Delta x}\left(\frac{\partial F_{i+\frac{1}{2},j}}{\partial U_{i,j}}\right)^n - \frac{\partial F_{i-\frac{1}{2},j}}{\partial U_{i,j}}\Big)^n\right) + \frac{\Delta t}{\Delta y}\left(\frac{\partial G_{i,j+\frac{1}{2}}}{\partial U_{i,j}}\right)^n - \frac{\partial G_{i,j-\frac{1}{2}}}{\partial U_{i,j}}\Big)^n\right) + \Delta t\,\frac{\partial S_{i,j}}{\partial U_{i,j}}\Big)^n\Bigg]\delta U_{i,j} \\ &+ \frac{\Delta t}{\Delta x}\,\frac{\partial F_{i+\frac{1}{2},j}}{\partial U_{i+1,j}}\Big)^n \delta U_{i+1,j} - \frac{\Delta t}{\Delta x}\,\frac{\partial F_{i-\frac{1}{2},j}}{\partial U_{i-1,j}}\Big)^n \delta U_{i-1,j} + \Delta t\left[\frac{\partial S_{i,j}}{\partial U_{i-1,j}}\Big)^n \delta U_{i-1,j} + \frac{\partial S_{i,j}}{\partial U_{i+1,j}}\Big)^n \delta U_{i+1,j}\right] \\ &+ \frac{\Delta t}{\Delta y}\,\frac{\partial G_{i,j+\frac{1}{2}}}{\partial U_{i,j+1}}\Big)^n \delta U_{i,j+1} - \frac{\Delta t}{\Delta y}\,\frac{\partial G_{i,j-\frac{1}{2}}}{\partial U_{i,j-1}}\Big)^n \delta U_{i,j-1} + \Delta t\left[\frac{\partial S_{i,j}}{\partial U_{i,j-1}}\Big)^n \delta U_{i,j-1} + \frac{\partial S_{i,j}}{\partial U_{i,j+1}}\Big)^n \delta U_{i,j+1}\right] \\ &= -\frac{\Delta t}{\Delta x}(F^n_{i+\frac{1}{2},j} - F^n_{i-\frac{1}{2},j}) - \frac{\Delta t}{\Delta y}(G^n_{i,j+\frac{1}{2}} - G^n_{i,j-\frac{1}{2}}) + \Delta t S^n_{i,j}\end{aligned} \tag{3.44}$$

Where $\delta U_{i,j} = U^{n+1}_{i,j} - U^n_{i,j}$.
Under compact form it reads : $M\delta U = D$ where M is a pentadiagonal matrix.
This system can be solved either by direct or iterative methods.

3.4.3 Riemann solver

The various fluxes in System (3.41) are computed with the HLLC Riemann solver [80]. At cell boundary $i + \frac{1}{2}$, it reads for the flux F^* :

$$F^*_{L,R} = \frac{1}{2}(F_L + F_R) - sign(S_L)\frac{S_L}{2}(U^*_L - U_L) - sign(S_M)\frac{S_M}{2}(U^*_R - U^*_L) - sign(S_R)\frac{S_R}{2}(U_R - U^*_R) \tag{3.45}$$

with

$$U = \begin{pmatrix} \rho Y_1 \\ \rho \\ \rho u \\ \rho E \end{pmatrix} \quad F = \begin{pmatrix} \rho Y_1 u \\ \rho u \\ \rho u^2 + P \\ (\rho E + P)u \end{pmatrix},$$

Where U and F represent the conservative variable vector and associated flux respectively. The subscripts L and R denote the left and right state of the Riemann problem, respectively, as shown in Figure (3.4).

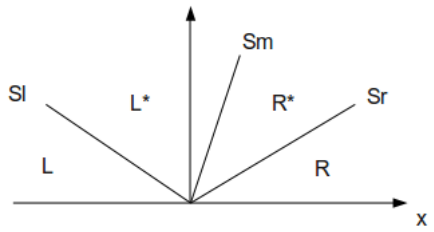

FIGURE 3.4 – Schematization of the System (3.37) Riemann problem under HLLC approximation in the absence of right hand sides (capillarity, relaxation and gravity effects).

The wave speeds S_R and S_L are estimated with Davis approximation [23],

$$S_R = Max(u_R + c_R, u_L + c_L) \tag{3.46}$$

$$S_L = Max(u_R - c_R, u_L - c_L) \tag{3.47}$$

while S_M is estimated under HLL [42] approximation :

$$S_M = \frac{S_R U_R(2) - S_L U_L(2) - (F_R(2) - F_L(2))}{S_R U_R(1) - S_L U_L(1) - (F_R(1) - F_L(1))} \tag{3.48}$$

The states U_L^* and U_R^*, in relation (3.45), are determined with the help of Rankine-Hugoniot jump relations across the S_R and S_L waves,

$$F_L^* - S_L U_L^* = F_L - S_L U_L, \tag{3.49}$$

$$F_R^* - S_R U_R^* = F_R - S_R U_R, \tag{3.50}$$

and contact relations : $u_L^* = u_R^* = S_M$ and $P_L^* = P_R^* = p^*$:

$$U_L^* = \frac{1}{S_M - S_L}[F_L - S_L U_L - (0, p^*, S_M.P^*)^T] \tag{3.51}$$

$$U_R^* = \frac{1}{S_M - S_R}[F_R - S_R U_R - (0, p^*, S_M.P^*)^T] \tag{3.52}$$

The implicit Godunov scheme (3.44) requires the flux expression given by (3.45) and its derivatives with respect to the conservatives variables. Corresponding formulas are given in Appendix A.

3.4.4 Low Mach preconditioning

As mentioned in the introduction, nucleate boiling flows involve compressible low Mach numbers flows. As shown in [38] and [53], Godunov-type scheme leads to huge errors without appropriate correction. Following the lines of Turkel [82] and Guillard and Viozat [38] in the context of single phase flows, the LeMartelot et al. [53] multiphase flows preconditioning method is used. This method consists in modifying the pressure equation associated with System (3.37) :

$$\frac{\partial P}{\partial t} + u\frac{\partial P}{\partial x} + \rho c^2 \frac{\partial u}{\partial x} = 0, \tag{3.53}$$

by a M^2 factor,

$$\frac{1}{M^2}\frac{\partial P}{\partial t} + u\frac{\partial P}{\partial x} + \rho c^2 \frac{\partial u}{\partial x} = 0. \tag{3.54}$$

This modification leads to the modified wave speeds : $u, u + \tilde{c}_+, u - \tilde{c}_-$, with,

$$\tilde{c}_- = \frac{(1-M^2)u + \sqrt{(M^2-1)^2u^2 + 4M^2c^2}}{2} \tag{3.55}$$

$$\tilde{c}_+ = \frac{(M^2-1)u + \sqrt{(M^2-1)^2u^2 + 4M^2c^2}}{2} \tag{3.56}$$

These wave speeds are directly used in the HLLC solver (3.45).
It is worth to mention that System (3.37) is modified in the Riemann problem resolution only through the wave speeds (3.55 - 3.56). With the fluxes computed with the HLLC solver, the Godunov method (3.41) is used with the formulation (3.37) and unmodified equation of state (3.16). This method obviously guarantees conservation and correct jumps across waves. It only acts on the numerical dissipation.
As the conservative formulation is used, even strong discontinuities can be handled by the method and, as shown in [53], the method is time accurate.

3.4.5 Heat conduction

In this section, the calculation of the heat flux present in the total energy conservation equation is addressed. For the sake of simplicity the analysis is carried out in 1D.
The heat flux at the cell boundary can be expressed as a function of T_i and T_{i+1} as :

$$q_{i,i+1/2} = q_{i+1,i-1/2} = -\frac{\lambda_{c,i}\lambda_{c,i+1}}{\lambda_{c,i} + \lambda_{c,i+1}} \frac{T_{i+1} - T_i}{\frac{1}{2}\Delta x} \tag{3.57}$$

Therefore, the 1D numerical approximation of term $div\,(\mathbf{q})$ for a i cell becomes :

$$div\,(\mathbf{q}) \simeq \frac{\Delta t}{\Delta x}\left(q^n_{i,i+1/2} - q^n_{i,i-1/2}\right) \tag{3.58}$$

The corresponding flux derivatives appearing in the implicit scheme (3.44) are given in Appendix B.

3.4.6 Surface tension computation

Surface tension effects are considered through the Continuum Surface Force (CSF) method of Brackbill [16]. The capillary force is modelled as,

$$\mathbf{F}_\sigma = \sigma\kappa\overrightarrow{\bigtriangledown C} \tag{3.59}$$

where :
σ represents the surface tension coefficient$(N.m^{-1})$,
κ represents the local curvature (m^{-1}),
C represents a color function whose goal is to locate the interface between the two phases.

In the present work, we use the mass fraction $C = Y_1$ as color function, as mass fractions are invariant across pressure waves.
In order to correctly evaluate surface tension effects, it is mandatory to know the local curvature, κ, as well as the gradients of the color function, $\overrightarrow{\bigtriangledown C}$.
The curvature is computed by,

$$\kappa = -div\left(\frac{\overrightarrow{\bigtriangledown C}}{|\overrightarrow{\bigtriangledown C}|}\right). \tag{3.60}$$

There are several issues regarding the curvature computation. On one hand, gradient computations require smooth color function profiles. On the other hand, the interface has to be located accurately. These two requirements are contradictory. In order to satisfy the second requirement, the color function is first reset :

$$\begin{cases} \text{If } C \geq 0.5 \text{ , C} = 1.0 \\ \text{Otherwise, C} = 0.0 \end{cases}$$

This provides a sharp profile for the colour function and accurate interface detection. Once the interface is localized, a diffusion operator is applied to the color function, C, in order to obtain a smooth function. In this work, a simple diffusion equation is used :

$$\frac{\partial C}{\partial \tau} = D_{diff} \bigtriangleup C \tag{3.61}$$

Where D_{diff} is a diffusion coefficient $(m^2.s^{-1})$. D_{diff} and τ are chosen such as the color function is diffused on about 4 cells.
The curvature is computed with the diffused color function. At the discrete level, the local curvature inside an i cell is determined with the following formulation :

$$\kappa_i = -\frac{1}{\Omega_i}\sum_{j\epsilon V(i)} \widehat{n_{ij}} \cdot \overrightarrow{n_{ij}} l_{ij} \tag{3.62}$$

Where vectors $\widehat{n_{ij}}$ represent the normalized color function gradients calculated between cells i and j, and Ω_i represents the volume of the i cell. The vector $\overrightarrow{n_{ij}}$ represents the vector

connecting the cell centers and l_{ij} the cell boundary length. A simple expression of the cell boundary interface normal vectors, $\widehat{n_{ij}}$, is given by :

$$\widehat{n_{ij}} = \frac{1}{2}\left(\widehat{n_j} + \widehat{n_i}\right) \tag{3.63}$$

where $\widehat{n_i} = \dfrac{\overrightarrow{\bigtriangledown C_i^n}}{|\overrightarrow{\bigtriangledown C_i^n}|}$.
In the frame of 2D Cartesian grids it reduces to :

$$\kappa_{ij} = -\left(\frac{1}{\Delta x}(\widehat{n}_{xi+\frac{1}{2},j} - \widehat{n}_{xi-\frac{1}{2},j}) + \frac{1}{\Delta y}(\widehat{n}_{yi,j+\frac{1}{2}} - \widehat{n}_{yi,j-\frac{1}{2}})\right) \tag{3.64}$$

The gradients are computed with the following second order approximation :

$$\overrightarrow{\bigtriangledown C_{ij}} = \frac{(C_{i+1j} - C_{i-1j})}{2\Delta x} \cdot \overrightarrow{i} + \frac{(C_{ij+1} - C_{ij-1})}{2\Delta y} \cdot \overrightarrow{j} \tag{3.65}$$

As for the previous convective and conductive fluxes, derivatives of the capillary term is needed. Details are given in Appendix C.

3.5 Validations

To check model's validity, a basic solution of one-dimensionnal sharp evaporation front is derived and the numerical solution using an diffuse interface formulation is compared to it. Then, capillary effects alone are considered in a 2D test case having exact solution.

3.5.1 1D evaporation front

The goal of this section is to determine the exact solution of an 1D steady evaporation front in order to check convergence of the method presented previously.
We consider the following configuration (Fig. 3.5), with boundary conditions :
-Liquid inlet at imposed temperature, $T = T_{LI}$
-Vapour outlet at imposed temperature, $T = T_{VO}$, with imposed heat flux, Q_0.
The stationary evaporation front is located at $x = 0$ and the corresponding temperature is equal to the liquid-gas saturation temperature, $T_{x=0} = T_{SAT}$.

FIGURE 3.5 – Geometry and boundary conditions.

Reference solution determination

As the interface is considered as a sharp discontinuity, the single phase Euler equations with heat diffusion are valid in each pure fluid :

$$\begin{aligned}
&\frac{\partial \rho}{\partial t} + \frac{\partial \rho u}{\partial x} = 0, \\
&\frac{\partial \rho u}{\partial t} + \frac{\partial \rho u^2 + p}{\partial x} = 0, \\
&\frac{\partial \rho E}{\partial t} + \frac{\partial (\rho E + p) u}{\partial x} - \frac{\partial}{\partial x}\left(\lambda \frac{\partial T}{\partial x}\right) = 0.
\end{aligned} \tag{3.66}$$

Each phase is supposed to obey the Stiffened-Gas (3.3) equation of state.
As we consider steady state solution, System (3.66) reduces to :

$$\begin{aligned}
&\rho \overline{u} = m = cst \\
&\frac{m^2}{\rho} + p_l = cst \\
&m(h_k + \frac{1}{2}\frac{m^2}{\rho^2} + q_k) - \lambda \frac{\partial T}{\partial x} = cst
\end{aligned} \tag{3.67}$$

Where $\overline{u}$ represents the velocity in the evaporation front frame of reference and $h = C_p T$ represents the enthalpy with q being the reference energy.

Quasi-isobar flow
By considering weak pressure fluctuations, the pressure is considered as a constant at leading order, $p(x) = p_0$. This hypothesis, widely used in combustion theory (see [21], for example) allows for the removal of the $\frac{1}{2}\frac{m^2}{\rho^2}$ term in the energy equation.

Therefore, total energy conservation between the liquid and the vapour sides reads :

$$mC_{p,liq}T_{LI} + mq_{liq} = mC_{p,vap}T_{VO} + mq_{vap} + Q_0 \tag{3.68}$$

T_{LI} and T_{VO} being known, a first relation between the mass rate, m and the heat flux, $Q_0 \left(Q_0 = -\lambda_{vap} \left. \frac{\partial T}{\partial x} \right)_{x=X_V} \right)$, is obtained :

$$Q_0 = m\left(C_{p,liq}T_{LI} + q_{liq} - C_{p,vap}T_{VO} - q_{vap}\right) \tag{3.69}$$

The temperature profiles on each side of the evaporation front are determined using the total energy conversation :

$$mC_{p,liq}T + mq_{liq} - \lambda_{liq}\frac{\partial T}{\partial x} = mC_{p,liq}T_{LI} + mq_{liq}, \tag{3.70}$$

$$mC_{p,vap}T + mq_{vap} - \lambda_{vap}\frac{\partial T}{\partial x} = mC_{p,liq}T_{LI} + mq_{liq}, \tag{3.71}$$

and the interface condition $T_{x=0} = T_{SAT}$. The following solutions are obtained :

$$\begin{aligned} T(x)|_{x<0} &= T_{LI} + (T_{SAT} - T_{LI})e^{\dfrac{mC_{p,liq}}{\lambda_{liq}}x} \\ T(x)|_{x>0} &= \frac{C_{p,liq}}{C_{p,vap}}T_{LI} + \frac{q_{liq} - q_{vap}}{C_{p,vap}} + (T_{SAT} - \frac{C_{p,liq}}{C_{p,vap}}T_{LI} - \frac{q_{liq} - q_{vap}}{C_{p,vap}})e^{\dfrac{mC_{p,vap}}{\lambda_{vap}}x} \end{aligned} \tag{3.72}$$

In order to determine the mass flux, m, another relation linking m and Q_0 is needed. The heat flux definition at the outlet is used :

$$\begin{aligned} Q_0 &= -\lambda_{vap}\left.\frac{\partial T}{\partial x}\right)_{x=X_V} \\ Q_0 &= -mC_{p,vap}\left(T_{SAT} - \frac{C_{p,liq}}{C_{p,vap}}T_{LI} - \frac{q_{liq} - q_{vap}}{C_{p,vap}}\right)e^{\dfrac{mC_{p,vap}}{\lambda_{vap}}X_V} \end{aligned} \tag{3.73}$$

Using relations (3.69) and (3.73), the mass flow rate is determined as :

$$m = \frac{\lambda_{vap}}{C_{p,vap}L_V}\ln\left(\frac{C_{p,vap}T_{VO} + q_{vap} - C_{p,liq}T_{LI} - q_{liq}}{C_{p,vap}T_{SAT} + q_{vap} - C_{p,liq}T_{LI} - q_{liq}}\right) \tag{3.74}$$

Then, Q_0 is determined with (3.69) and the temperature profile (3.72).

Numerical solution

We consider the same test case as depicted in Figure (3.5) with $T_{LE} = T_{SAT}$, $T_{VO} = 1000\,K$ and the two following fluids :
Liquid water :

$\gamma_{liq} = 2.62 \quad P_{\infty,liq} = 9058.29.10^5\,Pa \quad C_{v,liq} = 1606.97\,J.kg^{-1}.K^{-1} \quad \lambda_{liq} = 0.6788\,W.m^{-1}.K^{-1}$

Water vapour :

$\gamma_{vap} = 1.38 \quad P_{\infty,vap} = 0\,Pa \quad C_{v,vap} = 1192.51\,J.kg^{-1}.K^{-1} \quad \lambda_{vap} = 249.97\,W.m^{-1}.K^{-1}$

Using the analytic solution built in the previous section, the mass flow rate and the heat flux at the outlet are determined :

$$m = 1.1434\,kg.m^{-2}.s^{-1}n \quad Q_0 = -3.76.10^6\,W.m^{-2}$$

Corresponding temperature and velocity profiles are shown in Figures 3.6 and 3.7 in lines. The diffuse interface model in 1D,

$$\begin{aligned}
&\frac{\partial \rho Y_1}{\partial t} + \frac{\partial \rho Y_1 u}{\partial x} = \rho\nu(g_2 - g_1) \\
&\frac{\partial \rho}{\partial t} + \frac{\partial \rho u}{\partial x} = 0 \\
&\frac{\partial \rho u}{\partial t} + \frac{\partial \rho u^2 + P}{\partial x} = 0 \\
&\frac{\partial \rho E}{\partial t} + \frac{\partial (\rho E + P)u}{\partial x} = -\frac{\partial}{\partial x}(\lambda_c \frac{\partial T}{\partial x})
\end{aligned} \tag{3.75}$$

is solved numerically with the algorithm presented previously.
The boundary condition at the left inlet corresponds to an imposed mass flow rate and stagnation enthalpy, computed with the following set of variables :

$$m = 1.1434\, kg.m^{-2}.s^{-1} \quad T = T_{SAT} \quad P = 1.0\, Bar \quad \alpha_{liq} = 0.999999$$

At the outlet boundary condition, the heat flux is prescribed as well as the temperature :

$$Q_0 = -3.76.10^6\, W.m^{-2} \quad T_0 = 1000\, K$$

This quite huge heat flux is due to the chosen value for the gas thermal conductivity ($249.97\, W.m^{-1}.K^{-1}$). Indeed, the goal of these computations is to prove the ability of the method to converge to a solution with a sharp evaporating interface. Therefore, this conductivity has been chosen in order to lower the computational time required to converge to the exact solution. Another option could be to set the liquid gas interface close to the oulet section, but this is less convenient for both the computations and the representations.
The numerical solution has been computed using both the explicit and the implicit (3.44) schemes, the results are shown in Figures 3.6 and 3.7.

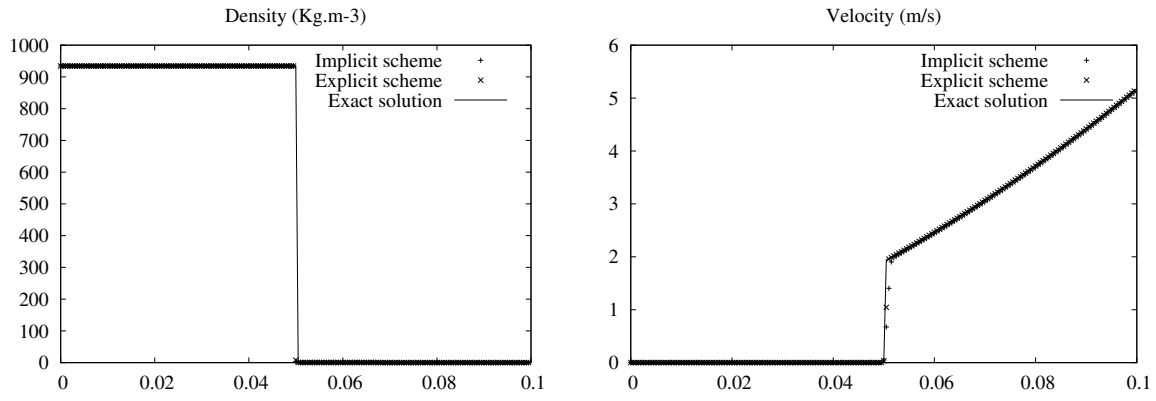

FIGURE 3.6 – Computed mixture density and velocity profiles using a mesh composed of 200 cells compared to the exact profiles. Excellent agreement is obtained.

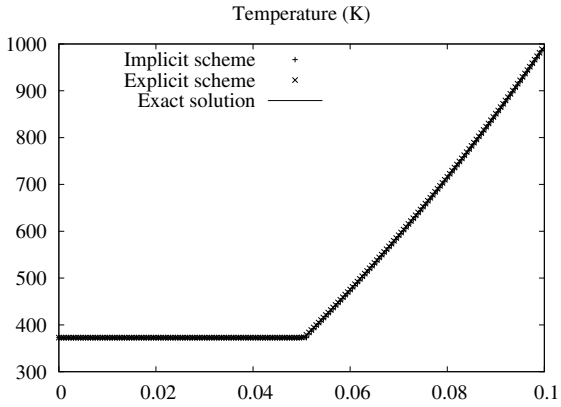

FIGURE 3.7 – Computed temperature profile using a mesh composed of 200 cells compared to the exact profile. Excellent agreement is obtained.

These results show the ability of the method to converge to the exact 1D steady solution containing a sharp evaporating interface. Therefore, it gives a first validation for the model and the way heat conduction and phase change are handled.

3.5.2 Laplace law

We consider a closed squared domain of 2.5cm x 2.5cm filled with liquid water. A gas bubble (radius = 5 mm) is placed at the center (Fig. 3.8).

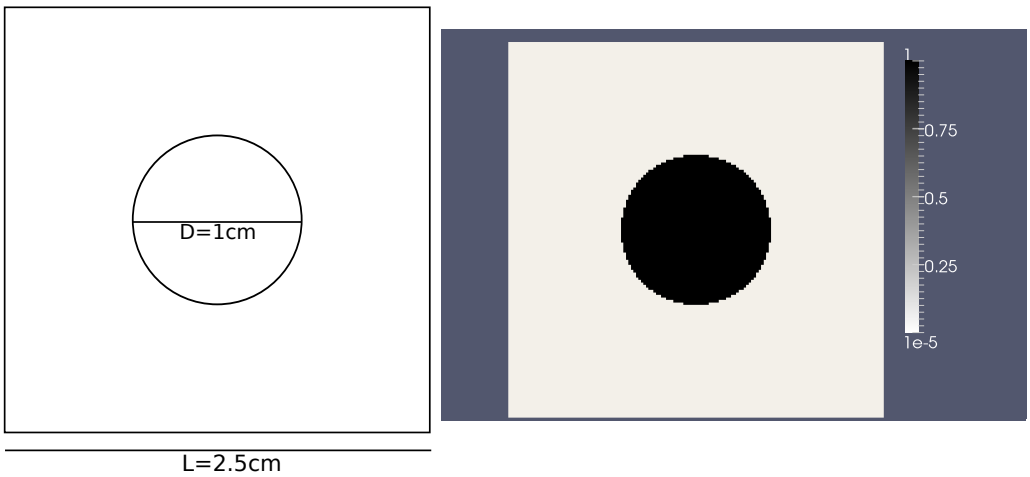

FIGURE 3.8 – Square domain filled with liquid water containing a incondensable gas bubble. Sketch of the configuration and initial volume fraction contours.

Initially, the pressure and the temperature are set equal to 1 Bar and 300 K everywhere while the volume fraction of vapour inside the bubble is 0.99999 and 10^{-5} outside. The surface tension coefficient is $\sigma = 73.10^{-3} N.m^{-1}$. Low Mach pre-conditioning (See section

4.4) is used with a reference Mach number equal to 0.1. The fluids SG (3.3) parameters are the following :
Liquid water :

$$\gamma_{liq} = 2.62 \quad P_{\infty,liq} = 9058.29.10^5\, Pa \quad C_{v,liq} = 1606.97\, J.kg^{-1}.K^{-1}$$

Gas :

$$\gamma_{gas} = 1.38 \quad P_{\infty,gas} = 0\, Pa \quad C_{v,gas} = 1192.51\, J.kg^{-1}.K^{-1}$$

The C_v parameter is required in this computation as the temperature equilibrium model (3.6) (without mass transfer) is used. Figure 3.9 shows the equilibrium state obtained on a 2D 125x125 mesh.

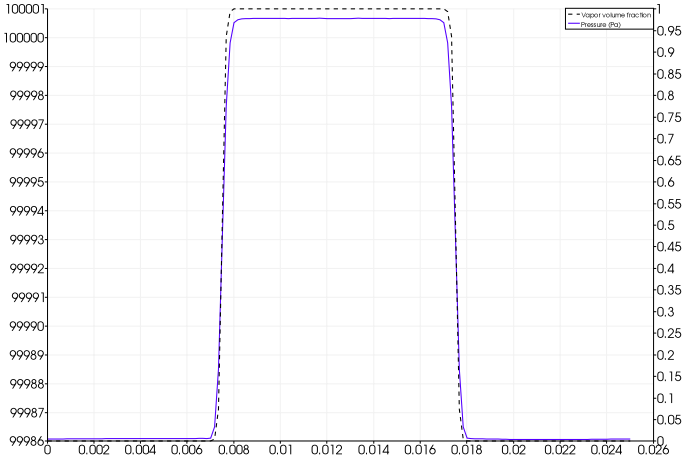

FIGURE 3.9 – Pressure and gas volume fraction profiles along the x-axis. The solid line represents the pressure while the dashed line represents the vapour volume fraction.

These results allow the determination of the numerical pressure jump, $(\Delta P)_{num} \simeq 14.9Pa$ which is to be compared to the Laplace's law, $\Delta P = \dfrac{\sigma}{0.5D} = \dfrac{73.10^{-3}}{0.005} = 14.6Pa$.
Therefore, the obtained pressure jump is in very good agreement with the exact solution, with an error of about 2.05%.

3.6 2D illustrations

In this part we consider a closed and adiabatic rectangular domain (12cm x 7cm) (Figure 3.10) in which the lower half is filled with liquid water and the upper half is filled with vapour. Moreover, three bubbles of vapour (radius = $3mm$) are initially present.

The surface tension coefficient is set to $\sigma = 73.0\, mN.m^{-1}$, the contact angle is taken constant and equal to $\theta = 45°$ and the gravity acceleration is set to $|\mathbf{g}| = 9.81\, m.s^{-2}$. The fluid

parameters are the following :
Liquid water :

$$\gamma_{liq} = 2.62 \quad P_{\infty,liq} = 9058.29.10^5\, Pa \quad C_{v,liq} = 1606.97\, J.kg^{-1}.K^{-1} \quad \lambda_{liq} = 0.6788\, W.m^{-1}.K^{-1}$$

Water vapour :

$$\gamma_{vap} = 1.38 \quad P_{\infty,vap} = 0\, Pa \quad C_{v,vap} = 1192.51\, J.kg^{-1}.K^{-1} \quad \lambda_{vap} = 0.0249\, W.m^{-1}.K^{-1}$$

At start, the initial volume fraction of vapour is $\alpha_{vap} = 0.0001$ in the lower half domain and $\alpha_{vap} = 0.9999$ in the upper part and inside the bubbles. Moreover, the initial pressure and temperature are initialised with the hydrostatic gravity profile with the constraint $T = T_{SAT}(P)$ in each cell.

The implicit scheme (3.44) and low Mach pre-conditioning (with reference Mach number equal to 0.1) are used with a mesh composed of 960 x 560 cells.

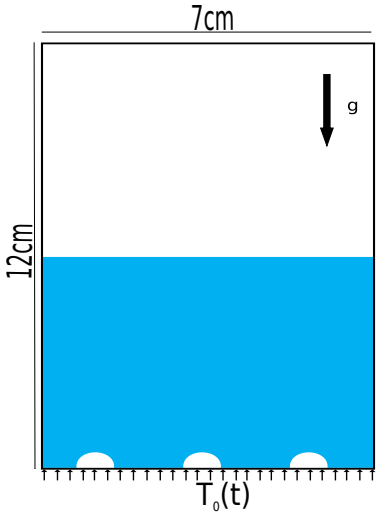

FIGURE 3.10 – A closed and adiabatic rectangular domain is considered. The lower half domain is filled with liquid water and the upper half is filled with water vapour. Three half bubbles of vapour (radius = $3mm$) are initially present. A temperature, $T_0(t)$, is imposed at the bottom wall

A temperature, $T_0(t)$, is imposed at the bottom wall such as :

$$T_0(t) = \begin{cases} T_{SAT} + (\dfrac{t}{\tau})\Delta T, \text{ if } t \leq \tau \\ T_{SAT} + \Delta T, \text{ if } t > \tau \end{cases} \tag{3.76}$$

With $\tau = 120\, ms$, $T_{SAT} = 372.79\, K$ and $\Delta T = 15\, K$. This smooth heating is set in order to avoid creation of a vapour film along the hot surface and strong pressure waves.

The computed volume fraction of water vapour is shown in Figure 3.11.

This Figure shows computed results from $t = 0\,s$ to $t = 180\,ms$. The first instants show the three first bubbles moving toward the surface due to the buoyancy while, as the bottom of the box is heated, water around them begins to boil and creates a film of vapour. Then, convective effects created by the three first bubbles combined with surface tension create new bubbles on the bottom of the box. Once created, theses new bubbles begin to rise and, as there is now, again, liquid against the bottom, new ones appear behind them and begin to grow.

It is worth to mention that the bottom of the box is a perfect surface, exempt of cavities or special treatment except for an uniform temperature and constant contact angle. This means that the new bubbles are created at these position thanks to convective rolls, surface tension and thermal conduction. According to the velocity profiles, the first bubbles seem to be created between the convective rolls, where the velocity is the lowest, as shown in Figure 3.12.

The three first bubbles are moving toward the surface due to buoyancy but, as the bottom of the box is heated, the water around them begins to boil and a vapour film appears. Theses newly created bubbles begin to rise as new ones appear behind them. The bottom of the box being a perfect surface, the new bubbles are created at different positions than the initial sites, meaning that their position and size is selected by convection, conduction and capillarity.

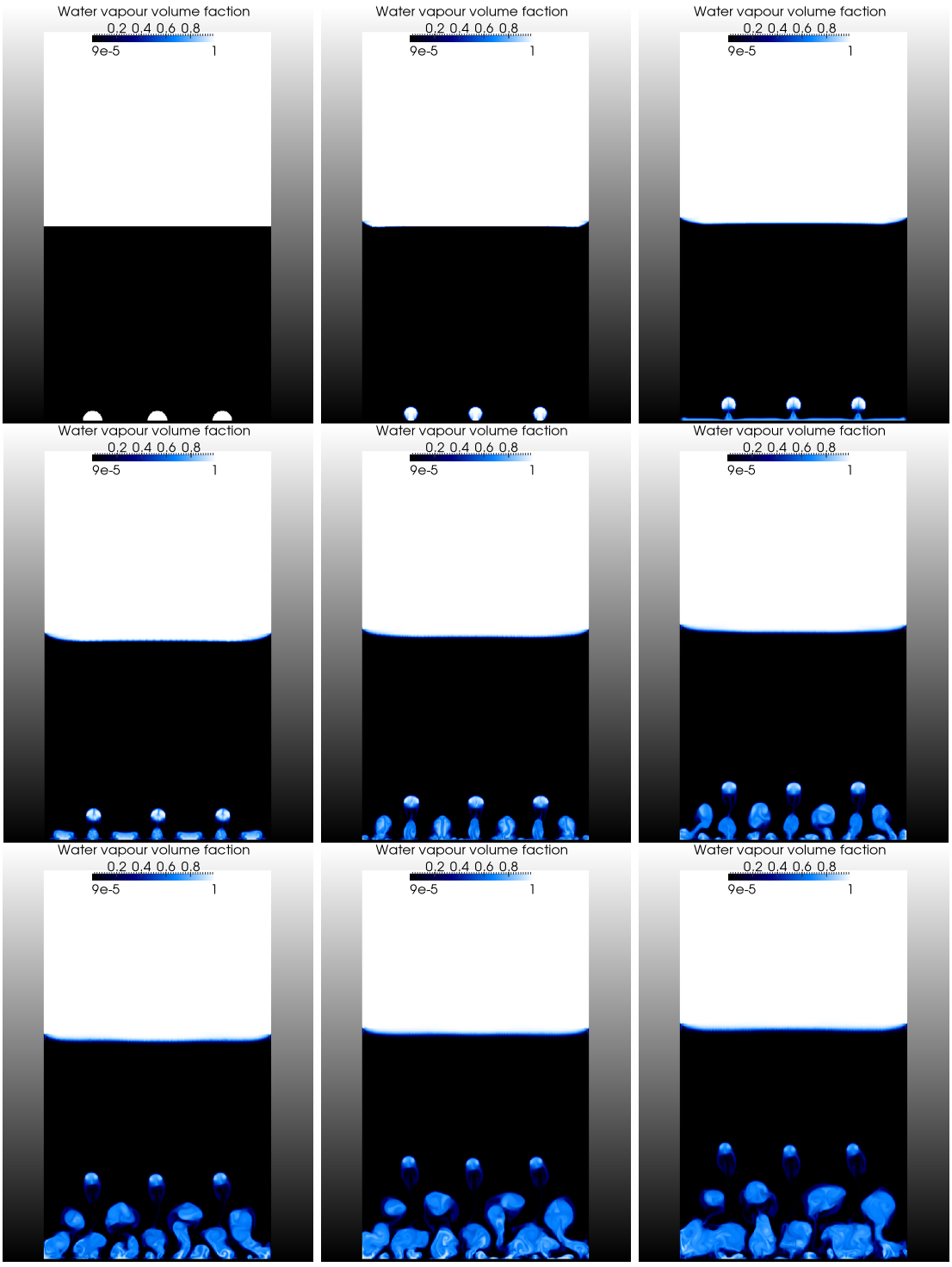

FIGURE 3.11 – Water vapour volume fraction at times $t = 0\,s$, $t = 20\,ms$, $t = 40\,ms$, $t = 60\,ms$, $t = 80\,ms$, $t = 100\,ms$, $t = 140\,ms$, $t = 160\,ms$, and $t = 180\,ms$.

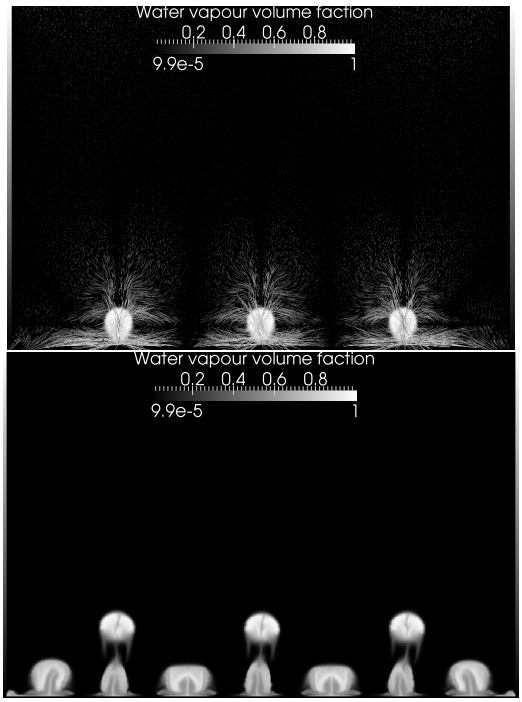

FIGURE 3.12 – Water vapour volume fraction and velocity vectors around the bubbles at time $t = 30\,ms$ and water vapour volume fraction at time $t = 70ms$.

These results tend to indicate that nucleation is needed at initial time only. The phenomenon is then self-sustained and selects the number of bubbles and their sizes, free of nucleation criterion.

3.7 Conclusion

As a first step towards the direct numerical simulation of nucleate boiling flows, a thermal and mechanical equilibrium model has been built. This model is compressible, hyperbolic and in agreement with the second law of thermodynamics. Moreover, it has no restriction regarding the flow speed, pressure and temperature conditions. Extra physics (surface tension [16], gravity, heat conduction and phase change[73][52]) has been added to this model. Nevertheless, as a nucleate boiling flow involves low Mach numbers, the preconditioned implicit scheme of LeMartelot et al [53] has been adopted to obtain accurate solutions.
The complete method has then been validated against an 1D steady sharp evaporation front exact solution and a 2D static bubble case, showing agreement with Laplace's law.
A 2D nucleate boiling flow simulation has been presented. The corresponding results show very good qualitative behaviour as well as method's ability to deal with such complex flows.

Acknowledgments The first author has been partly supported by CNES and SAFRAN Snecma, space Engines Division. Drs. S. Petitot and P. Boivin are gratefully acknowledged.

The authors would like to acknowledge fruitful discussions and works with Dr. F. Petitpas.

Appendix A - HLLC Riemann solver derivatives

The HLLC approximate Riemann solver is recalled hereafter :

$$F_{L,R} = \frac{1}{2}(F_L+F_R) - sign(S_L)\frac{S_L}{2}(U_L^*-U_L) - sign(S_M)\frac{S_M}{2}(U_R^*-U_L^*) - sign(S_R)\frac{S_R}{2}(U_R-U_R^*),$$

The flux vector derivatives are given by :

$$\frac{\partial F_{LR}}{\partial U_L} = \frac{1}{2}\frac{\partial F_L}{\partial U_L} - sign(S_L)\frac{S_L}{2}(\frac{\partial U_L^*}{\partial U_L} - 1) - sign(S_M)\frac{S_M}{2}(\frac{\partial (U_R^* - U_L^*)}{\partial U_L}) + sign(S_R)\frac{S_R}{2}(\frac{\partial U_R^*}{\partial U_L}) \tag{3.77}$$

$$\frac{\partial F_{LR}}{\partial U_R} = \frac{1}{2}\frac{\partial F_R}{\partial U_R} - sign(S_L)\frac{S_L}{2}\frac{\partial U_L^*}{\partial U_R} - sign(S_M)\frac{S_M}{2}(\frac{\partial (U_R^* - U_L^*)}{\partial U_R}) - sign(S_R)\frac{S_R}{2}(1 - \frac{\partial U_R^*}{\partial U_R}) \tag{3.78}$$

Where :

$$U_L^* = \frac{1}{S_M - S_L}[F_L - S_L U_L - (0, 0, P^*, S_M.P^*)^T] \tag{3.79}$$

$$U_R^* = \frac{1}{S_M - S_R}[F_R - S_R U_R - (0, 0, P^*, S_M.P^*)^T] \tag{3.80}$$

$$\frac{\partial U_L^*}{\partial U_L} = \frac{(\frac{\partial F_L}{\partial U_L} - S_L - \frac{\partial}{\partial U_L}(0, 0, P^*, S_M.P^*)^T)(S_M - S_L) - (F_L - S_L U_L - (0, 0, P^*, S_M.P^*)^T)\frac{\partial S_M}{\partial U_L}}{(S_M - S_L)^2} \tag{3.81}$$

$$\frac{\partial U_L^*}{\partial U_R} = \frac{-\frac{\partial}{\partial U_L}((0, 0, P^*, S_M.P^*)^T)(S_M - S_L) - (F_L - S_R U_L - (0, 0, P^*, S_M.P^*)^T)\frac{\partial S_M}{\partial U_R}}{(S_M - S_L)^2} \tag{3.82}$$

$$\frac{\partial U_R^*}{\partial U_L} = \frac{-\frac{\partial}{\partial U_L}((0, 0, P^*, S_M.P^*)^T)(S_M - S_R) - (F_R - S_R U_R - (0, 0, P^*, S_M.P^*)^T)\frac{\partial S_M}{\partial U_L}}{(S_M - S_R)^2} \tag{3.83}$$

$$\frac{\partial U_R^*}{\partial U_R} = \frac{(\frac{\partial F_R}{\partial U_R} - S_R - \frac{\partial}{\partial U_R}(0, 0, P^*, S_M.P^*)^T)(S_M - S_R) - (F_R - S_R U_R - (0, 0, P^*, S_M.P^*)^T)\frac{\partial S_M}{\partial U_R}}{(S_M - S_R)^2} \tag{3.84}$$

Using Relations (3.49), (3.50), and $P_L^* = P_R^* = P^*$, two expressions for P^* are obtained :

$$P^* = F_L(2) - S_L U_L(2) - S_M(F_L(1) - S_L U_L(1)) \tag{3.85}$$

and

$$P^* = F_R(2) - S_R U_R(2) - S_M(F_R(1) - S_R U_R(1)) \tag{3.86}$$

To have a more symmetric derivative, the following average expression is used for P^* :

$$P^* = \frac{F_R(2) - S_R U_R(2) - S_M(F_R(1) - S_R U_R(1)) + F_L(2) - S_L U_L(2) - S_M(F_L(1) - S_L U_L(1))}{2} \tag{3.87}$$

$$\frac{\partial P^*}{\partial U_L} = \frac{1}{2}\left[\frac{\partial F_L(2)}{\partial U_L} - S_L(0,0,1,0)^T - S_M\left(\frac{\partial F_L(1)}{\partial U_L} - S_L(0,1,0,0)^T\right) - (F_L(1) - S_L U_L(1))\frac{\partial S_M}{\partial U_L}\right] \tag{3.88}$$

$$\frac{\partial P^*}{\partial U_R} = \frac{1}{2}\left[\frac{\partial F_R(2)}{\partial U_R} - S_R(0,0,1,0)^T - S_M\left(\frac{\partial F_R(1)}{\partial U_R} - S_R(0,1,0,0)^T\right) - (F_R - S_R U_R)\frac{\partial S_M}{\partial U_R}\right] \tag{3.89}$$

$$S_M = \frac{S_R U_R(2) - S_L U_L(2) - (F_R(2) - F_L(2))}{S_R U_R(1) - S_L U_L(1) - (F_R(1) - F_L(1))} \tag{3.90}$$

$$\begin{aligned}\frac{\partial S_M}{\partial U_L} =& \frac{(\frac{\partial F_L(2)}{\partial U_L} - S_L\frac{\partial U_L(2)}{\partial U_L})(S_R U_R(1) - S_L U_L(1) - (F_R(1) - F_L(1)))}{(S_R U_R(1) - S_L U_L(1) - (F_R(1) - F_L(1)))^2} \\ & - \frac{(S_R U_R(2) - S_L U_L(2) - (F_R(2) - F_L(2)))(\frac{\partial F_L(1)}{\partial U_L} - S_L\frac{\partial U_L(1)}{\partial U_L})}{(S_R U_R(1) - S_L U_L(1) - (F_R(1) - F_L(1)))^2}\end{aligned} \tag{3.91}$$

$$\begin{aligned}\frac{\partial S_M}{\partial U_R} =& \frac{(S_R\frac{\partial U_R(2)}{\partial U_R} - \frac{\partial F_R(2)}{\partial U_R})(S_R U_R(1) - S_L U_L(1) - (F_R(1) - F_L(1)))}{(S_R U_R(1) - S_L U_L(1) - (F_R(1) - F_L(1)))^2} \\ & - \frac{(S_R U_R(2) - S_L U_L(2) - (F_R(2) - F_L(2)))(S_R\frac{\partial U_R(1)}{\partial U_R} - \frac{\partial F_R(1)}{\partial U_R})}{(S_R U_R(1) - S_L U_L(1) - (F_R(1) - F_L(1)))^2}\end{aligned} \tag{3.92}$$

These various derivatives require the knowledge of $\frac{\partial F_L}{\partial U_L}$ and $\frac{\partial F_R}{\partial U_R}$. They correspond to the Jacobian matrix of the considered System which requires the derivatives of the mixture pressure.

The mixture pressure reads :

$$P = \frac{1}{2}\left(A_1 + A_2 - (P_{\infty,1} + P_{\infty,2})\right) + \sqrt{\frac{1}{4}\left(A_2 - A_1 - (P_{\infty,2} - P_{\infty,1})\right)^2 + A_1 A_2} \tag{3.93}$$

Where $A_k = \dfrac{Y_k\left(\gamma_k - 1\right)C_{v,k}}{Y_1 C_{v,1} + Y_2 C_{v,2}}\left(\rho(e-q) - P_{\infty,k}\right)$.
Thus, the corresponding derivatives read,

$$\frac{\partial P}{\partial U} = \frac{1}{2}\left(\frac{\partial A_1}{\partial U} + \frac{\partial A_2}{\partial U}\right) + \frac{\dfrac{1}{2}\left[\dfrac{1}{2}\left(\dfrac{\partial A_2}{\partial U} - \dfrac{\partial A_1}{\partial U}\right)\left(A_2 - A_1 - (P_{\infty,2} - P_{\infty,1})\right) + A_1\dfrac{\partial A_2}{\partial U} + A_2\dfrac{\partial A_1}{\partial U}\right]}{\sqrt{\dfrac{1}{4}\left(A_2 - A_1 - (P_{\infty,2} - P_{\infty,1})\right)^2 + A_1 A_2}}, \tag{3.94}$$

where,

$$\begin{aligned}
\frac{\partial A_k}{\partial U} &= \left(\rho(e-q) - P_{\infty,k}\right)\left[\frac{\dfrac{\partial y_k}{\partial U}(\gamma_k - 1)C_{v,k}\rho(y_k(C_{v,1} - C_{v,2}) + \rho C_{v,2})}{\left(y_1 C_{v,1} + y_2 C_{v,2}\right)^2}\right] \\
&- \left(\rho(e-q) - P_{\infty,k}\right)\left[\frac{y_k(\gamma_k - 1)C_{v,k}\left(\dfrac{\partial \rho}{\partial U}(y_1(C_{v,1} - C_{v,2})C_{v,2}) + \rho(C_{v,1} - C_{v,2})\dfrac{\partial y_1}{\partial U}\right)}{\left(y_1 C_{v,1} + y_2 C_{v,2}\right)^2}\right] \\
&+ \frac{y_k(\gamma_k - 1)C_{v,k}}{\rho y_1(C_{v,1} - C_{v,2}) + \rho C_{v,2}}\left(\frac{\partial \rho e}{\partial U} - \frac{\partial \rho q}{\partial U}\right)
\end{aligned} \tag{3.95}$$

With :
$y_k = \rho Y_k$
$\rho e = \rho E - \dfrac{(\rho u)^2}{\rho} - \dfrac{(\rho v)^2}{\rho}$
$\rho q = y_1 q_1 + y_2 q_2$

Appendix B - Heat flux derivatives

The derivatives appearing in the heat conduction term read :

$$\frac{\partial q_{i,i+1/2}}{\partial U_i} = \frac{\lambda_{eq,i}\lambda_{eq,i+1}}{\frac{1}{2}\Delta x(\lambda_{eq,i} + \lambda_{eq,i+1})}\frac{\partial T_i}{\partial U_i} - \frac{T_{i+1} - T_i}{\frac{1}{2}\Delta x}\frac{\partial}{\partial U_i}\left(\frac{\lambda_{eq,i}\lambda_{eq,i+1}}{\lambda_{eq,i} + \lambda_{eq,i+1}}\right) \tag{3.96}$$

$$\frac{\partial q_{i,i+1/2}}{\partial U_{i+1}} = -\frac{\lambda_{eq,i}\lambda_{eq,i+1}}{\frac{1}{2}\Delta x(\lambda_{eq,i} + \lambda_{eq,i+1})}\frac{\partial T_{i+1}}{\partial U_{i+1}} - \frac{T_{i+1} - T_i}{\frac{1}{2}\Delta x}\frac{\partial}{\partial U_{i+1}}\left(\frac{\lambda_{eq,i}\lambda_{eq,i+1}}{\lambda_{eq,i} + \lambda_{eq,i+1}}\right) \tag{3.97}$$

$$\frac{\partial q_{i,i-1/2}}{\partial U_i} = -\frac{\lambda_{eq,i-1}\lambda_{eq,i}}{\frac{1}{2}\Delta x(\lambda_{eq,i-1} + \lambda_{eq,i})}\frac{\partial T_i}{\partial U_i} - \frac{T_i - T_{i-1}}{\frac{1}{2}\Delta x}\frac{\partial}{\partial U_i}\left(\frac{\lambda_{eq,i-1}\lambda_{eq,i}}{\lambda_{eq,i-1} + \lambda_{eq,i}}\right) \tag{3.98}$$

$$\frac{\partial q_{i,i-1/2}}{\partial U_{i-1}} = \frac{\lambda_{eq,i-1}\lambda_{eq,i}}{\frac{1}{2}\Delta x(\lambda_{eq,i-1} + \lambda_{eq,i})}\frac{\partial T_{i-1}}{\partial U_{i-1}} - \frac{T_i - T_{i-1}}{\frac{1}{2}\Delta x}\frac{\partial}{\partial U_{i-1}}\left(\frac{\lambda_{eq,i-1}\lambda_{eq,i}}{\lambda_{eq,i-1} + \lambda_{eq,i}}\right) \tag{3.99}$$

With :

$$\frac{1}{T} = \frac{\rho Y_1(\gamma_1 - 1)C_{v,1}}{P + P_{\infty,1}} + \frac{\rho Y_2(\gamma_2 - 1)C_{v,2}}{P + P_{\infty,2}} \tag{3.100}$$

$$\frac{\partial \lambda_{eq,i}}{\partial U_i} = \lambda_1 \frac{\partial \alpha_{i,1}}{\partial U_i} + \lambda_2 \frac{\partial \alpha_{i,2}}{\partial U_i} \tag{3.101}$$

$$\begin{aligned} \frac{\partial T_i}{\partial U_i} = &-T_i^2 \left[(\gamma_1 - 1)C_{v,1} \left(\frac{\frac{\partial y_{i,1}}{\partial U_i}(P_i + P_{\infty,1}) - y_{i,1}\frac{\partial P_i}{\partial U_i}}{(P_i + P_{\infty,1})^2} + \right) \right] \\ &+ -T_i^2 \left[(\gamma_2 - 1)C_{v,2} \left(\frac{\frac{\partial y_{i,2}}{\partial U_i}(P_i + P_{\infty,2}) - y_{i,2}\frac{\partial P_i}{\partial U_i}}{(P_i + P_{\infty,2})^2} + \right) \right] \end{aligned} \tag{3.102}$$

Where :

$$y_{i,k} = \rho Y_k \tag{3.103}$$

$$\begin{aligned} \frac{\partial \alpha_{i,k}}{\partial U_i} &= \frac{\partial \frac{y_{i,k}}{\rho_k}}{\partial U_i} \\ \frac{\partial \alpha_{i,k}}{\partial U_i} &= (\gamma_k - 1)C_{v,k} \left[\frac{(T_i \frac{\partial y_{i,k}}{\partial U_i} + y_{i,k}\frac{\partial T_i}{\partial U_i})(P_i + P_{\infty,k}) - y_{i,k}T_i\frac{\partial P_i}{\partial U_i}}{(P_i + P_{\infty,k})^2} \right] \end{aligned} \tag{3.104}$$

The pressure derivative, $\frac{\partial P_i}{\partial U_i}$, is computed using Relation (3.94)

Appendix C - Surface and body forces derivatives

• The derivatives corresponding to the surface tension effects are first considered :
The curvature, κ_{ij}^n, being taken as constant in each cell, expression (3.65) is used to obtain the derivatives :

$$\frac{\partial \overrightarrow{\nabla C}_{ij}^n}{\partial U_{ij}} = 0, \quad \frac{\partial \overrightarrow{\nabla C}_{ij}^n}{\partial U_{i-1j}} = -\frac{1}{2\Delta x}\frac{\partial C_{i-1j}^n}{\partial U_{i-1j}}, \quad \frac{\partial \overrightarrow{\nabla C}_{ij}^n}{\partial U_{i+1j}} = \frac{1}{2\Delta x}\frac{\partial C_{i+1j}^n}{\partial U_{i+1j}} \tag{3.105}$$

$$\frac{\partial \overrightarrow{\nabla C}_{ij}^n}{\partial U_{ij-1}} = -\frac{1}{2\Delta y}\frac{\partial C_{ij-1}^n}{\partial U_{ij-1}}, \quad \frac{\partial \overrightarrow{\nabla C}_{ij}^n}{\partial U_{ij+1}} = \frac{1}{2\Delta y}\frac{\partial C_{ij+1}^n}{\partial U_{ij+1}} \tag{3.106}$$

The color function being part of the unknown vector, U, its derivative is very simple.

• The derivatives corresponding to the gravity term read :

$$\frac{\partial \rho_{ij}\mathbf{g}}{\partial U_{ij}} = \mathbf{g}\frac{\partial \rho_{ij}}{\partial U_{ij}} \tag{3.107}$$

$$\frac{\partial \rho_{ij}\mathbf{g}\cdot\mathbf{u}_{ij}}{\partial U_{ij}} = \mathbf{g}\frac{\partial \rho_{ij}\mathbf{u}}{\partial U_{ij}} \tag{3.108}$$

Variables ρ_{ij} and $\rho_{ij}\mathbf{u}$ being part of the unknown vector, U, their derivatives are very simple.

Conclusion générale

Un modèle "d'interfaces diffuses" pour la simulation numérique directe d'écoulements bouillants à été développé. Ce modèle est composé, d'une part, d'un modèle d'écoulement diphasique en équilibre mécanique et thermique (les phases ont même pressions, vitesses et températures) et d'autre part, de termes permettant la prise en compte des nombreux phénomènes physiques mis en jeu dans l'ébullition tels que la tension de surface, la conduction de la chaleur ou encore le changement de phase. Associée à ce modèle, une méthode numérique permettant d'obtenir des résultats précis quels que soient les nombres de Mach présents dans l'écoulement a été mise en place.

Cet ensemble (modèle et méthode numérique) a été validé en utilisant des solutions analytiques mono-dimensionnelles et a permis la simulation numérique d'écoulements bouillants multidimensionnels. Les résultats de ces simulations montrent un comportement qualitatif très réaliste et intéressant permettant de s'assurer des capacités de la méthode. De plus, cette approche appliquée à un modèle d'écoulement diphasique en équilibre mécanique a aussi montré son efficacité pour la simulation des écoulements cavitants.
Ainsi, au niveau des perspectives, deux voies sont envisageables : la continuité de ces travaux en direction de la simulation 3D d'écoulements bouillants et l'utilisation des méthodes et modèles présentés dans ce manuscrit pour d'autres applications.

En ce qui concerne la simulation d'écoulements bouillants, on peut distinguer deux applications dont le but est le même, le refroidissement des moteurs spatiaux et le refroidissement des réacteurs nucléaires, le but étant la détermination de coefficients d'échanges de chaleur. Les étapes nécessaires restantes peuvent se résumer sous la forme suivante :
1] Extension de la méthode pour la réalisation de simulations 3D d'ébullition avec de nombreux sites de nucléation.
2] Travail sur l'efficacité des méthodes numériques car il s'agit de simulations très coûteuses en temps de calcul.
3] Introduction des effets visqueux.
4] Prise en compte des géométries complexes représentatives des géométries réelles.
5] Modélisation de l'angle de contact.
6] Validation des simulations sur des solutions analytiques et sur des tests en condition réelles.
7] Déterminations des coefficients d'échanges.

De plus, dans le cadre l'ingénierie des systèmes spatiaux, il faudrait utiliser des fluides cryogéniques dans les simulations.

Au niveau des autres applications possibles pour les modèles et méthodes numériques détaillés dans ce manuscrit, on peut citer les écoulements cavitants à hautes vitesses et la fragmentation de jets multiphasiques. Pour la première application (cavitation), l'exemple le plus connu est l'écoulement à l'intérieur des turbo-pompes spatiales où la cavitation est omniprésente et engendre des pertes de performance ainsi qu'une dégradation non-négligeable du matériel. Ainsi, avec la méthode présentée au chapitre 1, il serait possible, moyennant une extension à des géométries complexes, de traiter correctement ce type d'écoulement.

En ce qui concerne les jets multiphasiques, on retrouve, à nouveau, une application dans le domaine spatial, au niveau des injecteurs. En effet, il est possible d'avoir une injection simultanée de deux fluides dont les jets se fragmentent en changeant de phase simultanément. De ce fait, traiter ce type d'écoulement requiert la prise en compte de la tension de surface ainsi que du changement de phase liquide/vapeur au sein d'un écoulement multiphasique. La méthode présentée au chapitre 3 pourrait être étendue à ce type d'écoulement en considérant plus de deux phases et en tenant compte de la tension de surface pour plusieurs couples liquide/vapeur.

Bibliographie

[1] R. Abgrall. How to prevent pressure oscillations in multicomponent flow calculations : A quasi conservative approach. *Journal of Computational Physics*, 125 :150–160, 1996.

[2] T. Alazard. Low Mach number limit of the full Navier-Stokes equations. *Arch. Ration. Mech. Anal.*, 180(1) :1–73, 2006.

[3] D.M. Anderson, G.B. McFadden, and A.A. Wheeler. Diffuse-interface methods in fluid mechanics. *Annual Review of Fluid Mechanics*, 30 :139–165, 1998.

[4] D.P. Babii, S.K.Godunov, V.T. Zhukov, and O.B. Feodoritova. On the different approximations of overdetermined hyperbolic equations of classical mathematical physics. *Comp. Mathematics and Mathematics Physics*, 47(3) :427–441, 2007.

[5] M.R. Baer and J.W. Nunziato. A two-phase mixture theory for the deflagration-to-detonation transition (ddt) in reactive granular materials. *International Journal of Multiphase Flow*, 12(6) :861 – 889, 1986.

[6] S. Balay, J. Brown, K. Buschelman, V. Eijkhout, W. D. Gropp, D. Kaushik, M. G. Knepley, L. Curfman McInnes, B. F. Smith, and H. Zhang. PETSc users manual. Technical Report ANL-95/11 - Revision 3.4, Argonne National Laboratory, 2013.

[7] S. Balay, J. Brown, K. Buschelman, W. D. Gropp, D. Kaushik, M. G. Knepley, L. Curfman McInnes, B. F. Smith, and H. Zhang. PETSc Web page, 2013. http ://www.mcs.anl.gov/petsc.

[8] S. Balay, W. D. Gropp, L. Curfman McInnes, and B. F. Smith. Efficient management of parallelism in object oriented numerical software libraries. In E. Arge, A. M. Bruaset, and H. P. Langtangen, editors, *Modern Software Tools in Scientific Computing*, pages 163–202. Birkhäuser Press, 1997.

[9] F. Barre and M. Bernard. The Cathare code strategy and assessment. *Nuclear Engineering and Design*, 124(3) :257–284, 1990.

[10] S. Barre, J. Rolland, G. Boitel, E. Goncalves, and R. Fortes-Patella. Experiments and modeling of cavitating flows in Venturi : Attached sheet cavitation. *European Journal of Mechanics - B/Fluids*, 28(3) :444 – 464, 2009.

[11] M. Barret, E. Faucher, and J.-M. Hérard. Schemes to Compute Unsteady Flashing Flows. *AIAA Journal*, 40 :905–913, May 2002.

[12] T.J. Barth and D.C. Jespersten. The design and application of upwind schemes on unstructured meshes. *Proceedings of the AIAA 27th Aerospace Sciences Meeting (Reno, Nevada)*, 1989.

[13] R. A. Berry, R. Saurel, and O. LeMetayer. The discrete equation method (DEM) for fully compressible, two-phase flows in ducts of spatially varying cross-section. *Nuclear Engineering and Design*, 240(11) :3797 – 3818, 2010.

[14] P. Birken, G. Gassner, M. Haas, and C.D. Munz. Preconditioning for modal discontinuous galerkin methods for unsteady 3d navier-stokes equations. *Journal of Computational Physics*, 240(0) :20 – 35, 2013.

[15] P. Birken and A. Meister. On low Mach number preconditioning of finite volume schemes. *Proc. Appl. Math. Mech.*, 5 :759–760, 2005.

[16] J.U Brackbill, D.B Kothe, and C. Zemach. A continuum method for modeling surface tension. *Journal of Computational Physics*, 100(2) :335 – 354, 1992.

[17] B. Braconnier and B. Nkonga. An all-speed relaxation scheme for interface flows with surface tension. *Journal of Computational Physics*, 228(16) :5722 – 5739, 2009.

[18] J. Cahn and J. Hilliard. Free energy of a nonuniform system. part i : Interfacial free energy. *Journal of Chemical Physics*, 28 :258, 1958.

[19] A. Chinnayya, E. Daniel, and R. Saurel. Modelling detonation waves in heterogeneous energetic materials. *Journal of Computational Physics*, 196(2) :490–538, 2004.

[20] Y.H. Choi and C.L. Merkle. The application of preconditioning is viscous flows. *Journal of Computational Physics*, 105(2) :207–223, 1993.

[21] P. Clavin and P. Garcia. The influence of the temperature dependence of diffusivities on the dynamics of flame fronts. *Journal de Mécanique Théorique et Appliquée*, 2(2) :245–263, 1983.

[22] S. Clerc. Numerical simulation of the homogeneous equilibrium model for two-phase flows. *Journal of Computational Physics*, 161(1) :354 – 375, 2000.

[23] S.F. Davis. Simplified second-order Godunov-type methods. *SIAM J. Sci. Statist. Comput.*, 9 :445–473, 1988.

[24] S. Dellacherie, P. Omnes, and F. Rieper. The influence of cell geometry on the Godunov scheme applied to the linear wave equation. *Journal of Computational Physics*, 229(14) :5315 – 5338, 2010.

[25] P. Downar-Zapolski, Z. Bilicki, L. Bolle, and J. Franco. The non-equilibrium relaxation model for one-dimensional flashing liquid flow. *International Journal of Multiphase Flow*, 22(3) :473 – 483, 1996.

[26] D. G. Ebin. The motion of slightly compressible fluids viewed as a motion with strong constraining force. *Ann. of Math*, 105(1) :141–200, 1977.

[27] G. Faccanoni, S. Kokh, and G. Allaire. Numerical simulation with finite volume of dynamic liquid-vapor phase transition. In ISTE and Wiley, editor, *5nd International Symposium on : Finite volumes for complex applications - Problems and perspective*, page 391–398, 2008.

[28] G. Faccanoni, S. Kokh, and G. Allaire. Modelling and simulation of liquid-vapor phase transition in compressible flows based on thermodynamical equilibrium. *ESAIM : Mathematical Modelling and Numerical Analysis*, 46 :1029–1054, 8 2012.

[29] N. Favrie, S.L. Gavrilyuk, and R. Saurel. Solid-fluid diffuse interface model in cases of extreme deformations. *Journal of Computational Physics*, 228(16) :6037 – 6077, 2009.

[30] R. Fedkiw, T. Aslam, B. Merriman, and S. Osher. A non-oscillatory Eulerian approach to interfaces in multimaterial flows (the Ghost Fluid Method). *Journal of Computational Physics*, 152(2) :457–492, 1999.

[31] T. Flåtten and H. Lund. Relaxation two-phase flow models and the subcharacteristic condition. *Mathematical Models and Methods in Applied Sciences*, 21(12) :2379–2407, 2011.

[32] R. Fortes-Patella, O. Coutier-Delgosha, and J.L. Reboud. Evaluation of the turbulence model influence on the numerical simulations of unsteady cavitation. *J. Fluid Engineering*, 125(1) :38–45, 2003.

[33] Matteo Frigo and Steven G. Johnson. The design and implementation of FFTW3. *Proceedings of the IEEE*, 93(2) :216–231, 2005. Special issue on "Program Generation, Optimization, and Platform Adaptation".

[34] J. Giesselmann. *Modelling and Analysis for Curvature Driven Partial Differential Equations*. PhD thesis, Department of Mathematics and Physics, University of Stuttgart, München, Germany, 2011.

[35] J. Glimm, J.W. Grove, X.L. Li, K.M. Shyue, Q. Zhang, and Y. Zeng. Three dimensional front tracking. *SIAM J. Scientific Computing*, 19 :703–727, 1998.

[36] S.K. Godunov. A difference method for numerical calculation of discontinuous solutions of the equations of hydrodynamics. *Mat. Sb. (N.S.)*, 47(89) :271–306, 1959.

[37] S.K. Godunov. *Equations of mathematical physics*. Nauka, Moscow, 1979.

[38] H. Guillard and C. Viozat. On the behaviour of upwind schemes in the low Mach number limit. *Computers and Fluids*, 28 :63–86, 1999.

[39] Hervé Guillard. On the behavior of upwind schemes in the low Mach number limit. IV : P0 approximation on triangular and tetrahedral cells. *Computers and Fluids*, 38(10) :1969 – 1972, 2009.

[40] F. Harlow and A. Amsden. Fluid dynamics. *Monograph LA, Los Alamos National Laboratory, Los Alamos,NM*, LA-4700 :1678–1712, 1971.

[41] F. Harlow and A. Amsden. A numerical fluid dynamics calculation method for all flow speeds. *Journal of Computational Physics*, 8(2) :197 – 213, 1971.

[42] A. Harten, P.D. Lax, and B. van Leer. On upstream differencing and Godunov-type schemes for hyperbolic conservation laws. *SIAM Rev.*, 25 :35–61, 1983.

[43] D.R. Hartree. Some practical methods of using characteristics in the calculation of non-steady compressible flow. Technical report, Harvard Univ., 1953.

[44] C.W. Hirt and B.D. Nichols. Volume of fluid (VOF) method for the dynamics of free boundaries. *Journal of Computational Physics*, 3 :201–255, 1981.

[45] D. Jamet, O. Lebaigue, N. Coutris, and J.M. Delhaye. The second gradient method for the direct numerical simulation of liquid-vapor flows with phase change. *Journal of Computational Physics*, 169(2) :624–651, 2001.

[46] D. Juric and G. Tryggvason. Computations of boiling flows. *International Journal of Multiphase Flow*, 24(3) :387 – 410, 1998.

[47] A.K. Kapila, R. Menikoff, J.B. Bdzil, S.F. Son, and D.S. Stewart. Two-phase modeling of of deflagration-to-detonation transistion in granular materials : Reduced equations. *Physics of Fluids*, 13 :3002–3024, 2001.

[48] S. Klainerman and A. Majda. Singular limits of quasilinear hyperbolic systems with large parameters and the incompressible limit of compressible fluids. *Comm. Pure Appl. Math*, 34(4) :481–524, 1981.

[49] S. Kokh and F. Lagoutière. An anti-diffusive numerical scheme for the simulation of interfaces between compressible fluids by means of a five-equation model. *Journal of Computational Physics*, 229(8) :2773 – 2809, 2010.

[50] R. F. Kunz, D. A. Boger, D. R. Stinebring, T. S. Chyczewski, J. W. Lindau, H. J. Gibeling, S. Venkateswaran, and T.R. Govindan. A preconditioned Navier-Stokes method for two-phase flows with application to cavitation prediction. *Computers and Fluids*, 29(8) :849 – 875, 2000.

[51] B. Lafaurie, C.Nardone, R. Scardovelli, S. Zaleski, and G. Zanetti. Modelling merging and fragmentation in multiphase flows with SURFER. *Journal of Computational Physics*, 113 :134–147, 1994.

[52] O. Le Métayer, J. Massoni, and R. Saurel. Élaboration des lois d'état d'un liquide et de sa vapeur pour les modèles d'écoulements diphasiques. *International Journal of Thermal Sciences*, 43(3) :265 – 276, 2004. in French.

[53] S. LeMartelot, B. Nkonga, and R. Saurel. Liquid and liquid-gas flows at all speed. *Journal of Computational Physics*, 255(0) :53 – 82, 2013.

[54] S. LeMartelot, R. Saurel, and O. Le Métayer. Steady one-dimensional nozzle flow solutions of liquid-gas mixtures. *Journal of Fluid Mechanics*, 737 :146–175, 2013.

[55] S. LeMartelot, R. Saurel, and B. Nkonga. Towards the direct numerical simulation of nucleate boiling flows. *Internation Journal of Multiphase Flow - Submitted*, 2013.

[56] H. Lund. A hierarchy of relaxation models for two-phase flow. *SIAM J. Applied Math*, 72(6) :1713–1741, 2012.

[57] DJ. Mavripilis. Revisiting the least-squares procedure for gradient reconstruction on unstructured meshes. *AIAA 16th Computational Fluid Dynamics Conference*, page 3986, 2003.

[58] T. Menard, S. Tanguy, and A. Berlemont. Coupling Level Set/VOF/Ghost Fluid methods. Validations and application to 3D simulation of the primary break-up of a liquid jet. *Int. J. of Multiphase Flow*, 33(5) :510–524, 2007.

[59] R. Menikoff and B.J. Plohr. The Riemann problem for fluid flow of real materials. *Rev. Mod. Phys.*, 61 :75–130, 1989.

[60] G. Metivier and S. Schochet. The incompressible limit of the non-isentropic Euler equations. *Arch. Ration. Mech. Anal.*, 158(1) :61–90, 2001.

[61] G. Moretti and M. Abbett. A time-dependent computational method for blunt body flows. *AIAA Journal*, 4(12) :2136–2141, 1966.

[62] A. Murrone and H. Guillard. Behavior of upwind scheme in the low Mach number limit : III. preconditioned dissipation for a five equation two phase model. *Computers and Fluids*, 37(10) :1209 – 1224, 2005.

[63] S. Osher and S. Chakravarthy. Upwind schemes and boundary conditions with applications to euler equations in general geometries. *Journal of Computational Physics*, 50(3) :447 – 481, 1983.

[64] G. Perigaud and R. Saurel. A compressible flow model with capillary effects. *Journal of Computational Physics*, 209 :139–178, 2005.

[65] F. Petitpas, E. Franquet, R. Saurel, and O. Le Metayer. A relaxation-projection method for compressible flows. Part II : Artificial heat exchanges for multiphase shocks. *Journal of Computational Physics*, 225(2) :2214 – 2248, 2007.

[66] F. Petitpas, J. Massoni, R. Saurel, E. Lapebie, and L. Munier. Diffuse interface model for high speed cavitating underwater systems. *International Journal of Multiphase Flow*, 35(8) :747 – 759, 2009.

[67] F. Petitpas, R. Saurel, E. Franquet, and A. Chinnayya. Modelling detonation waves in condensed energetic materials : Multiphase CJ conditions and multidimensionnal computations. *Shock Waves*, 19 :377–401, 2009.

[68] V.H. Ransom, J.A. Trapp, and R.J. Wagner. Relap/mod3 code manual. *NUREG/CR-5535, INEL-95/0174*, 1995.

[69] Y. Saad. *Numerical methods for large eigenvalue problems.* Manchester University Press, 1992.

[70] R. Saurel and R. Abgrall. A multiphase Godunov method for multifluid and multiphase flows. *Journal of Computational Physics*, 150 :425–467, 1999.

[71] R. Saurel, O. Le Métayer, J. Massoni, and S. Gavrilyuk. Shock jump relations for multiphase mixtures with stiff mechanical relaxation. *Shock Waves*, 16 :209–232, 2007.

[72] R. Saurel, N.Favrie, F.Petitpas, M-H.Lallemand, and S.L. Gavrilyuk. Modelling dynamic and irreversible powder compaction. *Journal of Fluid Mechanics*, 664 :348–396, 2010.

[73] R. Saurel, F. Petitpas, and R. Abgrall. Modelling phase transition in metastable liquids : Application to cavitating and flashing flows. *Journal of Fluid Mechanics*, 607 :313–350, 2008.

[74] R. Saurel, F. Petitpas, and R. A. Berry. Simple and efficient methods relaxation for interfaces separating compressible fluids, cavitating flows and shocks in multiphase mixtures. *J. Comput. Phys.*, 228 :1678–1712, 2009.

[75] S. Schoch, N. Nikiforakis, B. J. Lee, and R. Saurel. Multi-phase simulation of ammonium nitrate emulsion detonations. *Combustion and Flame*, (0) :–, 2013.

[76] S. Schochet. The compressible Euler equations in a bounded domain : Existence of solutions and the incompressible limit. *Comm. Math. Phys.*, 104(1) :49–75, 1986.

[77] R. Shukla, C. Pantano, and J. Freund. An interface capturing method for the simulation of multi-phase compressible flows. *Journal of Computational Physics*, 229(19) :7411 – 7439, 2010.

[78] J. R. Simoes-Moreira and J. E. Shepherd. Evaporation waves in superheated dodecane. *J. Fluid Mech*, 382 :63–86, 1999.

[79] K.K. So, X.Y. Hu, and N.A. Adams. Anti-diffusion interface sharpening technique for two-phase compressible flow simulations. *Journal of Computational Physics*, 231(11) :4304 – 4323, 2012.

[80] E.F. Toro, M. Spruce, and W. Speares. Restoration of the contact surface in the HLL-Riemann solver. *Shock Waves*, 4 :25–34, 1994.

[81] G. Tryggvason, B. Bunner, A. Esmaeeli, D. Juric, N. Al-Rawahi, W. Tauber, J. Han, S. Nas, and Y.-J. Jan. A front-tracking method for the computations of multiphase flow. *Journal of Computational Physics*, 169(2) :708–759, 2001.

[82] E. Turkel. Preconditioned methods for solving the incompressible and low speed compressible equations. *Journal of Computational Physics*, 72(2) :277 – 298, 1987.

[83] E. Turkel and N.V. Vatsa. Local preconditioners for steady and unsteady flow applications. *ESAIM : Mathematical Modelling and Numerical Analysis*, 39 :515–535, 2005.

[84] B. Van Leer. Towards the ultimate conservative difference scheme, V.A second order sequel to Godunov's method. *J. Comput. Phys.*, 32 :445–473, 1979.

[85] Sankaran Venkateswaran, Jules W. Lindau, Robert F. Kunz, and Charles L. Merkle. Computation of multiphase mixture flows with compressibility effects. *Journal of Computational Physics*, 180(1) :54 – 77, 2002.

[86] P.P. Wegener. *Nonequilibrium flow*. Marcel Dekker Inc., New York, 1969.

[87] A. B. Wood. *A textbook of sound*. Bell Eds, 1930.